Università degli Studi di Padova

Università degli Studi di Padova
Centro Interdipartimentale "Centro Ricerche Fusione"

Universidade Técnica de Lisboa
instituto superior técnico

joint research doctorate in fusion science and engineering
Cycle XXVII

Wall conditioning studies and plasma-facing materials qualification for magnetically confined fusion experiments

Coordinator: Ch.mo Prof. Paolo Bettini

Supervisor: Ch.mo Prof. Leonardo Giudicotti

Supervisor: Dott.ssa Alessandra Canton

Supervisor: Dott. Paolo Innocente

Doctoral student: Bilel Rais

January 31, 2015

بِسْمِ ٱللَّهِ ٱلرَّحْمَٰنِ ٱلرَّحِيمِ

In the name of God, the Beneficent, the Merciful

لِأَبِي، رَحِمَهُ ٱللَّه

To my father, may God bless his soul

Abstract

In the framework of magnetically confined fusion plasmas, achieving a comprehensive understanding of Plasma-Wall Interaction (PWI) is fundamental to attain the improved confinement regimes, needed to produce fusion energy. A major issue is the lack of plasma density control observed in devices equipped with a carbon first wall. Carbon Plasma First Components (PFCs) offer the advantage of withstanding high power loads that can reach tens of MW/m^2, but present the drawback of high retention of hydrogenic fuel particles. Fuel recycling, that is the churning action of these retained fuel particles between the hotter fusion plasma edge and the colder plasma facing first wall surfaces, presents often a factor exceeding 1 and makes the task of density control extremely difficult.

Wall conditioning techniques have proven to be a great tool to overcome the carbon limiting performance factor. In the DIII-D tokamak [1] very high confinement regimes (VH-modes) were attained by solely applying a thin boron film on the plasma facing surfaces; earlier in the Tokamak Fusion Test Reactor (TFTR) [2] significant improvements in 'supershot' performances leading to a near doubling of the fusion power output were observed for the first time by injecting as small as a few milligrams of lithium during plasma discharges. The implementation and the optimization of wall conditioning techniques, together with the study of new Plasma Facing Materials (PFMs) is therefore clearly fundamental.

As many other fusion devices, RFX-mod is equipped with a polycrystalline graphite first wall. Improved confinement regimes were found during high current operation, the so called Single Helical-Axis states (SHAx) [3], characterized by a helical deformation of the plasma column and the formation of an internal transport barrier. However, the full attainment of such improved confinement regimes is hindered by a lack of density control. To address this issue, a set of wall conditioning techniques has been implemented, including Helium Glow Discharge Cleaning (HeGDC), boron wall conditioning by B_2H_6 + He glow discharge and recently lithium wall-coating by means of pellet injection and lithium evaporation. However the beneficial effects of these techniques on RFX-mod plasmas are limited due to a lack of optimization and understanding of the fundamental mechanisms that govern the enhanced PWI observed upon the conditioning of the first wall surfaces.
In this thesis, the optimization and further implementation of the wall

conditioning techniques has been undertaken. First, HeGDC has been characterized in terms of the glow discharge experimental parameters. Next, its efficiency combined with He plasma power discharges is examined in terms of H wall-depleting. On the other hand, a set of surface science techniques including SIMS, XPS, AES, EDS/X, SEM and RBS has been set up to investigate by *ex-situ* post-mortem analyses the underlining physical and chemical properties of boron and lithium thin film deposition after boron and lithium wall conditioning. Regarding the GDC optimization the main result is that a strong toroidal asymmetry was found and confirmed by measurements of the ion flux to the wall. Moreover, the preliminary analysis of intershot HeGDC wall cleaning strategy was found promising. With respect to the boronization optimization, evidence of a two-step boron growth with increasing glow discharge power was found. As for lithium wall conditioning, a correlation among the injected lithium dose and the chemical fraction of lithium carbonate was found.

Ultimately, a transition towards a metallic first wall in RFX-mod offering a low recycling surface has been recently considered as an alternative solution-path to overcome the graphite first wall drawbacks. Tungsten (W) coatings on graphite samples have been elaborated using two different Physical Vapor Deposition (PVD) techniques: High Power Impulse Magnetron Sputtering (HiPIMS) technique developed at the CNR-IENI laboratory in Padova, Italy, and Combined Magnetron Sputtering and Ion Implantation (CMSII) technology developed at MEdC-Romanian Euratom Association. The W-coatings were preliminary characterized by Scanning Electron Microscopy (SEM) and tested with adherence tests before exposing them to RFX-mod plasmas. Plasma exposure was made in experimental sessions of about 15 discharges, during which the interaction with the plasma has been locally enhanced by the active control system of the magnetic boundary in order to simulate the conditions of the PWI events. The CMSII technique, that gave the minor faults at the first stage, was then tested on full scale dimension by replacing 4 actual RFX-mod carbon tiles with W-coated ones. The tiles have been exposed to three months of normal RFX-mod operation over a large range of operational conditions, after which large damaged areas have been observed. The size of these damages and particularly the removal of the coating in some areas and its melting may discard this solution-path towards such a metallic PFC transition in RFX-mod. Thicker 100-200 μm W-coatings, that are still compatible with wall weight tolerance of RFX-mod mechanical structure, may offer a better solution for the machine upgrade.

Prefazione

Nell'ambito dei plasmi da fusione a confinamento magnetico, conseguire una comprensione globale dell'interazione plasma-parete è fondamentale per raggiungere regimi di confinamento migliorati, necessari per la produzione di energia da fusione. Un'aspetto problematico è la mancanza di controllo della densità di plasma, osservata in macchine con la prima parete in carbonio. Componenti in carbonio di fronte al plasma hanno il vantaggio di sopportare elevati carichi di energia, che possono raggiungere decine di MW/m^2, ma presentano lo svantaggio di un'alta ritenzione delle particelle di idrogeno presenti nel combustibile. Il riciclaggio di combustibile, cioé l'azione di scambio di queste particelle di combustibile tra la parte esterna e calda del plasma e la prima parete, presenta spesso un fattore superiore a 1 e rende il compito del controllo della densità estremamente difficile.

Le tecniche di condizionamento della prima parete hanno dimostrato gran successo come strumento per superare tale fattore limitante del carbonio. Nel tokamak DIII-D [1] sono stati raggiunti dei regimi di confinamento molto elevati (VH-mod) applicando solamente una pellicola sottile di boro sulla superficie della parete. Inoltre nel tokamak TFTR [2] sono stati osservati dei miglioramenti significativi nelle prestazioni 'SuperShot' che iniettando pochi milligrammi di litio durante scariche di plasma portano a un quasi raddoppio della potenza di fusione. E' fondamentale quindi l'implementazione e l'ottimizzazione delle tecniche di condizionamento della prima parete, insieme con lo studio di nuovi materiali.

RFX-mod come molte altre macchine da fusione, è dotato di una prima parete in grafite policristallina. Regimi di confinamento migliorati sono stati raggiunti ad alta corrente di plasma, i cosiddetti stati SHAx [3], caratterizzati da una deformazione elicoidale della colonna di plasma e dalla formazione di barriere di trasporto interno. Tuttavia, il pieno raggiungimento di tali regimi è stato ostacolato da una mancanza di controllo della densità. Per risolvere questo problema, è stato attuato un'insieme di tecniche di condizionamento della parete, tra cui scariche di plasma a basso livello di ionizzazione in elio (HeGDC), parete condizionata in boro utilizzando, B_2H_6 in scariche glow di elio e recentemente trattamento della parete con litio mediante iniezione pellet ed evaporazione di litio. Tuttavia gli effetti benefici di queste tecniche sui plasmi RFX-mod sono limitate a causa della mancanza di ottimizzazione e di comprensione

dei meccanismi fondamentali che governano la maggiore interazione plasma-parete.
In questa tesi è stata studiata l'ottimizzazione e l'ulteriore attuazione delle tecniche di condizionamento. HeGDC è stata caratterizzata in termini di parametri sperimentali, quindi la sua efficienza è stata esaminata in termini di H emesso dalla parete, in combinazione con scariche di plasma in He. D'altra parte, un insieme di tecniche di scienza delle superfici, tra cui SIMS, XPS, AES, EDS/X, SEM e RBS sono state utilizzate per indagare, attraverso *ex-situ* analisi post mortem, le proprietà fisiche e chimiche dei film sottili di boro e litio dopo il condizionamento della parete. Per quanto riguarda l'ottimizzazione della GDC il risultato principale è che una forte asimmetria toroidale è stata osservata e confermata dalle misure spettroscopiche. L'analisi preliminare di HeGDC tra scariche sperimentali come stategia per la pulizia della parete è promettente. Per quanto riguarda l'ottimizzazione della boronizzazione, è stata trovata evidenza di una crescita di deposizione di boro aumentando la potenza della scarica glow. Per quanto riguarda il condizionamento della parete con il litio, una correlazione tra la dose di litio utilizzata e la frazione di carbonato di litio è stata trovata.

Infine è stata recentemente considerata una transizione verso una prima parete metallica in RFX-mod, come una soluzione alternativa per superare gli inconvenienti della prima parete in grafite, in quanto offre un minor riciclaggio. Rivestimenti in tungsteno su campioni di grafite sono state elaborati utilizzando due diverse tecniche Physical Vapor Deposition (PVD): High Power Impulse Magnetron Sputtering (HiPIMS) è una tecnica sviluppata a livello locale presso il laboratorio CNR-IENI e Combined Magnetron Sputtering and Ion Implantation (CMSII), sviluppata presso il laboratorio MEdC-Rumeno Euratom Association. I rivestimenti di tungsteno sono stati preliminarmente caratterizzati da SEM e testati con prove di aderenza prima di esporli al plasma. L'esposizione al plasma è stata fatta in sessioni sperimentali che comprendono circa 15 scariche, durante le quali l'interazione con il plasma è stata migliorata localmente dal sistema di controllo attivo del limite magnetica per simulare le condizioni degli eventi di interazione plasma-parete. La tecnica CMSII, che ha dato i difetti minori nella prima fase, è stata poi testata sulle dimensioni di macchina sostituendo 4 attuali tegole di carbonio in RFX-mod con quelle rivestite in tungsteno. Le tegole sono state esposte a tre mesi di normale funzionamento in RFX-mod, e sottoposte ad una vasta gamma di condizioni operative; dopo tale esposizione sono state osservate grandi aree danneggiate. La dimensione di questi danni e in particolare la rimozione del rivestimento in alcune aree e la sua fusione potrebbero scartare questa soluzione verso una prima parete metallica in RFX-mod. Rivestimenti in W più spessi, dell'ordine di 100-200 μm, che siano compatibili con la tolleranza sul peso della parete nella struttura meccanica di RFX-mod possono offrire una migliore soluzione per l'upgrade della macchina.

Resumo

No âmbito dos plasmas de fusão confinados magneticamente, para atingir os regimes de confinamento melhorados, necessários para produzir a energia de fusão, é fundamental alcançar uma compreensão completa da interação plasma-parede. Um problema central é a falta de controle de densidade plasma observada em dispositivos equipados com uma primeira parede de carbono. PFCs de Carbono oferecem a vantagem de suportar altas cargas de energia que podem chegar a dezenas de MW/M^2, mas apresentam a desvantagem de alta retenção de partículas de combustível hidrogenóides. A reciclagem do combustível, que é a ação de agitação destas partículas de combustível retido entre a aresta mais quente do plasma de fusão e o plasma frio das superfícies em contacto com a primeira parede, apresenta muitas vezes um fator superior a 1 e torna a tarefa de controlo de densidade extremamente difícil.

Técnicas de condicionamento da parede provaram ser uma poderosa ferramenta para superar o fator limitante do desempenho de carbono. No tokamak DIII-D [1] regimes muito elevados de confinamento (modos VH) foram atingidos ao aplicar unicamente uma película fina de boro no plasma em contacto com as superfícies; no início do TFTR [2] foram observadas melhorias significativas no desempenho dos 'Supershot' levando pela primeira vez a uma quase duplicação da produção de energia de fusão através da injeção de meros miligramas de lítio durante as descargas de plasma. A implementação e otimização de técnicas de condicionamento da parede, juntamente com o estudo de novos PFMs são, portanto, inequivocamente fundamentais.

Como muitos outros dispositivos de fusão, o RFX-mod está equipado com grafite policristalino na primeira parede. Regimes de confinamento aperfeiçoados foram encontrados durante a operação com corrente elevada, os denominados 'estados uniaxiais helicoidais' (SHAx) [3], caracterizados por uma deformação helicoidal da coluna de plasma e a formação de barreiras de transporte interno. No entanto, a realização plena de tais regimes de confinamento melhorado é dificultado pela falta de controlo de densidade. Para resolver esse problema, um conjunto de técnicas de condicionamento da parede foram implementadas, incluindo HeGDC, parede de boro condicionada por uma descarga luminescente de B_2H_6 + He e recentemente revestimento de lítio na parede através da injeção de pastilha e evaporação de lítio. No entanto, os efeitos benéficos destas técnicas sobre

os plasmas do RFX-mod são limitados devido à falta de compreensão dos mecanismos fundamentais que governam a interação plasma-parede (PWI) melhorada que é observada quando ocorre condicionamento das superfícies primeira parede, consequentemente limitados também devido à falta de otimização destes mecanismos. Nesta tese foi realizada a otimização e implementação das técnicas de condicionamento da parede. HeGDC foi caracterizada em termos dos parâmetros experimentais de descarga luminescente, e seguidamente sua eficiência, combinada com descargas com Hélio foi estudada em termos do esgotamento de hidrogénio das paredes. Por outro lado, um conjunto de técnicas de ciência de superfície, incluindo SIMS, XPS, AES, EDS/X, SEM e RBS foi criada para investigação através de análises post-mortem que permitem aferir as propriedades físicas e químicas de boro e a deposição de filmes finos de lítio boro e lítio após condicionamento da parede. No que diz respeito à otimização GDC, encontrou-se uma forte assimetria toroidal, confirmada pelas medições do fluxo iónico para a parede. A análise preliminar da limpeza de parede por descarga intermédia HeGDC considerou esta estratégia promissora. Em relação à otimização da boronização, foram encontrados fortes indícios de crescimento de boro em dois passos com o aumento da potência da descarga luminescente. Já para o condicionamento da parede de lítio, foi encontrada uma correlação entre a dose de lítio injectado e fracção química de carbonato de lítio.

Em última análise, uma transição para uma primeira parede metálica no RFX-mod cuja superfície oferece baixos níveis de reciclagem foi recentemente considerada como uma solução alternativa para ultrapassar as desvantagens da primeira parede de grafite. Revestimentos de tungstênio em amostras de grafite foram elaborados utilizando duas técnicas de deposição de vapor (PVD): HiPIMS, técnica desenvolvida localmente no laboratório CNR-IENI, e tecnologia CMSII, desenvolvido na associação Euratom MEDC-Roménia. Os revestimentos da parece foram caracterizados preliminarmente por SEM e postos à prova com testes de aderência antes de expôlos aos plasmas do RFX-mod. A exposição ao plasma foi feita em sessões experimentais de cerca de 15 descargas, durante as quais a interação com o plasma foi melhorada localmente por o sistema magnético de controlo ativo, a fim de simular as condições dos eventos PWI. A técnica CMSII, que resultou em pequenas falhas na primeira fase, foi então testada em dimensão de escala completa, substituindo 4 telhas reais de carbono RFX-mod pelas revestidas a tungsténio. Os azulejos foram expostos a três meses de operação normal no RFX-mod ao longo de uma ampla gama de condições de funcionamento, após o que grandes áreas danificadas foram observadas. O tamanho destes danos e, particularmente, a remoção do revestimento em algumas áreas e a sua fusão pode descartar esta solução para o RFX-mod. Revestimentos de tungsténio mais espessos (100-200 μm), que ainda sejam compatíveis com as tolerâncias de peso da estrutura mecânica do RFX-mod, podem oferecer a melhor solução para futuras melhorias do dispositivo.

Acknowlegments

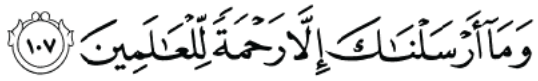

And We have not sent you, except as a mercy to the worlds

— (21:107)

All praise is due to God, the Lord of the Worlds. It is He alone that I worship and it is from Him that I seek help. I would not be here today without His blessings, favors, grace, and sustenance. Thank you my Lord.

The RFX-mod team as a whole was incredibly welcoming, helpful, and deserves recognition. I would like to thank in particular Alessandra Canton for her patience and Gianluca Spizzo for his invaluable support.

I would like to thank my dear friend *Al* from the United States Department Of Energy, his generosity is boundless. I would like also to thank Masa Ono, Charles Skinner and all the members of the NSTX team for always welcoming me in Princeton. Gratitude also goes to Bruce Koel and his group at Princeton University, Department of Chemical and Biological Engineering.

Finally, I would like to mention two names in arabic alphabets:

مَرْيِمْ

مَازِكُوْ

Abbreviations

HeGDC Helium Glow Discharge Cleaning

SIMS Secondary Ion Mass Spectrometry

XPS X-ray Photoelectron Spectroscopy

HR-XPS High Resolution X-ray Photoelectron Spectroscopy

AES Auger Electron Spectroscopy

EDS/X Energy Dispersive X-ray

SEM Scanning Electron Microscopy

RBS Rutherford Backscattering Spectroscopy

PVD Physical Vapor Deposition

PS Plasma Spray

HiPIMS High Power Impulse Magnetron Sputtering

CMSII Combined Magnetron Sputtering and Ion Implantation

GDC Glow Discharge Cleaning

GD Glow Discharge

MPI Multi-Pellet Injector

LPI Lithium Pellet Injector

MCF Magnetic Confinement Fusion

RFP Reversed Field Pinch

PMI Plasma-Material Interaction

PFM Plasma Facing Material

PFC Plasma First Component

PSI Plasma-Surface Interaction

PWI Plasma-Wall Interaction

SOL Scrape Off Layer

LCMS Last Closed Magnetic Surface

ELM Edge Localized Mode

CFC Carbon Fiber Composites

TFTR Tokamak Fusion Test Reactor

QSH Quasi Single Helicity

SHAx Single Helical-Axis states

MHD Magneto-Hydro-Dynamics

VS Virtual Shell

CMC Clean Mode Control

RGA Residual Gas Analyzer

CVD Chemical Vapor Deposition

LCPS Lithium Capillary Porous System

CPS Capillary Porous System

LLL Liquid Lithium Limiter

ISIS Integrated System of Internal Sensors

QMA Quadrupole Mass Analyzer

RF Radio Frequency

RG Radio-frequency-assisted Glow discharge

JET Joint European Torus

LoS Line of Sight

PECVD Plasma-Enhanced Chemical Vapor Deposition

UHV Ultra-High Vacuum

HHF High Heat Flux

TDS Thermal Desorption Spectroscopy

Contents

Abstract v

Prefazione vii

Resumo ix

Acknowlegments xi

List of Figures xvii

List of Tables xxi

1 Introduction and background 1
- 1.1 Fusion energy: a viable alternative source of clean energy . . . 1
- 1.2 Plasma-Wall Interaction - A key issue in progress towards fusion energy . . . 4
- 1.3 Wall conditioning - A way to mitigate and control plasma wall interaction . . . 7
- 1.4 Thesis motivation . . . 9
- 1.5 Thesis outline and main results . . . 12
- 1.6 Key contributions presented in this thesis . . . 15

2 RFX-mod experiment, wall conditioning techniques and diagnostics 19
- 2.1 Introduction . . . 19
- 2.2 RFX-mod facility . . . 19
- 2.3 Wall conditioning techniques in RFX-mod . . . 23
- 2.4 RFX-mod wall conditioning diagnostics . . . 32
- 2.5 Surface characterization methods . . . 44

3 Glow discharge optimization, efficiency and advantages of intershot HeGDC 55
- 3.1 Introduction . . . 55
- 3.2 GDC global parameters optimization . . . 56
- 3.3 Efficiency of intershot HeGDC in RFX-mod . . . 69
- 3.4 Advantages of routine intershot HeGDC in RFX-mod . . . 79
- 3.5 Conclusions . . . 83

4 A physical and chemical study of boron wall-conditioning in RFX-mod **87**
4.1 Introduction . . . 87
4.2 Brief summary of B wall conditioning benefits in RFX-mod . . 89
4.3 Physical analysis of boron deposition behavior correlated to experimental conditions . . . 92
4.4 Boron-graphite chemical interaction correlated to impurity content upon boronization . . . 120
4.5 Conclusions . . . 134

5 Lithium wall conditioning: a physical and chemical analysis **139**
5.1 Introduction . . . 139
5.2 Brief summary of Li wall conditioning benefits in RFX-mod . . 141
5.3 Lithium spatial deposition, erosion and redeposition . . . 144
5.4 High resolution surface chemical analysis . . . 160
5.5 Conclusions . . . 169

6 Qualification of plasma-facing materials towards RFX-mod^2 upgrade **171**
6.1 Introduction . . . 171
6.2 The choice of W as an alternative among other prominent candidates . . . 172
6.3 W-coating mock-ups elaboration and adhesion characterization 178
6.4 Exposure to RFX-mod power plasmas . . . 187
6.5 W-coatings post-exposure inspection . . . 195
6.6 Conclusions . . . 205

7 Summary and Future Work **207**
7.1 Conclusions . . . 207
7.2 Future work . . . 210

Bibliography **213**

List of Publications **231**

List of Figures

1.1 Diagram illustrating the tokamak principle . . . 3
1.2 Tokamak and RFP magnetic configuration . . . 3
1.3 Schematic of the prominent mechanisms of PMI . . . 6

2.1 Magnetic system of RFX-mod . . . 20
2.2 The set of 192 saddle active coils . . . 21
2.3 Picture of RFX-mod vessel interior graphite first wall . . . 22
2.4 Schematic view of RFX-mod torus . . . 24
2.5 Glow discharge plant in RFX-mod . . . 25
2.6 Image of the GDC antennae and plasma in RFX-mod . . . 26
2.7 Scheme of a typical boronization performed on RFX-mod . . . 26
2.8 Scheme of the room temperature pellet injector . . . 28
2.9 The Capillary Porous System (CPS) head after setup in RFX-mod . . . 28
2.10 View of the CPS system . . . 29
2.11 The experimental setup of the Multi-Pellet Injector (MPI) on EAST tokamak . . . 30
2.12 The experimental setup of the Multi-Pellet Injector (MPI) on RFX-mod . . . 31
2.13 RFX-mod general diagnostics layout . . . 32
2.14 Schematic view of ISIS system . . . 34
2.15 Passive Doppler spectroscopy . . . 35
2.16 Lines of sight configuration for emissivity measurements . . . 36
2.17 Schematic diagram of the RGA setup in RFX-mod . . . 37
2.18 Gas balance schematic in RFX-mod . . . 38
2.19 Pumping speeding determination for discharge fueling . . . 39
2.20 RGA systematic instrument error . . . 41
2.21 Calibration of the RGA for m/e=2 and m/e=4 . . . 41
2.22 RGA data visualization . . . 42
2.23 Material sample manipulator . . . 43
2.24 Secondary Ion Mass Spectrometry (SIMS) principle . . . 44
2.25 SIMS laboratory experimental setup . . . 45
2.26 X-ray Photoelectron Spectroscopy (XPS) principle . . . 47
2.27 HR-XPS laboratory setup at Princeton University . . . 49
2.28 RBS laboratory setup at Rutgers University . . . 51
2.29 RBS scattering chamber photo . . . 52

2.30 RBS spectrum of a boron-coated graphite sample 52
2.31 Scanning Electron Microscopy (SEM) principle 53

3.1 Simple schematic of a glow discharge 56
3.2 Glow discharge processes. 57
3.3 Obstructed and normal glow discharge regimes 57
3.4 Experimental setup for GDC characterization 58
3.5 Experimental arrangement for operating a RG discharge 60
3.6 Voltage-pressure characteristic with and without RF 61
3.7 Pre-ionization effect on glow discharge breakdown in RFX-mod 62
3.8 Characteristic V_A-I_A curves for different gas pressures 62
3.9 Obstructed GDC Voltage-Current characteristic 63
3.10 Gas exhaust analysis during HeGDC 64
3.11 Toroidal asymmetry analysis by post-mortem analysis 65
3.12 Toroidal asymmetry analysis by electrostatic measurements . . 66
3.13 Toroidal asymmetry analysis by spectroscopic measurements . 67
3.14 Intershot HeGDC experimental campaign 69
3.15 H exhaust induced HeGDC and by HeShot 70
3.16 H-ion-induced release cross section [102] 72
3.17 Plasma density dependence survey 72
3.18 H exhaust dependence with n_e and P_{Ohm} 73
3.19 RGA H partial pressure and exhaust rate 74
3.20 Hydrogen and helium dynamics after He discharges 75
3.21 H exhaust and influx correlation 76
3.22 Typical experimental campaign for evaluating density control . 77
3.23 H plasma parameters of discharges performed for density control evaluation 78
3.24 Advantages of routine intershot HeGDC 79
3.25 H influx behavior after intershot HeGDC campaign 80
3.26 Comparison with plasma restart subsequent to a boronization . 81
3.27 Drawbacks of routine intershot HeGDC 82

4.1 Boronization effect on impurity content and gas adsorption capacity 89
4.2 Boron wall conditioning effect on confinement 91
4.3 Material sample position in RFX-mod vessel 93
4.4 SEM images of graphite surface 95
4.5 Graphite characterization by 3D profilometry 95
4.6 SIMS spectra of blank and boronized sample 96
4.7 In-depth SIMS ion distribution of boron coated sample 97
4.8 SIMS spectra at different toroidal positions 98
4.9 Effect of temperature of boron deposition 98
4.10 Erosion and re-deposition caused by H plasmas 99
4.11 Experimental vs nominal boron thickness 101
4.12 Global inconsistency of boron deposition 102
4.13 Normalized SIMS thicknesses vs duration 103

4.14 Computed boron deposition rate . . . 104
4.15 Deposition rate of boron vs (IxV) . . . 105
4.16 Gas exhaust analysis . . . 106
4.17 H, C, B and O partial pressure vs (IxV) . . . 107
4.18 Boron deposition rate measured by gas exhaust analysis . . . 108
4.19 Surface morphological characterization . . . 110
4.20 2 MeV He^+ beam Rutherford Backscattering Spectroscopy (RBS) spectrum of samples #29 and #56 . . . 111
4.21 RBS depth concentration profile of B, C and O . . . 112
4.22 HR-XPS survey spectrum of samples #29 and #56 . . . 114
4.23 Surface High Resolution X-ray Photoelectron Spectroscopy (HR-XPS) composition of samples #29 and #56 115
4.24 Ar^+ step-wise etching HR-XPS survey spectra . . . 116
4.25 HR-XPS Ar^+ sputter depth profiles of B, C and O . . . 117
4.26 Comparison between gas exhaust and HR-XPS measurements . 118
4.27 B_{1s}, C_{1s} and O_{1s} spectra of samples #29 and #56 . . . 122
4.28 Surface and subsurface B_{1s}, C_{1s} and O_{1s} spectra . . . 126
4.29 B_{1s}, C_{1s} and O_{1s} spectra of the in-depth boron content of sample #29 . . . 129
4.30 B_{1s}, C_{1s} and O_{1s} spectra of the in-depth boron content of sample #56 . . . 130
4.31 Depth profiles of the chemical states of boron and contaminant impurities . . . 132
4.32 Depth profiles of the C–B^{sp3} and B–B bonds fraction . . . 133
4.33 The B–O bonds fraction in the O_{1s} . . . 134

5.1 Plasma performances post Li injection by LPI . . . 141
5.2 Plasma performances post Li evaporation by LCPS . . . 143
5.3 Experimental setup for Li physical and chemical analysis . . . 145
5.4 LPI pellet injection toroidal uniformity . . . 147
5.5 Li influx measurements after LPI lithiumization . . . 148
5.6 MPI pellet injection toroidal uniformity . . . 149
5.7 Li influx measurements after MPI lithiumization . . . 150
5.8 LCPS Li evaporation toroidal uniformity . . . 151
5.9 Li influx measurements after LCPS lithiumizations . . . 152
5.10 Shot-by-shout history of He/H shots for LPI lithiumization . . 153
5.11 Effect of plasma discharges on lithium redeposition . . . 154
5.12 Effect of plasma discharges on lithium erosion . . . 155
5.13 Effect of plasma discharges on toroidal asymmetry . . . 156
5.14 Effect of toroidal asymmetry on hydrogen recycling . . . 157
5.15 XPS survey scan of pristine and lithiated graphite . . . 161
5.16 HR-XPS spectra of samples #16 and #54 . . . 163
5.17 HR-XPS of sample #14 vs pristine and after Ar^+ ion etching . 165
5.18 HR-XPS spectra of samples #23 and #45 . . . 166
5.19 H plasma discharges performed after 1g of Li evaporation . . . 167
5.20 Comparison between HR-XPS spectra of sample #45 and #47 168

6.1 Typical physical sputtering yields [160] . . . 173
6.2 Particle reflection coefficients [161] . . . 174
6.3 Effect of high-Z PFMs on RFX-mod plasmas . . . 175
6.4 Tomographic inversion of SXR and total radiation during W-LBO . . . 175
6.5 Thermal expansion coefficients for W, Mo and RFX-mod graphite 177
6.6 Graphite mock-ups W-coated with CMSII technology. . . . 179
6.7 CMSII coating quality control . . . 180
6.8 Time trace of a heat cycle on CMSII W-coating . . . 180
6.9 SEM image of HiPIMS W-coatings grown with a low applied deposition bias . . . 182
6.10 SEM image of HiPIMS W-coatings grown with a high applied deposition bias . . . 182
6.11 Scratch test diagram of a 2.4 μm W-coating . . . 183
6.12 Scratch test optical micrographs . . . 184
6.13 Top view of a 5×4 cm W-PS graphite mock-up . . . 185
6.14 CAPS facility at Centro Sviluppo Materiali, Rome . . . 186
6.15 LISA manipulator for W-coating exposure . . . 187
6.16 Graphite sample design for W-coating exposure . . . 188
6.17 LISA graphite samples and CMSII W-coating prototypes . . . 189
6.18 Diagnostic setup for plasma exposure . . . 190
6.19 Visible fast-camera images of the two LISA samples . . . 191
6.20 Temperature profile measurements by the IR camera . . . 191
6.21 Typical experimental campaign with induced magnetic perturbation . . . 193
6.22 4 RFX-mod tiles W-coated by CMSII technology . . . 194
6.23 Images of bulk-C samples after 40 H_2/He discharges . . . 195
6.24 Images of CMSII W-coatings after 12 H_2 discharges . . . 196
6.25 Images of HiPIMS W-coatings after 14 H_2 discharges . . . 197
6.26 Picture of the 4 W-coated RFX-mod tiles . . . 198
6.27 HR images of a W-coated RFX-mod graphite tile . . . 199
6.28 OM images of a CMSII W-coated tile after plasma exposure . . . 200
6.29 SEM images of a CMSII W-coated tile after plasma exposure . . . 201
6.30 Scratch test on a W-coated tile after plasma exposure . . . 202
6.31 Scratch test optical micrographs of zone A, B and C. . . . 203

List of Tables

2.1 Main RFX-mod vacuum vessel, first wall and plasma parameters 21
2.2 Parameters for baking up to 170° C 23
2.3 Basic diagnostic methods in RFX-mod 33
2.4 Error analysis of the RGA 40
2.5 Values of XPS atomic sensitivity factors 48

3.1 H plasma parameters for density control evaluation 77

4.1 Experimental conditions for sample surface analyses 94
4.2 Mass spectra of the cracking of diborane 106
4.3 RBS percentage concentration of elements 112
4.4 EDS/X atomic percentage concentration of elements 113
4.5 C_{1s} and B_{1s} lines BE of the B-C species 121
4.6 Spectra deconvolution parameters 125

5.1 Graphite samples exposed for to lithium wall conditioning . . . 146
5.2 Film composition as determined by XPS 146
5.3 Experimental conditions of sample exposure and composition as determined by XPS 154

6.1 Properties of RFX-mod polycrystalline graphite 177
6.2 HiPIMS W-coatings parameter study 184
6.3 LISA blank/W-coated samples - plasma exposure 192
6.4 Post-mortem scratch test results 203

Chapter 1

Introduction and background

1.1 Fusion energy: a viable alternative source of clean energy

The continuing increase of the world's population, estimated to reach and exceed 9 billion people by 2050 [4], global warming due to the increasing atmospheric concentration of anthropogenic greenhouse gases, and a dramatic increase in energy demand of developing countries are probably the most important challenges facing human civilization during the past and coming 30 years. All these issues are linked together and are the main drivers of humanitarian crises such as civil wars, epidemic diseases and political turmoil. The common denominator to these issues is the unavailability of a clean, safe and unlimited source of energy. In fact, conflicts around the globe are mainly located in highly rich oil producing countries [5] and are driven by the need to secure oil wells in countries such in the Middle East or north Africa.

A change towards CO_2-free energy sources of the present energy supply system is needed to stabilize CO_2 concentrations in the atmosphere at safe levels. Despite huge investments and technology improvements [6] [7], the role of renewable sources, e.g. solar irradiation, wind and biomass remains minor although they have the potential to become a major source of energy. Progress in the nuclear industry based on fission can play a long term role in meeting the future energy demand and reduce the problem of greenhouse gas emission. However, nuclear fission has the drawback of long lived radioactive waste, risks for proliferation and the possibility of accidents.

In view of these considerations regarding the current global socio-political juncture, thermonuclear fusion energy can be considered a major feasible alternative energy source with many attractive features in terms of safety, fuel reserves and minimal damage to the environment stating in the latter half of this century. Fusion research on fusion aims to build and operate a power-generating plant by harnessing on Earth reactions taking place in stars such as the sun.

Thermonuclear fusion exploits nuclear fusion reactions among two light nuclei that fuse into a heavier one, releasing other reaction products such as

neutrons. In order for fusion to take place between different nuclei, they must be brought sufficiently close so that the short-range nuclear strong attractive force can overcome the Coulomb repulsive potential. For nuclear fusion, energies on the order of at least a few keV are needed. At these temperatures the positive charged particles can penetrate the Coulomb barrier by quantum mechanical tunnelling and fuse together to form heavier nuclei. The fusion fuel in these conditions is found to be fully ionized, as a quasi-neutral ensemble of ions and electrons known as *plasma*. For nuclear fusion reactors, the reaction of main interest is

$$D^2 + T^3 \rightarrow He^4 + n + 17.6MeV,$$

that is, the fusion of a deuterium (D) and a tritium (T) nucleus (deuteron and triton, respectively) to obtain a helium-4 nucleus (α particle), a neutron and a total energy excess of 17.6 MeV. Proving fuel self-sufficiency is the most critical issue for a fusion power plant. Deuterium is the stable isotope of hydrogen, it has an isotopic abundance of 0.015% and can be extracted from seawater [8]. Tritium is the radioactive isotope of hydrogen with a half-life time of about 12 years. It is currently available from heavy water fission reactors [9] however there is not enough available in nature for technical applications. It is expected to be bred in a Lithium "blanket" on future fusion reactors according to the reactions:

$$^6Li + n \rightarrow^4 He + T + 4.8MeV$$
$$^7Li + n \rightarrow^4 He + T + n - 2.8MeV$$

For nuclear fusion devices, two different approaches have mainly been considered: inertial and magnetic confinement. In this thesis, the discussion will be limited to Magnetic Confinement Fusion (MCF) devices, where magnetic fields are used to confine the thermonuclear plasma. Among the various MCF concepts, the most studied is the tokamak [10]. The word "tokamak" derives from the Russian acronym for "toroidal chamber with magnetic coils". The tokamak configuration, which was proposed by A.D. Sakharov and I. Tamm and initially developed in the USSR, consists of a toroidal axisymmetric chamber and an externally imposed toroidal magnetic field. The plasma generated in the center of the chamber is, effectively, the secondary winding of a large voltage transformer with the ohmic coils in the center post acting as the primary winding. The transformer action generates a toroidal current that, in turn, heats the plasma and generates a poloidal magnetic field which is needed for the creation of helically-twisted magnetic field lines. The helical field lines, which lie on toroidal flux surfaces, are needed to compensate particle drifts and instabilities and to confine the plasma (see fig. 1.1).

Alternative magnetic configurations used in MCF devices include the stellarator [11] (where external coils are used to generate the poloidal

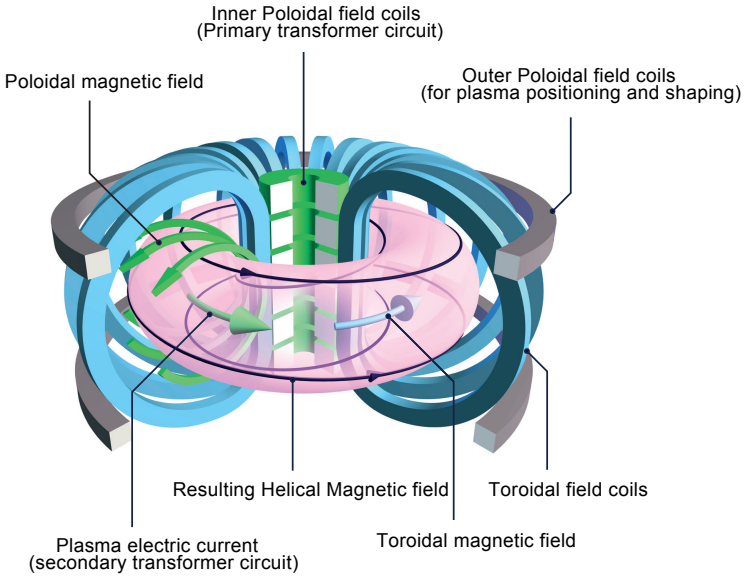

Figure 1.1: Diagram illustrating the tokamak principle: arrangement of magnetic field coils and the resulting magnetic field that confines the plasma. (Courtesy of https://www.euro-fusion.org/)

magnetic field) and the Reversed Field Pinch (RFP) [12, 13], which is an axisymmetric toroidal system in which the plasma is confined by a combination of a toroidal field B_ϕ, produced largely by poloidal currents in the plasma, and a poloidal field, B_θ, produced by the plasma current flowing around the torus, as shown in fig. 1.2.

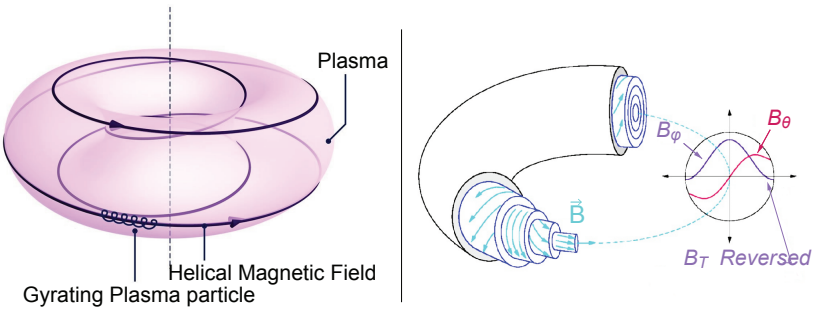

Figure 1.2: Sketch of the tokamak magnetic configuration (left) and the main RFP magnetic field configuration (right) with the radial profiles of B_ϕ (violet) and B_θ (red). (Courtesy of https://www.euro-fusion.org/ and of S.C. Prager, University of Wisconsin at Madison)

The RFP aims to confine the plasma, exploiting the same pinch effect also lying at the bottom of the Tokamak theory. The main difference is represented by the magnetic field components amplitude (being $B_\theta \approx B_\phi$ in the RFPs and $B_\theta \ll B_\phi$ in the Tokamaks) and behaviour (B_ϕ reverses its sign at the edge in the so called reversal region in the RFP). In fact, in the tokamak community it is customary to adopt the cylindrical tokamak ordering, where B_ϕ and the safety factor q are order unity, and $\epsilon = a/R$ and B_θ are small parameters, order ϵ. In the RFP a rather different ordering is valid, where B_ϕ and B_θ are both order unity, while q and a/R are order ϵ. As a result, most analytical expressions that are well-known in the tokamak community (trapped fractions, bounce time, neoclassical transport coefficients, ...etc), cannot be adopted for the RFP without significant corrections. From a more practical point of view, the RFP configurations may lead to less expensive reactor designs. In particular, the results presented in this thesis are obtained in the Reversed Field pinch eXperiment (RFX-mod) [14, 15], one of the world's largest RFP.

The performance of a fusion device can be measured by the triple product ($n_i T_i \tau_E$),where n_i is the ion density, T_i is the ion temperature and τ_E is the energy confinement time. Generating energy from fusion requires a plasma with a temperature of 100 million degrees Celsius. Strong magnetic fields are used to protect the wall of a fusion device and although this reduces the interaction of the plasma with the walls, they are still exposed to considerable loads that are inherently unavoidable. Hindered for a long time by major efforts to enhance the plasma parameters by studying instabilities occurring at higher triple product values, the interaction between the wall of the machine and the plasma is one of the major factor limiting its performance.

Recently, huge efforts have been dedicated to the Plasma-Material Interaction (PMI) topic to understand the fundamental mechanisms that govern the behavior of the PFCs of the machine first wall and the interaction with the plasma. The study of Plasma-Surface Interaction (PSI) and how the behavior of the plasma can be controlled is of paramount importance for the realization of a fusion plasma under steady state conditions and it is the focus of this thesis.

1.2 Plasma-Wall Interaction - A key issue in progress towards fusion energy

> *"We say that we will put the sun into a box. The idea is pretty. The problem is, we don't know how to make the box"*
>
> — Pierre-Gilles de Gennes, *French physicist and the Nobel Prize laureate in physics in 1991*

... and still today we don't know how to make the box, more than 20 years later. Research on magnetic fusion has long established the inextricable link

between the material boundary layer and the confined thermonuclear plasma since Lyman Spitzer's recognition in 1951 that sputtered impurities from the PFC surface could degrade or collapse magnetic plasma confinement [16]. The interaction of the plasma and the wall surface involves a number of processes on both sides in a feedback like behavior modifying the boundary and the core properties of the plasma and significantly affecting the engineering viability of the materials. Coming from the plasma core, towards the wall, three main regions can be found:

1. The region of closed field lines, where magnetic field line close onto themselves. This is still a region of plasma which is confined by the magnetic field, and where the usual scalings (neoclassical and/or turbulent) are found.
2. The Scrape-Off Layer, or SOL, which is the plasma region next the wall where magnetic field lines are open, they do not close into themselves and intercept the wall. As a consequence, in the SOL finite Larmor radius effects and particle losses parallel to the magnetic field become important. In a machine with a limiter, the boundary between the region of closed field lines and the SOL is the Last Closed Magnetic Surface (LCMS), which defines the plasma region which is shadowed by the limiter. In a diverted tokamak, the SOL boundary is the X-point separatrix.
3. The last plasma region before the material surface is the plasma sheath [17]: next the material surface, the ion and neutral pressure increases sharply, in a few Debye lengths (~mm) surrounding the material wall. As a consequence, the plasma potential has a sharp drop immediately adjacent to the PFCs, determined by the ambipolar condition on ion and electron motion to the wall.

Plasma-wall interaction is an enormously complex field, encompassing the PFC material surfaces, sheath plasma, the Scrape Off Layer (SOL), and the boundary plasma. An interdisciplinary approach based on experimental evidence, theoretical knowledge and computational models is therefore needed. Energy loss by radiation due to the release of impurities from the walls by plasma particle impact is a prominent example of such plasma surface interaction. Research on PWI includes all processes involved in the exchange of energy and mass between the surrounding surface wall and the plasma. In order to build and operate a power-generating fusion plant the surrounding material walls must meet three important tasks:

(i) absorb the power produced by the α-particles in the fusion processes and injected by auxiliary heating,
(ii) provide high vacuum conditions necessary to provide clean fusion plasmas,
(iii) enable the exhaust of the helium ash by thermalisation of the helium plasma ions on material surfaces in the vicinity of helium pumps.

These tasks are inherently linked to three main concerns: the assessment of material migration, tritium inventory and dust formation. These issues have a large impact on the economy and safety [18, 19] of next step fusion devices such as ITER [20] and DEMO [21] and their study is on the priority list of fusion research. Development of first-wall materials is a complex task considering the required properties and compatibility with other in-vessel components:

(i) good thermal conductivity to channel heat loads,
(ii) high thermal resilience to tolerate transient events (e.g. Edge Localized Modes (ELMs)),
(iii) low fuel inventory and neutron activation to minimize safety risks,
(iv) resistance to erosion to extend life-time of PFCs,
(v) compatibility with high-vacuum.

The majority of the present-day machines operate with PFCs made of graphite or Carbon Fiber Composites (CFC). However, the level of fuel retention and dust formation associated with the use of carbon surfaces is not acceptable for reactor class devices, such as ITER. High-Z PFCs have been considered lately as an alternative but many issues have been faced and will be discussed in this thesis.

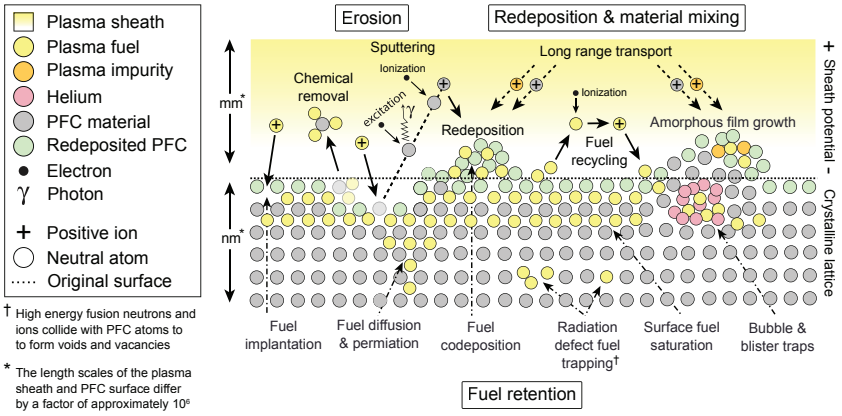

Figure 1.3: A schematic of the prominent mechanisms of PMI and their physical impact on the PFCs material surface. Erosion leads to the removal of PFC surface material (top left), where it can be promptly redeposited (top center) or remotely deposited after long range transport in the boundary plasma (top right). A wide range of physical mechanisms cause plasma fuel retention (bottom) in the original PFC material or in redeposited material layers. Figure adapted from [22].

The prominent mechanisms behind PMI occur in a shallow region known as the plasma sheath ($\sim mm$) that is immediately adjacent to the PFCs and

comprised in the first few monolayers ($\sim nm$) of the material surface. The PMI processes and PFC responses that occur in this region are depicted in fig 1.3. Regarding material modification in the boundary layer of magnetic fusion devices, the most important effects are the bulk retention of fusion fuel, the net erosion of the material, and the material migration, redeposition, and mixing that occurs after eroded material has left the surface. Hydrogen fuel retention and its release during plasma operation along with other impurities such oxygen is a crucial issue for plasma performances in today's fusion machines and next-step devices. Its control and the understanding of the fundamental mechanisms that govern the retention and release of fuel and impurities is the particular focus of this thesis.

1.3 Wall conditioning - A way to mitigate and control plasma wall interaction

The term "wall conditioning" in fusion science and technology refers to the modification of the wall-surface state in order to improve plasma performances. In the early 1990s, wall-conditioning of the DIII-D tokamak plasma facing surfaces [1] resulted in a regime of very high energy confinement, VH-mode. Earlier application of wall conditioning in TFTR resulted in significant improvement in 'supershot' performances [2] showing and demonstrating a way to mitigate and control PWI by circumventing its related detrimental features. Since PWI is inherently unavoidable in any fusion device, wall-conditioning makes up a window into high plasma performances regimes and allows to explore plasma parameters values never achieved before.

PMI processes take place in a thin near surface layer of typically a few tenths of nm. It is therefore straightforward that the physical and chemical structure and composition of the near surface can have a significant influence on plasma wall interaction processes and also on plasma performances. Methods to extract plasma fuel and other impurities intercalated into the plasma facing surfaces, as well a number of techniques to coat the entire surface the PFCs have been developed and are nowadays employed regularly on fusion experiments to assist plasma start-up, especially after leaks or disruptions [23–25]. These methods have led to a significant improvement of plasma performance such as higher density limits and stored energy. In ITER, based on the experience reached in present fusion devices, a number of wall conditioning techniques are needed to its initial phase operation. The aim of surface and wall conditioning techniques can be divided in two main areas:

(i) reduction of impurity influxes from the walls,
(ii) control of hydrogen recycling.

Regarding the control of impurity influxes, the control of oxygen is the

most important issue. Oxygen is present in all fusion devices and wall materials as metal oxide and hydroxides, water and various other components. It readily forms volatile gases such as CO, CO_2, H_2O and can also be released by photon impact in form of CO_2 and CO. All of the wall conditioning techniques were developed primarily to passivate or remove oxygen which is done by forming stable oxygen compounds that are not easily dissociated. On the other hand, it became evident that reducing hydrogen recycling could lead to a significant improvement in fusion plasma performance. Recycling is the exchange of neutral particles between the hotter fusion plasma edge and the colder plasma facing first wall surfaces. Wall conditioning techniques developed to tackle the fuel recycling issue consist mainly in sputtering chemically or physically the hydrogenic species from above the surface of the first wall or applying a thin low-Z films chemically reactive, that can readily combine with the hydrogenic species or other impurities (oxygen, carbon etc.) and form more stable compounds. A wide variety of techniques have been developed for this purpose and they are briefly presented here. These techniques will be further described in Section 2.3, when applied to the RFX-mod experiment.

Baking: Baking consists in the thermal desorption of water and other adsorbed species by the heating of the wall surfaces. The duration of baking sessions varies from hours up to several days in present days devices. Reduced plasma impurities and better vacuum conditions are obtained. Baking is usually performed after a period in which air was in contact with the wall, for instance after machine openings. Baking is a baseline wall conditioning technique in ITER and the planned temperatures are 350° C for the divertor and 240° C for the blanket [26].

Glow-Discharge Cleaning: Glow Discharge Cleaning (GDC) is the most effective method for surface impurity removal and it is routinely applied in almost all fusion devices. It is operated by introducing various electrodes into the vacuum vessel and then excite them with a power source to initiate and sustain the discharge. Electrodes serve as anodes and the grounded vessel walls serve as cathodes. This arrangement produces a flux of ions to the wall used for conditioning [27]. Glow Discharge (GD) plasmas have low temperatures and densities (around 10 eV and 10^{14} m^{-3}, respectively) so the desorbed particles are not promptly ionized and re-deposited before they are pumped out of the system. HeGDC is the most effective wall 'cleaning' techniques in terms of removal of hydrogenic species by physical sputtering. Other working reactive gases are used to induce chemical erosion of the wall surface. Wall impurities are released by reduction of metal oxides and hydrogenation of carbonaceous deposits when a hydrogen GDC is performed. Oxygen is used to erode carbon co-deposits through the formation of carbon oxides [28].

Thin film deposition: Improvements in plasma performance (energy confinement) due to reduction of plasma impurities and fuel recycling has been observed by coating the first wall with low-Z elements. Protective layers are produced by a variety of techniques including GD in a through-flow of a reactive gas. Typical film thickness is between 50 and 100 nm. The duration of the conditioning effect depends on the operation scenario and properties of the coating, but it is usually within few hundred seconds of plasma exposure.

The most prominent coating materials are boron and lithium. First conditioning coatings were performed in TEXTOR using methane (CH_4) as reactive gas in a process called carbonization [29]. In later experiments, methane and diborane (B_2H_6) were mixed to reduce chemical erosion of carbon layers and to improve oxygen gettering [30]. Boronization was used in other tokamaks with the same positive results [31]. Diborane is toxic and explosive so other less hazardous compounds based on boron such as trymethilborane ($B(CH_3)_3$) [32] and decaborane ($B_{10}H_{14}$) [33] were tested.

The use of lithium in magnetic fusion confinement experiments started in the 1990's in order to improve tokamak plasma performance as a low-recycling plasma-facing component PFC. Lithium is the lightest alkali metal and it is highly chemically reactive with relevant ion species in fusion plasmas including hydrogen, deuterium, tritium, carbon, and oxygen. Because of the reactive properties, lithium can provide strong pumping for those ions. It was indeed a spectacular success in TFTR where a very small amount (~ 0.02 gram) of lithium coating of the PFCs resulted in the fusion power output to improve by nearly a factor of two. The plasma confinement also improved by a factor of two [2]. This success was attributed to the reduced recycling of cold gas surrounding the fusion plasma due to highly reactive lithium on the wall

1.4 Thesis motivation

In light of these considerations regarding the importance of wall conditioning in any fusion device to control PWI and mitigate its effects, wall conditioning optimization in RFP is of great importance for the attainment of improved confinement regimes with particle control and stationary particle inventories, low recycling and a reduction in impurity sources.

In the Reversed Field Pinch experiment RFX-mod [15, 34] (R/a = 2.0/0.46m, $I_p \leq 2$MA) a very high plasma current is attainable and therefore its first wall is entirely covered by graphite tiles to sustain the high thermal load due to ohmic power dissipation. Graphite as first wall has proven to be a good solution in terms of allowable power load to the wall and impurity control, especially on RFP experiments where the critical role of the conductive shell proximity in the stabilization of magnetic instabilities prevents the use of a divertor. Moreover, on RFPs macroscopic deformations of the plasma often localize PWI producing a high thermal

power deposition that in RFX-mod can locally reach values of the order of tens of MW/m^2 [35]. In this framework the high sublimation temperature of graphite and the low Z of carbon help in keeping very low plasma Z_{eff} .

On the other hand a graphite first wall prevents hydrogen influx control. In RFX-mod indeed, graphite provides a recycling factor usually above one. In a few discharges, the plasma facing side of tiles becomes completely hydrogen saturated, after that graphite acts as a big hydrogen reserve resulting in a hydrogen influx that depends only on the power wall load. This prevents the operation at a desired density and becomes particularly unfavorable at high plasma current (Ip > 1.5MA) when power loads are very high. What is further detrimental is that the high hydrogen influx from the wall contributes in producing hollow density profiles with high density accumulation at the plasma edge. This seems to affect plasma performance making impossible the attainment of the improved confinement regime associated to the SHAx [3] at intermediate plasma density ($n/nG \geqslant 0.35$) [36].

The same problem of the main gas desorption leading to a lack of density control has been met in several experiments of magnetically confined plasmas. In order to minimize the desorption process various procedures of wall conditioning have been adopted to reduce adsorption on the wall. They include baking of the vacuum vessel, the use of a variety of weakly ionized plasma discharges to remove the adsorbed gas from the wall and the gettering of impurities such as oxygen by covering the wall with a clean metal film [10]. In the past, several of these wall conditioning techniques were implemented in RFX-mod to reduce hydrogen influx, such as sessions of He glow discharges, HeGDCs, wall boronization, wall baking and recently lithium wall coating. Every technique has its advantages and drawbacks.

Boronization is very effective in gettering oxygen and reducing hydrogen recycling however it is time-consuming; the boron coverage is non-uniform and the boron deposition on the wall is not efficient. Baking is effective in removing H_2O and other impurities but the baking temperature is limited to 170°C in RFX-mod to protect the in-vessel probes. HeGDC is effective to operate power discharges at low H_2 wall influxes but its already proven advantages are not fully gained. Lithiumization resulted very effective in controlling wall recycling. The technique provides or improves all the feature of boronization: increases hydrogen wall absorbing capacity, reduces the impurity content and improves the edge particle behavior providing a higher particle confinement time. However the beneficial effect of lithium wall conditioning does not extend to the plasma core and further implementation and optimization of the technique are of great benefit to RFX-mod goals.

Mitigation of impurity influxes and recycling control during plasma operation by means of wall conditioning is necessary in RFX-mod for the attainment of the improved confinement regimes associated to the SHAx states. The motivation of this thesis is to optimize the main conditioning techniques and implement further conditioning strategies to get maximum advantage of the present graphite first wall. In parallel, in RFX-mod an

activity has been engaged to study the possibility of substituting the present carbon wall with a metallic alternative compatible with the high power loads of RFX-mod and offering a non-recycling surface. These two interconnected activities are the core contribution presented in this thesis. The four main goals of the work described are:

A. Understand which glow discharge operational regimes in RFX-mod allow an enhanced impurity wall cleaning and investigate new strategies for helium glow discharge operation in RFX-mod. This requires: *(i)* evaluating wall cleaning efficiency by means of interconnected diagnostics comparing them with estimates from measurements obtained on other devices; *(ii)* evaluating H/He dynamics during and after HeGDC and understanding their impact with respect to the global GDC efficiency; *(iii)* understanding the changes in density behavior in subsequent hydrogen power discharges with application of different fueling sequences.

B. Understand which experimental conditions favor high boron deposition rates during boronizations in RFX-mod, and correlate it to the chemical properties of the boron content. This requires: *(i)* evaluating the gas exhaust during bornonization glow discharges and interpreting the data; *(ii)* assessing which glow discharge parameters strongly affect the deposition of boron on the wall; *(iii)* understanding which chemical interactions between the diborane radicals and the carbon wall are favored for the experimental conditions available in RFX-mod.

C. Understand which lithiumization technique in RFX-mod allows to obtain the largest lithium coverage and highest surface content, and relate the outcomes to the corresponding Li-graphite chemistry. This requires: *(i)* understanding the favorable conditions that allow a uniform lithium deposition; *(ii)* using multiple diagnostics to assess the deposition uniformity during and after lithium injection; *(iii)* assessing the extent of Li intercalation into the graphite bulk related to each Li deposition method .

D. Evaluate which metallic first wall material alternative is favorable in the case of RFX-mod machine. This requires: *(i)* understanding the compatibility of different non recycling metallic materials with RFX-mod mechanical structure; *(ii)* evaluating the strategies to undertake to test a possible path for the transition from carbon to a new wall material; *(iii)* assessing the compatibility after testing the chosen material with RFX-mod plasmas and environment.

1.5 Thesis outline and main results

This thesis is organized as follows:

In **Chapter 2**, the Reversed Field pinch eXperiment, where the work presented in this thesis was carried out, is described. The main operational parameters are introduced, together with a detailed discussion of wall conditioning techniques (baking, glow discharge cleaning, boronization and lithiumization), diagnostics for gas exhaust analysis and the material sample manipulator used to expose samples to wall conditioning sessions. The diagnostic development work carried out in this thesis is presented. This includes the data acquisition setup, calibration, and operation of a deferentially pumped Residual Gas Analyzer (RGA) along a pumping duct in RFX-mod. The surface science facilities used to perform the surface analyses are presented as well.

In **Chapter 3**, the glow discharge global parameters are characterized, the glow plasmas toroidal uniformity is discussed and the analysis of a new wall conditioning strategy by the combination of He power discharges and HeGDC is presented. The characterization has been performed by means of an extensive set of diagnostics including *ex-situ* post-mortem analyses, electrostatic probes and spectroscopic measurements. A scan in the operational parameters was done and the results have shown that: (i) in contrast with results found in TEXTOR, RF-assistance and pre-ionization have no apparent benefit in RFX-mod; (ii) a clear dependence on the glow current of the effectiveness in particle-depleting from the wall was observed, whereas no clear dependence on pressure or voltage alone could be deduced; (iii) I_{0V} measurements (ion flux to the wall) suggested that a lower in-vessel pressure is a favorable regime in RFX-mod, however spectroscopic data have shown an opposite behavior and further optimization is needed; (iv) a strong toroidal asymmetry was found by *ex-situ* post-mortem analysis and confirmed by measurements of the ion flux to the wall. The preliminary analysis of intershot HeGDC wall cleaning strategy in RFX-mod was found promising. The combination of He power discharges with short ±10 min HeGDC resulted relatively more efficient in enhancing hydrogen depleting from the graphite first wall compared to longer 40-60 min HeGDCs performed occasionally during an experimental day. As a macroscopic effect, a better control of the plasma density with a lower recycling was obtained in H test discharges subsequent to the intershot HeGDC experimental campaign. While immediate benefits of using routine intershot HeGDC were found in RFX-mod, the most detrimental effect consisted in the progressive He loading of the wall that in the long run may affect plasma impurity content.

In **Chapter 4**, a physical and chemical analysis of boron wall conditioning has been performed. In RFX-mod, several unfavorable aspects of boron deposition have been observed and needed to be addressed in order to gain further benefits of boron wall conditioning. The features that have been tackled in this chapter are: (i) the spatial uniformity of boron deposition; (ii) the correlation among the boron wall conditioning duration and the final boron content deposited on the first wall; (iii) the oxygen and hydrogen gettering efficiency of the boron-coated first surfaces. To address these issues, graphite samples have been exposed to a number of boronizations and *ex-situ* post-mortem analyses including SIMS, XPS, SEM, EDS/X, RBS and HR-XPS were carried out. The latter feature has been investigated by looking at the surface and bulk chemical states of boron related to hydrogen, carbon and oxygen. A strong toroidal asymmetry of boron deposition and an inconsistency among the boronization duration and the final boron content were found. The study of the effect of the wall temperature has shown a higher affinity of boron with hotter first wall surfaces. The inconsistency in boron deposition was resolved looking at the boron deposition rate measured by SIMS and gas exhaust analysis and correlated to the glow discharge parameters: boronizations performed at a low glow plasma power < 200 W have shown ~7× lower boron deposition rate compared to boronizations performed at a higher plasma power > 200 W. Accordingly, a morphological transition in boron deposition with increasing glow discharge plasma power has been found by SEM. XPS, EDS/X, RBS quantitative and qualitative measurements consistently confirmed the presence of this transition in boron growth, in agreement with previous studies found in literature [37–40]. The chemical analyses performed by HR-XPS have shown that boronizations performed at higher glow discharge plasma power provided oxygen-free and purer boron content which was related to lower concentrations of boron oxides in terms as B–O, O–B–O and B_2O_3 bonds. In terms of B–H bonds, the higher glow discharge plasma power provided a lesser H-contaminated boron content, suggesting that exposure to power plasmas of these low H- and O-contaminated boron films would lead to enhanced plasma performances. Future work include tests with these optimized boronizations in RFX-mod.

In **Chapter 5**, a physical and chemical analysis of the obtained lithiated graphite first wall with the different lithiumization techniques in RFX-mod have been performed by *ex-situ* analysis of material samples. At different toroidal locations around RFX-mod torus, the deposition uniformity for each technique has been assessed by SIMS and XPS measurements and the results were compared to Li spectroscopic emission during subsequent plasma discharges. The high resolution Li-graphite chemical analysis at varying lithium dose injection with and without plasma exposure has been conducted by HR-XPS measurements.

Consistent results among SIMS, XPS and Li spectroscopic measurements have shown that compared to lithium injection/evaporation using the LCPS injection method, the injection of lithium pellets/granules during plasma discharges allows a relatively more uniform toroidal coverage. The recently implemented lithiumization technique by multiple pellet injection has shown positive results in terms of lithium coverage and content. The increase in frequency injection allows to obtain a relatively less contaminated lithium content on the plasma facing surfaces compared to the injection of a single pellet at a time. The comparison of lithium coverage provided by the different avaialable techniques in RFX-mod has shown that it is more profitable to inject small amounts of Li such as with the pellet injection technique in order to sustain a surface Li coverage rather than depositing greater amounts that are more prompt to intercalation. Different results were found with regard to the effect of plasma operation during and following lithium deposition: (i) injection of lithium pellets in hydrogen plasmas resulted more efficient in depositing lithium on the first wall compared to the injection in helium plasmas; (ii) spectroscopic emission data have shown that the erosion and redeposition of lithium after multiple plasma pulses is not effective in establishing uniformity of wall conditioning; (iii) the toroidal asymmetry of lithium coverage was found to be detrimental as little or no influence on H influx was found at locations where lithium coverage is reduced.
The HR-XPS chemical analysis has shown several results correlating the amount of injected lithium to the chemical bonds among Li, C and O. In particular, lithium carbonate radicals (Li_2CO_3 at 290.2 eV) were systematically found in all the analyzed Li-coated samples in both C_{1s} and O_{1s} core spectra and their fraction among other chemical interactions correlates to the total injected lithium dose. In consistency also with results found in studies on Li-graphite chemistry in NSTX, at low doses of lithium injection $\leqslant$100-500 nm, the exposure of Li-coated graphite to H plasma discharges resulted ineffective in H pumping and, accordingly, few apparent changes in surface chemistry of the lithium coating have been observed post plasma exposure.

In **Chapter 6**, after the choice of tungsten (W) as the most suitable material for a transition from graphite to metallic first wall PFCs in RFX-mod, preliminary plasma exposure trials of W-coating on small scale specimens and full-scale tiles have been conducted. The choice of W is motivated by its high melting temperature allowing to sustain RFX-mod power loads which can reach tens of MW/m^2, its compatibility with the present mechanical structure, the high reflection energy of incident neutral atoms and the prediction of its low core plasma contamination and further peaking of density profiles compared to carbon and molybdenum.
Two different Physical Vapor Deposition (PVD) technologies providing thin 10-20 μm W-coatings have been tested in two different experimental

campaigns. First, small 5×6 cm W-coated graphite samples were exposed to series of about 15 H/He discharges by means of a dedicated manipulator allowing the exposure at different distances from the graphite first wall floor. CMSII coating technique (most suitable technique also tested in JET and AUG) and HiPIMS technique (made by CNR-IENI institute of the same laboratory in Padova, Italy) were tested. Second, full-scale tiles W-coated by CMSII technology were mounted for long term exposure during a second experimental campaign. Post-mortem analyses were carried out mainly by means of optical and electron microscopy. Overall, the coatings did not withstand the thermal and particle loads induced by induced magnetic perturbations on the samples. Several damages were observed including critical melting in many areas of the exposed surfaces and the CMSII technique has shown better results compared to the HiPIMS technique. The damages that have been observed were expected to a certain extent, however the size of these damages and particularly the removal of the coating in some areas and its melting may discard this solution path towards such a metallic first wall upgrade.

In **Chapter 7**, the conclusions and summary of the main results achieved in this thesis are presented. The results of the qualification of W-coatings on graphite PFCs towards RFX-mod^2 upgrade are also discussed. Possible directions for future work are given.

1.6 Key contributions presented in this thesis

The optimization, further implementation and characterization of the wall conditioning techniques in RFX-mod and the W PFCs qualification toward RFX-mod^2 upgrade was the result of extensive efforts by a group of talented collaborators. As a consequence, for the purposes of this thesis, it is important to distinguish the author's role in each task and the underlying science contributions. While these are presented in the main body of this thesis, it is appropriate to highlight them concisely here:

The author's role in the wall conditioning studies

- Led the implementation, data acquisition upgrade and calibration of the Residual Gas Analyzer (RGA) which has been extensively used in the characterization of the gas exhaust during all the wall conditioning techniques, in particular for the characterization of gas exhaust during HeGDCs and boronizations.

- Monitored the SIMS and SEM measurements that were performed at the CNR-IENI institute then analyzed and interpreted the results with surface science experts. The analyses were carried out on graphite and molybdenum samples and data were classified in an easy-access database.

- Set up a new collaboration with the Princeton Plasma Physics Laboratory (PPPL) and the Princeton University Chemical Engineering Department to perform high resolution surface analyses. In particular, HR-XPS, AES, SEM and EDS/X were used to study the surface and bulk physical and chemical properties of boron and lithium conditioned graphite samples exposed and unexposed to RFX-mod plasmas. The analyses were performed during a first trip to Princeton within a Euratom mobility grant in the period November-December 2013 and during a second return trip in October-November 2014.
- Established a collaboration with Rutgers University, Catalysis Research Center to perform Rutherford Backscattering Spectroscopy (RBS) measurements on boron conditioned samples that resulted important for the purpose of the ongoing analyses at Princeton.
- Carried out the analysis of the XPS an RBS data that required the proficient use of the *CasaXPS* software for the deconvolution and quantitative interpretation of the XPS spectra; and the *SIMNRA* simulations for the qualitative and quantitative interpretation of the RBS spectra.

The author's role in the qualification of W-PFCs

- Led the characterization of the initial W-coatings mock-ups provided by CMSII and HiPIMS technology suppliers which included the critical assessment of the coatings mechanical adhesion properties and resistance to heating and cooling cycles tests performed by electron beam.
- Participated in the first plasma exposure experimental campaign of LISA samples. Followed the second experimental campaign where full-scale W-coated tiles where exposed to H_2, D_2 and He plasmas in RFP and tokamak configurations.
- Performed the post-mortem analysis of LISA W-coated samples and tiles after plasma exposure to assess the surface and bulk modification of the coatings.

Science contributions

- The characterization of the glow discharge plasmas, although performed in the particular RFP configuration, is a valuable technical contribution towards the global understanding of glow discharges and their particular operational regimes in toroidal fusion devices. In next generation superconducting magnetic confined devices, such as ITER, GDC is a baseline requirement [26]. The results of the GDC optimization in RFX-mod have been published in [CBA+13].

- Provided the first evidence of a two-step boron growth in boronizations performed in fusion devices. The transition in boron growth deposited by PECVD has been first documented in a small-scale forced-convection plasma reactor [37–40], however the results were never applied for boron wall conditioning optimization in a fusion device. The first results were the subject of an oral talk presented at the 2014 Kudowa Summer School, a poster and a conference proceedings paper [tea14] presented during the 41^{st} European Physical Society (EPS) conference. A co-authored paper has been recently submitted [GLC+15] while the publication of the ongoing results are planned.

- Lithium has reached a pervasive position as an advanced material interface in nuclear magnetic fusion plasma-facing materials but also in novel applications including: solid-state batteries, hydrogen storage and reactive fuel cells. Therefore the study of its interaction with other materials in harsh environment such as in fusion device conditions constitutes a fundamental science contribution. The HR-XPS results of the Li-graphite chemistry performed at Princeton University, Chemical Engineering Department are important because they contribute to the huge ongoing research effort to decipher the fundamental mechanisms that take place at the plasma-wall interface which are responsible of enhancing plasma performances in fusion devices. A contributed work has been published in [IMR+14].

- The qualification of high-Z Plasma Facing Materials (PFMs) for RFX-mod^2 upgrade contributes to the global understanding of their applicability in fusion devices, in particular for the next generation of devices that will push towards reactor-like conditions. The preliminary results concerning the characterization of the W-coatings before plasma exposure were presented in a poster during the 2013 PFMC14 conference in Aachen-Germany, while the most recent results obtained after the exposure to RFX-mod plasmas are the subject of a contribution to the 2015 PFMC15 conference in Aix-en-Provence, France.

Chapter 2

RFX-mod experiment, wall conditioning techniques and diagnostics

2.1 Introduction

The optimization of wall conditioning techniques and the qualification of plasma first wall materials which will be presented in this thesis was carried out on the Reversed Field pinch eXperiment (RFX-mod) at the Ionised Gas Institute (IGI) [41] of the National Research Council (CNR) [42] of Padova. In this chapter, the RFX-mod facility, wall conditioning techniques, the main diagnostics and surface analysis facilities used for post-mortem analyses on material samples are presented. Section 2.2 introduces the RFX-mod facility and its operational parameters. Wall conditioning techniques used in RFX-mod are presented in details in Section 2.3. Diagnostics and data acquisition development work carried out in this thesis are described in Section 2.4 with a particular emphasis on the RGA and gas exhaust diagnostic. Surface analyses techniques, experimental setups and the material sample exposure manipulator used for post-mortem surface analysis on metallic and graphite samples are presented in Section 2.5.

2.2 RFX-mod facility

The *modified* **R**eversed **F**ield e**X**periment (RFX-mod) [15], the upgraded version of the previous RFX [14], is a toroidal device for the study of the magnetically confined plasma using the RFP magnetic configuration. It is operational since 2004 under the management of the Consorzio RFX, a research organization promoted by CNR, ENEA (the Italian National agency for new technologies, Energy and sustainable economic development) [43], University of Padova [44], Acciaierie Venete S.p.A. (a private partner) [45] and INFN (the Italian National Institute of Nuclear Physics) [46], within the framework of the Euratom - ENEA Association.

The mission-oriented RFX fusion science program is shaped to provide a focused contribution to ITER and its accompanying fusion program [47]. As in all RFPs, plasma heating is purely ohmic. Although a toroidal magnetic field ten times smaller (the whole magnetic system is shown in fig.2.1), this device allows exploring current regimes (up to 2 MA) comparable to those of the large tokamaks, using a ten times smaller toroidal magnetic field: in fact in the RFP configuration the confining magnetic field is produced mainly by a self-organization process of the magnetic field and not by the external inductive means, as in the tokamak. The main parameters of the RFX-mod device (the largest RFP in operation) are shown in tab.2.1.

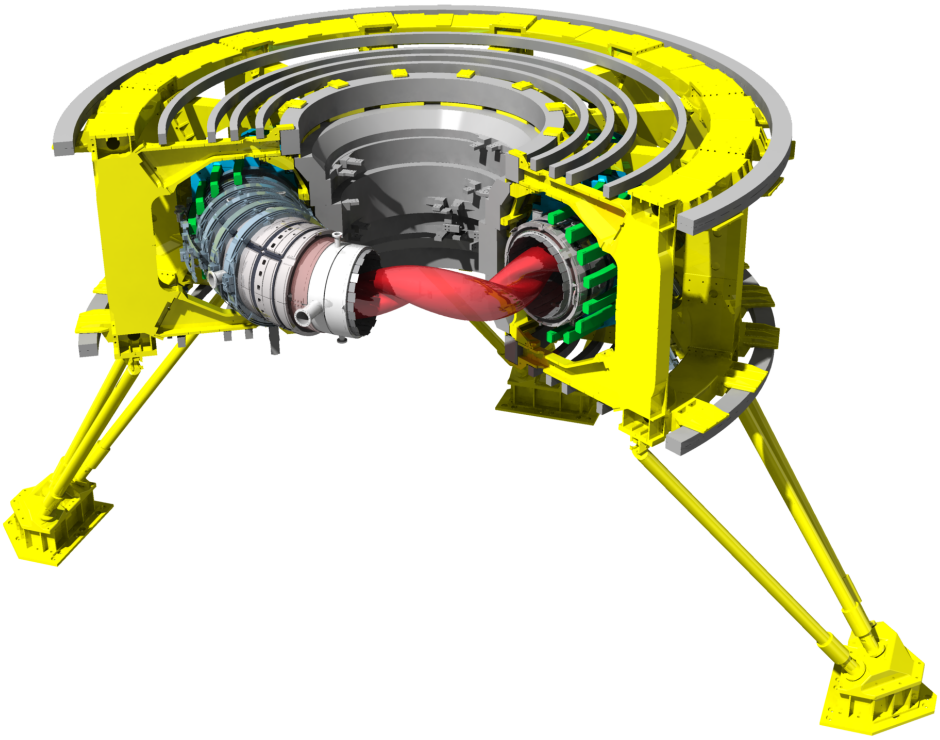

Figure 2.1: Magnetic system of RFX-mod: the magnetizing winding (grey), the field shaping coils (green), the toroidal ciricuit (blue).

With respect to the original RFX design, the present machine underwent some crucial modifications that allowed significant performance improvements. The original RFX thick stabilizing shell (which had a magnetic field penetration time constant $\tau_{shell} = 500$ ms) was replaced with a thinner one, whose time constant for penetration of vertical magnetic field ($\sim$ 50 ms) is $\sim$ 10x shorter than pulse duration. Moreover, RFX-mod has been equipped with one of the most advanced system for feedback control of Magneto-Hydro-Dynamics (MHD) instabilities with active coils among fusion devices. The system is based on 192 active saddle coils, which cover the whole plasma boundary (fig. 2.2). The coils are arranged in 48 toroidal locations; in each toroidal location there are 4 poloidal coils, according to

Table 2.1: Main RFX-mod vacuum vessel, first wall and plasma parameters

Vacuum vessel	Major radius	2m
	Minor radius	0.459 m
	Material	INCONEL 625
	Volume	10 m^3
	Gasket materials	Cu, AI, VITON
First Wall	Number of tiles	2016
	Mean dimension	l50x95x18mm
	Material	Graphite LCL 5890 PT
	Mean dimension	l50x95x18mm
	Surface exposed to the vacuum	120 m^2
Plasma parameters	Toroidal magnetic field	$\leq$ 0.7 T
	Plasma current	$\leq$ 2 MA
	Discharge duration	$\leq$ 0.5 s
	Plasma density range	$\approx 1 \div 10 \times 10^{19} m^{-3}$
	Plasma volume	$\sim$ 10 m^3

the low m/high n structure of MHD modes in the RFP (where m and n are the poloidal and toroidal mode numbers, respectively).

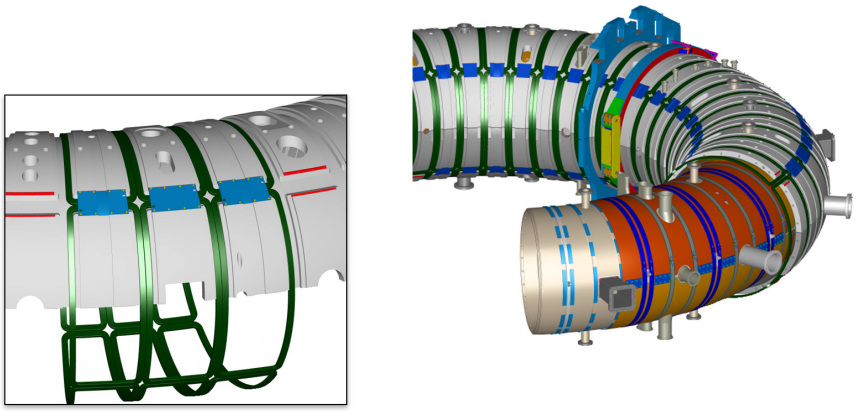

Figure 2.2: Set of 192 saddle coils (4 poloidal positions × 48 toroidal positions) surrounding the RFX-mod shell

Each coil is independently driven by individual power supplies and can produce a radial magnetic field up to 50 mT dc and 3.5 mT at 100 Hz [15, 48–50]. Different algorithms for real-time tearing modes control have been developed to exploit the full capability of the feedback system, the most important being the Virtual Shell (VS) scheme [49] and the Clean Mode Control (CMC) [51]. The latter, in particular, has drastically changed the performance of the device, reducing the amplitude of the dynamo modes at the plasma boundary, mitigating their phase and wall locking and finally

removing the aliasing of the sidebands limiting the VS control scheme [52].

Other important modifications concerned the first wall, composed by 2016 tiles made of polycrystalline graphite (manufacturer Carbone Lorraine, type 5680PT), covering completely the inner part of the vacuum vessel (see fig. 2.3). In the new machine the tiles have been redesigned to achieve a more uniform power deposition on the plasma facing surface, to minimize the emissivity due to PWI and finally to give housing to a large number of in-vessel probes. These design requirements led to a substantial reduction of the tile thickness with respect to the original design [53].

The most evident achievement in the RFP configuration in RFX-mod was gained with a plasma current increase to the 2 MA design achieved in 2010. A breakthrough that considerably enhanced the interest about the RFX-mod developments and enriched the RFP physics. The discovery consisted in a spontaneous transition from the traditional picture of a poor confinement characterizing the RFP plasmas towards self-organized equilibria, namely the *Q*uasi *S*ingle *H*elicity QSH and the *S*ingle *H*elical *Ax*is SHAx states.

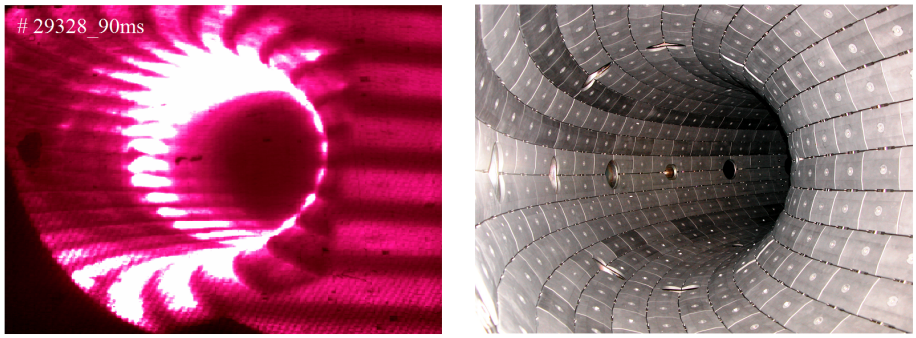

Figure 2.3: Picture of RFX-mod vessel interior graphite first wall (right) and CCD camera image of the helical footprint of PWI in QSH states for the shot #29328 (left).

For a longtime, the RFP self-organization due to the dynamo process [54–56], led to a unfavorable chaotic configuration. The destabilization of a wide spectrum (in terms of Fourier components with m and n respectively the poloidal and the toroidal periodicity) of $m = 1$ modes (*M*ultiple *H*elicity states) and the subsequent superposition of the associated resonating plasma layers caused the magnetic surfaces destruction giving rise to a stochastic plasma core [57].

The power load on the portion of the wall wetted by the helix is of the order of 5 MW/m^2. However, when a back-transition from the QSH to the chaotic state occurs and modes are locked to the wall, the interaction region is smaller, and the power load can locally increase up to tens of MW/m^2. Therefore, it is mandatory to protect the vacuum chamber against these strong local interactions. At the same time, RFX-mod can offer a good environment to test materials and plasma wall conditioning also for non-RFP devices.

The advent of the previously depicted improved confinement regimes occurs only at low collisionality values, with $n_e/n_G \leq 0.25$, being n_G the Greenwald parameter [58]. At high n_e values the QSH and SHAx states usually can not be observed which draws a kind of empirical limit for the RFX-mod operations. These phenomena are likely due to a non uniform PWI at the edge [59]. Localized PWI, poor density control in RFX-mod discharges together with high fuel (hydrogen) recycling [60] would highly favor the formation of hollow density profiles, thereby promoting the disappearance of the transport barriers characterizing the improved SHAx regimes. RFX-mod research strategy has taken two parallel approaches to tackle the high density regimes issue that is crucial to make the confinement improvements fusion relevant. Different wall conditioning techniques have been implemented to mitigate the graphite wall response to the plasma interaction. However, optimization of all the techniques applied to RFX-mod need to be optimized and take into the account the particularities of the machine in terms of geometry, magnetic field configuration and PWI peculiarities. On the other hand, a transition towards a metallic less recycling first wall has been undertaken.

2.3 Wall conditioning techniques in RFX-mod

Careful conditioning of the RFX-mod vessel must be performed in order to obtain high performance plasma discharges. The principal methods for conditioning the graphite tiles for plasma discharge operation are baking, HeGDC and thin film deposition. These methods are discussed and their application procedure in RFX-mod are presented.

2.3.1 Baking

Table 2.2: Parameters for baking up to 170° C

UHV pump system configuration	12 turbo pumps
Starting pressure	$5{\times}10\text{m}^{-6}\text{Pa}$
Time to reach the final temperature	30 h
Pressure reached at 170° C	$9{\times}10\text{m}^{-4}\text{Pa}$
Pressure after 36 h at 170° C	$9{\times}10\text{m}^{-5}\text{Pa}$
Pressure after 60 h at 170° C	$2{\times}10\text{m}^{-5}\text{Pa}$

RFX-mod vessel is routinely baked up to an average temperature of 170° C. Baking reduces absorbed impurities such as water, oxygen (primarily as CO), and nitrogen. In addition, baking lowers the bulk concentration of hydrogen in the tiles allowing for better density control during a plasma discharge. Hydrogen is released from the tiles as H_2 hydrocarbons, and as H_2O. Baking is imperative after a machine shut-down and air-exposure of the vacuum vessel. Following such events the vessel is vented with N_2 then baked to 170° C with the parameters described in tab.2.2. During the baking

sessions the gas exhaust of gas species can be monitored with a Residual Gas Analyzer (RGA). When the final temperature is reached, water vapor corresponding to amu=18 is dominant and it is one order of magnitude larger than the other signals. After baking, all the signals are observed to decrease by a factor of 5-10 except the hydrogen signal which decreases by a factor of 2.5.

2.3.2 H_2 and He glow discharge cleaning

a. Overview

Most of the wall treatments performed at RFX-mod are based on GDCs, cold and weakly ionized plasma sessions with different process gases, He, H_2 or a mixture of He(90%) - B_2H_6(10%). When using hydrogen, surface cleaning is enhanced by chemical action with the formation of hydrocarbons together with H_2O and CO, that can be pumped away. In systems with mainly carbon walls, GDC in helium has been found to release oxygen, usually by forming CO. HeGDC also desorbs implanted hydrogen isotopes when performed before plasma runs. Typically lasting for one to two hours it lowers the near surface concentration of hydrogen and controls oxygen levels. Short 10 min glow sessions before every plasma discharge have been tried in the past with improved results, however its use during plasma operation in RFX-mod needs optimization to gain full advantage of the technique capabilities.

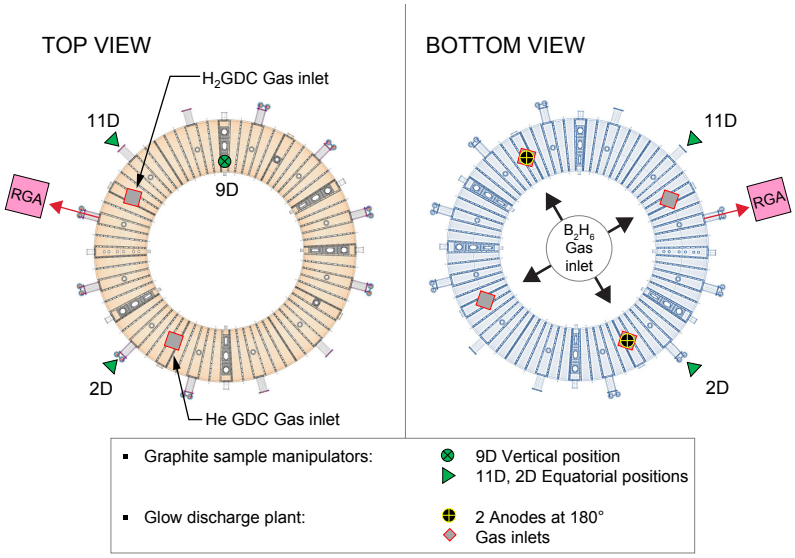

Figure 2.4: Schematic view of RFX-mod torus and the GDC and bornonization gas inlets.

In fig. 2.4, a schematic of RFX-mod vessel with gas inlet and diagnostics (discussed in section 2.4) is shown. When performed in a helium-diborane gas

mixture the GDC allows to deposit thin boron films. Boron wall conditioning technique will be further introduced in the following section.

b. Glow discharge plant

The GDC plant (fig. 2.5) was designed for a maximum discharge current density of 0.25 $A \cdot m^{-2}$ and to operate with a wall temperature up to 350° C and a maximum gas pressure of approximately 2 Pa. The system was equipped by four antennae (anodes, the wall being the cathode), equally spaced in the toroidal direction, in order to reduce the maximum power dissipated by each one. At present only two of them, toroidally opposed, are used, whereas the two other dedicated portholes are utilized for the in-vessel inspection system. The head of each antenna is composed of ten 80 mm diameter turns made by internally air-cooled Inconel tube and, during GDs, it is located in the center of the poloidal section. An image of the head of the GDC antennae is shown in fig. 2.6. The d.c. power supply, which consists of a thyristor converter with a maximum voltage of 1200 V and a total current of 10 A (2.5 A/antenna), is current controlled. Aimed at the reduction of the breakdown voltage, calculated by the Paschen law to be approximately 1 kV for H_2 at the maximum pressure of 2 Pa, the GDC system is provided with one Radio Frequency (RF) amplifier rated to 1 kW at a frequency of 4 MHz [61].

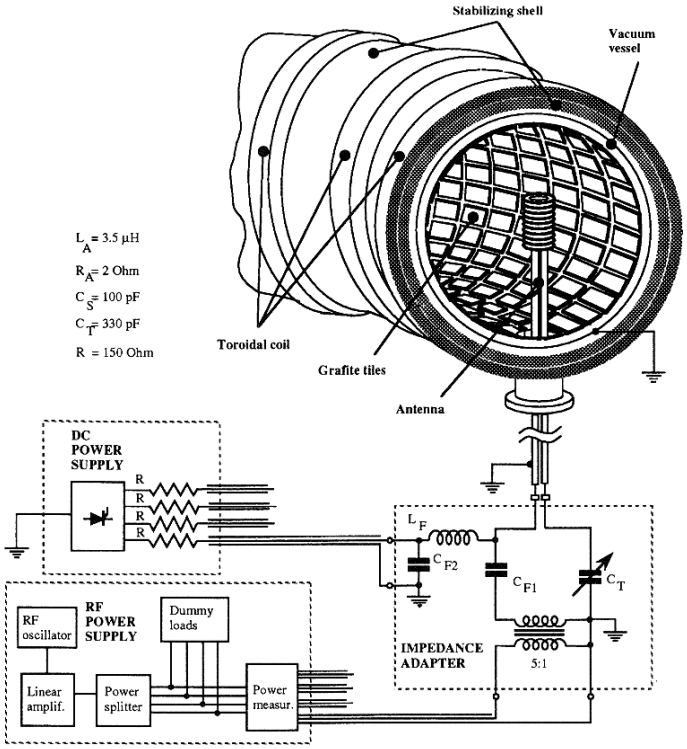

Figure 2.5: Glow discharge plant in RFX-mod.

A characterization of the glow discharge plant actual performances has

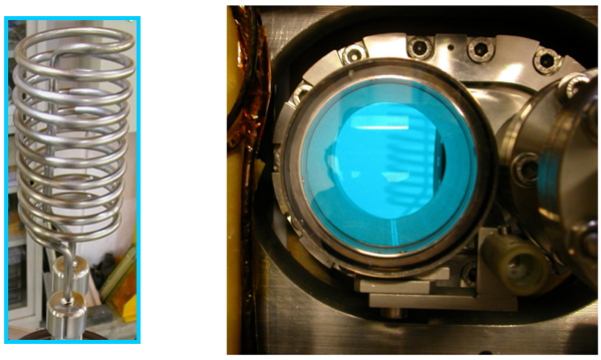

Figure 2.6: Head of the GDC antennae (left) and view of the head through a diagnostic window during a HeGDC(right).

been done in this thesis and the results will be discussed in Chapter 3. The characterization has been performed operating the discharge with single or double anode, with or without pre-ionizing filaments, using or not additional RF power, varying the anodes current/voltage and the gas pressure. He power plasma discharges are also used to induce H_2 sorption. In this thesis, the implementation and optimization of the combination of He power plasma discharges with single or multiple subsequent HeGDCs is presented.

2.3.3 Boron wall conditioning: boronization

Boronization, first done on the TEXTOR tokamak [30], is a Chemical Vapor Deposition (CVD) technique implemented in RFX-mod to deposit a thin boron film (up to 200 nm) over the entire surface of the machine first wall. An example of a boronization sequence performed after a machine venting is reported in fig. 2.7.

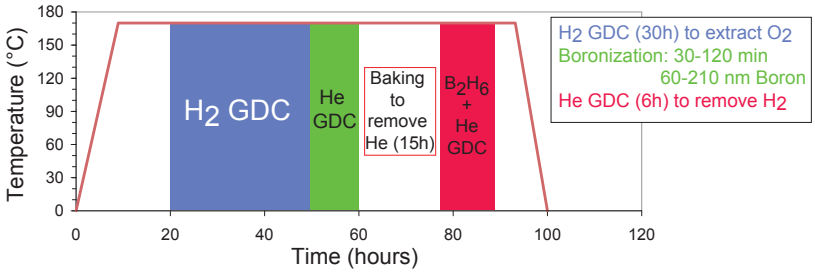

Figure 2.7: Scheme of a typical boronization performed on RFX-mod.

In RFX-mod the boronization is usually performed as part of a long lasting wall treatment procedure that assures a good cleaning of the carbon prior to

the boron deposition. In such a way the boron deposited on the wall keeps a high level of purity that assures the best effectiveness as impurity getter. At the beginning the temperature of the vessel is raised up 170° C and for 4 hours the contaminating atoms are removed from the tiles and pumped out. H_2 GDC is then performed for 30 hours to remove oxygen from the tiles, followed by 6 hours of HeGDC to remove the H_2. After other 15 hours to pump out the helium, a mixture of diborane (B_2H_6) at 10% and helium at 90% is introduced for a variable time depending on the desired thickness of the deposited layer. The sequence ends with other 3 hours of HeGDC to remove the H_2 coming from the diborane, other 15 hours to pump out the helium and then the temperature is decreased again to room temperature.

In RFX-mod plasma discharges are characterized by a recycling parameter always equal to one. A fresh boronization is initially able to lower the recycling parameter but then, after few hundreds of discharges, the effect disappears. In order to improve the boronization effect it is important to understand the physics underlining hydrogen and oxygen capture by the boron films and the reason of its run out. To this aim graphite samples have been exposed during boronizations and plasma operation in RFX-mod, then they have been studied by surface science techniques including SIMS, XPS, AES, EDS/X, SEM and RBS. The discussion of the results will be presented in Chapter 4.

2.3.4 Lithium wall conditioning: lithiumization

To improve density control and plasma performance over those of boronization, lithium wall-coating has been tested in RFX-mod, with the aim of reproducing the good results obtained on many tokamaks [62–65], heliotrons [66] and stellarators [67]. In RFX-mod, lithium wall conditioning has been tested with multiple scopes: to improve density control, to reduce impurities and to increase energy and particle confinement time. Lithiumization methods presently used on tokamak devices have limited applicability on the RFX-mod device, due to magnetic characteristics and geometrical constraints of the latter. For this reason, to improve lithium deposition, in RFX-mod different techniques have been tested since 2010: large single lithium pellet injection, Lithium Capillary Porous System (LCPS), lithium evaporation and, recently, small lithium granules injection using a high frequency Multi-Pellet Injector (MPI).

a. Single pellet injection

The first technique implemented in RFX-mod [68] is the injection of lithium pellets during plasma discharges by means of a Lithium Pellet Injector (LPI) injecting relatively large right-circular cylinders (⌀1.5 mm, l=5 mm) lithium pellets. The room temperature pellet injector along with the pellet parameters are shown in fig. 2.8. The injector is loaded with solid pellets in the frontal hole of cylindrical sabots. Sabots are accelerated by a driver gas till they hit a bumper where they are stopped by the bumper while pellets can fly to the plasma through a central hole in the bumper.

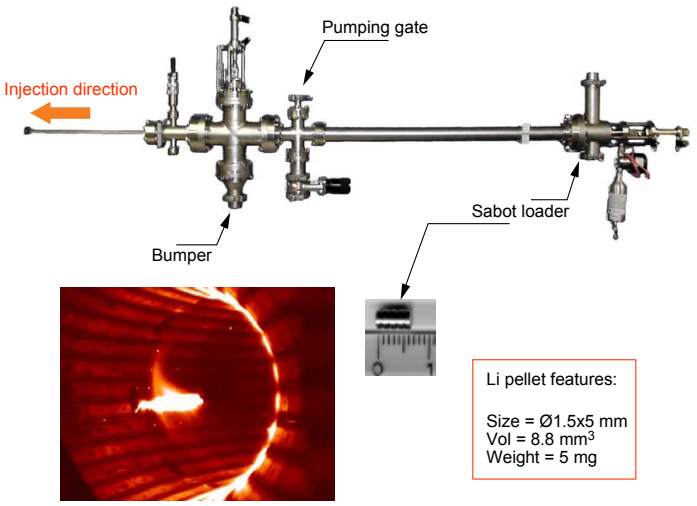

Figure 2.8: Scheme of a the room temperature pellet injector used in RFX-mod for lithium pellet injection (top), CCD image of pellet ablation and pellet characteristics (bottom).

This allows to inject pellets with a maximum speed of 200 m/s.

Back in 2010 several lithiumization experimental campaigns have been performed. The technique provided and improved all the features of wall conditioning by bornonization: increased hydrogen wall absorbing capacity and reduced the impurity content. It was also able to improve the edge particle behavior providing a higher particle confinement time. The absorbing wall capacity allowed for the first time operating RFX-mod close to its 2 MA maximum target plasma current. The results are were published in [68].

b. Liquid Lithium Limiter

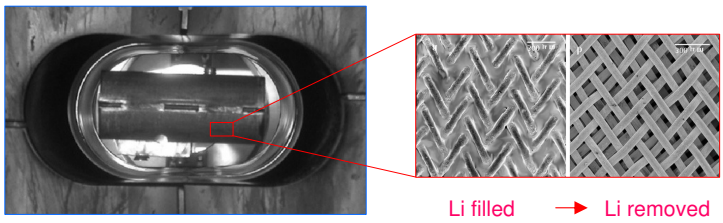

Figure 2.9: The CPS head after setup into RFX-mod torus (left) and the heating, melting and evaporation of the lithium above the CPS mesh (right).

After the first positive results obtained by the LPI, in order to enhance the deposition uniformity and coverage lithiumization moved to the following year to a Lithium Capillary Porous System (LCPS) [69] named Liquid Lithium Limiter (LLL) in RFX-mod as melted lithium is brought in contact with

the plasma in a limiter configuration [70]. In fig. 2.9 a picture of the CPS head after setup in RFX-mod torus is shown. Plasma in contact with the CPS head promptly ionizes lithium atoms allowing their deposition on the first wall along the magnetic field lines. A strong toroidal component of the magnetic field is therefore needed to allow a uniform lithium deposition around the torus. In fig 2.10, the experimental setup in RFX-mod is displayed. Due a strong poloidal field characteristic of the RFP magnetic configuration, lithium transport and deposition in RFX-mod was limited to the neighboring region of the poloidal position of the limiter. Nonetheless, the LLL proved to be a good candidate to overcome the problems of heat load and erosion on the first wall, keeping a very low recycling regimes and improved energy confinement time [64, 65].

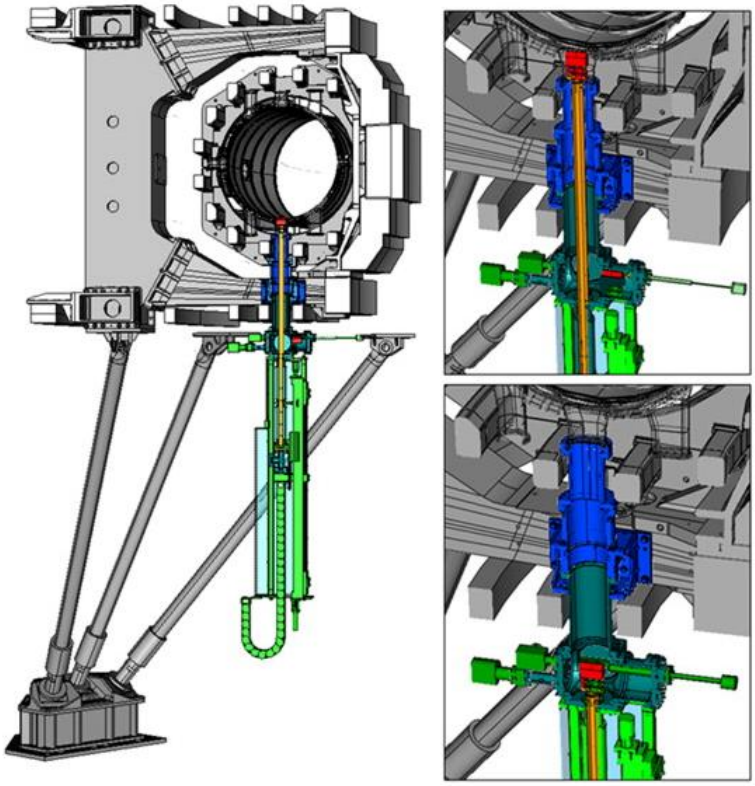

Figure 2.10: View of the CPS system: the CPS head (red) on top of the motion tube (orange), the 200 mm side cubic vacuum chamber (dark green) anchored to the vessel (grey) through an extension pipe (blue), below the field shaping and magnetizing coils. On the top right: the CPS exposed to the plasma. On the bottom right: the CPS extracted. Courtesy of Alfier et al. [70].

c. Lithium evaporation

Evaporation of melted lithium in a dedicated conditioning session before plasma operation [60] has been performed after operation with the LLL was interrupted due an irreversible failure on the CPS head. Instead of using the LLL in a limiter configuration during plasma operation, after the apparatus is brought to the level of the torus envelop (see fig. 2.9), the CPS head is heated to induce lithium release into vacuum and accelerated towards the first wall. This technique allows a large quantity of lithium deposition, however very localized in a narrow region nearby the insertion position of the apparatus. More than 500 nm were measured by post-mortem analyses on a graphite sample exposed just in front of the evaporator during the lithiumization.

d. High frequency Multi-Pellet Injector (MPI)

Lithium pellet injection in RFX-mod proved effective in providing a uniform lithium coating over the whole wall surface. The drawback is that conventional injectors require a high number of conditioning discharges to reach an adequately thick lithium coating. Recently in 2013, to overcome this problem, in RFX-mod a new Multi-Pellet Injector (MPI) developed by the Princeton Plasma Physics Laboratory originally for ELM pacing [71] has been tested. The aims of this technique were: (i) the injection of a high amount of lithium deep into the plasma core of helium conditioning discharges to provide a uniform thick lithium deposition on the wall; (ii) lithium injection also on hydrogen discharges to continuously refurbish the wall with 'fresh' lithium during normal operation.

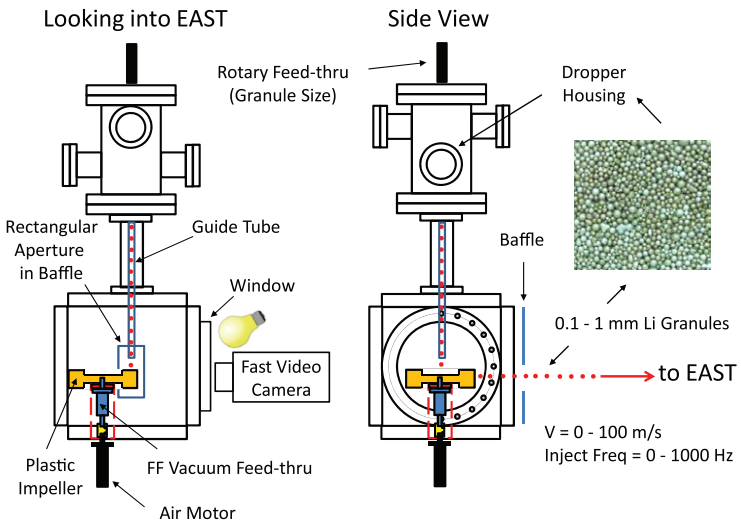

Figure 2.11: The experimental setup of the Multi-Pellet Injector (MPI) on EAST tokamak [71].

A detailed description of the new MPI developed by the Princeton Plasma Physics Laboratory can be found in ref. [71], where its application on EAST tokamak device for ELM pacing is described (see fig. 2.11). In that case 0.7 mm diameter lithium spheres were injected at a frequency of 25 Hz. These parameters are inadequate to inject a large amount of lithium in the RFX-mod discharges, which have typical duration of 0.3-0.5 s. To increase the injection rate, lithium spheres of 1.0 mm diameter (the maximum one presently commercially available) have been selected; furthermore the dropper frequency has been increased by installing a piezoelectric disc (PZD) with a 4.0 mm central aperture instead than the 2.5 mm one used on EAST. Initially a serious problem was the high number of pellets lost in the vacuum duct between the impeller and the plasma, due to the spread in the granule injection angle and the small size (38 mm) of the CF40 vacuum port available for the installation. To maximize the injection efficiency, the RFX-mod interface has been modified to use the whole aperture of the vacuum port and the injector has been moved as close as possible to the vacuum vessel.

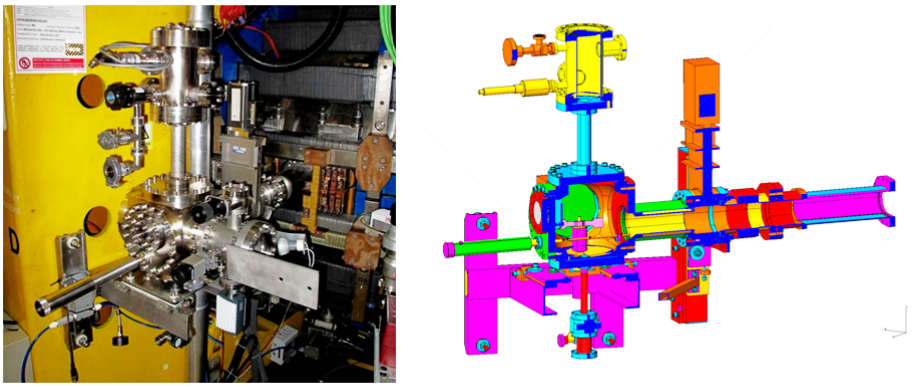

Figure 2.12: The experimental setup of the Multi-Pellet Injector (MPI) on RFX-mod.

In fig. 2.12 it is possible to see the final installation. With this arrangement 1 mm lithium spheres have been injected in RFX-mod at the maximum frequency of 250 Hz for a lithium mass injection of 70 mg/s, yielding a deposition on the wall of about 25 mg on each discharge. Compared to the 4 mg/discharge previously obtained by means of the single pellet injector this corresponds to a 7× increase in deposition efficiency.

Finally, extensive surface analyses techniques have been performed on samples exposed during the different lithiumizations in RFX-mod to study the deposition uniformity and the lithium-graphite chemistry obtained for each technique. The results are shown and discussed in Chapter 5.

2.4 RFX-mod wall conditioning diagnostics

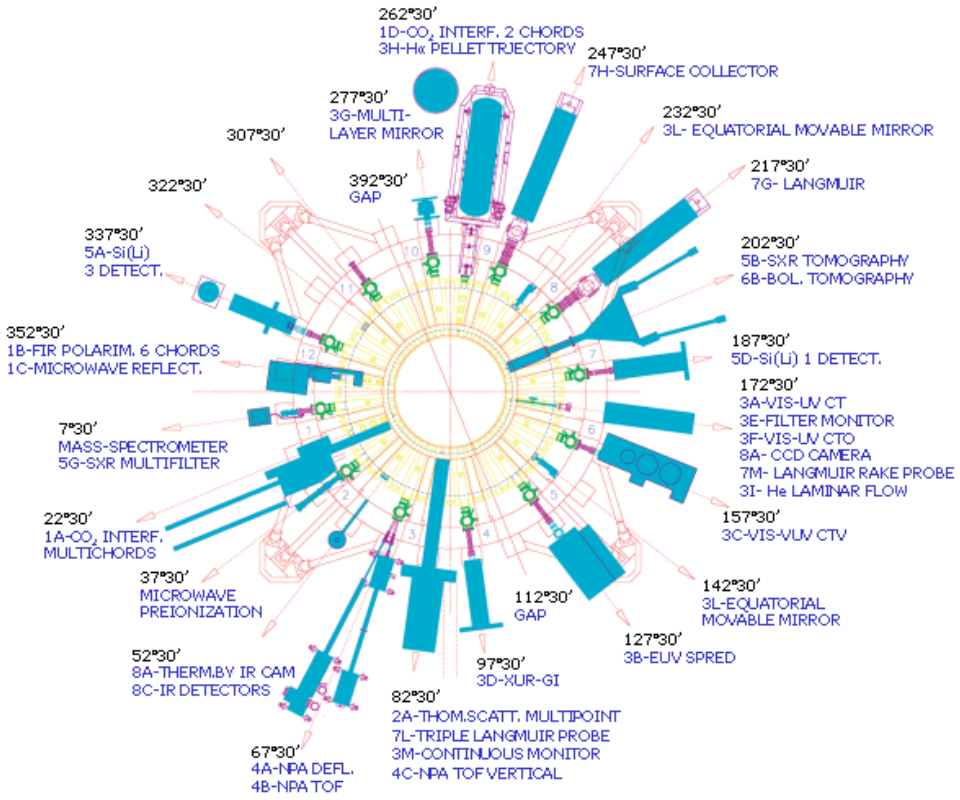

Figure 2.13: RFX-mod general diagnostics layout.

2.4.1 Brief introduction to RFX-mod diagnostics system

In order to achieve its mission as the largest RFP device and provide fusion-relevant physics understanding of high β ohmically heated plasmas, a systematic program of measurements of the spatial and time evolution of the basic plasma parameters such as electron and ion temperatures T_e and T_i, electron density n_e, energy and particle confinement times τ_E and τ_p, impurity content, and magnetic fields is needed. The diagnostic systems implemented in RFX-mod are similar to those used in tokamak experiments, they differ however in some aspects related to the peculiarities of the RFP configuration, characterized in general by higher electron density and larger fluctuations of the physical parameters. Plasma and magnetic field fluctuations are in fact related to the so-termed dynamo effect, i.e. the magnetic field regeneration process sustaining a steady state RFP configuration.

The most significant diagnostic systems operating in RFX-mod are listed in tab. 2.3 and the general layout is shown in fig. 2.13. A comprehensive list of the implemented instrumentation and diagnostics has been reported in

[72], together with a general survey of the grounding systems and the cables layout.

Table 2.3: Basic diagnostic methods in RFX-mod

Measurements	Diagnostics methods
Electron density	– CO_2 interferometer
	– Multipoint and multipulse Thomson scattering
	– Microwave reflectometer
Electron temperature	– Multipoint and multipulse Thomson scattering
	– Si(Li) pulse height analyser (PHA)
	– Spectroscopy (line intensily ratio)
	– Soft X-ray (SXR) two-filter monitor
Ion temperature	– Multichannel spectrometer
	– E‖B neutral particle analyser (NPA)
	– Time-of-flight (TOF) NPA
Impurities	– Multichannel visible UV spectrometer
	– Flat-field survey spectrometer
	– Vacuum CTV spectrometer
	– Interference filter array
	– Grazing incidence spectrometer
	– SXR bolometric tomography
	– Bolometer arrays
	– Multilayer filters SXR spectrometer
	– Si(Li) PHA
Fluctuations	– SXR monitor array
	– Electrical probe arrays
	– CO_2 interferometer
	– Microwave reflectometer
	– Far-IR (FIR) polarimetry
Edge plasma,	– Movable Langmuir probes
plasma wall interaction	– Surface collector and erosion probes
	– Microwave reflectometer
	– Interference filter array
	– Charge-coupled device (CCD) cameras
Internal magnetic field	– Magnetic probes
	– FIR polarimeter

The optimization of the wall conditioning techniques in RFX-mod that is the subject of this thesis has been diagnosed by four main diagnostics. A set of electrostatic probes have been used to investigate the ion flux at the first wall during glow discharges. The probes are embedded in the graphite first wall which is part of the Integrated System of Internal Sensors (ISIS) and are presented in Section 2.4.2. A multichord spectroscopic diagnostic system has been used for the characterization of the glow discharge plasma emissivity, it is documented in Section 2.4.3. A Residual Gas Analyzer (RGA) has been adapted for both glow discharge gas exhaust and power plasmas exhaust measurements; the implementation, data acquisition upgrade and calibration work are discussed in details in Section 2.4.4, dedicated to the gas fueling and exhaust diagnostics. A set of material-sample manipulators employed for

exposure of samples during film deposition and for metallic coating testing are presented in Section 2.4.5.

2.4.2 The Integrated System of Internal Sensors

RFX-mod vacuum chamber is equipped with a large set of calorimetric, electrostatic and magnetic probes located inside the vacuum vessel, which constitute the Integrated System of Internal Sensors (ISIS) diagnostic. They are placed at r/a $\simeq$ 1, behind the graphite tiles which cover the first wall of the machine and protect the sensors from the plasma. This system is mainly devoted to the acquisition of high frequency data in order to provide a thorough description of fluctuating quantities in the RFX-mod edge plasma. In fig. 2.14 a schematic of the probes configuration in RFX-mod is shown.

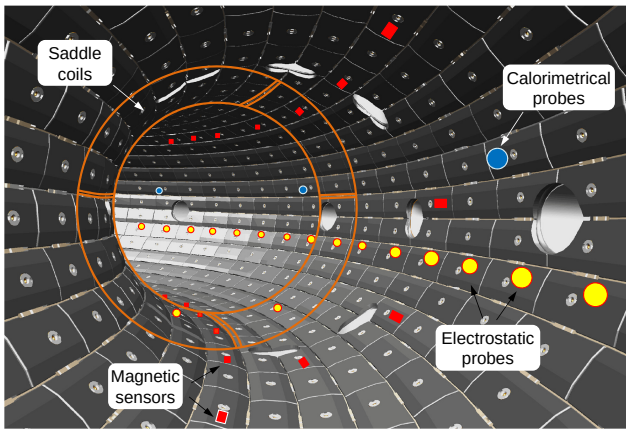

Figure 2.14: Schematic view of ISIS system: electrostatic and magnetic toroidal arrays and some calorimetric sensors are indicated.

As above-mentioned, ISIS is composed of three subsystems:

(1) The thermal probes are thermocouples, measuring the average temperature of the whole tile, mounted on the back of some of the first wall graphite tiles. The system consists in one partial toroidal array of 8 probes, located at the poloidal angle θ = 6.5°, on the outboard side, and adjacent to the pumping ports, which allow easy access for maintenance.

(2) The electrostatic sensors (Langmuir probes) are electrodes, measuring the floating potential V_f , that is the potential of an electrically insulated object immersed into the plasma. The system is composed of a toroidal array of 72 pins equally spaced located at θ = 340.7°, a poloidal array of 8 triple probes at θ = 248.6° and of additional single and triple probes. A description of the sensors is available in [73].

(3) The magnetic sensors are saddle and pick-up coils located on the back of the first wall graphite tiles: the nominal radial position of the

measurements is r/a = 1.03.

During the reversed-field pinch plasma operations the electrostatic probes behave like usual Langmuir probes, with characteristic (V, I) curves that allow the estimation of edge electronic temperature and electric field. During the GDC sessions, however, the wall is the cathode of the glow discharge. In front of it, and hence in front of the probe itself, a cathode sheath with a typical dimension of 1 m arises and wall and probes are exposed to ion bombardment. In these conditions, (V, I) characteristic curves different from the typical Langmuir ones have been measured. Notwithstanding this, a significant measure is still possible: the current collected by each probe when the bias against the wall potential is 0 V estimates the ion flux at the first wall. The measurement is affected by secondary emission (up to 30% according to a rough estimation) not considered in the analysis reported in chapter 3.

2.4.3 Multichord Doppler spectroscopic diagnostic

A multichord Doppler spectroscopic diagnostic based on line-of-sight integrated measurements is set up in RFX-mod used mainly for plasma flow measurements [74]. It is arranged with a set of 18 Lines of Sight (LoSs), all located at the same toroidal position to cover a poloidal cross-section as displayed in fig. 2.15, both for observations in the visible spectrum (solid pink lines) and in the ultraviolet (dashed cyan lines).

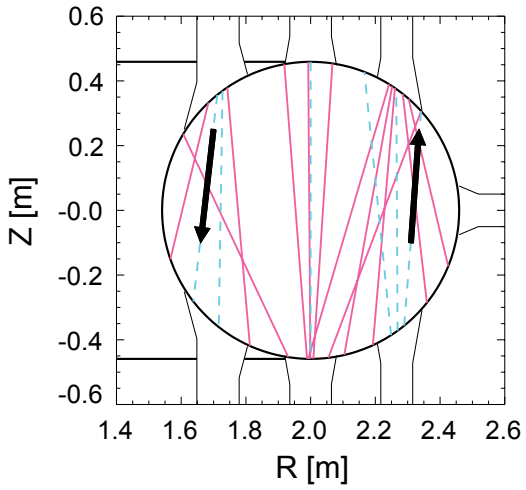

Figure 2.15: Set of lines of sight for passive Doppler spectroscopy in the visible (pink lines) and UV (dashed cyan lines) range.

Three different spectrometers are used, one in the UV, dispersion 0.16 Å/pixel, two for visible radiation: a Littrow instrument, dispersion 0.13 Å/pixel, and an ARC-750 spectrometer, dispersion 0.27 Å/pixel. This configuration allows simultaneous measurements of different impurity ion

radiation, with a time resolution of 5 ms (limited by the intensity of the signal). The reconstructions of the line emissivity in typical 1.5 MA plasmas are obtained by a one-dimensional collisional-radiative impurity transport model [75].

For the optimization of the glow discharge global parameters, the emission spectrum of the GDC discharge is measured along 5 LoSs (see fig. 2.16) by a Czerny-Turner ARC-750 spectroscope. One is aligned to intersect a region very close to one anode, 3 lie in a radial-toroidal plane far from the electrode, and have different impact parameters in order to obtain measurements at three radial positions (normalized impact parameters r/a 0.71, 0.42 and 0.18). The fifth line of sight is located close to the three far from the anode but lies on a poloidal plane, with r/a 0.56.

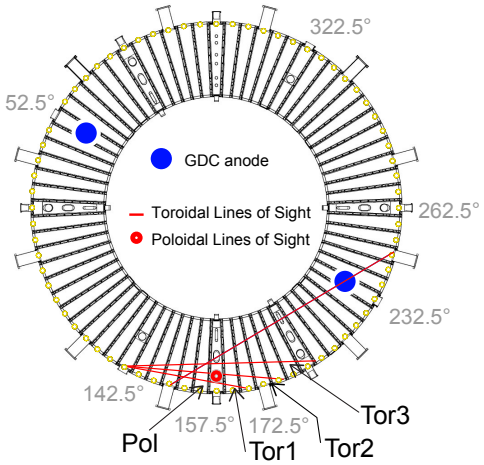

Figure 2.16: Lines of sight configuration for emissivity measurements of the glow discharge plasmas in RFX-mod.

2.4.4 Gas fueling and gas exhaust diagnostics

To understand the recycling as well as the impurity behavior in RFX-mod, the analysis of the partial pressures in the gas surrounding the plasma before, during and after power discharges represents a well suited experimental tool. The fueling gas molecules observed during the discharges result directly from plasma particles recycled at the walls. They are then ionized and contribute to the plasma refueling making density behavior extremely unpredictable. In 2009, a gas fueling diagnostic name DESO has been set up in RFX-mod to carefully compute the total gas molecules fueled to the plasma and the gas desorbed immediately after the discharge [76]. The tool uses total pressure measurements from pressure gauges mounted around the vessel. While it is able to compute a precise number of molecules for a single fueled gas, the desorbed figure includes many species that are retained in the first wall from which the desorption occurs. In this thesis, the diagnostic development work carried out consists in upgrading the use of an already present Residual

Gas Analyzer (RGA) to monitor gas exhaust during and after plasma power discharges. The apparatus in RFX-mod has been used only for gas exhaust during wall conditioning sessions such as baking and GDCs, therefore the task consists in adapting its operation to plasma discharges modifying the time resolution and data acquisition system.

The Residual Gas Analyzer (RGA) data acquisition system, its calibration and operation for the 2012-2014 RFX-mod experimental campaigns are presented. The main purposes of the upgrade of the RGA data acquisition procedure is to make available the instant in-vessel gas exhaust data on daily basis, monitor the gas species during glow discharge sessions and more importantly extend the sampling of the mass analyzer during RFX-mod power discharges readily switching back and forth for plasma runs that includes short glow discharges during the experimental day. Ultimately the main goals of the diagnostic development presented in thesis are:

i. Examine the efficiency of the wall conditioning techniques particularly the GDC sessions
ii. Enhance density control by drawing up a particle inventory of the graphite wall at any time of operation
iii. Develop an operation support diagnostic that introduces a fuel retention indicator in RFX-mod

a. RGA arrangement and gas flow considerations in RFX-mod

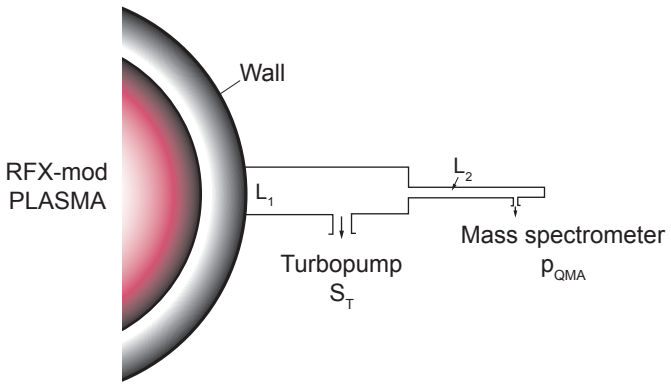

Figure 2.17: Schematic diagram of the RGA setup in RFX-mod.

A molecular gas flow is assumed within the duct connecting the Quadrupole Mass Analyzer (QMA) to RFX-mod vessel. It is also understood that the particles escaping from the plasma are ionic or atomic and energetic. Moreover, using the molecular random flow conditions for the particle transport within the tube to the position of the QMA does not lead

to large errors assuming that upon approaching the vacuum vessel or the entrance of the tube these species are neutralized and thermalized. Thus the direct flux of atomic particles entering the tube decreases rapidly with increasing distance from the entrance. Fig. 2.17 displays the RGA setup in RFX-mod. With these basic considerations, the neutral gas pressure p at RFX-mod vacuum wall under steady-state conditions has to be evaluated from the measured pressures p_{QMA} at the QMA by:

$$p = p_{QMA}\left(1 + \frac{S_T}{L_{1,2}}\right) \tag{2.4.1}$$

where S_T, is the pumping speed of the turbopump for the measured species and $L_{1,2}$ are the effective vacuum conductances of the tube system. A simplified layout of the vessel, plasma and the RGA is shown in fig. 2.18.

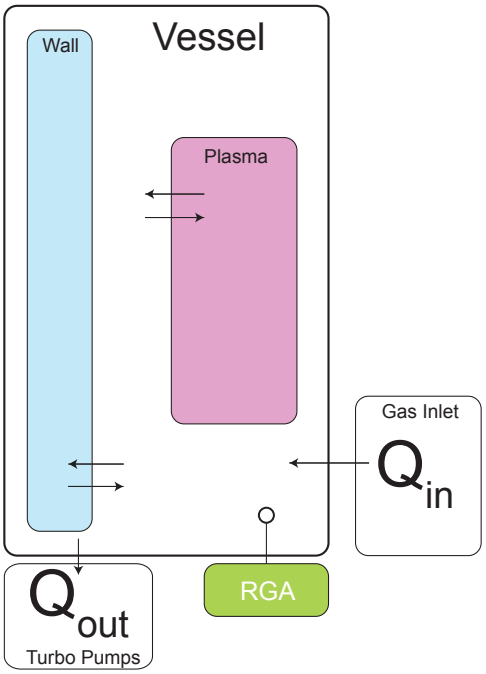

Figure 2.18: Gas balance schematic in RFX-mod.

With the previous measure of the pressure at the vessel duct it is possible to achieve a gas balance and compute the number of gas particles retained in the graphite first wall after each discharge using the following empirical formula:

$$\Delta part = Q_{in} - Q_{out} \tag{2.4.2}$$

$$\Delta part = \frac{1}{K_B T}\kappa_\tau S_p \int_{t_{start}}^{t_{end}} p dt \tag{2.4.3}$$

Where:
κ_τ corrective factor for truncated integral
S_p pumping speed evaluated where pressure is measured
p pressure

b. Effective pumping speed, experimental error and calibration

The speed of a pump is related to the inlet pressure. During a plasma discharge the fueled or puffed gas is evacuated with an exponential pressure decay and the pumping speed is usually pressure and gas species dependent. The pumping is therefore different for H and He and a precise determination is crucial to compute an accurate gas balance. The pump speed can be related to the pressure and expressed as:

$$p(t) = p_0 exp^{-\frac{S}{V}t} \tag{2.4.4}$$

The pressure experimental data retrieved from the RGA are fitted with an exponential fit and the evacuation speed is computed from the decay constant. It is assumed that in the range 10^{-3}-10^{-5} mbar the evacuation speed is constant. However, the measured partial pressures in RFX-mod plasma discharges can reach up to 10^{-1} mbar, therefore the pumping speed is not constant and a dynamic fitting of the data has been adopted. In fig. 2.19 each three successive data points are fitted with an exponential function and a sequential evacuating speed is determined (S1, S2, S3, ...etc).

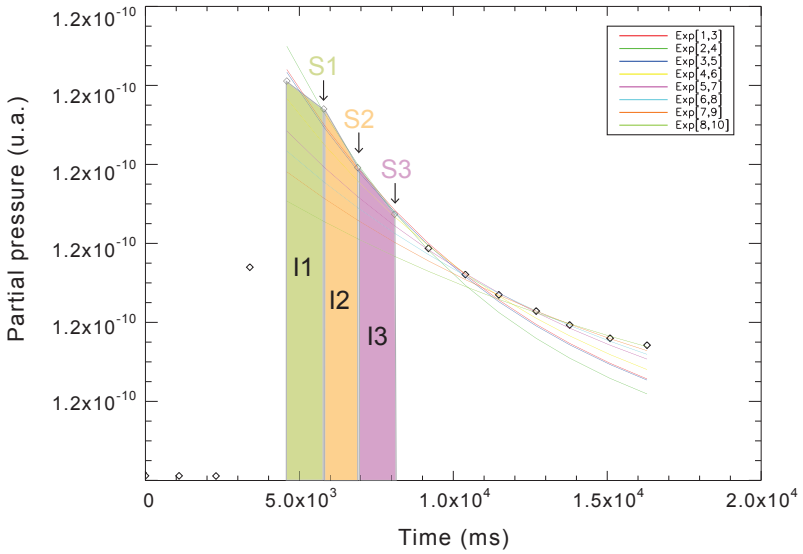

Figure 2.19: Accurate determination scheme of the pumping speeding for each discharge in RFX-mod.

From eq. 2.4.4, the total number of gas neutrals evacuated is computed step by step associating a pumping speed S_i to a pressure integral I_i and then obtaining a total evacuated number of molecules N_{mol}^{tot}. The pressure is integrated for a duration of 5 seconds from the discharge t=0.

$$N_{mol}^{tot} = \frac{1}{K_B T} \kappa_\tau \sum_{i=1}^{n} S_i I_i \tag{2.4.5}$$

The RGA is executed with a procedure that is set up with adequate parameters to monitor either plasma discharges or wall conditioning sessions. Two recipes of the RGA are used for each task: during GDC sessions a recipe set up with a 1-100 amu range and a time resolution of 10 seconds is used, whereas during plasma discharges a second recipe with 5 amu configuration and a time resolution of $\simeq 1$ second is used. The RGA is set up to automatically generate an ASCII report file with data columns of the partial pressures of the selected amu corresponding to the monitored gases in millibar. The device can be set up with the two configurations of the scan frequency either with an auto scan of the masses where data is collected and an approximate time per scan is defined by the device or with a pre-specified frequency scan. Therefore, the resolution of the device depends only on the number of the scanned masses and is defined by the internal measure system of the spectrometer.

Although the scan frequency of the RGA depends on the number of monitored masses, the time resolution has been examined looking at the collected data. The time resolution of the device has been analyzed during HeGDC and He plasma discharges. In order to estimate the deviation of the scan frequency, the intervals between each scan have been analyzed from the collected data both during GDCs and plasma discharges. In tab. 2.4, the results of the statistical analysis of the time interval of the RGA scans over 5 HeGDC and 10 He discharges are shown.

Table 2.4: Error analysis of the RGA

Task	N masses	σ (ms)	μ (ms)	Max (ms)	Min(ms)
HeGDC	100	87,72	9997,65	10838	8426
HeShot	5	52,22	1155,49	1360	220

Smaller deviation from the setting time resolution has been observed for a 5-amu configuration of the RGA. Monitoring only 5 gas species allows not only a higher time resolution but also a higher accuracy in the effective measurement of the partial pressures. During plasma operation hydrogen amu=2, helium amu=4, water amu=18, nitrogen amu=28 and oxygen amu=32 are monitored. Future use of the RGA with higher resolution and accuracy is planned with only 2-amu configuration to only monitor hydrogen and helium.

The RGA has been set up with the 5-amu configuration of the QMA and the measured He partial pressure during He plasma discharges with a gas filling of about 1.18×10^{20} (H atoms) are shown in fig. 2.20. An overall 15%

error has been observed allowing the introduction of the subsequent y-error bars.

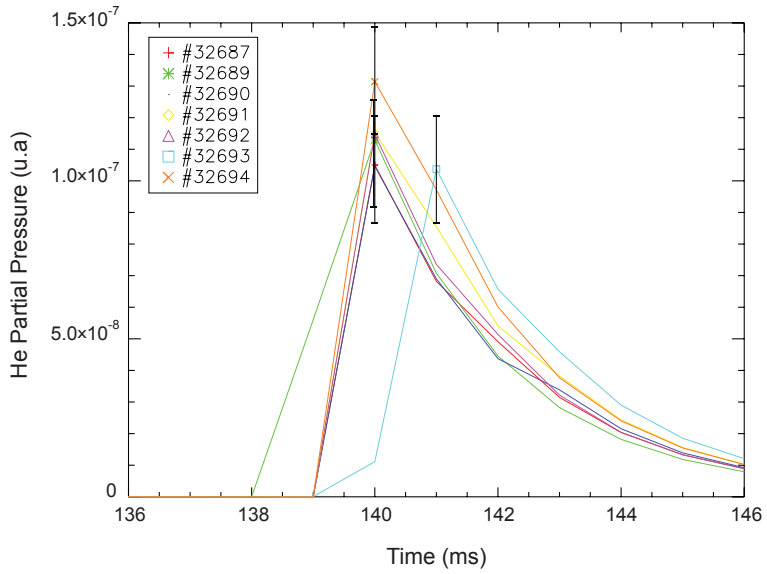

Figure 2.20: Evaluation of RGA systematic instrument error for a set of five consecutive He power discharges in RFX-mod.

In RFX-mod the RGA is used with a base pressure higher than the pressure range needed to accomplish calibrated measurements during plasma discharges. Therefore, the device has been manually calibrated for amu=2 (hydrogen) and amu=4 (helium) by simultaneously monitoring the QMA partial pressure of H_2 and He while performing H_2 and He glow discharges and the total pressure by a gauge mounted on RFX-mod vessel.

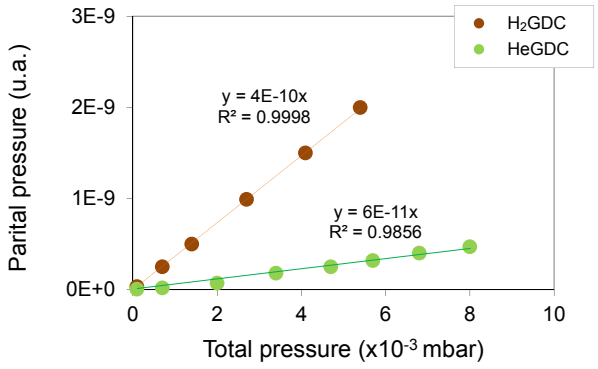

Figure 2.21: Calibration of the RGA for m/e=2 (hydrogen) and m/e=4 (helium).

In fig. 2.21 the calibration at pressures ranging from 0-8 $\times 10^{-3}$ mbar is

shown as well as the linear fitting giving the calibration constants.

c. The new data acquisition implementation

Up to present the RGA has been setup in RFX-mod for monitoring gas exhaust only during wall conditioning sessions such as baking and glow discharges. Therefore, the data acquisition system is only adapted for local operation and the data are only stored in a local computer. In order to make the data available at the end of every experimental day and include partial pressure measurements during plasma discharges, the sampling of the mass spectrometer has been increased and the new data storage system has been implemented using the MSDplus [77] data handling system.

The RGA data is collected during the experimental day using two different recipes for plasma power discharges and glow discharges. At the end of the experimental day the data is processed and stored in a daily MDSplus pulse file then made available for data analysis at the beginning of the next experimental run. A procedure has been setup to allow the recipe-swap and a routine data-copy was made. In fig. 2.22 a screen shot of the jTraverser window (showing the tree sequence of the pulse file) and the jScope window (data visualization) is shown.

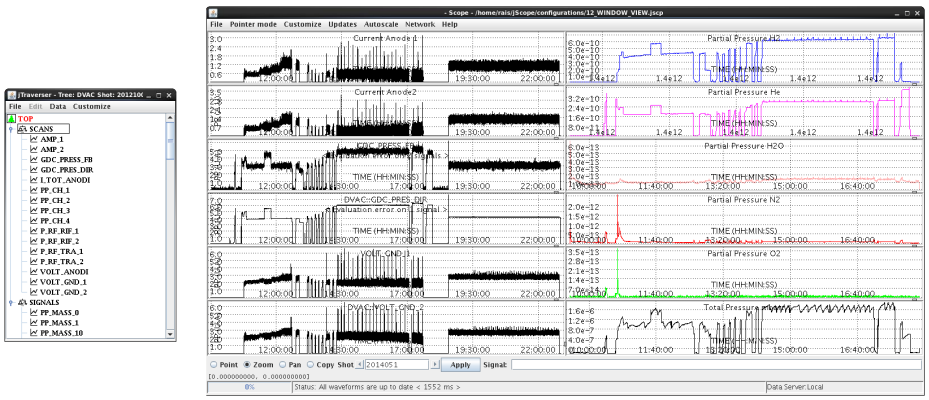

Figure 2.22: RGA data visualization with the jScope program and the tree configuration performed by the MSDplus data handling system.

The pulse file includes both the partial pressure scans either during power discharges and glow discharges, hence an easy access and comparison of the data can be performed. Along with the visualization tool of MSDplus, an easy access to the data using multiple programming languages such as IDL operations on the raw data became very handy. The pulse file of the RGA also includes data from the glow discharge parameters such as the plasma current, voltage and pressure.

2.4.5 Material-sample manipulator

In RFX-mod, material sample exposure is routinely performed to investigate the deposition of the wall conditioning thin films by *ex-situ* analyses. Mostly, the samples exposed are made from the same graphite of the first wall tiles (manufacturer Carbone Lorraine (now MERSEN), type 5680PT) that completely cover the Inconel 625 vacuum vessel, but other materials such as molybdenum can also be used. The insertion of the samples up to the graphite first wall envelope is made possible thanks to a manipulator. Fig. 2.23 displays the manipulator arrangement in RFX-mod and the design of the graphite samples. The manipulator heads are composed of up to 4 samples of about 1×1 cm each, which are exposed simultaneously but can be removed independently. The 4 samples are designed to be aligned to the surrounding graphite tiles. In RFX-mod, two manipulators are set up in vertical ports at different toroidal positions 45° away to investigate in particular toroidal asymmetries in thin film deposition during wall conditioning.

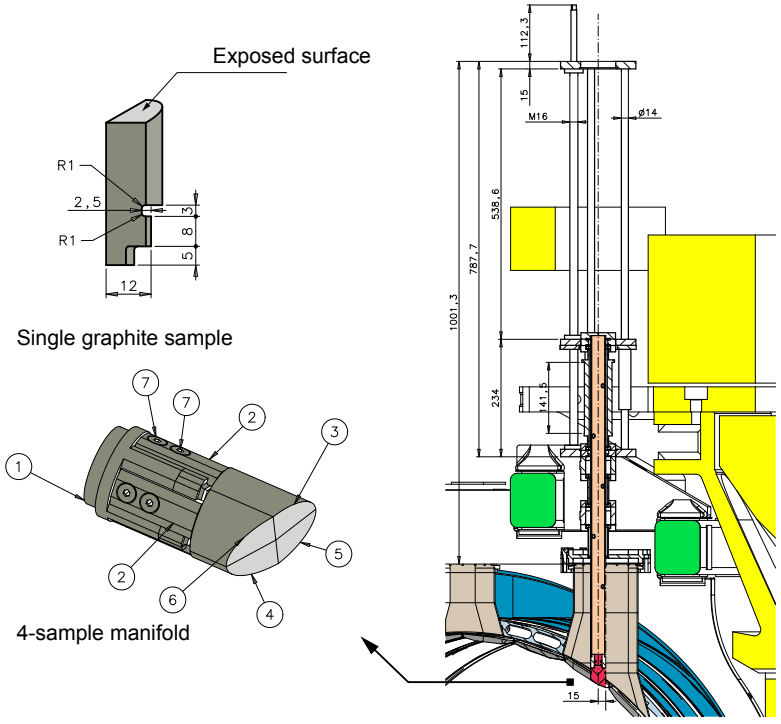

Figure 2.23: Material sample manipulator and graphite samples design.

2.5 Surface characterization methods

The surface characterization of the samples exposed to wall conditioning in RFX-mod has been conducted with an extensive set of surface analysis techniques in collaboration with external laboratories. The techniques include Secondary Ion Mass Spectrometry (SIMS), Scanning Electron Microscopy (SEM), Energy Dispersive X-ray (EDS/X), High Resolution X-ray Photoelectron Spectroscopy (HR-XPS) and Rutherford Backscattering Spectroscopy (RBS).

2.5.1 Secondary Ion Mass Spectrometry

a. SIMS principle

Secondary Ion Mass Spectrometry (SIMS) is a surface analysis technique based on the phenomenon of secondary ions emitted by the specimen upon impact of a primary ion beam. Introduced in 1962 [78], it relies on the bombardment of primary ions onto the surface of a sample, triggering a cascade of atomic collisions (see fig. 2.24). Some of the ejected particles can be spontaneously ionized as atoms or clusters and are representative of the composition of the target area. In a SIMS instrument, "secondary ions" are accelerated and separated in function of their mass/charge ratio (m/z) before detection. SIMS has the capability of analyzing the entire periodic table with isotopic discrimination and typical detection limits on the ppm level.

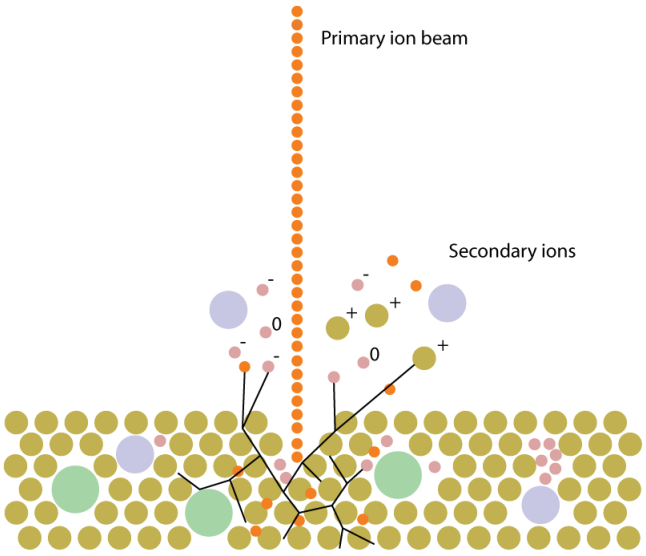

Figure 2.24: Schematic drawing of the secondary ion emission process initiated by the impact of a primary ion.

b. Experimental facility

Dr. Barison Simona from Padova CNR-IENI laboratory performed the SIMS measurements. In particular the SIMS profiles of the samples have been obtained eroding the sample by a monochromatic (6 keV) O_2^+ primary ion beam collimated to 50 mm was generated in a mass-filtered duoplasmatron ion gun (model DP50B, VG Fisons, UK). An EQS1000 (Hiden, UK) mass energy analyzer with high transmission 45° sector field electrostatic energy analyzer and a quadrupole mass filter were used for negative- and positive-ion detection in counting mode. Lens and energy analyzer potentials, quadrupole electronic control units and the detection system were controlled via a Hiden interface. The chamber pressure was typically 5×10^{-10} mbar, while, when the oxygen was introduced for the primary ion beam generation, the working pressure was around 3×10^{-9} mbar. The ion species were identified by resolving the overlapped m/z signals with an isotope pattern simulation program. Border effects were avoided with electronic gating, since only secondary ions coming from the central 50% rastered area were collected. The erosion rate, measured by a Tencor P-10 mechanical profiler having a 2 nm vertical resolution, was estimated to be about 8 nm/min with the maximum available depth resolution. Fig. 2.25 displays the laboratory experimental setup.

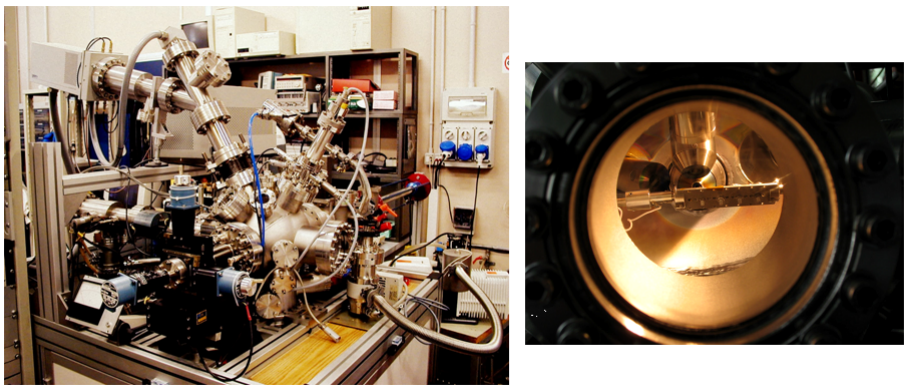

Figure 2.25: SIMS laboratory experimental setup at Padova CNR-IENI institute (left), sample holder (right).

2.5.2 High Resolution X-ray Photoelectron Spectroscopy (HR-XPS)

X-ray Photoelectron Spectroscopy (XPS), also known as electron spectroscopy for chemical analysis (ESCA), is a quantitative spectroscopic technique that yields information on the electronic structure, elemental composition and chemical state in the near surface region (< 5 nm) of a material. This experimental technique is based on the photoelectric effect,

where a surface hit by photons emits electrons. The effect was discovered by Heinrich Hertz in 1887 [79] and later explained by Albert Einstein in 1905 [80] who was awarded the Nobel Prize in Physics in 1921 for this contribution. The process of using photons (light) to remove electrons from a material is called photoemission, and the emitted electrons are called photoelectrons.

a. Principles of X-ray Photoelectron Spectroscopy

When light irradiates a sample, the energy is conserved following the equation:

$$E_i + h\nu = E_f + E_{kin} \tag{2.5.1}$$

where E_{kin} is the kinetic energy of the ejected electron, $h\nu$ is the energy of the impinging photon, and E_i and $E_f$are the initial and final state energies of the system, respectively. The energy difference between the initial and final state of the system is the ionization potential. For the photoemission process to take place, i.e., for an electron to be ejected from the surface, the energy of the impinging photon must be such that the photoelectron has sufficient energy to overcome its binding energy E_B and the work function of the sample Φ_s. Replacing the ionization potential, the kinetic energy is expressed as:

$$E_{kin} = h\nu - (E_B + \Phi_s) \tag{2.5.2}$$

In order to obtain accurate binding energies of the emitted electrons, the kinetic energy distribution of the emitted photoelectrons is measured. Fig. 2.26 displays the main features and the energies involved in the photoemission process. In XPS experiments the electron analyzer and the sample are electrically grounded, hence their Fermi levels will align. The sample and the electron analyzer may have different work functions as shown in fig. 2.26(a). The binding energy of the photoelectron is referenced to the Fermi level, i.e., the zero of the binding energy scale is at the Fermi level. Hence, it is the spectrometer and not the sample work function that must be accurately known.

In general, standard samples are used to calibrate and determine the work function of the spectrometer prior to the photoemission experiments. Consequently, the electron binding energy can be calculated using the measured kinetic energy of the photoelectrons as:

$$E_B = h\nu - E_{kin} - \Phi_A \tag{2.5.3}$$

An electron analyzer is used to calculate the kinetic energy of the photoelectrons. In fig. 2.26(b), a typical XPS setup with a hemispherical type electron analyzer is displayed. The surface of a sample is irradiated by monochromatic photons of selected energy which produce photoelectrons. The emitted photoelectrons are collected, energy selected, and focused by electrostatic lenses into the electron analyzer entrance slit of the

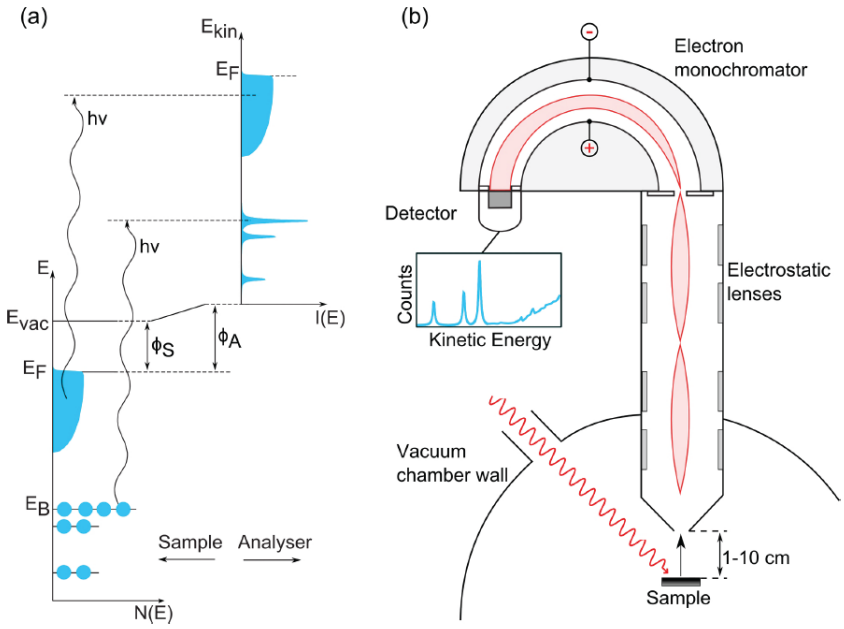

Figure 2.26: (a) Schematic illustration of the photoemission process. (b) Sketch of a XPS measurement system using a hemispherical electron analyzer with a lens system. The figure has been adapted from [81].

hemisphere. Only electrons with the right kinetic energy, the so-called pass energy, are transmitted through the electron analyzer to the detector. The electron analyzer is a concentric hemispherical analyzer (CHA), which is made of two concentric hemispheres with different applied voltages in each hemisphere, such that there is an electric field between the two hemispheres. Electrons traveling faster than the designated energy will impinge on the outer hemisphere, while if they are traveling slower, they will hit the inner hemisphere. The CHA disperses the incoming electrons according to kinetic energy and momentum in a narrow energy range. Electrons accelerated onto the phosphor screen give off a light flash which is counted by a charge-coupled device (CCD) camera. The photoemission intensity spectrum is obtained by measuring the photoelectron yield (counts per energy interval) as a function of the kinetic energy of the electrons that reach the analyzer. The whole setup is evacuated to UHV, typically with pressure in the order of $\sim 10^{-10}$ mbar.

b. Atomic sensitivity factor

Quantitative data such as the relative concentration of the various constituents can be obtained from peak areas of XPS spectra. A sensitivity factor for each element has to be either known or determined in order to calculate the relative concentration for each constituent. For a sample that is homogeneous in the analysis volume, the number of photoelectrons per

second in a specific spectral peak I is given by [82]:

$$I = nf\sigma\theta y\lambda AT \tag{2.5.4}$$

where n is the atomic concentration of the element (atoms/cm^3), f is the x-ray flux (photon/cm^2-sec), σ is the photoelectric cross-section for the atomic orbital of interest (cm^2), θ is the instrumental angular efficiency factor between photo path and detected electron, y is the efficiency in the photoelectric process for formation of photoelectrons of the normal photoelectron energy, λ is the mean free path of the photoelectrons in the sample, A is the area of the sample from which photoelectrons are detected and, T is the detection efficiency for electrons emitted from the sample. The atomic sensitivity factor S is then defined as:

$$S = f\sigma\theta y\lambda AT \tag{2.5.5}$$

With sensitivity factors known, the stoichiometric ratio of two elements A and B can be determined from the peak height or peak areas:

$$\frac{n_A}{n_B} = \frac{I_A/S_A}{I_B/S_B} \tag{2.5.6}$$

where S_A and S_B are the sensitivity factors for the elements, which are tabulated and listed in literature [82]. The expression may be used for all homogeneous samples if the ratio S_A/S_B is matrix-independent.

Table 2.5: Values of XPS atomic sensitivity factors used in this work [82].

	Li_{1s}	B_{1s}	C_{1s}	O_{1s}
Sensitivity Factor	0.025	0.159	0.296	0.711

c. Depth profiling using XPS

XPS can be used for depth profiling and obtain the in-depth distribution analysis of the chemical or elemental composition of a sample. From XPS spectra, the chemical state composition versus depth analysis can be obtained either by destructive or non-destructive techniques. The destructive depth profiling technique involves removal of the top layer of samples while XPS spectra are analyzed. Usually ion sputtering with a known sputtering rate is used. This method allows for the determination of the composition over a wide range of thickness (from nanometers to microns). However, in some cases sputtering can easily lead to a change in surface stoichiometry and structure.

d. HR-XPS instrumentation: Princeton University

The HR-XPS measurements were carried out at Princeton University, Chemical and Biological Engineering department within a collaboration with the Princeton Plasma Physics Laboratory setup to study in particular the physical chemistry of lithium and boron coated RFX-mod graphite samples exposed and unexposed to plasma discharges. High-Resolution XPS (HR-XPS) uses a monochromator which provides the following advantages over a standard x-ray source:

(i) An x-ray energy distribution with reduced energy width improves chemical selectivity by narrowing the spectral peaks.
(ii) A lower spectral background.
(iii) The elimination of unwanted x-rays from satellites and anode impurities, which simplifies spectral analysis.
(iv) The elimination of Bremsstrahlung and thermal radiation from the x-ray source, which greatly reduces x-ray source induced damage.
(v) A focused x-ray spot on the sample increases the sensitivity on small samples.

The surface analyses were performed in two periods during which the student has monitored in person the activity at Princeton University. The first analyses were carried out during the 2013 fall and a second set of analyses were performed in the 2014 fall during a return trip to Princeton. Fig. 2.27 displays a photo of the laboratory setup.

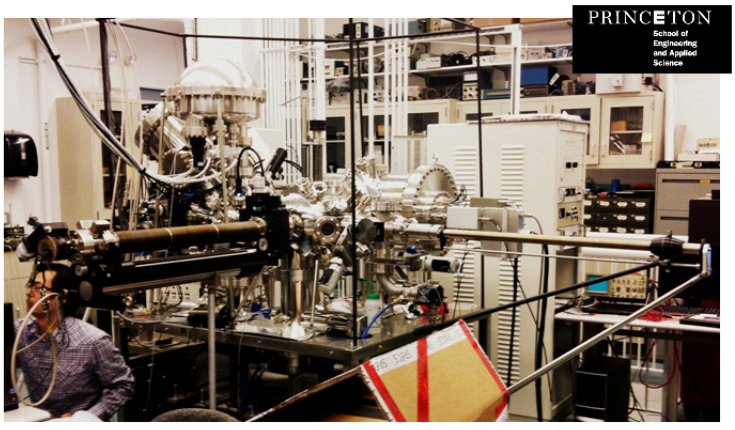

Figure 2.27: Photo of the HR-XPS laboratory setup at Princeton University, Chemical Engineering department.

In particular, the analyses were performed on a Scienta ESCA 300 spectrometer equipped with an 7.5 kW-rotating anode and seven toroidally bent α-quartz crystals [82] for providing monochromated AlKα (hν =

1486.7 eV, PHI 04-548 dual anode X-ray source) radiation. A 300 mm radius hemispherical analyzer (SPECS PHOIBOS 100-5 MCD) and position-sensitive detector was used for signal detection, which provides high energy resolution at improved signal-to-noise ratios. Samples were mounted on a stainless steel stub and transferred to the analysis chamber (2.0×10^{-10} Torr). Spectra were obtained using a takeoff angle of 90° with respect to the surface plane of the sample stub. Survey scans of the samples were obtained at 300 eV pass energy, while scans of smaller energy regions were obtained at 150 eV pass energy.

2.5.3 Rutherford Backscattering Spectroscopy (RBS)

Rutherford Backscattering Spectroscopy (RBS) [83] is a method to determine the composition of a sample based on bombarding a sample with high energy ions and measuring the energy of the backscattered ions. This ion beam analysis technique allows the determination of both the atomic mass and concentration of each elemental target constituents as a function of the depth from 10 nm to a few μm under the surface, as well as the crystal structure in the case of single crystal materials, in a non-destructive manner.

a. Rutherford Backscattering Spectroscopy (RBS) principle

In RBS measurements, the remaining fraction of the initial ion energy after collision is defined as the kinematic factor. The kinematic factor measures the efficiency of the momentum transfer in the collision. It depends exclusively on the masses of the interacting particles and the scattering angle. The kinematic factor establishes that the lower the mass of a target element, the lower the energy of the backscattered ion. It also establishes that projectiles only scatter backwards from elements with higher masses than their own.

The scattering probability is given by the Rutherford cross-section. It is proportional to the square of the atomic number of the target atom. This means that the sensitivity of the method is higher for heavier elements. Rutherford formula deviates from actual measurements at high energies. Deviation is caused by the presence of short-range nuclear forces. To avoid this effect the energy of $^4He^+$ beams is usually limited below 2.5 MeV.

Impinging ions lose energy when they go through a material due to electron excitation and collisions with atomic nuclei. Therefore, particles backscattered from an element at some depth will have less energy than particles backscattered from the same element on the surface of the material. Knowing the stopping power of a material for the incoming ion allows the measurement of depth profiles. Probed depth for a 2 MeV $4He^+$ beam on a carbon substrate is approximately 2 μm.

b. Instrumentation: Rutgers University

Rutherford Backscattering spectra were taken at the 2 MeV Tandetron Accelerator facility in the Laboratory for Surface Modification at Rutgers University. Electrons are accelerated to 2 MeV and shot into the sample. The exit and scattering angles are set to 17 and 163 degrees, respectively. Fig. 2.28 is a picture of the facility, with the particle accelerator in the background and the alpha particles moving in the direction of the camera towards the central chamber in the forefront, which deflects the beam to the chamber seen to the left.

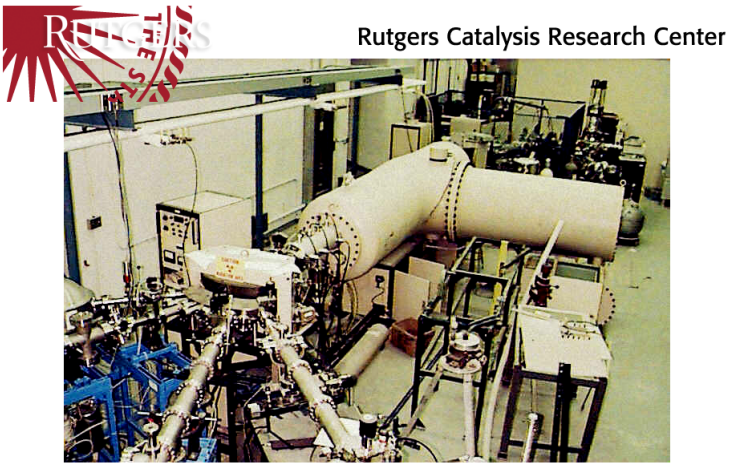

Figure 2.28: A picture of the 2 MeV Tandetron Accelerator Facility in the Laboratory for Surface Modification at Rutgers University.

The chamber is pumped down to high (10^{-6} Torr) vacuum, and it contains the sample holder, a camera for aligning the 2 × 2 mm beam spot, and an ORTEC surface barrier detector with energy resolution 15 keV. Fig. 2.29 displays an image of the scattering chamber showing in particular the beam path, the sample holder and the *in-situ* camera. The manipulator is a goniometer with translational and rotational degrees of freedom. The samples are mounted on a metal plate, held vertical in the manipulator, between the two dark shields. Fig. 2.30 shows an RBS spectrum obtained with a 2 MeV $^4He^+$ beam from a graphite sample exposed in RFX-mod during a boron wall conditioning.

It is possible to identify: boron from wall conditioning, carbon from the substrate and oxygen. The position of the peaks is determined by the kinematic factor, and the concentration of the species is determined by the scattering cross-section.

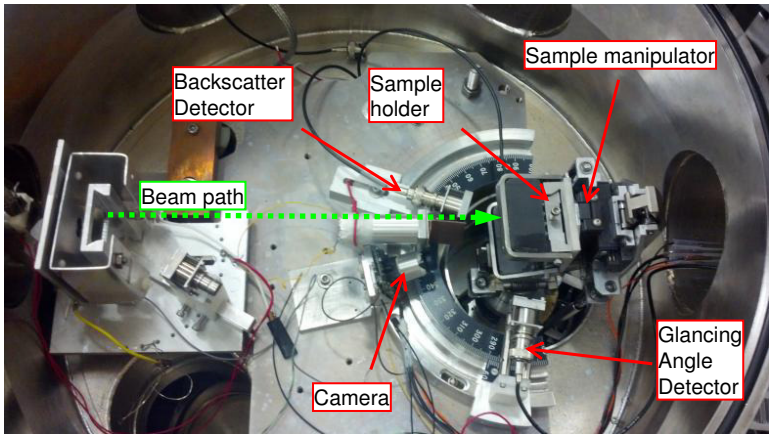

Figure 2.29: A view inside the RBS scattering chamber with the key components labeled. The top of the sample holder is the wedge shaped piece of metal mounted in the manipulator.

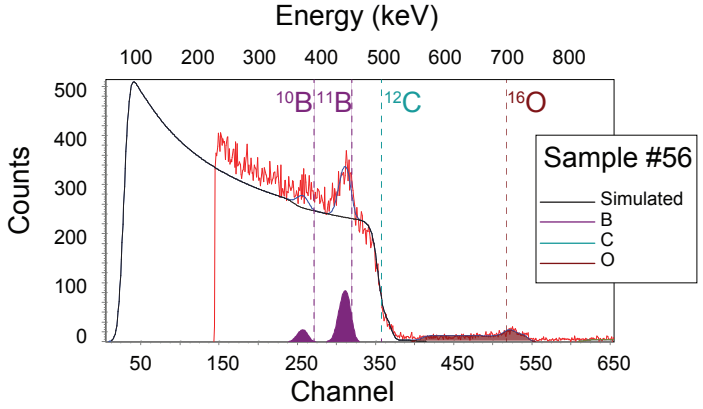

Figure 2.30: RBS spectrum obtained with a 2 MeV $^4He^+$ beam from a graphite sample exposed in RFX-mod during a boron wall conditioning.

2.5.4 Scanning electron microscopy/energy dispersive x-ray spectroscopy (SEM/EDS)

a. SEM, EDS/X principle

A SEM image is generated by a focused electron beam that scans over the surface of a specimen [84]. Elastic or inelastic scattering of the high energy electrons that strike the specimen can occur. Elastic scattering generates the backscattered electrons (BSEs) which are incident electrons scattered by the atoms in the specimen, while inelastic scattering generates

the secondary electrons (SEs), which are electrons emitted from atoms in the specimen [84]. SEs are useful for achieving topographic contrast, while BSEs are advantageous for obtaining the elemental composition contrast [84].

The zone of production of BSEs is larger than that of SEs, because BSEs have high energy which prevents them from being absorbed by the sample, but these result in a lower resolution [85]. The volume and depth of the interaction region increase with an increase of beam energy or a decreasing atomic number of the elements in the specimen (fig. 2.31) [85].

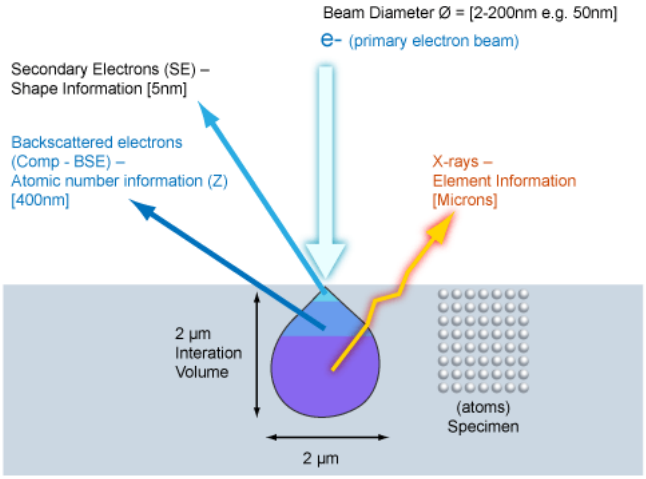

Figure 2.31: Illustration of interaction volumes for various electron-sample interactions.

X-ray analysis in a SEM implies the identification of radiation of a specific energy or wavelength for elemental analysis of the sample [85]. When a high energy particle (X-ray photon, electron, or neutron) strikes an electron in the inner shell of an atom, the energy of the particle can be high enough to knock an electron out of its original position in an atom [84]. The knocked-out electron leaves the atom as a "free" electron and the atom becomes ionized. Ionization is an excited state and for this reason the atom will quickly return to its normal state by refilling the inner electron vacancy with an outer shell electron. The energy difference between an outer shell electron and an inner shell electron will generate an X-ray photon [84]. The energy of characteristic X-rays is well defined and dependent on the atomic number of the atom [84]. X-ray analysis can be utilized to obtain both qualitative and quantitative information, with lateral resolution in the range of micrometers (ca. 1-3 μm, fig. 2.31) [85, 86].

b. SEM, EDS/X instrumentation

In this thesis, the microstructure of boron-, lithium- and tungsten-coated graphite samples has been characterized by Scanning Electron Microscopy (SEM) and Energy Dispersive X-ray (EDS/X). Different instruments were used: a high-resolution field-emission SEM (FEI XL30 FEG-SEM) equipped with an EVEX EDS/X has been used to characterize the boron and lithium coated samples for wall conditioning optimization studies presented in Chapter 4 and Chapter 5), and a Sigma Zeiss Field Emission SEM equipped with Oxford XMax EDS/X-Silicon Drifted detector has been used for the characterization of the tungsten coatings in Chapter 6. The former instrument is located at the Imaging and Analysis Center (IAC) at Princeton University and has an optimum image resolution of 2 nm and is accessed completely using a computer terminal, while the second instrument is located at CNR-IENI, Padova.

Chapter 3

Glow discharge optimization, efficiency and advantages of intershot HeGDC

3.1 Introduction

This chapter is dedicated to the optimization of the global parameters of the GDC sessions in RFX-mod and the analysis of the efficiency and advantages of performing HeGDC before every plasma discharge. It is organized in two parts: the first part deals with the optimization where an extensive set of diagnostics has been used to characterize the GD plasmas in the different operative conditions; and the second part presents and discusses a dedicated plasma campaign where a sequence of He plasma discharges were alternated with short ±10 min HeGDC to study the efficiency, advantages and drawbacks of such a wall conditioning strategy in terms of hydrogen wall removal and density control. The first part of the chapter is constructed as follows: in Section 3.2.1 the physical background of the weakly ionized glow discharge plasmas is presented, in Section 3.2.2 the experimental setup for the characterization of GDC plasmas is described; the characterization of the glow global parameters, in-vessel pressure, anodes voltage and anodes current is addressed in Section 3.2.3; whereas the spatial uniformity of the GDC plasmas and the results are discussed in Section 3.2.4 and 3.2.5 respectively. The second part of the chapter is divided in two sections: in Section 3.3 the efficiency of the intershot HeGDC strategy is addressed, while in Section 3.4, the advantages and disadvantages of this technique in RFX-mod is discussed.

3.2 GDC global parameters optimization

3.2.1 Physical background of glow discharges

A typical DC discharge experiment contains two electrodes separated by a specific distance and held at a certain pressure. After a high enough DC voltage is applied, breakdown occurs and current flows [87]. The simplest glow discharge configuration consists of two parallel electrode plates being held on different electrical potential. One electrode is called cathode and is negatively charged, the other is the anode that is on positive potential. Once the glow discharge is established the potential drops rapidly close to the cathode, varies slowly in the plasma, and changes again close to the anode. Consequently, the electric field is strong in the vicinity of the cathode (Cathode Dark Space, CDS) and the anode (Anode Zone). The plasma, or more precisely the positive glow is virtually field free. The electric fields in the system are restricted to sheaths adjacent to the electrodes. Fig. 3.1 shows a schematic of the simplified glow discharge mechanisms.

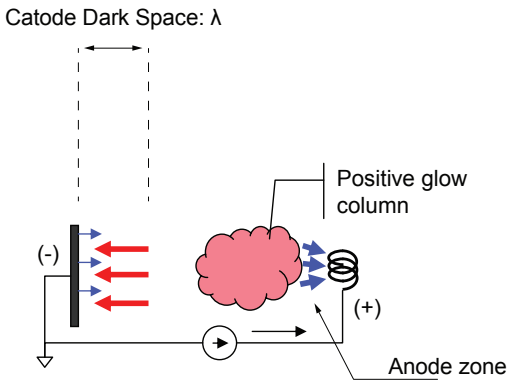

Figure 3.1: Simple schematic of a glow discharge.

In the case of a glow discharge in a toroidal fusion device such as in RFX-mod, the first wall plays the role of the cathode. The ions are accelerated towards the wall and a complex interaction among the charged species occur in the cathode sheath where a strong electric field, a positive space charge and a relatively high ion density develop. In this region the electrons are accelerated by the electric field. Positive ions are accelerated towards the cathode. They cause the sputtering of the cathode material and the emission of secondary electrons. These electrons will be accelerated and cause the creation of new ions through collision with neutrals. Fig. 3.2 shows the principle of a glow discharge in a fusion device. When the electrode separation in a glow discharge is decreased and reach a certain value shorter than the cathode dark space, an abrupt rise of the discharge voltage is observed. If the

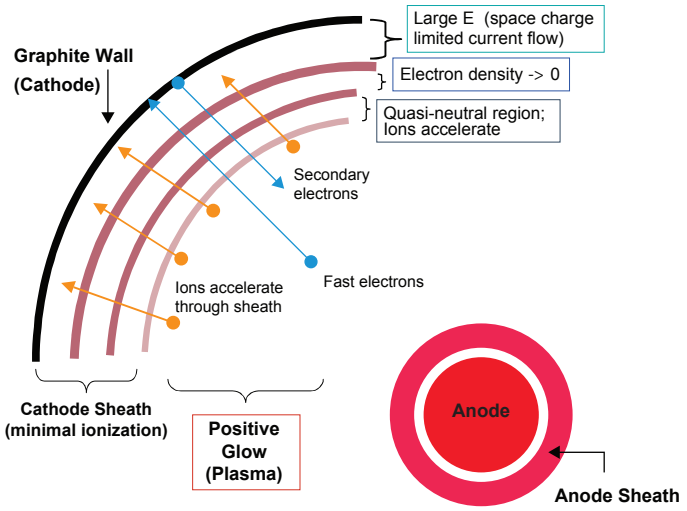

Figure 3.2: Glow discharge processes.

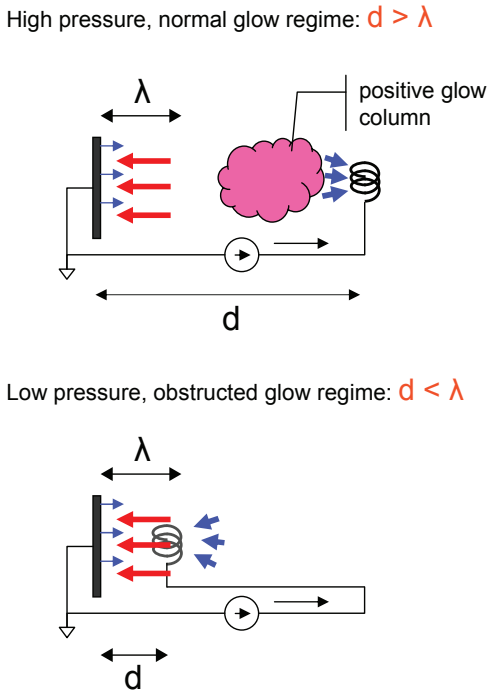

Figure 3.3: Schematic illustrating the obstructed and normal glow discharge regimes [88].

cathode-anode separation is further decreased this effect is more pronounced and known as the obstructed discharge [89] (fig. 3.3).

3.2.2 Experimental setup

The GDC plant in RFX-mod is described in Section 2.3.2. The apparatus is equipped with gauges for the measurement of the voltage and of the current of the anodes. The absolute in-vessel gas pressure is obtained by a capacitive gauge. The composition of the gas extracted by the pumping system is measured by a Residual Gas Analyzer (RGA), composed by a quadrupole type 0-100 AMU mass spectrometer, connected to the vacuum vessel through a differential pumping group. An adjustable needle valve chokes the flow of gases to be analyzed, coming from the vessel, so that the pressure in the spectrometer head volume is maintained within the operational range ($\leqslant 10^{-3}$ Pa).

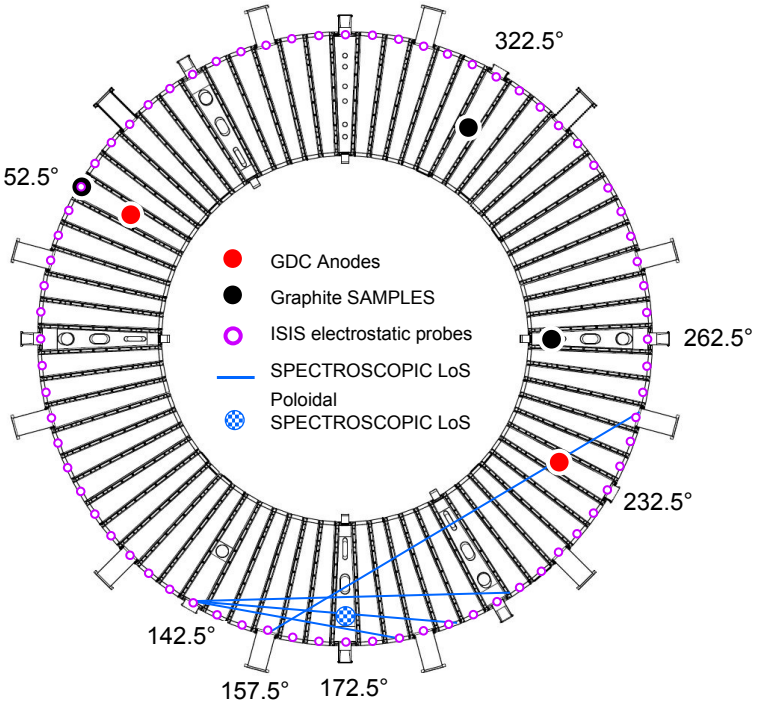

Figure 3.4: RFX-mod vessel schematic with spectroscopic and electrostatic probes diagnostics, GDC anodes and sample exposure positions.

Edge plasma properties are studied with a diagnostic system constituted by a toroidal array of 72 equally spaced electrostatic probes, which is part of ISIS (Integrated System of Internal Sensors), a complex system (see fig. 3.4) of in-vessel magnetic, electrostatic and thermal sensors [73]. The electrostatic probes are, actually, electrodes embedded in the first wall graphite tiles. During the reversed-field pinch plasma operations the probes

behave like usual Langmuir probes, with characteristic (V, I) curves that allow the estimation of edge electronic temperature and electric field. During the GDC sessions the wall is the cathode of the glow discharge. In front of it, and hence in front of the probe itself, a cathode sheath with a typical dimension of 1 m arises, the wall and the probes are exposed to ion bombardment (see fig. 3.2). In that condition (V, I) characteristic curves different from the typical Langmuir ones have been measured. Notwithstanding this, a significant measure is still possible: the current collected by each probe when the bias against the wall potential is 0 V estimates the ion flux at the first wall. The measurement is affected by secondary emission (up to 30% according to a rough estimation) not considered in the analysis reported here.

The emission spectrum of the GDC discharge is measured along 5 Lines of Sight (LoS). One is aligned to intersect a region very close to one anode, 3 lie in a radial-toroidal plane far from the electrode, and have different impact parameters in order to obtain measurements at three radial positions (normalized impact parameters r/a 0.71, 0.42 and 0.18). The fifth line of sight is located close to the three far from the anode but lies on a poloidal plane, with r/a 0.56 (see fig. 3.4). The light (in the visible range of wavelengths) is analyzed through spectrographs.

The principal characterization of the spatial asymmetry of RFX-mod GDCs has been performed by means of *ex-situ* post-mortem analysis of graphite samples inserted at three toroidal positions along the torus, the first at 0° from one anode, the second at 30° from the other anode, the third at 90° from the anodes [90]. The samples are mounted on manipulators (see Section 2.4.5) that allow their insertion inside the vessel up to the first wall envelope surface, and are kept at the same potential as the wall. The graphite samples are analyzed by Secondary Ion Mass Spectrometry (SIMS) to measure the depth profiles of the present species [91]. The significant species followed by SIMS are carbon, oxygen, boron and lithium (the last two coming from wall cleaning treatments), whereas hydrogen and helium coming from plasmas and GDCs are not directly detectable by SIMS. The *ex-situ* post-mortem characterization is then compared to the electrostatic and spectroscopic measurements.

3.2.3 Characterization of the operational regimes

In RFX-mod, GDCs can be assisted with radio-frequency (RF) waves launched from the anodes with varying frequency to couple energy transfer to the weakly ionized plasma, thereby allowing reliable discharge breakdown at lower pressures. The method of conditioning stainless-steel vacuum vessels by Radio-frequency-assisted Glow discharge (RG) in hydrogen has been developed and optimized in experiments in TEXTOR tokamak [92–94]. The basic arrangement in RFX-mod is shown in fig. 3.5; it consists of RFX-mod vessel connected as a cathode and one electrodes insulated from the vessel and connected as an anode. The figure also shows the gas inlet and pumping system with a differentially pumped mass spectrometer for gas analysis. The anode is designed as a multiturn inductance coil. In addition to the RF-assistance, similarly to the original design in TEXTOR, the plant is also equipped with a set of two pre-ionization coils that helps the ignition of the discharge. The effect of the RF-assistance and the pre-ionization coils in RFX-mod is evaluated as a first step. Second, the characterization of the operational regimes of the GDC plant has been carried out with a wide scan on the global parameters: in-vessel pressure (p_0), anodes voltage (V_A) and anodes current (I_A).

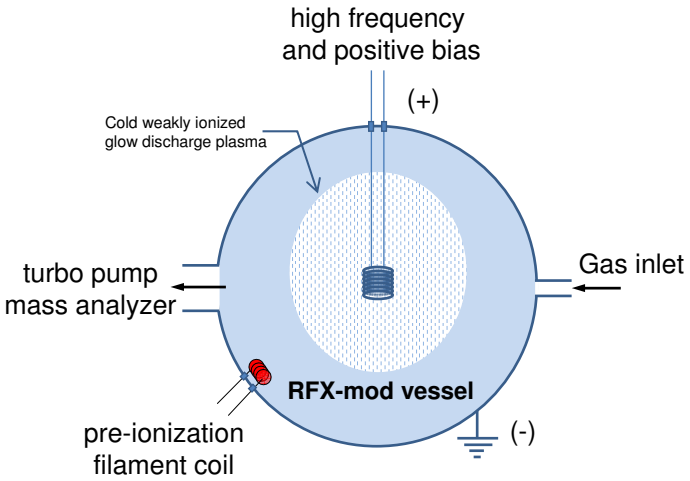

Figure 3.5: Experimental arrangement for operating a Radio-frequency-assisted Glow discharge (RG) in RFX-mod: gas inlet, gas exhaust turbo pump, mass analyzer and pre-ionization filament coil are shown.

a. Effect of RF assistance in RFX-mod

The glow discharge voltage-pressure characteristics at $I_A = 1.2$ A with and without RF have been measured and shown in fig. 3.6. About 30W per anode of transmitted RF power fraction have been measured. However since

the breakdown conditions were found to be the same with or without the RF assistance, its influence on the breakdown voltage, though documented in the literature (for example in [24]), was not found in RFX-mod, as was also observed in JET [95]. Just as the experience in JET with Radio-frequency-assisted Glow discharge (RG) discharges, RF assistance in RFX-mod offers no advantage for the maintenance of glow at low pressure. The differences in the geometry of electrodes and vessels may possibly explain the difference in results seen in different machines.

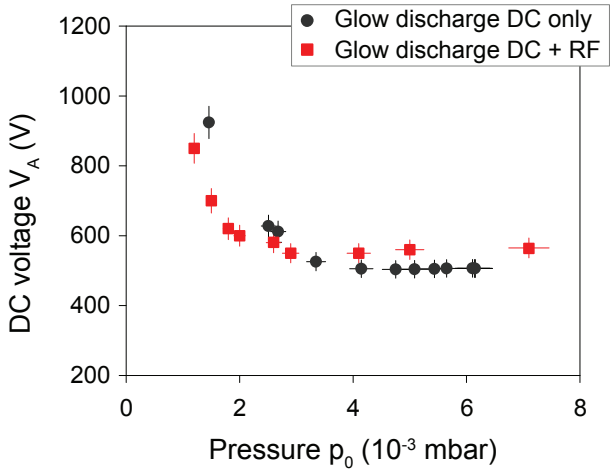

Figure 3.6: Voltage-pressure characteristic for a 1.2 A glow discharge in RFX-mod with and without RF.

The effect of the RF assistance has been also investigated in terms of changes in the V_A-I_A quantity at different gas pressures and no effect has been found as it can be seen in the typical V_A-I_A curves plotted in fig 3.8. In the following all the results have been obtained with the RF power switched off. The evaluation of the actual antenna-plasma coupling is planned in RFX-mod and is the subject of future work.

b. Effect of the pre-ionization glow discharge filament

The GDC plant in RFX-mod is also equipped with two pre-ionization filaments (see fig. 3.5) that are used to reduce the breakdown thresholds and improve stability near the low pressure limit. The characterization has been performed by recording the minimal pressure that allows a reliable breakdown and ignition of the glow discharge using one filament at a time. The experiment has been done for H_2GDC and HeGDC. Fig. 3.7 shows the obtained breakdown pressures. For hydrogen, 0.64×10^{-3} mbar was measured using only one filament and 0.52×10^{-3} mbar using both filaments. The minimal breakdown pressure for HeGDC was 1.02×10^{-3} mbar using one filament and 0.62×10^{-3} mbar adding the second filament. RF power has also

been switched on when applying the pre-ionization filaments but no clear combined effect was observed.

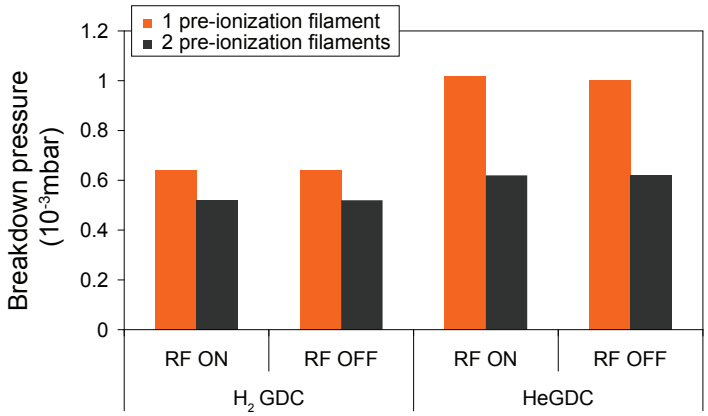

Figure 3.7: GDC breakdown pressure as a function of the number of pre-ionization coils measured with RF-assitance ON and OFF.

c. Global GD parameters characterization

The typical V_A-I_A curves at different gas pressures found with helium glow discharges in RFX-mod are shown in fig. 3.8. Whereas fig. 3.9 compares the V_A-p_0 dependence at $I_A = 1.2$ and the V_A-d_c dependence (d_c being the length of the cathode sheath region).

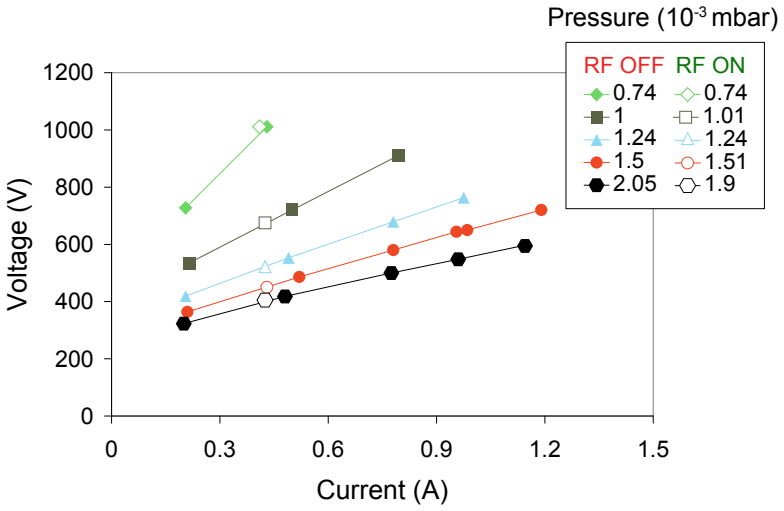

Figure 3.8: Characteristic V_A-I_A curves for different gas pressures.

The strong voltage rise at pressure lower than about 3×10^{-3} mbar shown

in 3.9 is characteristic of the obstructed glow discharge regime [88]. In the case of RFX-mod, the extent of the cathode sheath region is in the range of 1-15 m, decreasing with increasing pressure [96], whereas the minimum anode-cathode distance is the minor radius of the torus, i.e. 0.5 m.

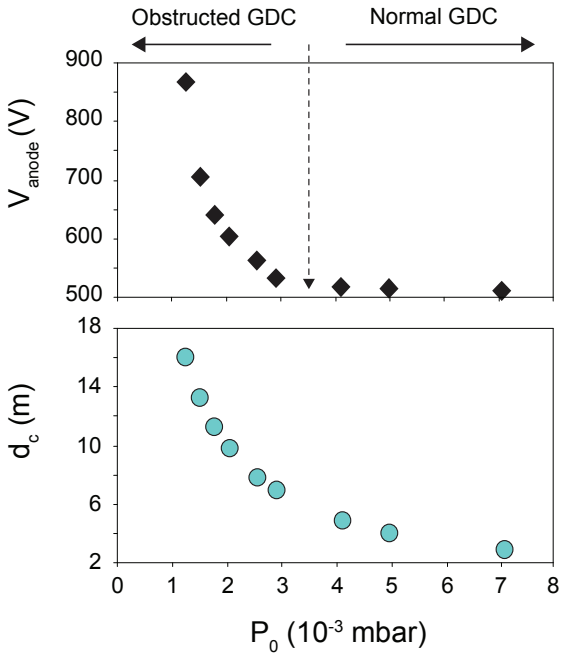

Figure 3.9: Obstructed GDC Voltage-Current characteristic in RFX-mod.

The effect of the variation of the global parameters p_0, V_A and I_A on the GDC effectiveness in particle-depleting from the wall is illustrated in 3.10, which shows the partial pressure of the H_2 molecules measured by the RGA and the traces of p_0, V_A and I_A. The partial pressure has an obvious dependence on the current (i.e. the flux of He molecules on the wall) whereas no clear dependence on pressure or voltage alone can be deduced.

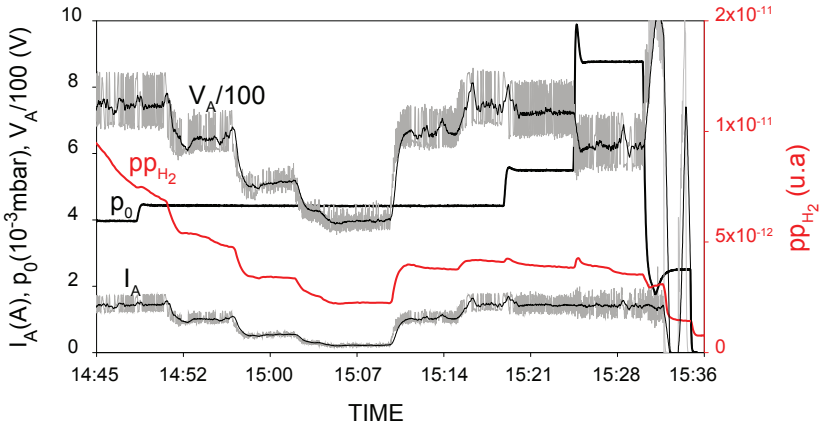

Figure 3.10: Time behavior of the partial pressure of H_2 in the gas extracted during HeGDC. In the same plot, in-vessel pressure, anodes current and anodes voltage divided by 100.

3.2.4 Spatial uniformity characterization

The effectiveness of a GD in particle sputtering from the first wall is closely linked to the ion current density and energy values in the sheath region of the cathode, i.e the graphite first wall. In this thesis the toroidal uniformity of these quantities has been investigated. The thickness of thin boron films deposited during boron wall conditioning glow discharges (90% helium working gas and 10% B_2H_6) has been measured by *ex-situ* post-mortem analysis on graphite samples and the results were compared to the local spectroscopic measurements of the GD plasma emission and to the ion current density distribution measured by the embedded electrostatic probes of the ISIS system [73]. The results of this work have been published in [97].

a. *Ex-situ* post-mortem analysis

Fig. 3.11 displays the depth profile and the total content of boron (computed by integrating the number of counts/s of the $^{10}B^+$ SIMS ions), measured at three different positions: at 0°, 30° and 90° from either GDC anodes. Both depth profiles and total boron integrated content show a strong toroidal asymmetry with 10× higher content in front of the anode compared to the closest position, 30° displaced toroidally.

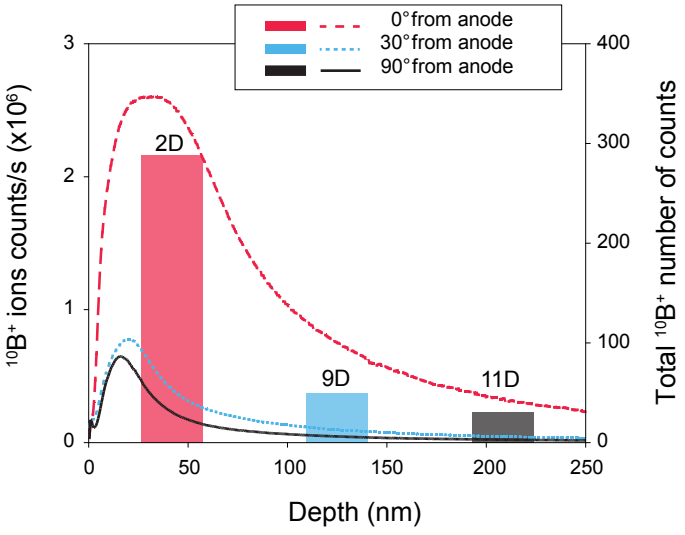

Figure 3.11: Depth profiles of ^{10}B measured by SIMS spectrometry in three graphite samples exposed during He-B_2H_6 GDC at three toroidal positions (at 0°, 30° and 90° from the anode). The bars chart refers to the total number of counts recorded along the first 250 nm.

b. Electrostatic probe ISIS measurements

The previously depicted toroidal asymmetry found in the post-mortem analyses is confronted to the measurements of the ion density from the electrostatic probes. The current density , measured by the electrostatic probes at different toroidal angles, is shown when the probe bias is zero (I_{0V}) in 3.12 (a) and the probe voltage bias (V_f) with respect to the wall (i.e. the cathode) when the probe current is zero is shown in fig. 3.12 (b).

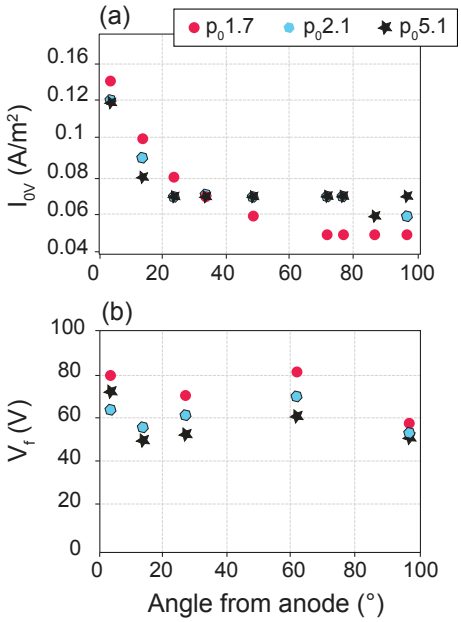

Figure 3.12: Data from electrostatic probes: (a) current density when the probe voltage is zero; (b) probe bias when the current is zero and, measured at different toroidal angles and for different in-vessel pressures: (red) 5.0×10^{-3}mbar, (blue) 2.1×10^{-3}mbar, (black) 1.7×10^{-3}mbar.

Both quantities have been measured at different in-vessel pressures p_0. V_f can be interpreted as an average stopping potential for the ions striking the wall, giving the estimation of the ion average energy of the order of 60-70 eV, growing with p_0, whereas I_{0V} represents the ion flux to the wall. A strong toroidal non-uniformity of ion density at the edge has been measured by the electrostatic probes, with peaks localized at the toroidal positions of the anodes and of the filaments. In addition, the electrostatic measurements and the knowledge of ion current and energy allow an estimation of ion density at the wall of the order of 10^{13} m^{-3}, corresponding to a ionization fraction of 10^{-6}. On the other side, ionization equilibrium of helium atoms with such a ionization fraction gives a rough estimation of the electron temperature Te $\simeq$ 0.7 eV.

c. Line of sight spectroscopic measurements

A similar disuniformity has been seen in the emission intensity measured by spectroscopic LoS. Data from spectroscopic measurements are shown in fig. 3.13. In particular the monitored lines are HeI at λ=492 and 507 nm. In figure 3.13 (a) the average emission intensities of the three lines of sight lying in the radial-toroidal plane far from the anode are plotted as a function of the impact parameters of the chords, giving an average radial profile of the electron density with a maximum at r/a ~ 0.4. Figure 3.13 (b) is the emission intensity along the five lines of sight at different in-vessel pressures. Since the neutral profile is flat in this very weakly ionized plasma and since temperature dependence of the emission should be negligible in cold plasmas, the intensity pattern gives an indication of the region were electrons are localized.

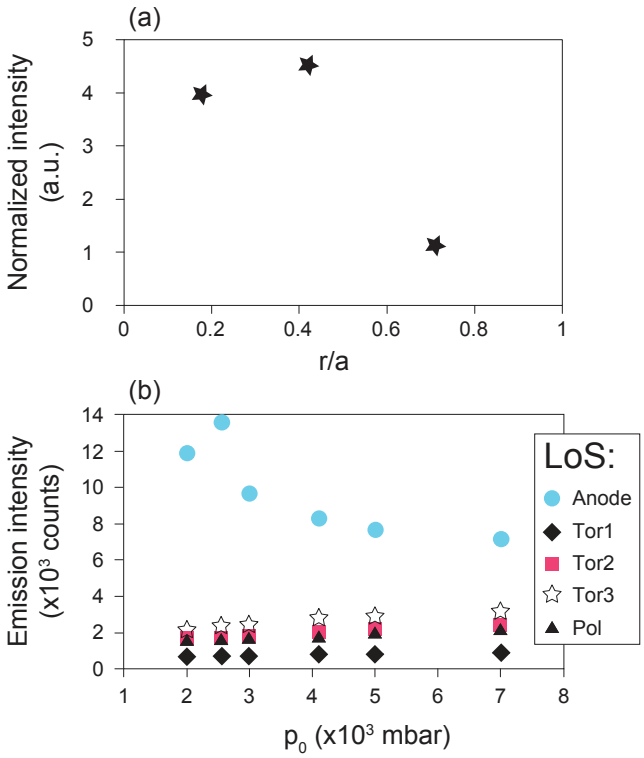

Figure 3.13: (a) Emission intensities of the three lines of sight lying in the radial-toroidal plane far from the anode (normalized to the length of the chords) as a function of the impact parameters of the line, at in-vessel pressure of 3×10^{-3} mbar; (b) emission intensity at different in-vessel pressures along the five LoS: (circle) chord crossing the anode region, (diamond), (square) and (star) chords in the radial-toroidal plane far from the anode at normalized impact parameters 0.71, 0.42 and 0.18 respectively, (triangle) chord in the poloidal plane far from the anode.

3.2.5 Discussion

Glow discharge plasma used in RFX-mod as a treatment for the graphite first wall has been characterized by means of an extensive set of diagnostics. Strong toroidal asymmetry of GDC plasmas has been found in RFX-mod by means of *ex-situ* post-mortem analysis and confirmed by measurements of the ion flux to the wall.

Both the ion current density measured by electrostatic probes (fig. 3.12 (a)) and the light emission (3.13 (a)) exhibit a toroidal non uniformity, not clearly seen on V_f measurements (fig. 3.12 (b)) and hence referable to a pattern in the ion/electron density and not in the ion energy. I_{0V} has a maximum in correspondence of the anode and drop to a minimum level about 30 degrees apart from it, keeping then the same value for larger angles. Similarly, the light emission of the chord crossing the region close to the electrode is much stronger than that of all the other chords, and this is verified at any value of the pressure.

A scan in the operational parameters was done, in order to find out the conditions that give the most uniform ion flux. I_{0V} measurements (fig. 3.12 (a)) suggest that a lower in-vessel pressure is a favorable regime, as foreseen by simulations on other machines [96], instead spectroscopic data (3.13) show an opposite behavior since the difference between the emission measured by the chords at the anode and those far from it decreases with increasing pressure. Furthermore, electrostatic and spectroscopic measurements are dominated by ion flux and electron density respectively, and the two quantities can behave in different manner with respect to pressure changes. Moreover, while electrostatic measurements allow the reconstruction of a pure toroidal profile at the wall, the spectroscopic ones are lines-of-sight integration along long chords and are influenced by the combination of radial and toroidal profiles modifications.

3.3 Efficiency of intershot HeGDC in RFX-mod

In a dedicated RFX-mod plasma campaign, short 10-20 min glow discharges in helium have been performed between helium plasma discharges to study the efficiency of combining glow and plasma power discharges effect on hydrogen wall cleaning. Different sequences have been performed in order to assess which combination leads to an enhanced hydrogen exhaust. Plasma performances in terms of density control of subsequent hydrogen discharges have been analyzed after a number of sequences of HeGDC-He power discharges. External gas puffing has been used on these hydrogen discharges to evaluate density behavior. Hydrogen and helium influxes have been monitored and the results have been compared to the amount of gas exhaust in order to study the glow discharge and power plasma discharges dynamics in terms of retention and release of hydrogen enclosed in the graphite first wall.

3.3.1 Experimental campaign

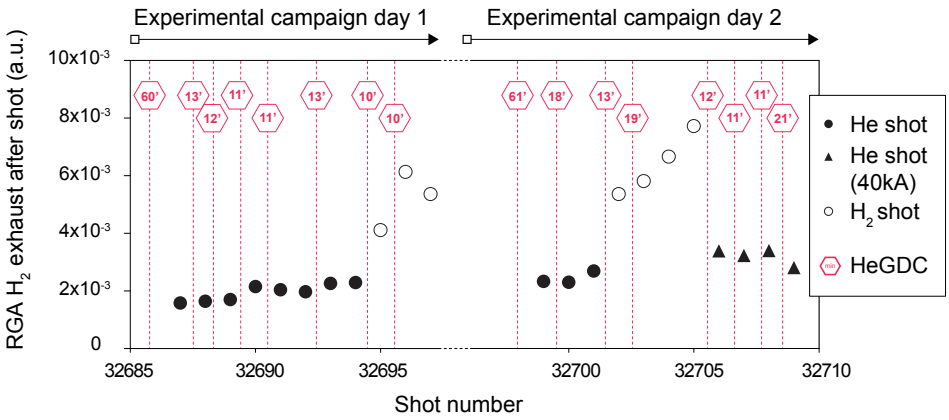

Figure 3.14: Typical experimental campaign alternating short 10' HeGDC with He plasma discharges.

A two-step experimental procedure has been undertaken for the aim of the analysis: the first consisted in alternating one short 10-20 min HeGDC with only one He plasma power discharge and the next step consisted in performing one short 10-20 min glow discharges with a set of two He plasma power discharges. During the process, the Residual Gas Analyzer (RGA) monitors the gas exhaust during both the HeGDC and the He power discharge (see Section 2.4.4 where RGA acquisition for this campaign has been adapted) and spectroscopic LoS monitor impurity emission at the plasma edge. He plasma discharges were performed keeping the same gas filling of about 1.18×10^{20} (He atoms) in order to cancel out filling contribution on the final density and evaluate the contribution of hydrogen/helium influxes from the wall during

the discharge. At the end of the experimental campaign, He plasma discharges with higher plasma current discharges were performed to evaluate the effect on hydrogen wall-cleaning. Early in each experimental day before starting the experimental campaign a 60-min HeGDC is performed as it is usually the practice in RFX-mod. In fig. 3.14 the sequences of HeGDC and He plasma discharges during the two experimental days are shown. The data of hydrogen exhaust measured by the RGA are shown as well but discussed below. Subsequently to the HeGDC/He power discharge sequences, a set of H discharges with varying fueling have been performed to evaluate in particular the resulted density behavior after HeGDC wall cleaning campaign.

3.3.2 Wall hydrogen exctration efficiency

The analysis is limited to the first day of the experimental campaign to discard the effect of wall loading by the hydrogen discharges. Fig. 3.15 shows the shot by shot measured exhausts as well as the plasma density of the He discharges.

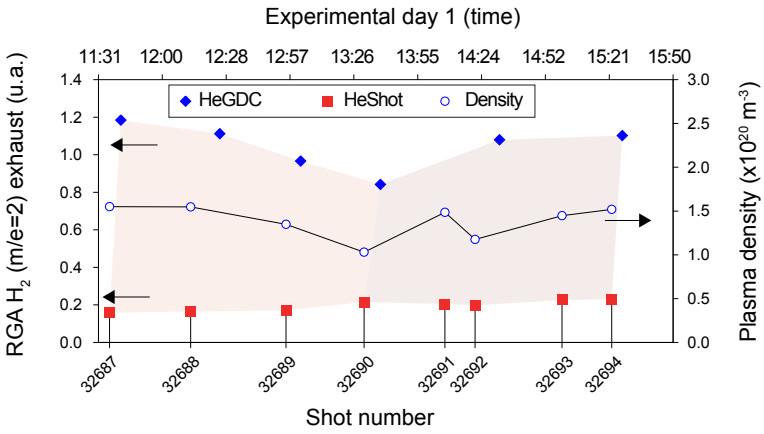

Figure 3.15: Comparison of the hydrogen exhausts induced by HeGDC and He plasma discharges. The measured average flat top density during the He plasma discharges are plotted and shown on the secondary y-axis.

The hydrogen exhausts induced by HeGDC and He discharges were measured by the RGA and computed from the hydrogen partial pressure. As expected, HeGDC is more efficient in depleting hydrogen from the wall than He power discharges. H exhaust induced by HeGDC is about 5-6× higher than the exhaust induced by He discharges. However, a non trivial correlation among the two exhausts can be seen.

On the one hand, two phases of hydrogen exhaust are observed. In the first phase where only a single HeGDC is combined with one He discharge for four consecutive sequences, hydrogen exhaust induced by HeGDC progressively decreases; then in a second phase where a set of two He

discharges are combined with one HeGDC, the exhaust of hydrogen is reset to its initial value (exhaust of the first HeGDC of the experimental day) then it is maintained at the same value in the following sequence, as opposite to the first phase. Interestingly, in both phases the decrease of hydrogen exhaust induced by HeGDC is correlated to an opposite behavior of the exhaust induced by the power discharges. The correlation may be slightly hindered by the lower time resolution of the mass spectrometer for acquisition during plasma discharges (see Section 2.4.4 for more details about RGA resolution). The correlation among the exhaust shows that a cause and effect relationship exists among the two processes of hydrogen depleting from the graphite by HeGDC and by He discharge. The much higher heat flux on the first wall during He discharges compared to HeGDC plasma, very likely induces an inward/outward diffusion of hydrogen in the graphite bulk that influences hydrogen removal by sputtering in the subsequent HeGDC. We propose that the latter may take place by thermal diffusion and may be governed by an equilibrium of hydrogen recall from the bulk graphite and its release at the surface.

On the other hand, the further analysis shows a subtle correlation of the density with the combined HeGDC/HeShot hydrogen exhaust. The effective reduction in hydrogen release (sum of the exhaust induced either by HeGDC or by He discharge) correlates to a decrease of density in both phases: a maximum of plasma density corresponds to a maximum of the combined hydrogen exhausts and conversely. Since comparable He gas filling was used during all the discharges, the changes in density is due to hydrogen influxes from the first wall as it will be discussed below. Considering that the graphite first wall is a large reservoir of hydrogen species [76], the observed correlation of density with hydrogen exhaust in the subsequent HeGDC can be reasonably related to the previously depicted picture of thermal desorption mechanism of hydrogen.

3.3.3 H release from graphite by He-ions bombardment

The study of helium-ion-induced release of hydrogen from hydrogen saturated graphite has been widely documented in literature (see ref. [98–101]). In particular, Langley in [102] differentiates the hydrogen detrapping, retrapping, and recombination time constants under He-ion bombardment and shows that the cross section for helium-ion-induced release of hydrogen from hydrogen saturated graphite decreases with increasing energy from 300 eV to 2.5 MeV as reported in fig. 3.16.

A survey of the dependence of the plasma density with the plasma parameters has been carried out. Fig. 3.17 displays the dependence of plasma density of the He discharges performed during the experimental campaign with the ohmic power, the loop voltage, the average electron temperature and the maximum plasma current. On the other hand, the dependencies with the electron temperature and the homic power of the hydrogen exhaust induced by He discharges and HeGDC are shown in fig.

3.18.

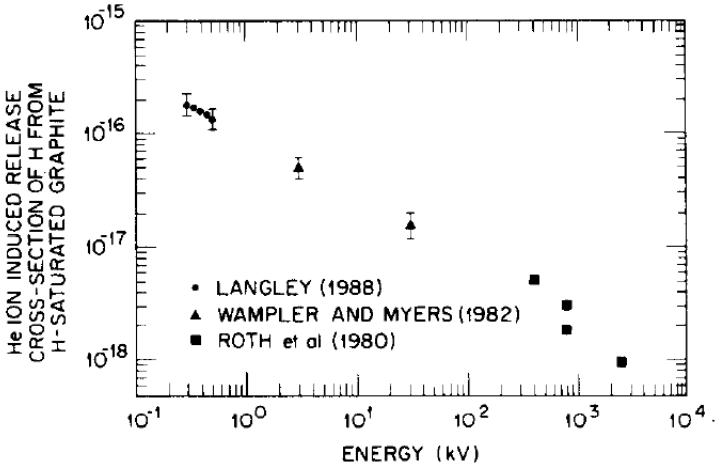

Figure 3.16: Helium-ion-induced release cross section of hydrogen from hydrogen-saturated graphite, taken from [102].

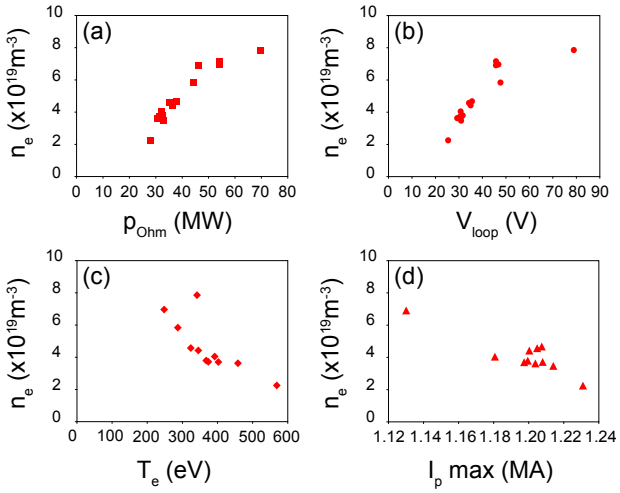

Figure 3.17: Average flat-top density as a function of (a) the ohmic power, (b) the loop voltage, (c) the electron temperature and (d) the maximum plasma current during the entire experimental campaign.

While an increase in ohmic power and loop voltage are correlated to a linear increase of the plasma density, an opposite trend is seen with the electron temperature and plasma current. The previously seen correlation of the plasma density with the hydrogen exhaust (fig. 3.15) can be an effect of

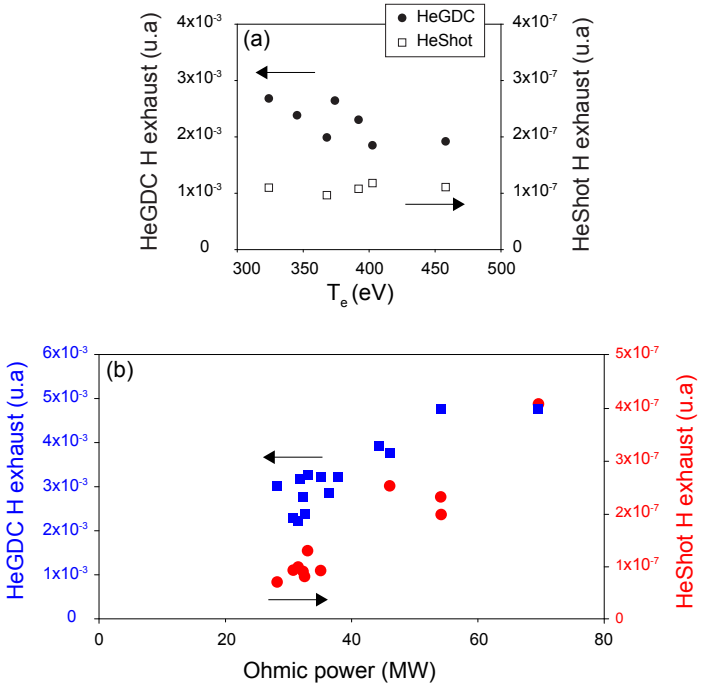

Figure 3.18: Dependence of the hydrogen exhaust with (top) the electron temperature and (bottom) the delivered ohmic power (the data are extended to the entire 2-day experimental campaign).

an acting plasma controllable parameter such as the delivered ohmic power. The heat and particle fluxes at the graphite first wall are directly proportional to ohmic power and hydrogen exhausts induced by both HeGDC and He discharges linearly increases with increasing ohmic power as shown in fig. 3.18(b). The present result is consistent with the previously depicted thermal desorption mechanism of helium-ion-induced release of hydrogen [102]. As it is shown in fig. 3.18(a), the increase in plasma electron temperature relates to a decrease in hydrogen exhaust, more particularly seen in the exhaust induced by HeGDC. Therefore, this result is in agreement with Langley investigations in which the helium-ion-induced release of hydrogen decreases with increasing energy.

A possible scheme of the hydrogen sorption from the graphite can be depicted as follows. Hydrogen retained in the graphite first wall is adsorbed on the wall surface by bombardment of energetic He-ions during He plasma discharges and subsequently desorbed and extracted from the vessel during the following HeGDC. However, this result is an overall measure of hydrogen release from the graphite first wall. As described by Langley in [101], different mechanisms of hydrogen detrapping, retrapping, and recombination with different time constants take place in the graphite matrix.

3.3.4 Changes in H exhaust rate by different combinations of HeGDC and He discharges

As discussed earlier, the combination of only one or a set of two He plasma discharges with a HeGDC led to different behavior of the effective hydrogen exhaust. At any case, the two different combinations have shown a greater hydrogen cleaning of the wall compared to a HeGDC performed randomly in former experimental campaigns. In order to investigate the dynamics of the two phases depicted in fig. 3.15, the time behavior of the partial pressure measured by the RGA and its time derivative which gives an approximation of the exhaust rate are further analyzed for the two different combinations tried in the experimental campaign and shown in fig. 3.19.

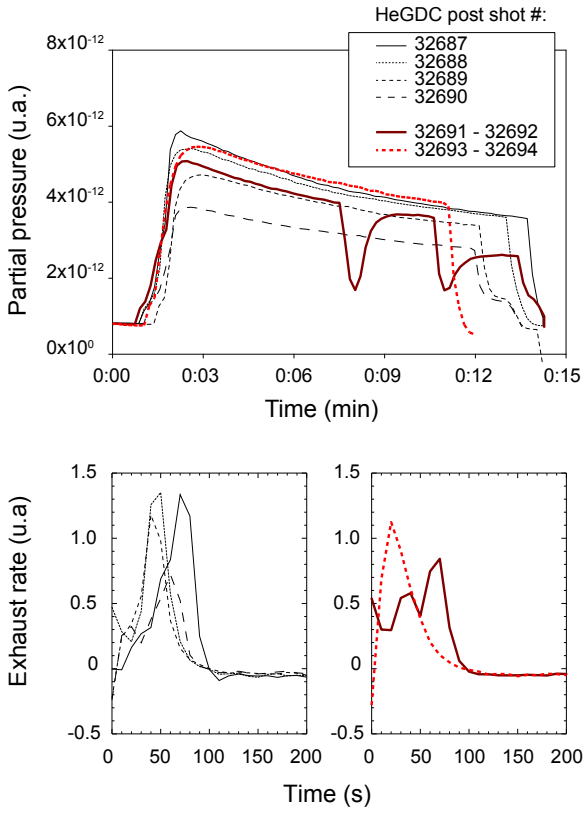

Figure 3.19: Top panel: time behavior of the hydrogen partial pressure measured during HeGDC performed during the experiment campaign. Bottom panel: exhaust rate observed during HeGDC performed after a single He power discharge (left) or two consecutive discharges (right).

It can be seen that the exhaust rate estimated from the time derivative of the shown curves in the case of the two consecutive He discharges (right plot) is broader than in the case of the single shot, although initially it is slightly lower compared to the first combination of single discharges. The

latter can also be seen from the difference between the slopes of the partial pressure. The difference in the derivative shape is an indication of different dynamics of hydrogen desorption from the wall: the smoother decrease of the time derivative in the case of the two consecutive He discharges is likely due to a higher content of hydrogen on the graphite surface that is progressively pumped out from the vessel. A greater accumulation of hydrogen on the graphite surface that is thermally induced by the two consecutive He power discharges can explain such a feature. Therefore, combining a set of two He power discharges with HeGDC can be favorable to induce thermal diffusion of subsurface hydrogen retained by the graphite tiles. On the other hand, the efficiency of a single discharge combined with a subsequent HeGDC decreases by a factor of $\simeq 2$ throughout the sequence as it can be seen in the partial pressure from discharges #32687 to #32690.

3.3.5 H/He dynamics during and after He plasma discharges

In order to decipher the mechanisms that allow an enhanced wall cleaning with the combination of He discharges and HeGDC glow discharges, the dynamics of H and He influxes have been compared to the gas exhaust measurements. As observed in fig. 3.15, the flat top density of the helium discharges performed before each HeGDC is correlated with the amount of hydrogen extracted during the GDC, despite that the helium filling was kept constant for all the discharges. Therefore the increase in density can only be related to an increase of gas influxes from the wall during the discharge. In fig. 3.20 hydrogen and helium exhausts are plotted as a function of the gas desorption measured by pressure gauges immediately after the discharge.

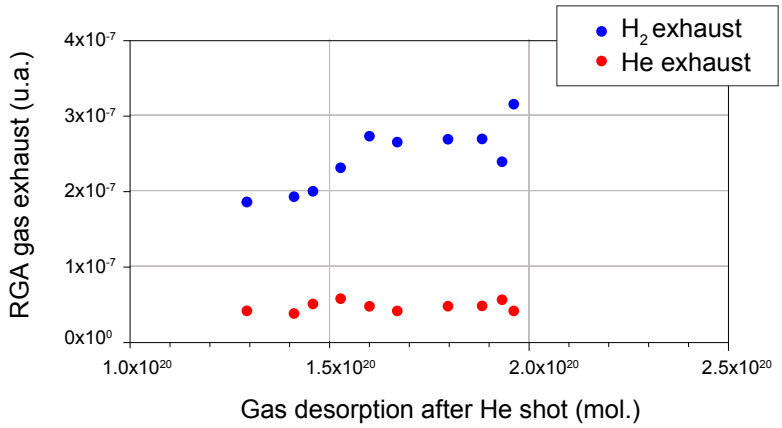

Figure 3.20: Hydrogen and helium exhaust after He discharges as a function of the total computed gas molecules obtained from in-vessel pressure gauges.

As it can be seen the increase in gas desorption immediately after the discharge is only related to an increase in hydrogen exhaust while the

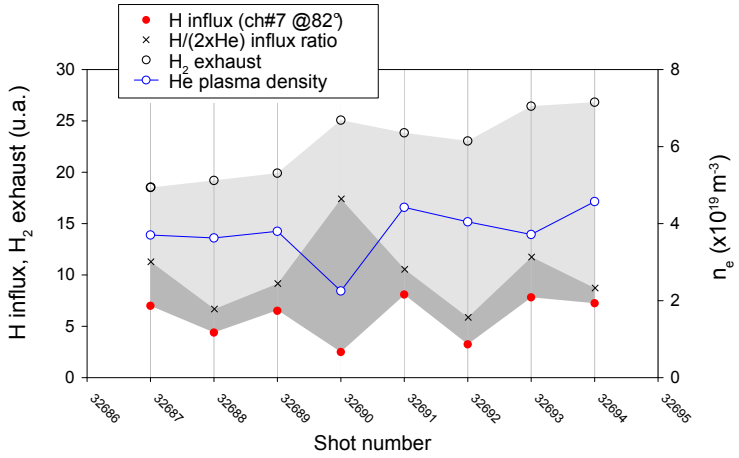

Figure 3.21: H influx, H/2×He influx ratio, H_2 exhaust measured by the RGA and plasma density obtained at each discharge of the experimental campaign dedicated to the study of HeGDC/HeShot hydrogen cleaning efficiency.

helium exhaust remains constant. It corroborates thus the previously depicted picture of induced sorption (adsorption + desorption) of hydrogen by energetic He-ions during He discharges. In fig. 3.21 the hydrogen influx, the hydrogen/2×helium influx ratio, He plasma density and H_2 exhaust during the discharge observed throughout the experimental campaign are shown. An increase in H influx is clearly correlated to an increase in the H_2 exhaust recorded by the RGA. Changes in the discharge density also follow a similar behavior. The increase in density can be related to a main contribution from hydrogen influx as already shown in fig. 3.20. A peculiar density decrease is observed in shot #32690 corresponding to an increase in hydrogen exhaust and it is the matter of further investigations.

As a side remark on the global behavior of the discharges during the campaign, a global 2× increase of the plasma density and hydrogen exhaust is seen between the first discharge and the last one. However the H/He influx ratio shows an opposite behavior with a 2× decrease, which shows that the discharges are progressively less hydrogen-contaminated. Hydrogen sorption and exhaust from the wall is therefore enhanced throughout the campaign with a reduction in impurity contamination of the He discharges.

a. Density behavior in following H power discharges

In order to evaluate the density behavior during and after the 'wall-cleaning' experimental campaign, as shown in fig. 3.14 hydrogen 1.2 MA power discharges have been performed using both pre-filling and puffing fueling techniques. H/He influxes, plasma density and H_2 exhaust during the discharges have been monitored. A typical experimental sequence is shown in fig. 3.22.

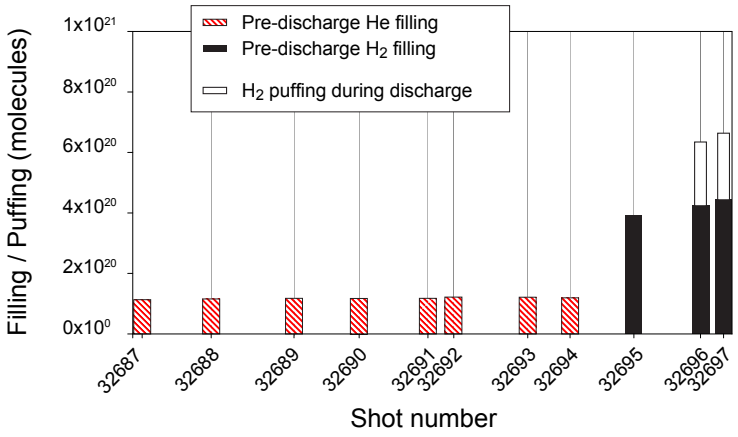

Figure 3.22: Typical experimental campaign for evaluating density control. Hydrogen power discharges are performed with and without puffing to evaluate correlation with density changes.

To evaluate the contribution of desorbed species to the changes in plasma, discharges #32695-32697 have been analyzed in details, in particular the average density, maximum plasma current, average Hα influx and discharge fueling are shown in tab. 3.1. In fig. 3.23 the time evolution of the plasma parameters for these discharges are shown. The flat top plasma current in the discharge #32696 is improved with longer duration compared to #32695 where no puffing were applied. The latter is particularly seen in the following discharge #32697. Plasma density shows a similar behavior corresponding to a controlled increase due to the puffing occurrence.

Table 3.1: H plasma parameters of discharges performed for density control evaluation

Shot #	32695	32696	32697
$< n_e >$ (10^{19} m^{-3})	1.39	1.62	1.90
I_p max (MA)	1.21	1.25	1.26
Hα (u.a.)	8.02	8.17	17.07
H_2 filling (10^{20} mol.)	3.91	4.24	4.43
H_2 puffing (10^{20} mol.)	-	2.11	2.20

A better control of the plasma density with a lower recycling was therefore obtained as a macroscopic effect, as observed in fig. 3.23 which shows that the time evolution of the electron density in a plasma discharge following the cleaning campaign is well correlated to the gas puffing. In particular, density decreases after the gas pulse (with a delay due to the effective gas entrance

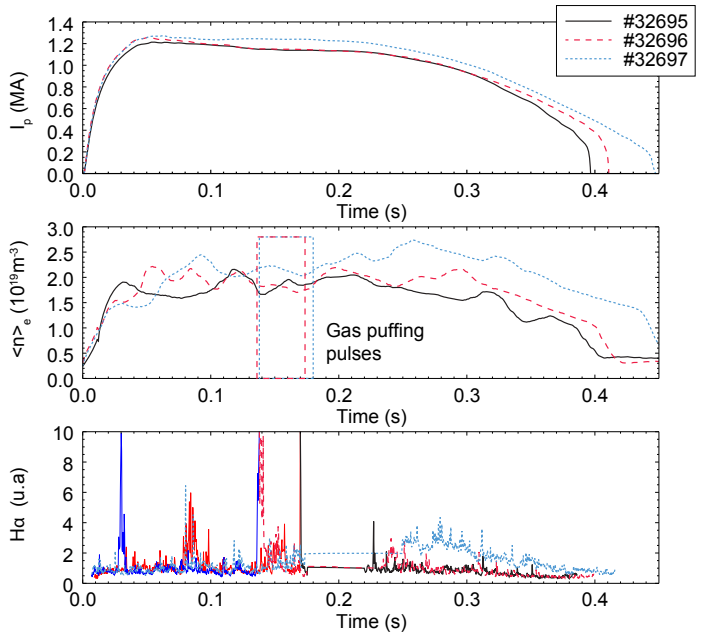

Figure 3.23: Plasma current, density and Hα signal in RFX-mod H discharges after HeGDC cleaning campaign. The first H control discharge #32695 was performed with H_2 filling only whereas the subsequent #32696 #32697 were performed puffing $\simeq 2\times10^{20}$ H_2 molecules after filling the vessel with $\simeq 4\times10^{20}$ molecules.

into the plasma after the inlet valve pulses) which is a clear sign that recycling $R < 1$.

3.4 Advantages of routine intershot HeGDC in RFX-mod

3.4.1 Immediate and long term benefits

The advantages and the utility of this technique in RFX-mod is two-fold: from one side, after a machine shutdown and vessel venting, instead of the time-consuming wall treatments such as long baking sessions, the restart of plasma operation can be assisted by this technique that offers more flexibility and reduces the plasma operation restart time duration. On the other side, during plasma operation, a subtle combination of He discharges with HeGDC can help reach higher plasma performances. In past plasma campaigns, reaching high plasma performances in terms of high plasma currents was made difficult due to high hydrogen influxes from the wall. To be able to reduce those influxes and operate at a desired plasma current, long 40 min to 1 h HeGDC are sometimes unavoidable.

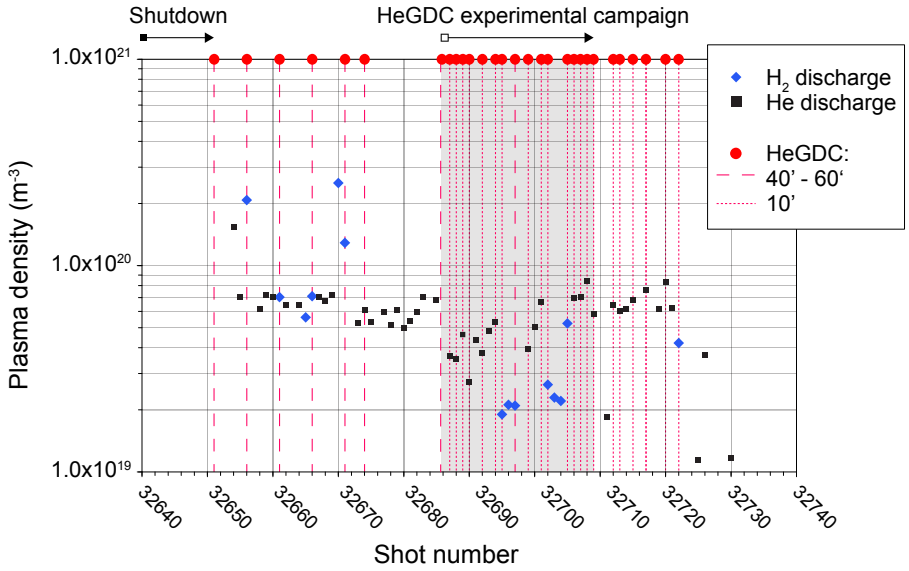

Figure 3.24: Post shutdown experimental campaign for plasma operation restart and test of routine intershot HeGDC performance in RFX-mod. Shot by shot plasma density of hydrogen (◆) and helium (■) discharges. Intershot HeGDC (●) are displayed with the vertical dashed lines.

The previously described cleaning experimental campaign has been performed after a vessel opening to test its applicability in RFX-mod as a strategy for the restart of plasma operation. Baking of the vessel was performed before the beginning of the campaign in addition to 30h of H_2GDC and 5h of HeGDC. For reference, initially the restart has been carried out with routine procedure that mostly include HeGDC, He and H

discharges (H discharges are generally performed to test plasma performances in terms of density and plasma current during the plasma operation restart phase). The first phase also included a daily 40-60' HeGDC but none was applied in a combination sequence with He discharges. After about 30 He discharges and 5 long HeGDC, a second phase of plasma restart was carried out using the short ±10 min intershot HeGDC strategy. Fig. 3.24 displays the two phases of the experimental campaign along with the density of He discharges and H test discharges. The data shows the difficulty of achieving a low and controllable density in the first phase, while in the second phase where short HeGDCs have been applied, density of test H discharges resulted reduced and controlled. Only as a few as 4 sequences of HeGDC/He power discharges reduced by 2× the measured density and allowed to keep it at lower values in six consecutive H discharges. Similarly, the measured average hydrogen flux is reduced by nearly an order of magnitude when the short HeGDC campaign was performed, as it can be seen in fig. 3.25.

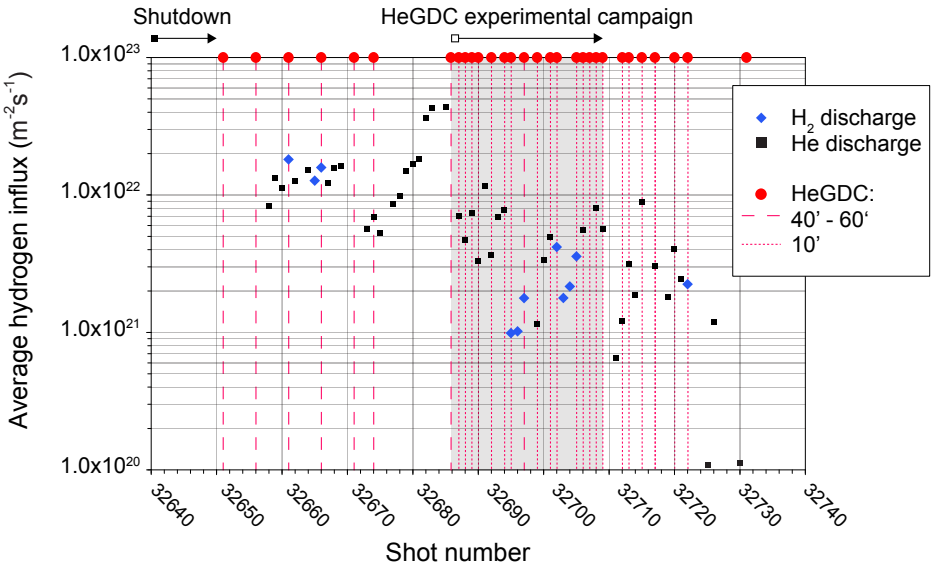

Figure 3.25: Shot by shot hydrogen influx measured during hydrogen (◆) and helium (■) discharges. Intershot HeGDC (●) are displayed with the vertical dashed lines.

3.4.2 Comparison with plasma operation restart subsequent to a fresh boronization

The performance obtained with the intershot HeGDC experimental campaign has been compared with the performance observed following a machine shutdown during which the vessel was vented and a fresh

boronization was performed before plasma operation restart. The discharge number #32705 (last highest hydrogen discharge plasma current and density of the experimental campaign) is compared to two post-boronization hydrogen discharges: one discharge obtained subsequent to an equal number of discharges from the restart of plasma operation (#36137) and a second intermediate one (#36206). Plasma current, density, hydrogen influxes and electron temperature are compared and shown in fig. 3.26.

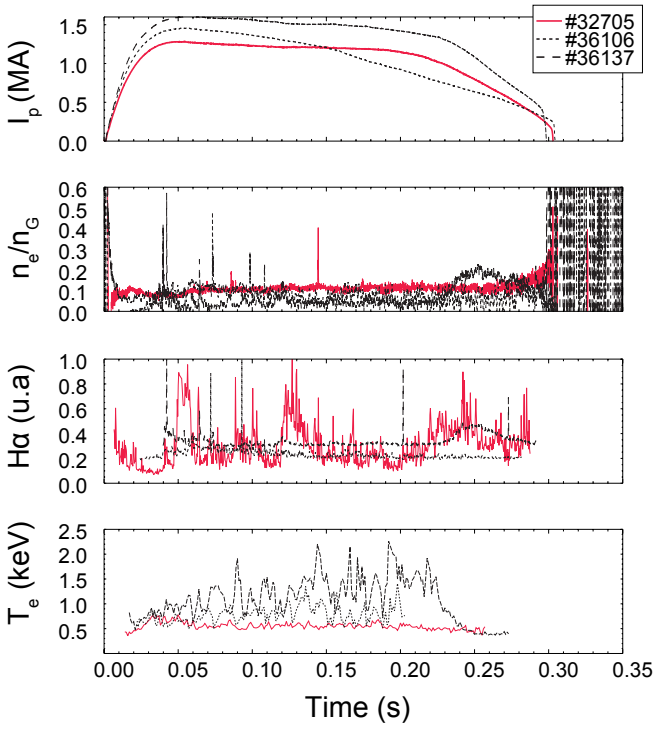

Figure 3.26: Comparison between plasma restart subsequent to the intershot HeGDC experimental campaign (discharge #32705 dashed line) and a more recent plasma restart with a fresh boronization following a machine opening (discharges #36106 and #36137).

While the plasma restart after the boronization is characterized with lower hydrogen influxes compared to the post HeGDC campaign restart (characteristic of boron wall conditioning) and about 2× higher electron temperature, a comparable flat top plasma current among the two wall conditioning techniques can be seen. Moreover, the normalized plasma density in the case of the intershot HeGDC procedure resulted a factor of 2 higher than in the case of the post boronization plasma operation restart.

The present results are in agreement with the application of the similar wall conditioning intershot HeGDC strategy tried in the DIII-D tokamak

[103]. The graphite conditioning with HeGDCs before tokamak power discharges was found to be more efficient than baking, hydrogen glow cleaning, or helium or hydrogen power pulsed discharge cleaning. In addition to the benefits of such a technique for recovery from a machine opening, long term benefits were obtained in terms of plasma performances. Since the implementation of the intershot HeGDC procedure in DIII-D, low safety factor q plasma operation (which refers to the resulting stability of the plasma) was achieved on the first plasma attempt of an experimental day, as opposite to normal operation without the use of intershot HeGDC in which the same operation typically requires from 10 to 20 pre-conditioning discharges.

3.4.3 Drawbacks of routine intershot HeGDC

The analysis of the data obtained during the intershot HeGDC experimental campaign has shown a progressive shot-by-shot increase in He influx compared to the earlier usual plasma restart phase, where fewer but longer HeGDC were applied. Fig. 3.27 shows the shot-by-shot He influx behavior in the two different phases previously described.

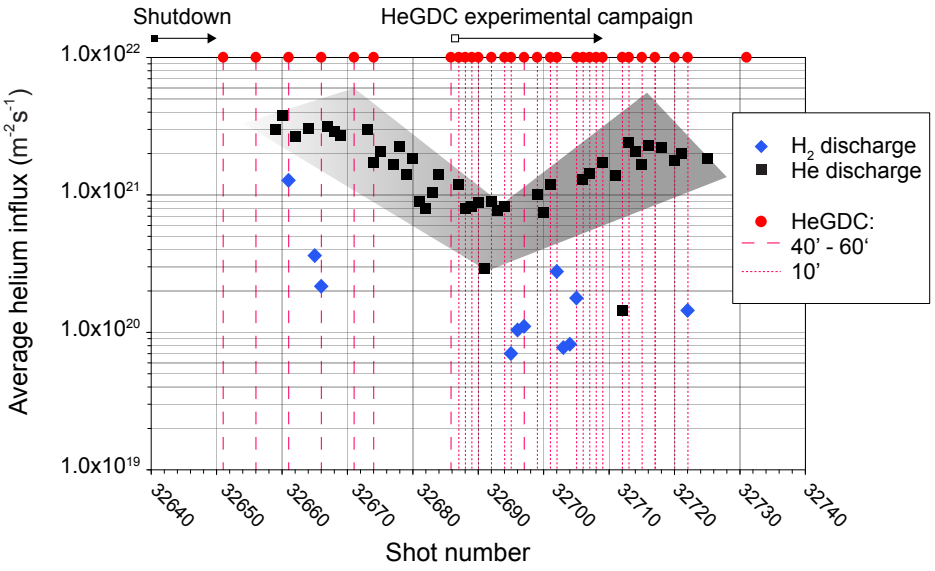

Figure 3.27: Shot by shot helium influx measured during helium (■) and hydrogen (◆) discharges. Intershot HeGDC (●) are displayed with the vertical dashed lines.

As it can be seen, while during the first phase before the start of the intershot HeGDC experimental campaign the He influxes gradually decrease in both He and He plasma discharges, the beginning of the intershot HeGDC phase shows an opposite behavior with a gradual increase not only

during He discharges but also during the test H discharges. The latter can be explained by the higher wall-loading with helium particles with the increase in the frequency of HeGDC, although with shorter duration compared to the first phase. This result is however, in conflict with the previous gas exhaust analysis in which the He fraction in the total gas exhaust remained constant throughout the entire intershot HeGDC experimental campaign (see fig. 3.20). The overall gradual increase of He influxes observed here with spectroscopic measurements maybe more factual than the RGA measurements during plasma discharges characterized by low time resolution of the quadrupole mass spectrometer.

The present He-wall loading drawback of routine intershot HeGDC in RFX-mod is also consistent with similar works in DIII-D [103]. As a consequence of routine HeGDC, some residual helium was found to remain in the tiles and to desorb subsequently from the graphite tiles during a tokamak discharge. Nonetheless, the amount of helium desorbed did not result large enough to affect Z_{eff}, however it did create interfering spectral lines in electron temperature profiles diagnostics such as in the Thomson scattering spectrum.

3.5 Conclusions

In this chapter, the characterization of the operational regimes of glow discharges in RFX-mod and the analysis of the efficiency and advantages of intershot HeGDC were presented.

The characterization of the glow discharge has been performed by means of an extensive set of diagnostics: the operational regimes were examined by a wide scan on the global parameters in terms of in-vessel pressure (p_0), anodes voltage (V_A) and anodes current (I_A) while the spatial boron deposition uniformity was studied by *ex-situ* post-mortem analysis on material samples and compared to edge electrostatic and spectroscopic measurements.

In contrast with results found in TEXTOR, Radio-Frequency assistance in RFX-mod offers no advantage for the maintenance of the glow discharge at low pressure and the use of pre-ionization filaments to reduce the breakdown thresholds and improve stability near the low pressure limit resulted ineffective. These results are similar to those found in JET [95] and the difference in the vessel geometry and electrodes in RFX-mod is a proposed explanation. Typical V_A-I_A curves were found while the V_A-p_0 dependence has shown a strong voltage rise at pressure lower than about 3×10^{-3} mbar which is characteristic of the obstructed glow regime. In the case of RFX-mod, the extent of the cathode sheath region was established in the range of 1-15 m, decreasing with increasing pressure, whereas the minimum anode-cathode distance is the minor radius of the torus, i.e. 0.5 m. At last, the effect of the variation of the global parameters p_0, V_A and I_A on the GDC effectiveness in particle-depleting from the wall has been

investigated. A clear dependence on the current (i.e. the flux of He molecules on the wall) of the partial pressure was observed, whereas no clear dependence on pressure or voltage alone could be deduced. The electrostatic data, in particular I_{0V} measurements suggest that a lower in-vessel pressure is a favorable regime, as foreseen by simulations on other machines [96], however spectroscopic data (3.13) have shown an opposite behavior.

With regard to the characterization of the spatial uniformity of GDC plasmas, a strong toroidal asymmetry was found by *ex-situ* post-mortem analysis and confirmed by measurements of the ion flux to the wall. Both the ion current density measured by electrostatic probes and the light emission exhibit a similar toroidal asymmetry shape, corresponding to patterns in the ion flux and electron density respectively: the flux has an enhanced value in a region of ±30° around the electrodes. The non-uniformity seems mitigated when working at lower in-vessel pressures, even if some discrepancies between the measures of different diagnostics should be deepened.

The preliminary analysis of intershot HeGDC wall cleaning strategy in RFX-mod was found promising. The combination of He power discharges with short ±10 min HeGDC resulted relatively more efficient in enhancing hydrogen depleting from the graphite first wall compared to longer HeGDC randomly performed during an experimental day. The combined efficiency studied by RGA gas exhaust analysis and influx measurements was found to increase with increasing ohmic power during the He power discharges. A thermal diffusion scheme of H from the bulk to the graphite surface was proposed, nonetheless the underlying mechanisms of hydrogen release are more complex and go beyond a simple scheme. In fact, the subject has been extensively documented in literature [98–102], in particular the cross section of H release from H-saturated graphite induced by He-ion bombardment was reported to decrease with increasing particle energy. The combination of only one or a set of two He plasma discharges with a HeGDC leaded to different behavior of the effective hydrogen exhaust. The analysis of the gas exhaust has shown that the combination of a set of two He plasma discharges with one HeGDC leads to a higher exhaust rate.

As a macroscopic effect, a better control of the plasma density with a lower recycling was obtained in H test discharges subsequent to the intershot HeGDC experimental campaign. To evaluate the applicability of such a technique in RFX-mod as a strategy for a flexible and less time-consuming restart of plasma operation, the intershot HeGDC cleaning experimental campaign has been compared to routine plasma operation restarts. Compared to a restart that mainly include a long baking session and several hours of H_2 and HeGDC, the intershot HeGDC resulted more prompt in achieving plasma discharges with a reduced and controlled density and hydrogen influxes. Only as a few as 4 sequences of HeGDC/He power discharges reduced by 2× the measured density and allowed to keep it

at lower values in six consecutive H discharges. Compared to a plasma restart after a fresh boronization, similar plasma performances were reached. While immediate benefits of using routine intershot HeGDC were found in RFX-mod, the most detrimental effect consisted in the progressive He loading of the wall that in the long run may affect plasma impurity content, although helium desorption did not result large enough to affect Z_{eff} in other devices, such in the DIII-D tokamak.

Chapter 4

A physical and chemical study of boron wall-conditioning in RFX-mod

4.1 Introduction

Similarly to what was found in a number of fusion experiments world-wide, boron wall conditioning in RFX-mod has resulted very effective in reducing plasma impurity content mainly by trapping oxygen as well as decreasing hydrogen recycling. With reduced recycling, the edge plasma density decreases and the edge electron temperature increases, leading to a significantly lower edge plasma collisionality, thereby resulting in improved fusion plasma confinement and plasma performance. However, the fundamental mechanisms that govern the interaction between the light boron atoms and the plasma edge environment that lead to the observed improvements are not fully understood. Recently, huge efforts have been dedicated in fusion research to correlate the improved plasma regimes to the chemical and physical interaction of the low-Z applied materials with the plasma edge impurities, such as oxygen, carbon and hydrogen.

In order to enhance the effects of the boronization in RFX-mod, several issues must be addressed, such as (i) the strong toroidal asymmetry of boron deposition; (ii) the global inconsistency between the boron wall conditioning duration and the final boron content deposited on the first wall; (iii) why the layer becomes ineffective after few hundreds discharges; (iv) why the boronization is effective in reducing not only O but also H/D release from the wall; (v) what are the mechanisms of hydrogen and oxygen trapping on the boron surface; (vi) the hydrogen and oxygen trapping are surface or bulk dominated. To this aims, the physical and chemical structure of boron content obtained with boronizations is analyzed by means of post-mortem surface analyses on graphite samples. The

boronizations were performed at different experimental conditions in terms of glow discharge parameters (current, voltage and pressure), duration and wall temperature in order to explore a wide range of parameters that directly affect boron deposition and boron interaction with the machine main impurities that are oxygen and carbon. On the one hand, the physical analysis has been carried out by means of SIMS to obtain the broad elemental in-depth composition of the deposited content, XPS to obtain high sensitivity measurements of the surface and near subsurface elemental composition, SEM to characterize the surface morphology and EDS/X and Rutherford Backscattering Spectroscopy (RBS) to probe the bulk physical properties. On the other hand, in order to interrogate the fine chemical structure of the boron deposition and the interactions of boron atoms with oxygen, carbon and hydrogen, a chemical analysis has been performed by means of High Resolution X-ray Photoelectron Spectroscopy (HR-XPS).

This chapter is organized in two parts: after giving a brief summary of the boronization beneficial effects in RFX-mod in Section 4.2, the first part presented in Section 4.3 deals with the physical analysis of the boron content and correlates it to the experimental conditions; then in Section 4.4, the chemical analysis that addresses the chemical states of boron correlated to the impurity content is presented in a second part.

The first part is constructed as follows: the experimental setup and the material sample arrangement are described in Section 4.3.1; the boron deposition spatial asymmetry and the effect of plasma operation and wall temperature are discussed in Section 4.3.2; the global deposition inconsistency is introduced in Section 4.3.3, the boron growth dependence on the glow discharge parameters is presented in Section 4.3.4; and at last with regard to the physical analysis, the surface morphology and composition characterization and its correlation to the glow discharge plasma power are given in Section 4.3.5.

With regard to the chemical analysis, first, qualitative considerations about the boron carbide chemical structure are given in Section 4.4.1. Second, The surface, near subsurface and bulk chemical states analysis of boron and its main chemical interactions and bonds with oxygen, carbon and hydrogen are presented in Sections 4.4.2 and 4.4.3.

4.2 Brief summary of B wall conditioning benefits in RFX-mod

In order to evaluate the improvements in plasma performance with boron wall-conditioning, a set of high plasma current discharges > 1.5 MA performed well before boronization in RFX-mod and an other set performed just after the boronization have been analyzed in terms of impurity influxes, gas adsorption capacity, confinement time, radiative power and plasma edge profile measurements [60, 104].

4.2.1 Impurity influxes and gas adsorption capacity

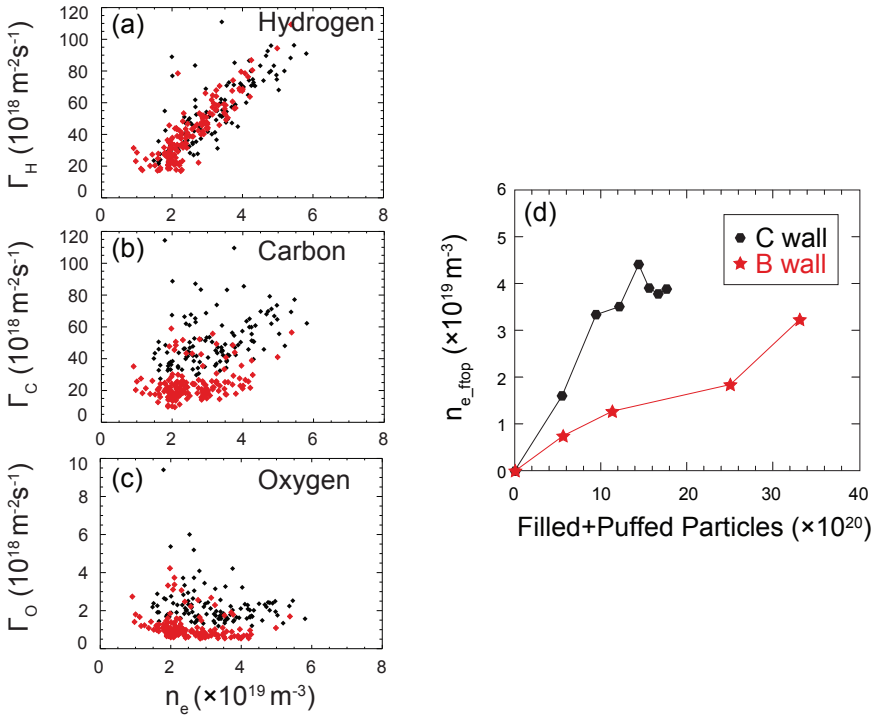

Figure 4.1: Hydrogen (a), carbon (b) and oxygen (c) influxes; (d) flat-top electron density versus total filled + puffed particles for a set of discharges performed well before (black) and right after (red) boron wall-conditioning in RFX-mod.

Hydrogen, carbon and oxygen influxes derived from light emitted by the plasma have been measured and compared in the two set of plasma discharges before and after boron wall conditioning. In fig. 4.1 the H, C, and O influxes for the set of discharges performed far from boron wall-conditioning (black) and discharges in experimental campaigns following boronisation (red) are shown. As it can be seen from fig. 4.1 (a), the influx of H (from Hα) at

comparable densities is slightly reduced in the boronisation case. The clear correlation between the electron density n_e and the H influx seen in the figure is due to the experimental observation in RFX-mod of enhanced H release into the higher density plasma.

Boronization affects the influx of C particles as well. The interaction of the plasma with the graphite tiles is the source of the C impurities in RFX-mod plasmas. The reduction in C influx is likely due to the reduced direct interaction of the plasma with the graphite first wall, hindered by the application of the boron coating. Boron wall-conditioning also affects oxygen content at the edge as a reduction in the influx of O has been observed as well and shown in fig. 4.1 (c).

After boronization in RFX-mod, discharges with a similar density required a higher quantity of hydrogen gas to ignite the discharge. Boron wall-conditioning therefore increases the capability of the graphite wall to adsorb hydrogen. By comparing the flat-top density as a function of the total number of hydrogen particles provided to a sequence of H plasma discharges, an evaluation of boron wall-conditioning effectiveness in terms of density control has been performed. In fig. 4.1 (d), the average flat-top density for the two sequences of high current discharges corresponding to two wall status mentioned above is plotted. Compared with the clean graphite case, after boronization the density increase is lower for the same amount of gas. Boron wall-coating allows therefore a better control of plasma density depicted by the increased absorbing capacity. This has been further observed when strong gas puffing and hydrogen pellets require more discharges to saturate the wall, and operation at high densities is possible without losing density control.

4.2.2 Confinement time, radiative power and plasma edge density and temperature profiles

A sign of increased plasma performance can be estimated from the energy and particle confinement time. Fig. 4.2 shows the particle and energy confinement time τ_p and τ_E for the same set of discharges performed well before (black) and right after (red) the boron wall-conditioning session. The particle confinement is calculated from the influx measurements averaging over the plasma volume. Compared to the standard discharges, there is nearly no increase in the particle confinement time with the boron first wall, except at low plasma density discharges where a slight increase of τ_p is seen. There is no clear dependence of τ_p on n_e, however fig. 4.2 (b) shows that there is a n_e dependence of τ_E, the energy confinement time, with increased energy confinement for higher density plasmas. The energy confinement is observed to be slightly increased in the case of the boron wall-conditioned case.

For the same two high current discharge types discussed above - no wall conditioning (black) and boronized wall (red) - fig. 4.2(c) shows how the line-averaged P_{rad} is maintained at the lowest value of standard discharges when

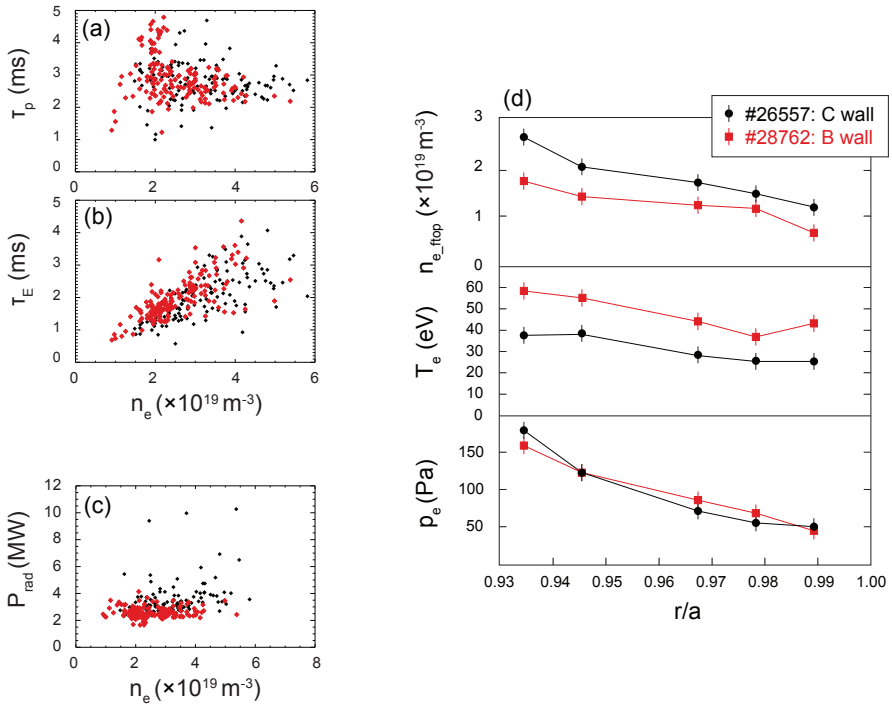

Figure 4.2: Particle (a) and energy (b) confinement times and (c) radiated power for a set of discharges performed well before (black) and right after (red) boron wall-conditioning in RFX-mod. Density, temperature and pressure radial profiles at the edge (d) for a discharge with clean graphite (26557) and for a discharge after boronization (28762).

boron wall-coating is applied. The radiated power is kept at value $< 3MW$ compared to a carbon wall where radiation can reach values of up to $10MW$.

After boron wall-conditioning in RFX-mod a higher edge temperature and lower edge density were observed whilst, although n_e profiles away from the edge do not show large differences. In fig. 4.2 (d), measurements of the edge electron temperature, density profile and pressure radial profile for the two sequences of high current discharges corresponding to two wall status mentioned above are plotted.

4.3 Physical analysis of boron deposition behavior correlated to experimental conditions

The efficiency of boron wall-coating in improving plasma performances in any fusion device is intimately linked to the intrinsic properties of the boron content deposited on the first wall. In order to study the behavior of boron deposition in RFX-mod, the diagnostic network dedicated to wall conditioning studies has been extended with the installation of material sample manipulators that allow the insertion of samples inside the vessel up to the first wall envelope surface (see section 2.4.5 where the setup on the torus is presented). The network already included a Residual Gas Analyzer (RGA) that has been upgraded in order to facilitate the gas exhaust data analysis (see 2.4.4 where the data acquisition system, calibration and operation of the device for the 2012-2013 RFX-mod experimental campaigns are presented). The glow discharge apparatus used for boron wall conditioning and a typical boronization cycle have been presented in Chapter 2, Sections 2.3.2 and 2.3.3, while a layout of the vessel illustrating the different material sample exposure manipulators, RGA and glow discharge gas inlets and anodes can be found in fig. 2.4.

4.3.1 Experimental setup and graphite surface roughness

a. Experimental setup

Three manipulators for the exposure of graphite samples to the GD plasma have been set up in RFX-mod (see more details in Section 2.4.5). They are placed at three different toroidal positions, named 2D, 9D and 11D. The samples can be inserted inside the vessel up to the first wall envelope surface and are kept at the same potential as the wall. At position 2D one graphite disc of about 1.5 cm of diameter faces the plasma from an equatorial port. At positions 9D and 11D the manipulator heads are composed of up to 4 samples of about 1×1 cm each, which are exposed simultaneously but can be removed independently. The 4 samples are designed to be aligned to the surrounding graphite tiles and the manipulators use vertical ports, in the high field side in the case of 9D, in the center for 11D. The three toroidal locations of exposure are at different distances from the anodes, in particular at position 2D one of the two anodes is also located, position 9D is at 30° in toroidal direction form the other electrode, position 11D is at 90° from both. Fig. 4.3 is the top view of RFX-mod vessel, with the positions of the anodes and of the samples. The samples exposed to plasma have been cut from the same graphite blocks used to make the tiles of RFX-mod, in order to track the status of the wall of RFX-mod with samples as similar as possible to the tiles. The material for tiles is a fine-grained polycrystalline graphite produced by isostatic pressing and having grain size ≤ 50 mm, open porosity ≤ 15%, density at 20°C ≥ 1.75 g/cm^3 and electrical resistivity ≥ 10 mΩcm. After the removal from the vessel, the exposure time of samples to air was as short as possible to minimize their

contamination.

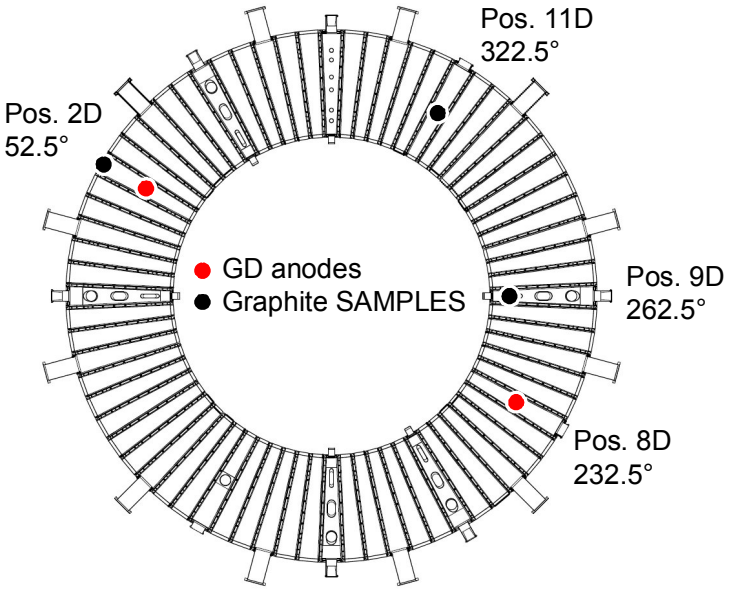

Figure 4.3: Top view of RFX-mod vessel with the position (identified by name and toroidal angle) of the samples (black dots) and of the GD electrodes (red dots).

The exposed samples have been analyzed by field emission SEM (Scanning Electron Microscopy, SIGMA, Carl Zeiss) and by a 3D profilometry (Tencor P15) of a 1×1 mm section to highlight the morphology and to get some information on the surface elemental composition. SIMS spectrometry has been used to measure the depth profiles of the present species. SIMS analyses were performed by a customized instrument [105]. A monochromatic (6 keV) O_2^+ primary ion beam collimated to 50 mm was generated in a mass-filtered duoplasmatron ion gun (model DP50B, VG Fisons, UK). An EQS1000 (Hiden, UK) mass energy analyzer with high transmission 45° sector field electrostatic energy analyzer and a quadrupole mass filter were used for negative- and positive-ion detection in counting mode. Lens and energy analyzer potentials, quadrupole electronic control units and the detection system were controlled via a Hiden interface. The chamber pressure was typically 5×10^{-10} mbar, while, when the oxygen was introduced for the primary ion beam generation, the working pressure was around 3×10^{-9} mbar. The ion species were identified by resolving the overlapped m/z signals with an isotope pattern simulation program. Border effects were avoided with electronic gating, since only secondary ions coming from the central 50% rastered area were collected. The erosion rate, measured by a Tencor P-10 mechanical profiler having a 2 nm vertical

resolution, was estimated to be about 8 nm/min with the maximum available depth resolution. Tab. 4.1 displays the experimental conditions and surface analysis techniques used to obtain the results presented throughout the chapter.

Table 4.1: Summary of graphite samples and experimental conditions for surface analyses

Surface analysis	Sample ID	Boronization duration (min)	First wall temperature (°C)	GDC Plasma power (W)
SIMS	9D_IX	120	170	213
	2D_V	120	170	213
	9D_XXX	240	170	520
	2D_XI-A	240	170	520
	11D_VII	240	RT	520
	11D_XI	240	170	205
	2D_I	30	170	244
	2D_II	30	170	244
	9D_I	30	170	244
	9D_II	30	170	244
EDS/X	9D_XXVII	360	170	100
RBS	9D_XXVIII	360	170	100
XPS	9D_XXIX	360	170	100
HR-XPS	9D_XXXVII	240	RT	205
	9D_L	900	RT	435
	9D_LVI	360	170	535

*RT: room temperature

b. Graphite surface roughness evaluation

SEM images performed on the graphite samples cut from RFX-mod first wall tiles and used for thin film boron wall-conditioning have shown a highly porous surface. In fig. 4.4 two SEM images at two different scales that highlight the roughness and porosity of the graphite are shown. The material exhibit a surface made of several graphite grains and plates of various dimensions ranging from 0.1 to 1μm. Deep pores which extend for fraction of microns in the thickness of the sample can also be identified in the images.

3D profilometry performed on a number of samples revealed the same very high roughness. For example, in fig. 4.5 (a) a sample that has been surface finished presented a roughness (RMS) of 1.12μm while in fig. 4.5 (b) a not finished sample was characterized by a roughness as high as of 4.06μm. This feature implies that an epitaxial growth of boron as on a flat surface is not possible and uncertainties associated to the determination of the depth of the B-C interface will be significant. Nonetheless, by comparing different profiles taken on the same sample, the effect of the high surface roughness and porosity of graphite on the depth resolution of the measurement has been evaluated and a 10% error on the depth measure was estimated. This

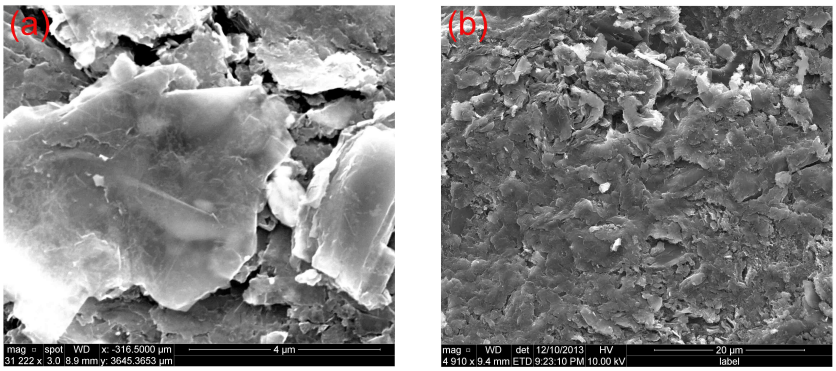

Figure 4.4: SEM images characterizing the highly porous graphite surface at two different magnification: (a) ×31222 and (b) ×4910.

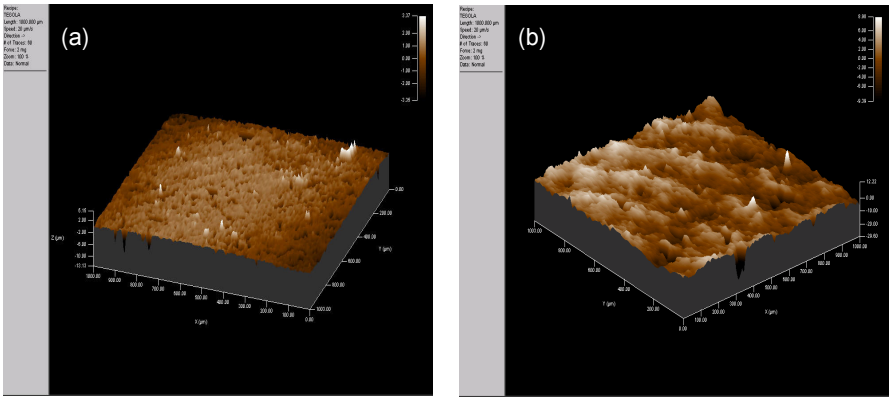

Figure 4.5: 3D Profilometry of a 1×1 mm section of the surface of sample: a) a surface finished sample and (b) a not finished sample.

assumption is reasonable taking into account the surface averaging performed from the beam size.

4.3.2 Boron deposition spatial asymmetry and effect of plasma operation

a. Toroidal non-uniformity of boron deposition

In order to assess the uniformity of boron deposition, graphite samples exposed during a number of boronizations at the three different positions illustrated in fig. 4.3 were analyzed by SIMS spectrometry to measure the boron content deposited on the graphite substrate. A blank graphite sample has been analyzed as well for comparison with samples exposed to boron wall-conditioning. In fig. 4.6 a comparison between the in-depth positive ion distributions of a blank sample (a) and of a sample after a 120-min boronization duration (b) is shown. All the signals show long tails that could be due to the presence of pores and high surface roughness and hence to different sampling depths, in addition to the effect of the in-depth SIMS resolution.

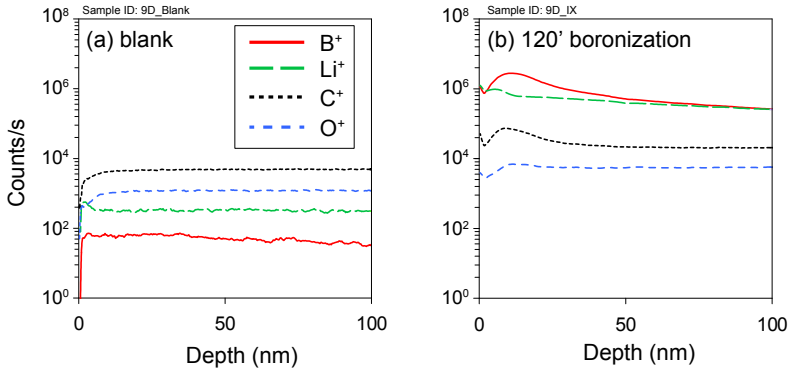

Figure 4.6: Positive ions SIMS spectra (6keV O_2^+) from of some ion species recorded in a blank sample (a) and a second sample exposed to a 120 min boronization (b).

The boron signal is at noise level in the blank sample, while in the sample exposed to boronization the boron presence is quite evident. In order to confirm the boron trend the ^{10}B related signals were also recorded and a $^{11}B/^{10}B \simeq 4$ ratio was obtained, corresponding to the natural isotopic ratio of boron. Previous lithium wall conditioning performed in the torus is the source of lithium increase observed in the bornized sample, consequent to the re-deposition process from other tiles during the glow discharge. Oxygen shows an increase in correspondence of the peak of boron, suggesting a co-deposition of the two species during the boronization and it is likely due to the presence of oxygen as impurity inside the chamber. This picture is also confirmed by the fact that the analysis of the gas extracted from the chamber by the vacuum system shows a presence of oxygen before the beginning of the boronization and its reduction when the breakdown voltage is applied

to the anodes. The oxygen content during the boronization will be further investigated by gas exhaust analysis and in the chemical analysis that will be presented in Section 4.4). The carbon signal follows a similar behavior to the boron signal, a behavior ascribed to the isobaric interference with the BH^+ signal. So to obtain a cleared information about the C/B interface, the negative ion distributions were also analyzed. Fig. 4.7 shows the trends of boron and carbon-related signals registered as positive (a) then negative (b) ions in a sample exposed to a 360 min boronization.

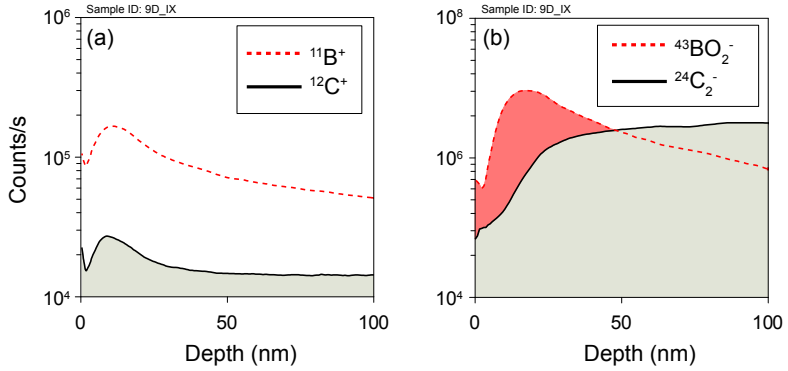

Figure 4.7: In-depth SIMS ion distributions in a graphite sample exposed to a 360-min boronization: positive (a) and negative (b) ions.

The negative ions distribution clearly show a minimum for carbon signal corresponding to the maximum of boron signal. Therefore, the negative ions in SIMS are more illustrative of the boron/carbon interface.In the following, when a rough estimation of the boron/carbon interface is needed, the negative SIMS ions are used. However, when comparing a single element the positive ion signals are preferred to discard possible difference in the chemical structure of the boron films that may affect the final measure by the SIMS mass spectrometer.

Figure 4.8 reports the positive ion signals of boron registered in samples exposed to the same boronization but placed in the three different toroidal positions. A clear reduction of the boron depth was observed between the sample that is located at the anode sector and the one displaced by 30°. A further slight reduction was observed for the sample at 90°. These measurements show a strong asymmetry in boron deposition and have been further confirmed in other subsequent boronizations performed in RFX-mod. The observed boron non-uniformity is also in agreement with the plasma behavior observed during the experiments of glow discharge optimization in Chapter 3.

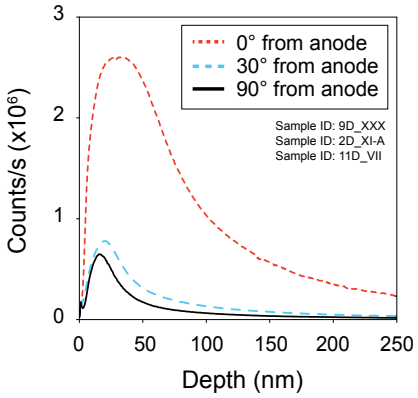

Figure 4.8: B^+ SIMS ion signal registered in samples placed in three different positions in the torus (in front of the anode, and 30° or 90° from anode).

b. Effect of the wall temperature on boron deposition

A further experimental condition that may affect the boron deposition is the wall temperature during the boronization and subsequent plasma discharges. In order to evaluate if the heating of the graphite tiles before the boronization results fundamental on the conditioning effectiveness, two graphite samples have been exposed to the same boronization. While one has been inserted cold in the vacuum vessel, the other one has been heated gradually to 170°C before the ignition of the boronization.

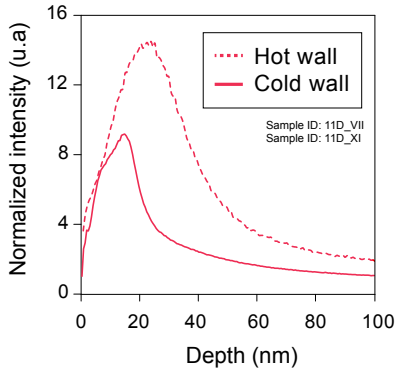

Figure 4.9: Boron SIMS signal registered in samples exposed to the same boron conditioning process but with (- - -) or without (—) a pre-heating of the sample at 170°C.

Fig. 4.9 shows the SIMS boron negative ions signals (normalized to the carbon signal) of the samples with or without a pre-heating. The boron deposition effectiveness progressively increased with the increasing of the sample temperature which gradually tended to reach the 170°C chamber

temperature. The total boron deposition content is doubled for the heated sample depicting an enhanced boron affinity with hot surfaces. This matter will be further investigated and discussed in Section 4.4 where the carbon-boron chemistry is analyzed for a boronization performed at room temperature in contrast with a boronization performed with a baked wall.

c. Boron erosion and re-deposition caused by plasma operation

In order to estimate the quantity of boron eroded and re-deposited after 25s of power plasma operation, two sets of graphite samples were used at two different positions: one set in front of the GD anode named 2D and an other set 30° away toroidally named 9D. Among the set of 2D samples, one has seen the boronization only while the other one was exposed to H plasma without being exposed during the boronization in order to only estimate the re-deposited boron. On the other hand, one sample at the 9D position was exposed either to the boronization and the plasma discharges while the other one was retrieved before plasma operation. In fig. 4.10 the boron positive ions (normalized to oxygen) from SIMS spectra are shown. The normalization to the oxygen signal is motivated in this case by the fact that in these samples, the oxygen signal was not perfectly constant due to a possible slight sample oxidation. So in order to exclude any influence of oxygen content in boron and carbon in-depth distribution, a ratio between two species is a good way to circumvent this issue. The boron content after hydrogen plasma in the sample at the GD anode position (left panel) gives an estimation of the re-deposition that can be compared with the variation of boron profile at the position that is 30° away toroidally (right panel).

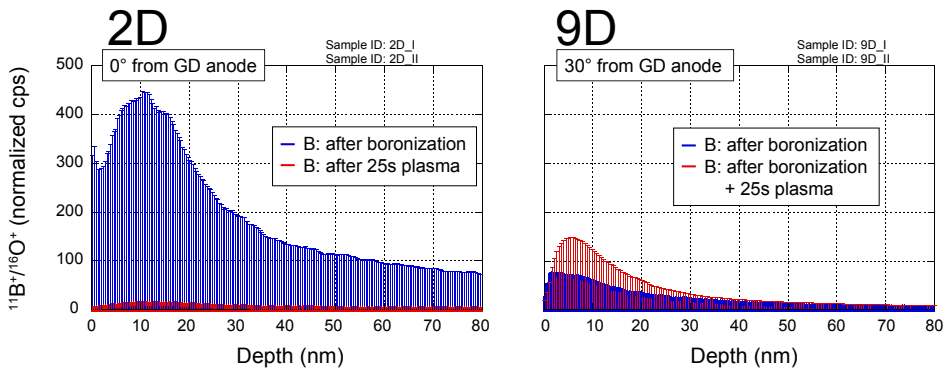

Figure 4.10: SIMS boron positive ions (normalized to oxygen) for a boronization (blue) followed by 25s of RFX-mod plasma operation (red). Right panel shows the spectra of the sample exposed in front of the GD anode and left panel the ones for the sample 30° away toroidally.

The variation in boron content post plasma operation seen on the sample 9D seems larger, and the reason is likely because of the presence of boron

nearby that could have facilitated the growth of the re-deposited boron layer. As already discussed earlier, the toroidal non-uniformity of boron content can also be noticed in the redeposited boron layer. In fact, the sample exposed far from the anode has shown a boron content that doubled after plasma operation while the boron content redeposited at the position in front of the anode is only 3% of the total boron content after boronization. In earlier work performed boronizations in RFX [106], the re-deposited layer was found also rich in carbon, and this is in agreement with the fact that the influx of carbon during hydrogen plasmas is only halved (fig. 4.1) in the case of a boronized wall, with respect to a not conditioned wall.

4.3.3 Global deposition inconsistency and boron growth dependence on glow discharge parameters

a. Inconsistency among experimental and nominal thicknesses

The toroidal non-uniformity of boron deposition around the torus is a detrimental feature to boron wall-conditioning in RFX-mod. In addition, an inconsistency has been observed among the measured boron content upon a boronization and the computed nominal thicknesses. The computation of the nominal thickness takes into account the flux of diborane continuously supplied during the GDC process and the percentage of diborane, in terms of partial pressure, present in the vessel during the treatment, the latter being evaluated by mass spectroscopy from the RGA. In fig. 4.11, the boron contented measured and nominally computed for a short 30' boronization and a longer 120' boronization are compared at two different toroidal positions.

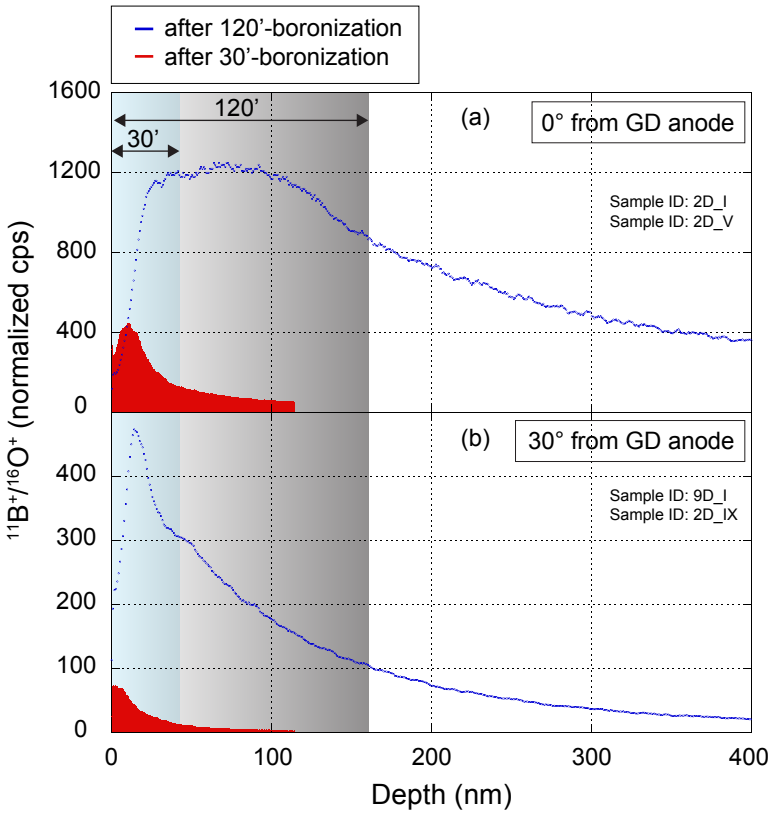

Figure 4.11: SIMS boron positive ions (normalized to oxygen) for a 120' boronization (blue) and a 30' boronization (red). Top panel shows the spectra of the sample exposed in front of the GD anode and bottom panel the ones for the sample 30° away toroidally. The nominal thicknesses are indicated with the horizontal rectangles.

The nominal thicknesses of the boron layers are 45 and 160 nm and are represented in the figure by two color rectangles. Panel (a) shows the boron profiles for the samples that are located at the same toroidal section of one anode, while panel (b) display those referred to the samples located in a section 30° from the other anode. The boron content for the 30 min boronization is well comparable to the nominal one in the case of the samples in front of the anode, whereas at the other position the experimental thicknesses are shorter than nominal ones for both samples. At both positions, the longer boronization gave not only a thicker deposit, but also a layer that shows a higher boron content.

b. Inconsistency among boron content and boronization duration

Fig. 4.12 displays a rough estimation of boron thickness measured by SIMS for boronizations of different duration and at different locations around the torus. A global inconsistency has been observed among boronization duration and the rough estimation of boron thickness. The plot also illustrates more clearly the previously depicted strong toroidal asymmetry characterizing the boron deposition with a higher boron content around the anode position.

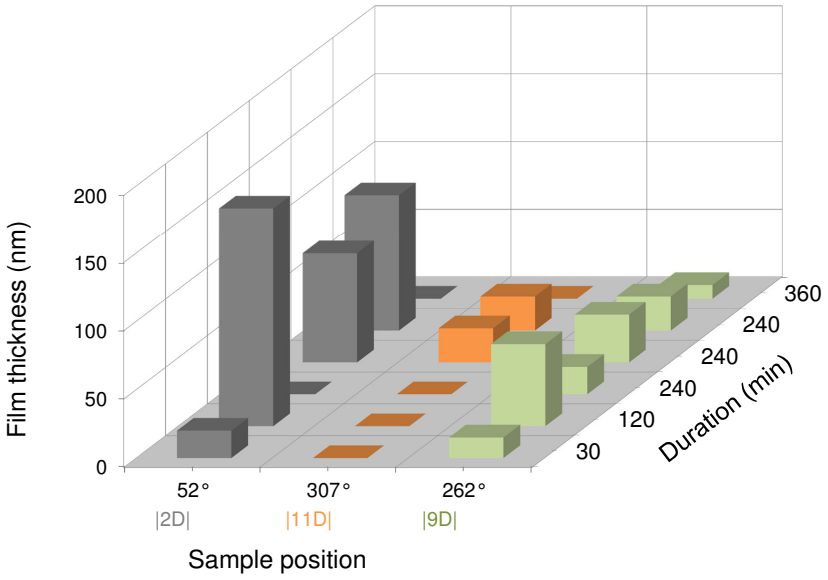

Figure 4.12: Boron maximum concentrations measured with SIMS at different toroidal positions and after different boronization duration: anode sector (grey), 30° away (green) and 90° away toroidally (orange).

In order to take into account the effective concentration of boron in the gas mixture the thicknesses measured by SIMS at the 9D sector in fig. 4.12 were normalized to the boron gas concentration measured by the RGA before the ignition of the boronization and while the chamber was filled with diborane.

The measured and normalized thicknesses are shown in fig. 4.13.

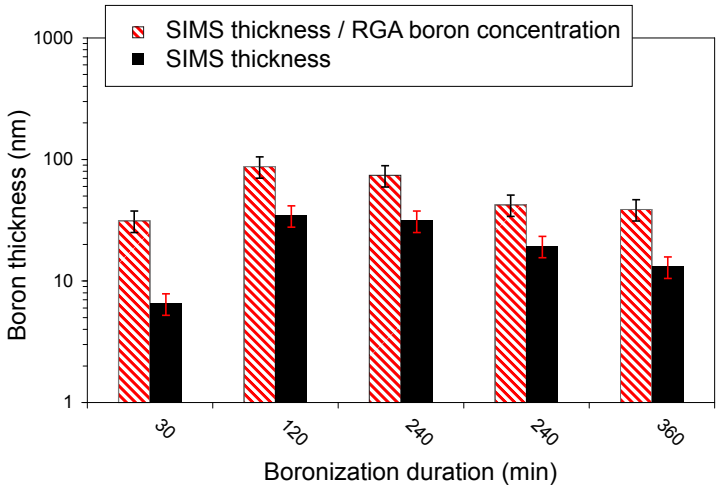

Figure 4.13: Boron film thickness measured by SIMS spectroscopy after boronizations of 30', 120', 240' and 360' duration (black bars). The thicknesses measured by SIMS are normalized to the working boron concentration during the boronization (red hashed bars). Error bars represent uncertainty in depth quantification by SIMS (~10%).

The figure shows that the measured boron thickness does not correlate to the duration of the coating process. Some parameters of glow discharge parameters must hence be significant in determining the boron deposition efficiency as already discussed in the previous chapter dedicated to the characterization of the glow discharge operational regimes. It was found that the HeGDC efficiency in terms of H-depleting from the wall increases with increasing glow discharge plasma current, while no clear evidence was found of the effect of pressure or voltage alone. Since boron wall conditioning in RFX-mod is performed by glow discharge with 90% of He in the working gas and only 10% of diborane, the boronization can be substantially considered as a HeGDC with comparable physical sputtering processes. However, the presence of diborane radicals that are deposited in a vapor deposition-like mechanism may have a different dependence with respect to the glow discharge main parameters, that are the plasma current, voltage and pressure.

4.3.4 Boron growth rate correlated to the glow discharge parameters

a. Boron deposition rate dependence

A rough estimation with 10% error (SIMS depth profile error) of the boron deposition rate has been computed dividing the thickness obtained from SIMS

by the effective duration of the bornization. The computed deposition rate at the 9D sample-exposure position obtained for a number of boronizations performed in RFX-mod has been related to the glow discharge plasma current, voltage and working pressure and displayed in fig. 4.14.

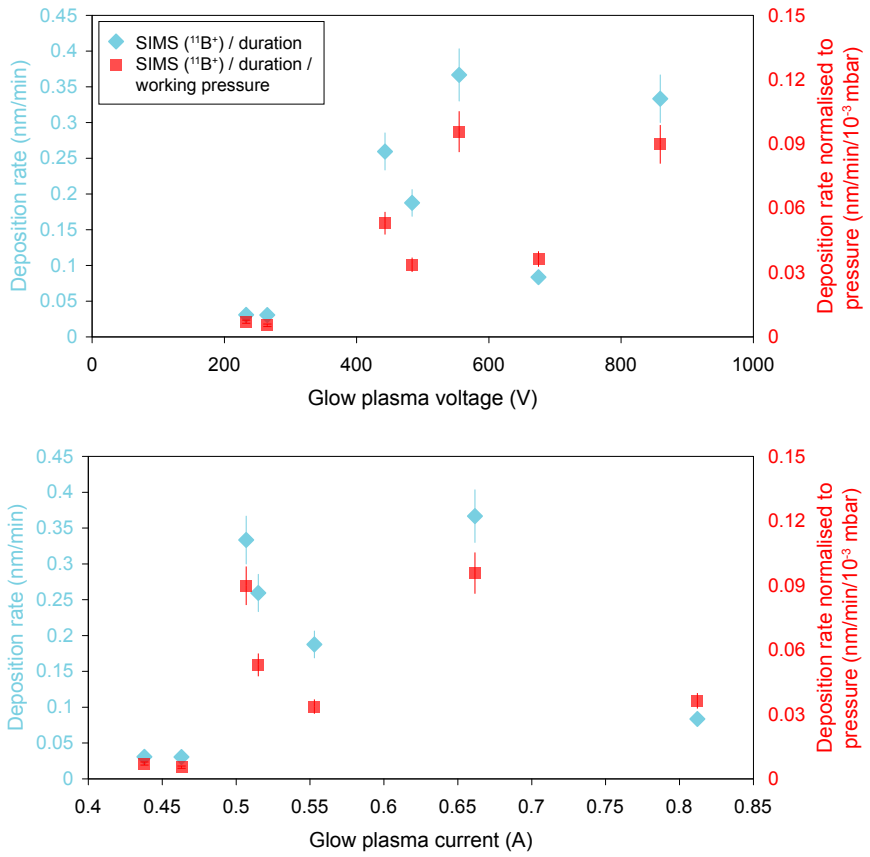

Figure 4.14: Computed boron deposition rate as a function of the glow plasma current (bottom panel) and glow plasma voltage (top panel). The secondary y-axis normalizes the deposition rate to the working pressure.

The boron deposition rate, in contrast with the characterization of HeGDC discussed in Chapter 3 Section 3.2.3, shows a slightly different dependence with the glow plasma discharge voltage and current. While the hydrogen-depleting during HeGDC is highly correlated with the glow discharge plasma current, diborane GDC shows a more pronounced dependence with the glow discharge voltage. In addition, normalizing the deposition rate to the average working pressure shows a greater correlation.

Given the clear dependence on the glow plasma current and voltage, in fig. 4.15 the previously computed boron deposition rate is plotted as a function of the glow plasma power ($I \times V$). Two separate groups of data with a power threshold are identified in the plot: a boronization performed

at a glow plasma power lower than 200 W is correlated to a low boron deposition rate while boronizations achieved at a glow power higher than 200W have shown a significantly higher (~ 10×) deposition rate.

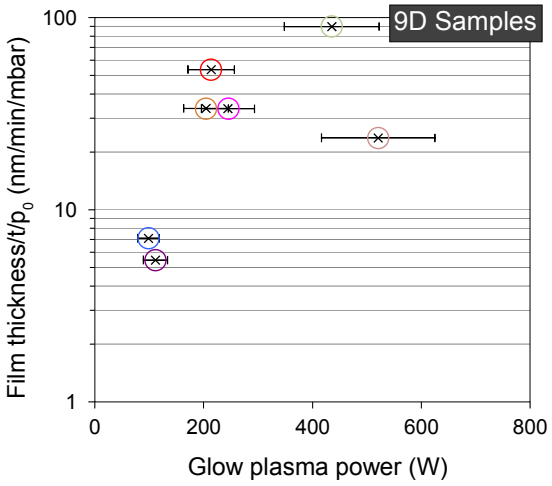

Figure 4.15: Deposition rate of boron as a function of the glow plasma power (IxV).

The later result is consistent with other studies on boron deposition in Plasma-Enhanced Chemical Vapor Deposition (PECVD) performed by Komatsu et. al in ref. [37–40]. The apparent reaction orders for the growth of boron films were measured as a function of the plasma power, which ranged from 0.4 to 1.6 kW. It was found that the reaction order (n) makes a transition from 1/2 to 1 at 900 W with an increase of the plasma power, and which accompanied a corresponding morphological transition. In the following, the later result will be further investigated looking at the gas exhaust during single boronizations.

b. Gas exhaust analysis

The partial pressure of diborane gaseous radicals during a boronization has been monitored to assess the real time efficiency of boron deposition on the first wall. Changes in partial pressure of the boron gaseous radicals (such as B_2H_2, B_2H, B_2H_4 ...etc) and impurities such as oxygen, hydrogen and carbon relate directly to changes in the number of boron atoms sticking to the first wall. In tab. 4.2 the m/e used for the analyses are shown, m/e 26 was considered as base 100 and m/e 22, 23, 24, 25 and 27 were monitored by the RGA.

An example of the measured partial pressures is shown in fig. 4.16. The working total pressure measured during the boronization by an absolute pressure gauge and the glow plasma power computed as the product of the measured anodes current and voltage ($I \times V$) are shown in the same plot on

Table 4.2: Mass spectra of the cracking of diborane (B_2H_6) used for RGA analyses in RFX-mod. (*m/e=26 was considered base 100 in the cracking %).

m/e	Relative intensity of pure B_2H_6 (%)
22	10.8
23	48.5
24	94
25	57.7
26	100
27	95.2

a secondary axis. It is clearly seen that an increase in the glow discharge power is correlated to a decrease in the partial pressure of diborane gaseous components at a constant total in-vessel pressure (constant He+B_2H_6 flux).

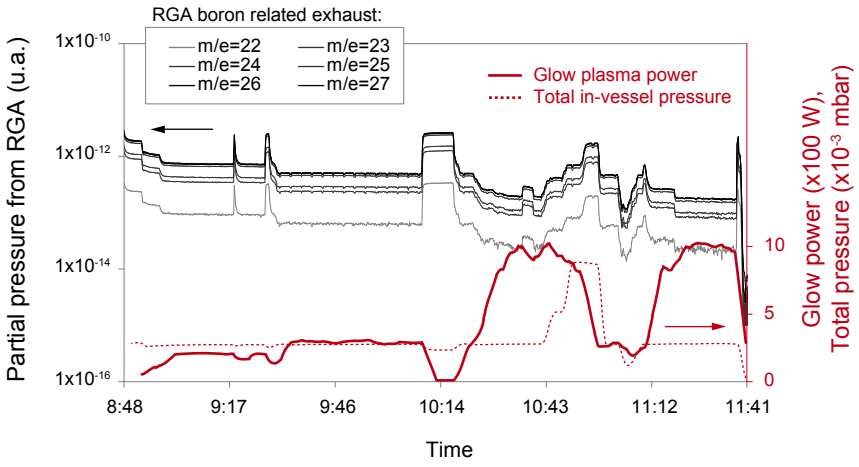

Figure 4.16: Instant partial pressure of m/e 22-27 measured by the RGA during a boronization in RFX-mod (grayscale curves). Working pressure measured by an absolute pressure gauge (- - -) and glow discharge plasma power (—) are displayed for comparison.

In fig. 4.17 the partial pressure of m/e=2, m/e=12, m/e=26 and m/e=[32+0.5×28] respectively characteristic of the hydrogen, carbon, boron and oxygen concentration in the gas exhaust during the same boronization are plotted as a function of the instant plasma power of the glow discharge. In order to assess changes in the impurity content with increasing plasma power, a constant diborane flux during the boronization has been maintained. The in-vessel pressure has been kept constant and the data are plotted for two phases at $p_0 = 3.6\times10^{-3}$ and 1.0×10^{-2} mbar.

At a constant in-vessel pressure of 1.0×10^{-2}, by increasing the glow discharge plasma power from 100W up to 1200W, the boron exhaust decreases by a factor of ~7, the oxygen and carbon exhausts are reduced by

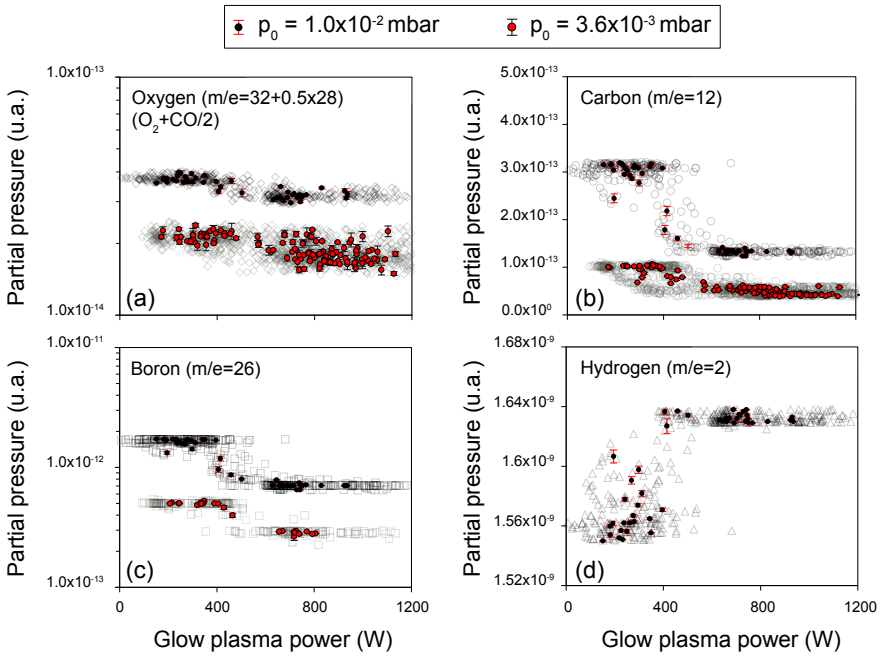

Figure 4.17: Instant partial pressure of m/e=2, m/e=12, m/e=26 and m/e=[32+0.5×28] respectively of the hydrogen (△), carbon (○), boron (□) and oxygen (◇) during a 360-min boronization as a function of the instant glow plasma power. The close circles refer to the moving average of the data.

a factor of ~2 while the hydrogen exhaust slightly increases by 10%. Since the GDC is performed with 90% He+10% B_2H_6, the effect of hydrogen physical sputtering by He ions is most likely the reason of the H exhaust increase as already discussed in Chapter 3. A reduction in boron exhaust is undoubtedly linked to an enhanced deposition of boron atoms on the graphite first wall and the simultaneous reduction in oxygen and carbon is most probably linked to a co-deposition of these impurities with boron. The changes in the chemical properties of the boron film with increasing plasma power will be further investigated below and the carbon and oxygen content in co-deposited layers will be discussed in 4.4.

From the boron exhaust the actual boron deposition rated can be obtained by subtracting the boron partial pressure in fig. 4.17 (c) from the initial boron partial pressure measured by the RGA before the ignition of the boronization. In fig. 4.18 the boron deposition rate measured from gas exhaust for a 360-min boronization is shown. The latter can be compared to the boron deposition rate measured by SIMS post-mortem analysis in fig. 4.15.

A qualitative and a good quantitative consistency can be seen confirming the presence of a boron deposition transition as already predicted by Komatsu [37–40] in a smaller scale PECVD device. The presence of such a transition explains therefore the observed discrepancy of

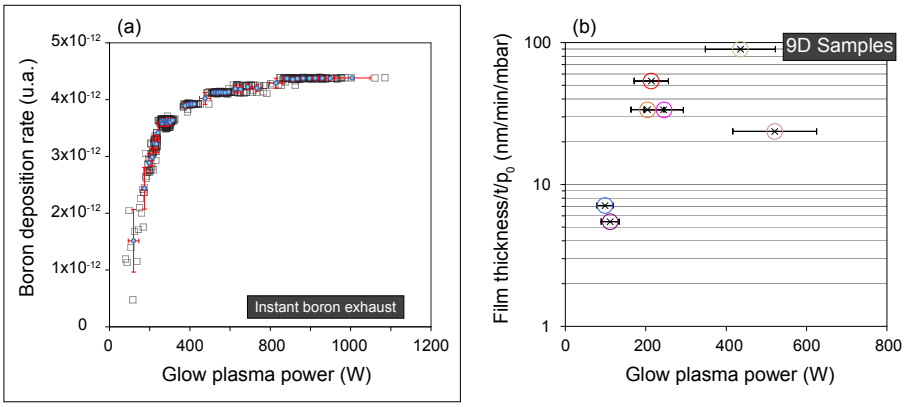

Figure 4.18: Boron deposition rate measured by gas exhaust analysis of boron partial pressure during a 360-min boronization (left panel). For comparison, fig. 4.15 (right panel) is shown.

boron wall coverage after boronizations in RFX-mod. Komatsu highlighted the presence of a corresponding morphological transition of the boron deposit. This feature will be further investigated below by means of SEM and EDS/X surface analyses.

4.3.5 Surface morphology and composition correlated to plasma power

The experimental results presented in the previous sections indicate that the glow plasma power plays an important role in the physical processes that govern the deposition of boron on RFX-mod graphite first wall during boron wall conditioning. In this section, the boron deposit obtained after boronizations performed at different experimental conditions of glow plasma power but also wall temperature and duration is extensively scrutinized with high resolution surface analysis techniques in order to characterize the surface morphology, subsurface and near-subsurface elemental composition. SEM microscopy combined with EDS/X spectroscopy is used to characterize the surface morphology. RBS spectroscopy is used to perform a non-destructive analysis of the surface and in-depth composition. EDS/X is used in a second step to probe the 1μm bulk elemental composition. The near-subsurface properties that is where most of the interaction of the plasma occur are probed with high resolution XPS spectroscopy.

The analyses were achieved on graphite samples exposed in front of the GDC anode at the 9D sector (see fig. 4.3). Three different boronizations performed at different conditions of glow plasma power, duration and working temperature are considered: (i) a 360 min boronization performed at 100 W glow discharge plasma power (I×V) while baking the vessel at 170° C; (ii) a 360 min boronization performed at 535 W while maintaining the vessel temperature at 170° C (the coatings obtained with these two boronizations will be named type I and type II respectively in the remaining sections of the chapter); and (iii) a 900 min boronization performed at room temperature and 435 W. A summary of the exposed samples and experimental conditions can be found in tab. 4.1.

a. Surface morphological characterization

All three samples #29, #56 and #50 have been analyzed by SEM and EDS/X. While samples #29 (type-I coating) and #56 (type-II coating) have only a difference in glow plasma power, sample #50 has been exposed to a room temperature boronization. The latter was performed tofurther investigate the effect of the wall temperature on the boron deposition as earlier SIMS measurements (fig. 4.9) have shown greater boron coverage when the wall is pre-heated before the ignition of the boronization. In fig. 4.19 the SEM pictures of the samples surface along with the corresponding EDS/X spectra, elemental weight and atomic concentrations are shown. A straightforward difference can be clearly seen between sample #29 that was exposed to a 100 W boronization and sample #56 exposed to a higher glow plasma power of 535 W. The SEM image of the latter shows the presence of well-faceted crystallites of several μm above the graphite surface similarly to what has been documented by Komatsu in [37–40]. Sample #50 shows a highly condense and profuse surface aspect. In addition, the EDS/X measurements on the latter show a 3× higher boron coverage compared to

sample #29.

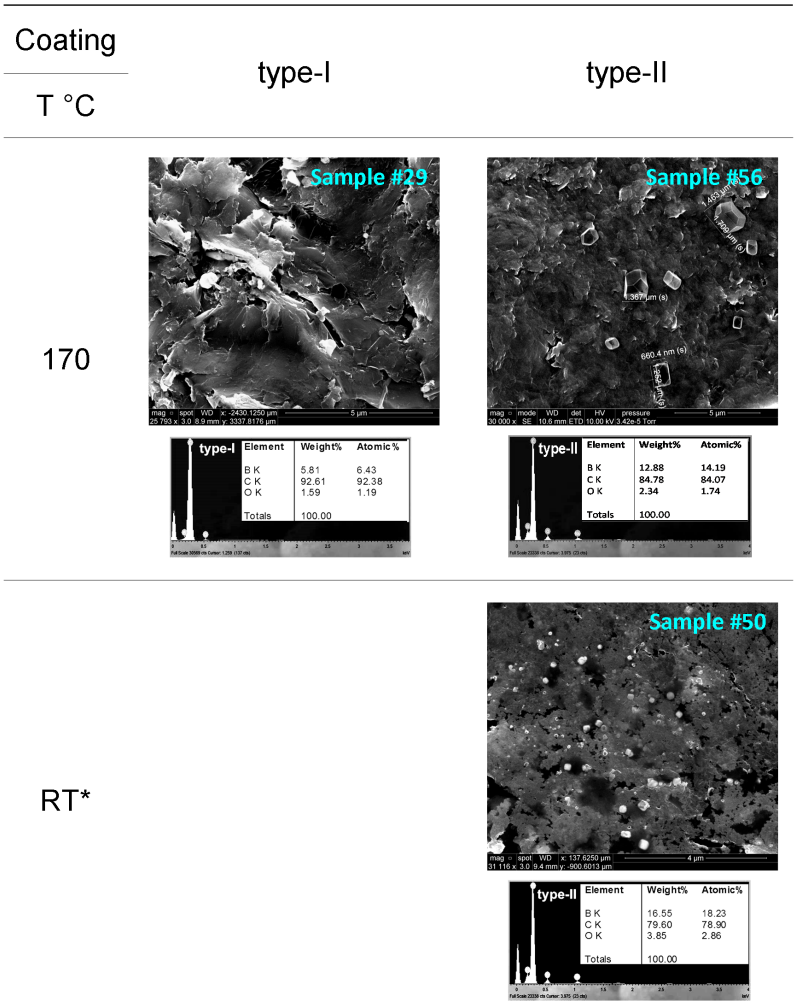

Figure 4.19: SEM pictures of samples #29, 56 and 50 at respective magnifications of ×25793; ×30000 and ×31116. Under each image the corresponding EDS/X measurements are shown.

The previously depicted picture of boron deposition transition at increasing glow plasma power is confirmed in terms of the boron-graphite morphology. SEM images of the type-I coating revealed a similar aspect of the graphite surface as a non-boronized surface shown in fig. 4.4 while the type-II coating has a more condense structure evidenced by the covering of the porous graphite surface. The dense, 2× higher boron coverage and profuse aspect of the type-II coating is undoubted the result of the high glow plasma power.

b. Bulk elemental composition

RBS measurements

In order to preserve the homogeneity and chemical stability of the films, RBS measurements with a 2 MeV He^+ beam were conducted using the Rutgers University Physics Department facility introduced in Chapter 2. Samples #29 and #56 were analyzed to non-destructively measure the composition of the first layers of the surface. From RBS measurements it has been possible to determine, with some resolution limitations (~5nm), both the atomic and mass relative concentrations of the elemental sample constituents as a function of the sample depth. Fig. 4.20 shows the RBS spectrum of the two boronized samples, where the elements (O, C and B) with their multiple isotopes that compose the film are marked. The simulation and analysis of the RBS spectra were done with the SIMNRA code [107], that allows the qualitative and quantitative analysis of the non-Rutherford backscattering spectra.

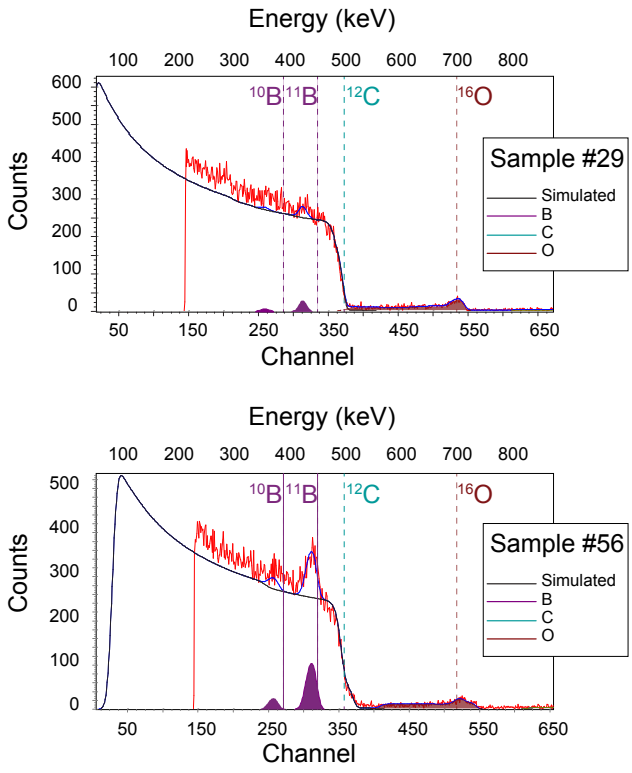

Figure 4.20: 2 MeV He^+ beam RBS spectrum with the corresponding SIMNRA simulation curve of samples #29 (top) and #56 (bottom) respectively exposed at 100 W and 535 W glow discharge plasma power.

The relative concentrations of the elements that are present in both

samples are shown in tab. 4.3. The results show a 5× greater boron concentration in sample #56 for the same oxygen concentration, a result consistent with previous considerations. The difference in boron/oxygen ratio could be understood in terms of the boron-oxygen interaction during the film formation since the samples were not exposed to any plasma discharge in RFX-mod after exposure to boronizations.

Table 4.3: Percentage concentration of elements found in samples #29 and #56.

Sample ID	Boron	Carbon	Oxygen
#29 (type-I)	0.74	98.20	1.06
#56 (type-II)	3.55	95.53	0.92

Boron oxidation occurs only under oxygen ion bombardment since it is highly inert against atmospheric molecular oxygen as Zehringer et al. states in [108]. Therefore, the higher boron/oxygen ratio obtained with a higher glow plasma power is due to low boron oxidation compared to sample #29, as both samples were exposed during the same boronization duration of 360 min. Fig. 4.21 shows the elemental depth profiles obtained from the simulation of the spectra.

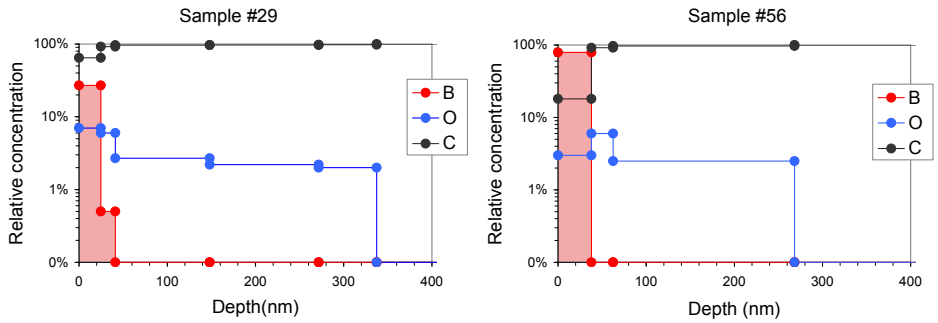

Figure 4.21: Depth concentration profile of boron, oxygen and carbon determined from RBS measurements on samples #29 (left) and #56 (right) respectively exposed at 100 W and 535 W glow discharge plasma power. The boron concentration is emphasized with areal red color.

The depth profiles allow the characterization of the elemental concentration changes along the first 400nm probed layers. It can be seen that in the case of the type-I coating (sample #29), the boron maximum relative concentration is about 30% in the first 20nm layer, it drops to as low as 5% in the following 20nm then it goes under the detectable concentration in the following layers. Whereasin the case of the type-II coating (sample #56), the boron content above the graphite surface shows a steady 80% relative concentration in the first 40nm layer then becomes undetectable in the following probed depth. With regards to the oxygen

content, a significant high concentration (2× higher compared to the surface) can be observed laying under the boron layer in the case of the type-II coating, as if the boronization has buried a graphite lattice rich with oxygen on the surface or that the fresh deposited boron is highly oxidized then the subsequent deposited boron during the boronization is oxygen-free. The latter pictured image is consistent with the SEM images in fig. 4.19 and with the gas analyses earlier discussed (fig. 4.17) where the oxygen concentration drops by a factor of two with the initial phase of the plasma power increase. In fact, the latter image is also consistent with the low plasma power case shown in fig. 4.21 where a similar surface oxygen relative concentration of about 8% was observed in the case of sample #29 . The difference in oxygen concentrations among samples #29 and #56 can be explained with the fact that the oxygen feature observed in the case of the type-I coating is simply the buried feature observed in type-II case. In other words, oxygen gettering during the boronization itself can be attenuated by performing a high power glow discharge boronization that would induce oxygen gettering in the first boron layers then offer a pure boron content on the surface of the graphite first wall, allowing better performances of power discharges with a more gettering availability of the boron content.

EDS/X measurements

Energy Dispersive X-ray (EDS/X) spectroscopy has a depth of x-ray generation of about one micron. Therefore the information obtained of the elemental composition is related to a subsurface volume including the boron deposit with co-deposited impurities but more importantly a significantly large fraction of the carbon substrate. While RBS is a measure of the back-scattered elements along the energetic 2 MeV He^+ ion beam, the EDS/X measurement is an integrated measure over a ~1μm^3 volume of the generated x-rays. The two measures are expected to give comparable qualitative and quantitative results in terms of the elemental composition of the probed samples. The already presented EDS/X spectra shown in fig. 4.19 are summarized and shown again in tab. 4.4.

Table 4.4: Volumetric atomic percentage concentration of elements found in samples #29 and #56 measured by EDS/X spectroscopy.

Sample ID	Boron	Carbon	Oxygen
#29 (type-I)	6.43	92.38	1.19
#56 (type-II)	14.19	84.07	1.74

The EDS/X measurements qualitatively confirm what has been already observed with the RBS technique: more than 2× boron coverage is measured in the case of the type-II coating (sample #56), combined to a higher boron/oxygen ratio. At a certain extent, a quantitative consistency is also obtained considering the difference in the probed approach of the two techniques previously discussed. While RBS measurements on the two

samples have given a more accurate information of the boron distribution along a straight 400 nm line into the samples depth, the EDS/X measurements take into account the surface roughness of the graphite and has given an overall information about the boron coverage.

c. Near-subsurface high resolution analysis

Highly sensitive surface analysis techniques have been used to probe the near-subsurface of the boronized graphite samples to investigate the first 10 nm elemental composition. Although the life time of the boron content upon exposure to power plasmas is linked to how thick and boron-rich is the total deposited boron layer after boronizations of the wall, the large scale fusion plasma is, in principle, dominated by a very thin surface layer at the plasma-wall interface and its properties are more intimately linked to the beneficial effects of boron wall-conditioning on plasma performances. In fact, in a fusion plasma the average incident particle energy of H particles at the walls varies between 10 and 200 eV/amu. Under these conditions, the penetration depth is below 10 nm. As already discussed in the previous RBS and EDS/X measurements, performing a boronization under a high glow plasma power well above 200W leads to higher quality of boron content above the graphite substrate, such as a thicker oxygen-free and pure boron film. In this section, the previously identified features are further investigated within the penetration extent of XPS spectroscopy probing beams, namely 1-12 nm.

'As received' HR-XPS measurements

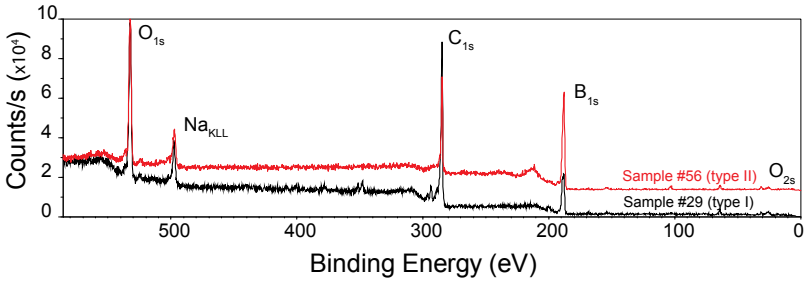

Figure 4.22: HR-XPS survey spectrum of samples #29 and #56 surface. The major XPS peaks are marked for B, C and and O. A significant Na KLL Auger peak appears at about 500 eV.

High-resolution XPS(HR-XPS, 0.5 eV) measurements were conducted using the Princeton University Chemical Engineering Department facility introduced in Chapter 2. The measurements were performed in an Ultra-High Vacuum (UHV) chamber that is equipped with a Scienta ESCA 300 spectrometer. The instrument has an 8 kW rotating anode source and a

7-crystal monochromator for providing highly monochromated Al Kα X-rays (1486.7 eV), and a 300-mm radius hemispherical analyzer and position-sensitive detector for high-energy resolution and enhanced signal-to-noise. For quantification, standard sensitivity factors of 0.159, 0.296 and 0.711 for B_{1s}, C_{1s} and O_{1s} [109], respectively, were used.

In fig. 4.22 the 'as received' HR-XPS survey spectra of samples #29 and #56 are shown. Boron, carbon and oxygen are the major peaks observed in the survey. A significant Na KLL Auger peak appear in the spectra at about 500 eV on both samples and it is attributed to the residual Na interpolated into the graphitic matrix. The approximate composition of the surface of the analyzed samples has been determined by dividing the individual peak area, after appropriate background subtraction, by their respective atomic sensitivity and the result is shown in fig. 4.23.

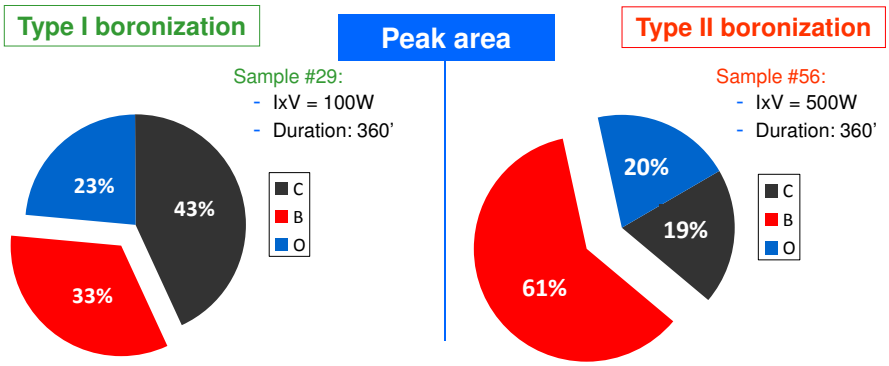

Figure 4.23: Surface HR-XPS composition of samples #29 and #56. The relative composition was determined by dividing the individual peak area of B, C and and O by their respective atomic sensitivity.

Boron content measured on sample #56 exceeds #29 by a factor of 2, while the boron/oxygen ratio is minor in the case of the high glow plasma power. The qualitative HR-XPS results are consistent with previous RBS and EDS/X measurements. Quantitatively, HR-XPS gives an extra information regrading the abundance of boron facing the plasma upon boronizations performed at different glow plasma power. While RBS and EDS/X have shown that boronizations peformed under high plasma power of about 500 W, a thick and rich boron oxygen-free (< 3%) film is deposited on the graphite substrate, HR-XPS shows that in addition, the very first thin 10 nm of the boron film that will be in contact with the power plasmas has a 2× richer boron content for the same oxygen content compared to boronizations performed at a plasma power < 200 W. Therefore, in terms of oxygen gettering capability of the boron film, when a boronization is performed under a high plasma power of about 500 W, oxygen gettering during power plasmas is likely to be enhanced by a factor of 2.

Ar^+ etching depth profiling HR-XPS measurements

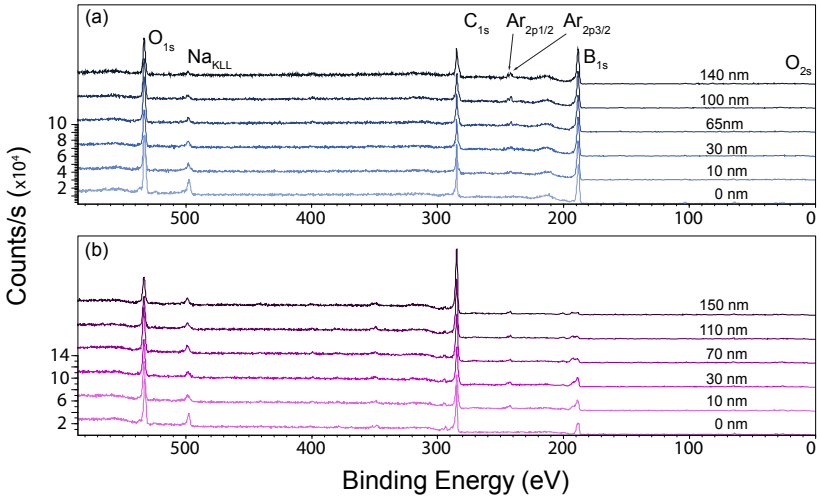

Figure 4.24: Ar^+ step-wise etching HR-XPS survey spectra of sample #56 (a) and sample #29 (b). The major XPS peaks along the sputtered depth are marked for B, C and and O. A significant Na KLL Auger peak appears at about 500 eV and low Ar peaks due to the argon sputtering beam can be seen around 241 eV.

The previous results particularly from RBS spectroscopy and surface HR-XPS have confirmed the beneficial effect of performing boronizations with high plasma power glow discharges. The results have also shown differences in the near-surface and subsurface boron/oxygen contents. Since the boron film upon exposure to power plasmas is gradually eroded and the plasma comes progressively to contact with the subsurface boron layers, an accurate evaluation of the elemental composition of the boron sub-layers is therefore important. To this aim, step-wise HR-XPS measurements have been performed by sputtering the surface of samples #29 and #56 using a 2 keV and 0.01 nA/mm^2 Ar^+ etching beam. The sputtering rate for carbon was estimating using:

$$q_C = q_{Si} \times (\rho_C/\rho_{Si})$$

where q_C and q_{Si} are the graphite and silicon sputtering rates, respectively. q_{Si} was easily determined by measuring the depth of a crater on a flat Si (100) sample obtained after a sputtering time Δt using the same beam energy, and current density used in the analyses, ρ_C and ρ_{Si} are the bulk density for graphite and silicon respectively. For the beam used, the previous technique gave q_C=0.5nm/s. The uncertainty associated to q_C using this method can be as high as 30%.

Fig. 4.24 shows the Ar^+ step-wise etching HR-XPS survey spectra of samples #29 and #56. In addition to what was observed and commented in fig. 4.22, $Ar_{2p1/2}$ and $Ar_{2p3/2}$ can be seen in the spectra immediately after the first Ar^+ sputtering of the surface. The Ar relative concentration was never higher than 1% even for the depth profiles for both samples and therefore considered without effect on the chemical properties of the boron film.

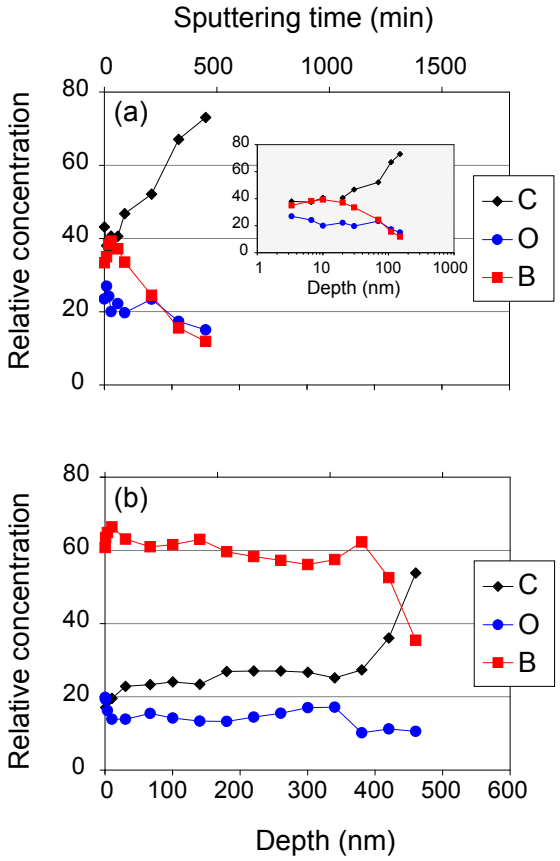

Figure 4.25: HR-XPS Ar^+ sputter depth profiles of boron, carbon and oxygen for sample #29 (top panel) and sample #56 (bottom panel). On a secondary x-axis the sputtering time corresponding to the computed depth is shown as well.

In fig. 4.25 the depth profiles of boron, carbon and oxygen for samples #29 and #56 are shown. The previously measure surface 60% relative boron concentration in the case of sample #56 is observed to be maintained throughout the subsequent in-depth 380 nm then it drops to 50% at 420 nm and 35% at 460 nm. In the case of the sample #29, however, the 30% surface abundance of boron is only conserved in the subsequent 30 nm with a little increase of 5% then it drops to less than 20% in the following 60 nm. With regard to the oxygen abundance in the boronized sub-layers, in the

case of sample #56, the mean oxygen relative concentration in the sub-layers was about 15% while in the case of sample #29, a 20% was recorded. In both samples, a remarkable 60% increase of oxygen abundance is observed at the boron/carbon interface, likely due to the highly reactive primary boron layers that induce enhanced oxygen gettering from the in-vessel residual gas at the very beginning of boron deposition above the graphite surface. The latter result is consistent with similar studies performed on boron films in TEXTOR tokamak [108, 110].

Comparaison between HR-XPS measurements and boron gas exhaust

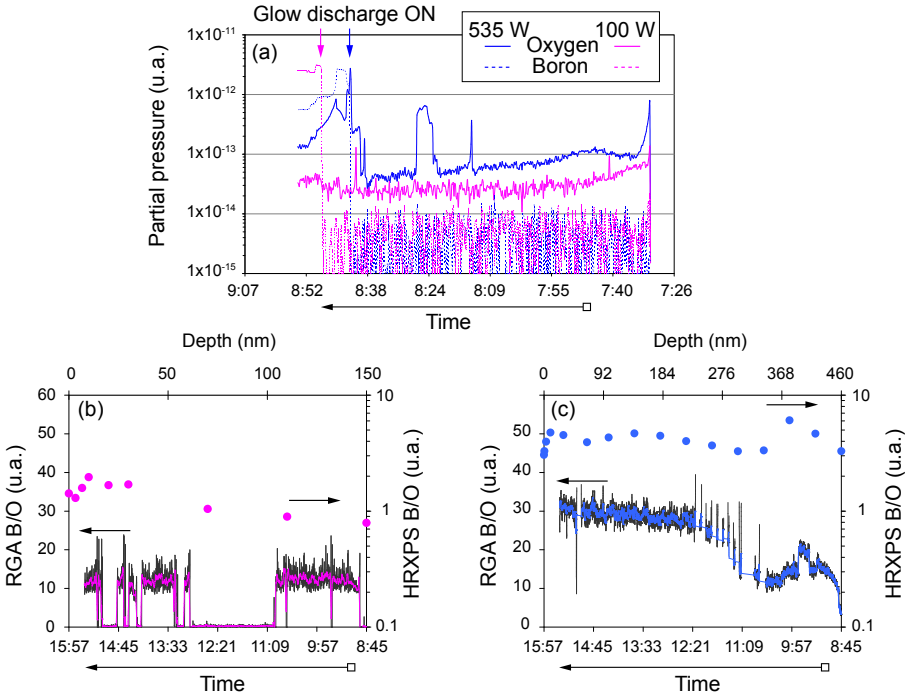

Figure 4.26: Top panel (a): initial oxygen (–) and boron (- -) exhaust partial pressure of a 100 W boronization and a 535 W boronization. Bottom panels: Ar^+ sputter depth profile of boron/oxygen ratio measured by HR-XPS (•) for #29 (b) and sample #56 (c) and the corresponding time history of the partial pressure of boron/oxygen ratio measured by RGA during the respective 100 W and 535 W boronizations. For visualization rendering, the time primary x-axis are reversed.

With the aim to further investigate the difference in oxygen abundance observed in the two boronizations previously discussed, the boron/oxygen ratio measured by HR-XPS has been opposed to the boron/oxygen partial

pressure ratio measured in the gas exhaust during both boronizations by the RGA and shown in fig. 4.26. The initial oxygen partial pressure measured by the RGA in the gas exhaust before and immediately after the beginning of the two boronizations is shown in the top panel. Very similar oxygen abundance in the vessel is reported showing the comparable wall state before the start of the boronization. A clean RFX-mod graphite first wall has been obtained with the pre-boronization cleaning cycle presented in 2.3.3. Any subsequent change in the oxygen abundance in the vessel is, therefore, only due to the boronization glow discharge. Immediately after the beginning of the boronization performed at high glow discharge plasma power of 535 W, a remarkable decrease in oxygen exhaust is observed in contrast with the boronization performed at 100 W. The latter can be explained by the high gettering availability of the initial boron deposition, however it is in contradiction with the fact that boronization is main a helium glow discharge with 90% of helium gas and only 10% of diborane. It is already known that boronizations performed with a similar gas mixture are effective in sputtering O_2 from graphite [111], but the effect here is not clear. Therefore, not only the benefit in performing boronizations with high glow discharge plasma power can be seen in terms of higher content of pure boron but can also be seen in the reduction of the oxygen content at the beginning of the treatment, thereby reducing boron oxidation and providing an oxygen-free boron deposit on the first wall.

The time history of boron/oxygen ratio shows a similar behavior as the measured HR-XPS depth profiles, particularly seen in the case of sample #56. It is reasonable to consider valid, therefore, the hypothesis of a direct link between what is measured by the RGA in terms of partial pressure in the gas exhaust and what is deposited on the first wall during the boronization. The 7× increase of the oxygen abundance at the boron/graphite interface is also observed in the gas exhaust time behavior. While the HR-XPS boron/oxygen ratio in the boronization performed at low 100 W glow discharge plasma power slightly exceeds unity (in correspondence to a ratio of 10 measured by the RGA gas exhaust), when the boronization is performed at 535 W, the HR-XPS boron/oxygen ratio ranges between 3 and 6 (in correspondence to a ratio measured by the RGA ranging between 20 and 30). As a consequence, the boron content deposited by a high glow discharge plasma power boronizations is remarkably oxygen-free which would allow an enhanced oxygen gettering during power plasma operation.

4.4 Boron-graphite chemical interaction correlated to impurity content upon boronization

In this final section of the chapter, a chemical approach has been undertaken to investigate the chemical interactions of the boron atoms and the in-vessel impurities during a number of boronizations in RFX-mod and further investigate the effect of the glow discharge plasma power on the boron/impurities chemistry. In particular, the main questions that are addressed in this section are:

(i) Boron carbide chemical structure
(ii) Oxygen/boron surface and near subsurface chemical interactions
(iii) Hydrogen and oxygen contamination in the bulk of the deposited boron film

XPS spectrum is sensitive to the chemical environments of materials, which is an effective technique to identify and analyze the changes in chemical existing states of materials. The previously performed high-resolution XPS (HR-XPS, 0.5 eV) measurements are further analyzed with main focus on the B_{1s}, $C_{1s}$and C_{1s} core lines. The absolute binding energies of the photoelectron spectra were determined by referencing to the C_{1s} transition at 284.7 eV (from adsorbed species). While surveys scans were measured with steps of 0.2 eV, high resolution spectra were measured within the spectral range of interest (±20 eV around the core level emission peaks of interest), with 0.08 eV steps. The data were curve fitted using CasaXPS VAMAS [112] processing software version 2.3.16 (Devon, United Kingdom) with a Shirley background subtraction and 70%-to-30% Gaussian-Lorentzian line shapes.

4.4.1 Qualitative considerations about the boron carbide chemical structure

A full boron carbide structure behaves as semiconductor and therefore the BE of the C_{1s} and B_{1s} lines are affected by surface charging, so that a way to circumvent the problem is to look at their difference to characterize the chemical state [110, 113]. The differences in binding energy of the B-C components under the C_{1s} and B_{1s} lines throughout the depth of the two samples #29 and #56 are analyzed and reported in tab. 4.5. Excluding the values obtained at the surface, that can be affected by surface contamination, hydrocarbons adsorbed at the surface, different terminating bonds ...etc, one can notice that these differences are almost constant throughout the depths and that their average values are very close in both samples (~96.3 ± 0.2 eV). Polycrystalline boron carbides obtained by Chemical Vapor Deposition (CVD) show typically values of 94 eV in the (C_{1s}-B_{1s}) BE and requires substrate a high temperature (~800 °C), much higher than that of RFX-mod wall temperature during a boronization. Instead, the (C_{1s}-B_{1s}) BE associated to amorphous hydrogenated boron

carbide (a-B/C:H) obtained by B_2H_6/He mixture shows a value of 95.2 eV [113]. Taking into account that the deposition carried out in ref. [113] was on a pure Si substrate, it seems reasonable to assign to the B-C bond the feature of an a-B/C:H structure.

Table 4.5: Binding energy under the the C_{1s} and B_{1s} lines of the B-C species obtained in the fitting and their differences. The averages are calculated excluding the values at the surface and at the boron/graphite interface that is highly oxygen-contaminated as it will be discussed below.

Sample #29				Sample #56			
Depth (nm)	C_{1s} (eV)	B_{1s} (eV)	Δ	Depth (nm)	C_{1s} (eV)	B_{1s} (eV)	Δ
0	284.8	188.4	96.4	0	284.6	187.8	96.8
3	284.7	188.2	96.4	1	284.7	188.1	96.6
7	284.7	188.5	96.2	3	284.7	188.2	96.4
10	284.6	188.6	96.0	10	284.5	188.5	96.0
20	284.7	188.6	96.0	30	284.7	188.2	96.4
30	284.6	188.9	95.7	67	284.8	188.2	96.6
70	284.7	192.6	92.0	100	284.7	188.3	96.4
110	284.8	192.1	92.7	140	284.6	188.4	96.2
150	284.6	189.4	95.2	180	284.6	188.4	96.2
				220	284.7	188.5	96.2
				260	284.7	188.4	96.3
				300	284.5	188.2	96.4
				340	284.6	188.5	96.1
				380	284.3	188.5	96.8
				420	284.4	188.7	96.6
				460	284.5	188.8	96.7
Average Δ:		96.2 ± 0.16		Average Δ:		96.4 ± 0.17	

4.4.2 Surface and near subsurface chemical states

a. HR-XPS peak shape and binding energy shifts

Fig. 4.27 presents the B_{1s}, C_{1s} and O_{1s} spectra of samples #29 (left panel) and #56 (right panel) obtained for the 'as received' surface before (dotted line) and after (continuous line) 10' of Ar^+ sputtering. Before sputtering, several chemical states can be identified. The C_{1s} spectrum is dominated by a peak at 284.7 eV with a high BE shoulder. In the B_{1s} case, the most intense peak is at 188.4 eV in addition to a high BE shoulder. The O_{1s} spectrum centered at 532.4 eV is broad and asymmetric suggesting more than one chemical state. Angle-resolved measurements showed that the intensity of the high BE shoulders in both B_{1s} and C_{1s} spectra decreased for higher collecting angles, while that of the low BE energy in the C_{1s} spectrum increased. These results indicate that the high BE peaks are related to surface contamination. Overall, the most prominent feature is the high BE shoulder on the high energy side in the C_{1s} and B_{1s} spectra. Theses shoulders are assigned to

oxide-related states. We conclude that the boron film in both samples do not consist of a homogeneous single phase since there are at least two non-equivalent carbon sites present in the B_{1s} and C_{1s} core lines .

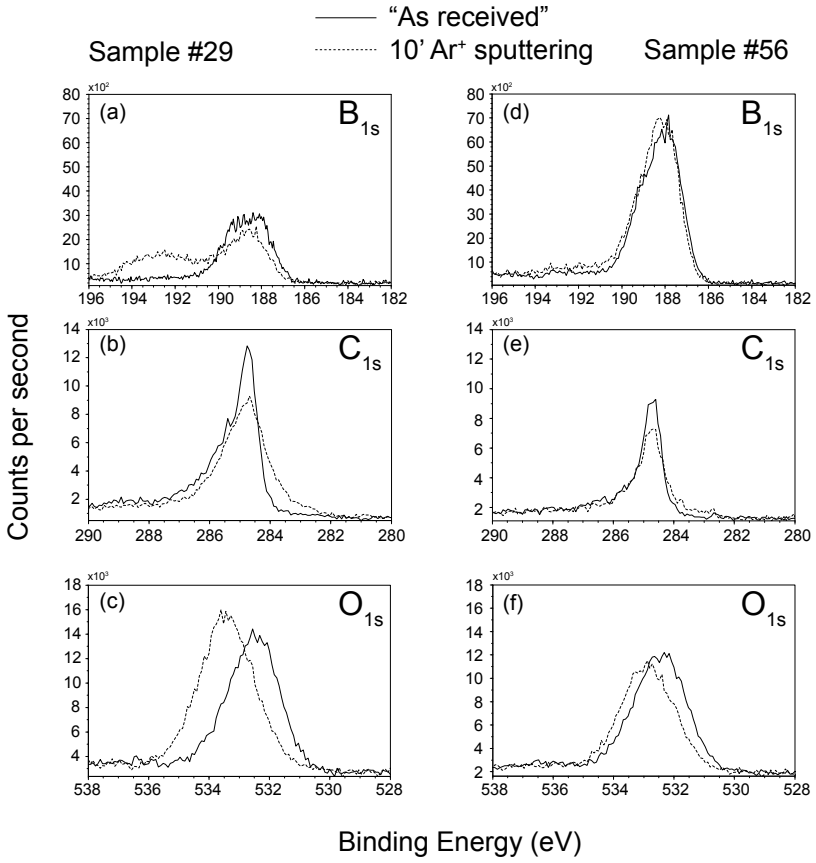

Figure 4.27: B_{1s}, C_{1s} and O_{1s} spectra of samples #29 (left panel) and #56 (right panel) for the 'as received' surface before (dotted line) and after (continuous line) 10' of Ar^+ sputtering.

In the case of sample #29 and particularly in sample #56, the surface (before sputtering) C_{1s} peak appears very narrow of about 0.7 eV at ~284.7 eV which indicates that only C-C bonds are present on the surface, very likely due to hydrocarbons adsorbed at the surface, the so called "adventitious carbon". In fact, after 10' of Ar^+ sputtering the line appears 0.5 eV wider very probably due to the uncovering of other chemical states that were buried by the adventitious carbon. In both sample cases, the B_{1s} surface core line appears with the same FWHM of ~2.1±0.2 eV exhibiting similar boron chemical states, however after sputtering, the peak shapes are very different with the advent of a wide boron-oxide high BE tail in the case of sample #29. The O_{1s} core line FWHM, before and after sputtering of the surface, is similar in both samples. However the peak shifts by ~1 eV

towards higher BE in the case of sample #29 and by only ~0.5 eV in the case of sample #56, in consistency with the changes observed in the B_{1s} line.

Overall, the analysis of the peaks shape and shifts shows a clear chemical difference among the two analyzed samples. The difference is more evidenced in the subsurface rather than in the surface where contamination by adventitious carbon may be hindering the underlining chemical states of boron.

b. HR-XPS peak deconvolution

With regard to the B_{1s} spectrum, as it has been established by many former investigations on boron carbide films [114–117] it is considered in this analysis that boron atoms are bound to each other and build up the network of boron films. In fact it has been reported that B–B bond as pure boron, B–C bond as boron carbide, B–C bond as boron hydroxide B–OH, and B–O bond as boron oxide were located at 188 eV, 189 eV , 189.5 eV and 190-193.5 eV, respectively. Separately in parallel investigations, Jacobsohn et al. [118] and Lyu et al. [119] finely divided B–O bond into BC_2O and $BCOC_2$ at 190.0 and 192.0 eV. They also observed B_2O_3 bond at 193.2 eV. In light of theses considerations, in this analysis, the B–O bond includes the existing states of BC_2O and BCO_2, and the B_{1s} spectra are deconvoluted into B-B bond (187.5 ± 0.2 eV), B–C bond (188.4 ± 0.2 eV), B–H bond (189.5 ± 0.2 eV), B–O bond (191.0-192.0 eV), and B_2O_3 bond (193.5 ± 0.2 eV), respectively.

Regarding the C_{1s} spectra, oxides occur at the highest binding energies (C–O at 286 eV; C=O at ⩾288 eV [120] and [121]), C–C graphitic bonds at 284.5-285 eV [82], [120] and [121], and B–C at ~283 eV [122], [123], [124] and [121]. While most works report a single B–C chemical state, some others report multiple B–C chemical environments [123], [125] and [126]. Cermignani et al. [125] suggested the presence of two different chemical environments in CVD deposited carbon films with low B contents (up to 15 at.%). They used XPS to probe the B_{1s} line and found that B–C bonds with C atoms in a graphitic state are at 188.5 eV while B–C bonds in a B_4C environment are at 187.5 eV [123]. Their conclusions are similar to those of Jimenez et al. [126] who identified two chemical environments in commercial polycrystalline boron carbide samples in the C_{1s} spectra, B–C bonds from C atoms in the C–B–C chains at 281.8 eV (sp^2 hybridization) and in the icosahedra at 283.7 eV (sp^3 hybridization). Based on these considerations, the deconvolution of the C_{1s} peak in the present analysis has been performed associating the BE at 287.6 ± 0.2 eV and 288.8 ± 0.2 eV to the species of –C=O bond (e.g., ketone, aldehyde) and O–C=O^- bond (e.g., carboxylic, ester) as it was widely documented in literature (these bonds are relatively easy to remove when CO_2 forms during the boron deposition process and/or adsorbed from air moisture). Moreover, four further chemical states, namely B–C–B bond, B–C bond, C–C bond and C–O bond located at 281.8 ± 0.2 eV, 283.5 ± 0.2 eV, 284.7 ± 0.2 eV and 285.8 ± 0.2 eV, respectively [127].

The O_{1s} spectra of boron films showed evidence of four chemical states at 531.5 ± 0.2 eV, 532.3 ± 0.2 eV, 533.2 ± 0.2 eV and 534.2 ± 0.2 eV, which can be assigned to C–O bond, O–O bond, B–O bond and B–OH bond [114], respectively. Deconvolution parameters of the experimental spectra are presented in tab. 4.6.

Table 4.6: Spectra deconvolution parameters (peak position, full width at half maximum and Gaussian weight to the peak simulation).

	B_{1s}				C_{1s}				O_{1s}		
	pos. (eV)	FWHM (eV)	Gauss (%)		pos. (eV)	FWHM (eV)	Gauss (%)		pos. (eV)	FWHM (eV)	Gauss (%)
B-B	187.5	1.2	70%	C–C, C–H	284.7	0.718	70%	C–O	531.5	1.2	70%
B-C	188.4	1.2	70%	C–OH, C–O–C	285.8	1.2	70%	O–O	532.3	1.2	70%
B-H	189.5	1.2	70%	C=O	287.6	1.2	70%	B–O	533.2	1.2	70%
B-O	191.3	1.2	70%	O–C=O	288.7	1.2	70%	B–OH	534.2	1.2	70%
O-B-O	192.6	1.2	70%	C–B^{sp3}	283.3	1.2	70%				
B_2O_3	193.5	1.2	70%	C–B^{sp2}	281.9	1.2	70%				

In fig. 4.28, the B_{1s}, C_{1s} and O_{1s} spectra of the surface and after 3 nm of Ar^+ sputtering for samples #29 (top a, b, and c panels) and #56 (bottom d, e and f panels) are shown respectively along with the core line deconvolution using the previously commented chemical bonds.

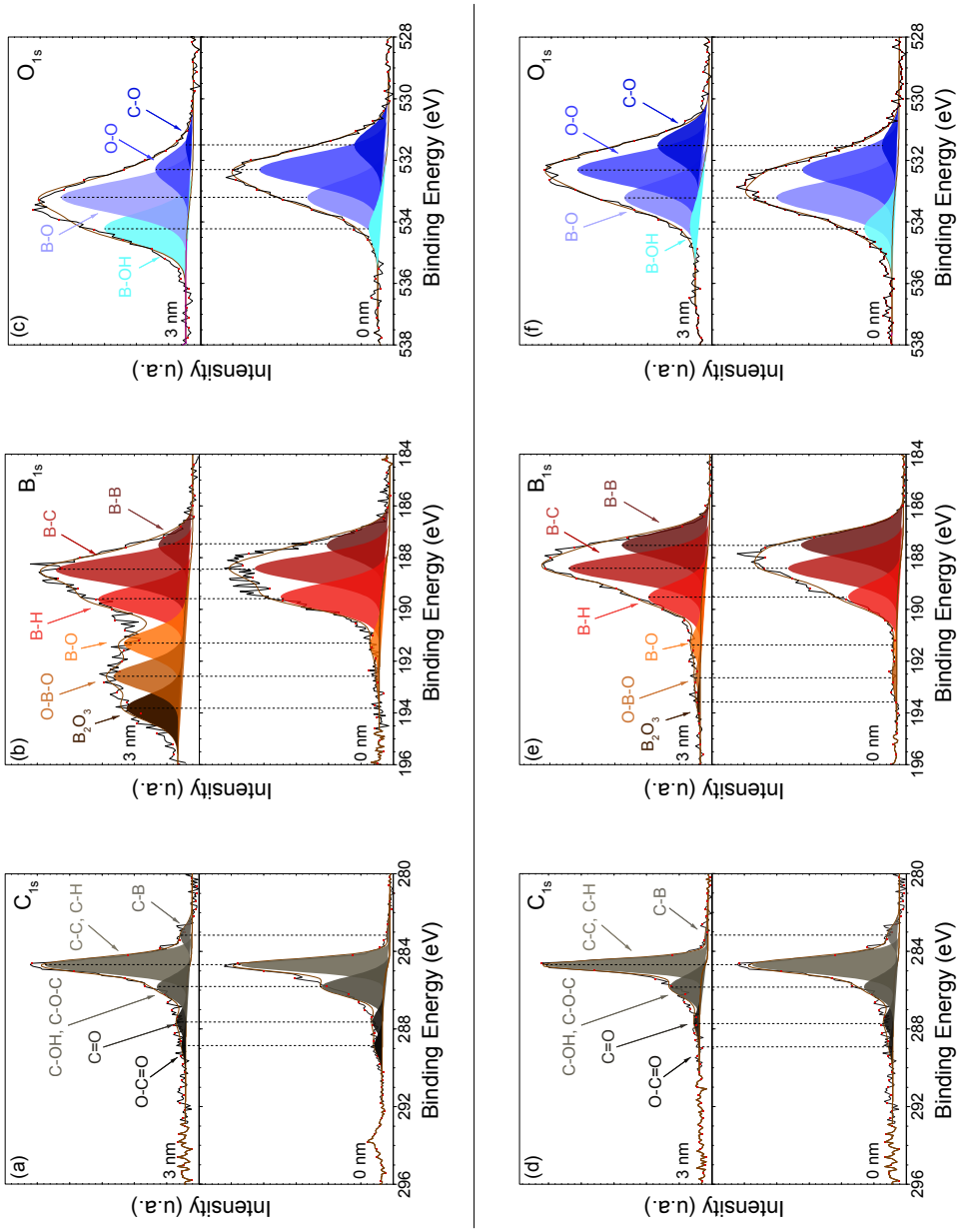

Figure 4.28: B_{1s}, C_{1s} and O_{1s} spectra of the surface and after 3 nm of Ar^+ sputtering for samples #29 (top a, b, and c panels) and #56 (bottom d, e and f panels) and the core line deconvolution.

The surface chemistry of the two samples shows a noticeable difference in

all three core lines in terms of boron interactions with oxygen and hydrogen. According to the B_{1s} spectra of sample #56 that was exposed to the highest glow discharge plasma power, the B–C and B–B bonds are the predominant existing state of boron with high B–B bonds while in the case of sample #29 a prominent B–H bond is observed with weaker B–B bonds deconvoluted peak. The latter is consistent with the C_{1s} line where the surface C–B bonds are at noise level. According to the deconvoluted results of O_{1s} spectra, in the case of sample #29 about half of the oxygen exists as O–O bond (i.e. free oxygen) while in the case of sample #56 the dominant B–B surface bonds observed in the B_{1s} spectra correlate to a predominant B–O and B–OH bonds. According to the deconvoluted results of the surface C_{1s} line, in both samples a prominent 0.7 eV peak corresponding to the C–C bond is dominant in the deconvolution. The latter is very likely due to an adventitious hydrocarbon layer adsorbed on the surface. In fact, after Ar^+ sputtering of only as little as 3 nm below the surface the same deconvoluted peak is 0.5 eV wider exhibiting more complex chemical states. In correlation with the higher overall boron concentration in sample #56 compared to sample #29, the C_{1s} line shows a noticeable C–B bonds fraction and an almost noise level respectively in sample #29 and #56.

With regard to the chemical states after Ar^+ sputtering 3 nm below the surface, the most prominent feature is observed in the B_{1s} core line. A prominent boron oxide tail appears in the case of sample #29, while in sample #56 very tiny oxide boron components are deconvoluted. B–O, O–B–O and B_2O_3 bonds 1 eV equally separated are the most dominant. Similarly in the O_{1s} core line, more than half of the oxygen exists as B–O and B–OH bonds in consistency with the deconvoluted peaks of the B_{1s} line.

In a summary, the surface analysis of the boron chemical states among the two different boronizations has shown a higher surface oxygen and hydrogen contamination in the case of the 100 W boronization mainly in the form of O–O and B–H bonds. A layer of adventitious hydrocarbon adsorbed on the top has been revealed in both cases. The contamination of the boron layer is more pronounced after 3 nm Ar^+ sputtering below the surface. The hydrogen content bounded with boron is more noticeable in the case of the 100 W boronization as it can be seen in fig. 4.28 (b). A reasonable explanation could be the fraction of B-H radicals in the working gas during the boronization. A strong glow discharge plasma power may induce higher cracking of the diborane molecules into B atoms that impinge into the surface while a low glow discharge plasma power may only induce cracking of a smaller fraction of diborane leading to hydrogenated boron atoms impinging the graphite surface and leading to a higher hydrogen content in the boron coating the surface.

4.4.3 Bulk chemical states analysis

a. General characterization

The in-depth chemical states of boron bounded with oxygen, hydrogen and the carbon substrate is further analyzed in details performing Ar^+ sputtering until reaching the graphite/boron interface. In fig. 4.29 and 4.30, respectively, the B_{1s}, C_{1s} and O_{1s} spectra of samples #29 and #56 are shown at different sputtering depth along with the core line deconvolution similarly performed as in the previous section.

Sample #56 exposed during a high 535 W glow discharge plasma power boronization is characterized with a thicker boron content of about 450 nm, as already discussed earlier. Therefore the spectra of this sample are shown at different in-depth stages compared to sample #29. The analysis of the spectra of the two samples has shown a clear difference in terms of boron bonds and the carbon substrate. While in sample #29, according to the C_{1s} spectra, the C–B^{sp3} bond slightly exceeds 1/4 of the the C–C bond at halfway of sputtering the entire boron film, in sample #56 it exceeds 3/4. This feature implies that the boron atoms in the latter are not only highly intercalated into the graphite matrix but also strongly bounded to the carbon atoms. The latter conclusion is further demonstrated by the presence of C–B^{sp2} bonds in sample #56 while in in sample #29, it is nearly absent. The carbon chemical states with regard to oxygen are mainly present in the form of C–OH and C–O–C bonds, with a constant peak area along the entire depth profile in both samples. Terminal oxygen bonds in the form of C=O and O–C=O are nearly at noise level. Consequently, since oxygen bonds abundance along the profile of the samples do not change, the difference in oxygen concentration previously discussed in fig. 4.22 is only due to oxygen atoms that are bound to boron atoms rather than carbon atoms.

According to the B_{1s} spectra, the previously depicted near subsurface high 40% oxidation in sample #29 increases to up to 60% at halfway depth and 50% at the boron/graphite interface while in the case of sample #56 is boron oxidation ranges between 7% and 15% only between 3 nm below the surface and the graphite interface. The bulk boron content in the former sample can be considered nearly oxygen-saturated which is a detrimental feature for the boronization purposes.

According to the O_{1s} spectra, the average fraction of O–O bonds along the depth profile of sample #29 is ~ 25% while it reaches ~ 36% in the case of sample #56. Therefore, a greater unbounded free oxygen chemical state can be reasonably considered as a footprint of purer boron content in the case the boronization performed at 535 W glow discharge plasma power. This feature will be further investigated in a detailed analysis of the depth profile of the boron-oxygen and boron-hydrogen bonds in what follows.

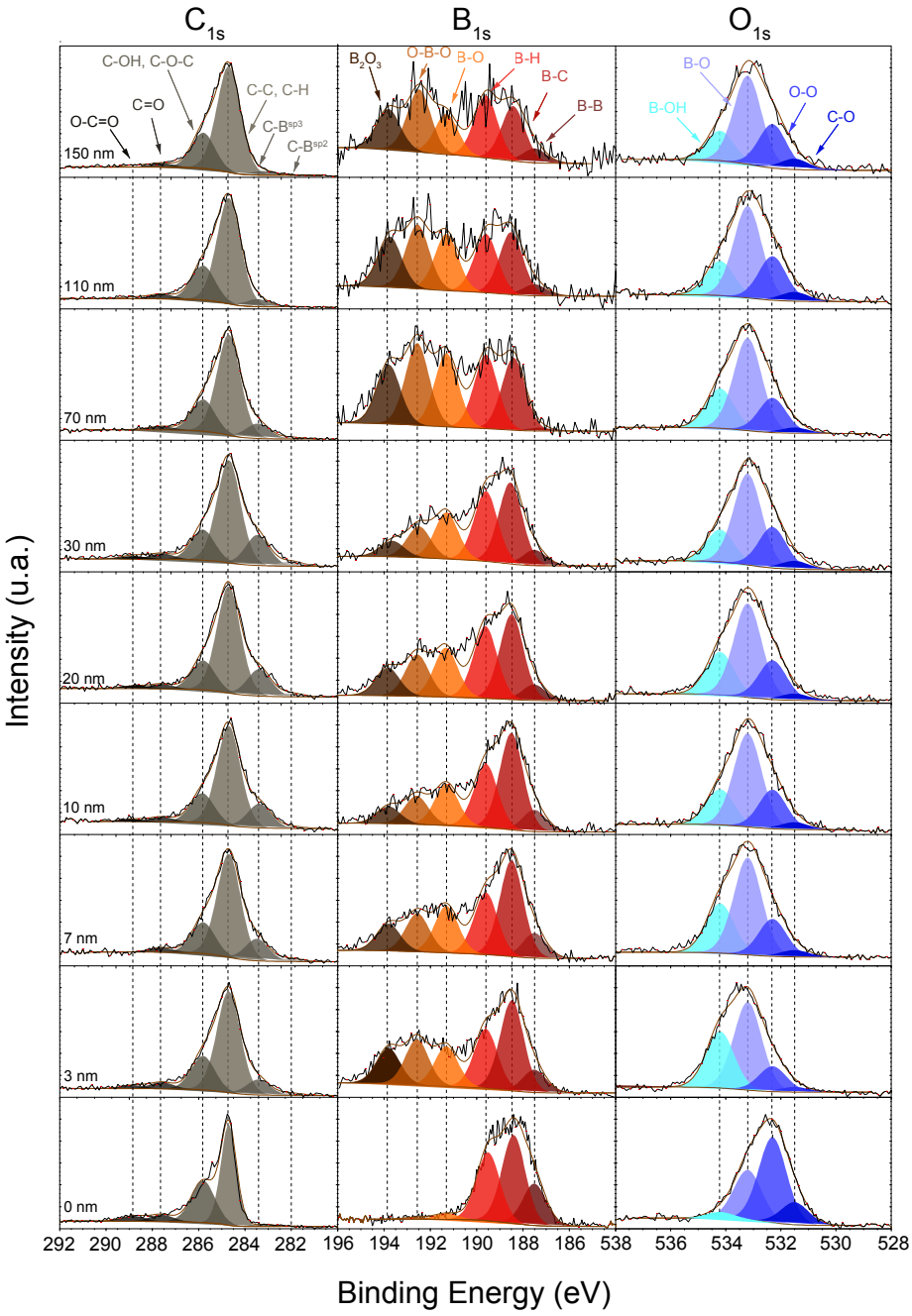

Figure 4.29: B_{1s}, C_{1s} and O_{1s} spectra of the in-depth boron content with a stepwise Ar^+ sputtering of sample #29 (100 W boronization) along with the core line deconvolution.

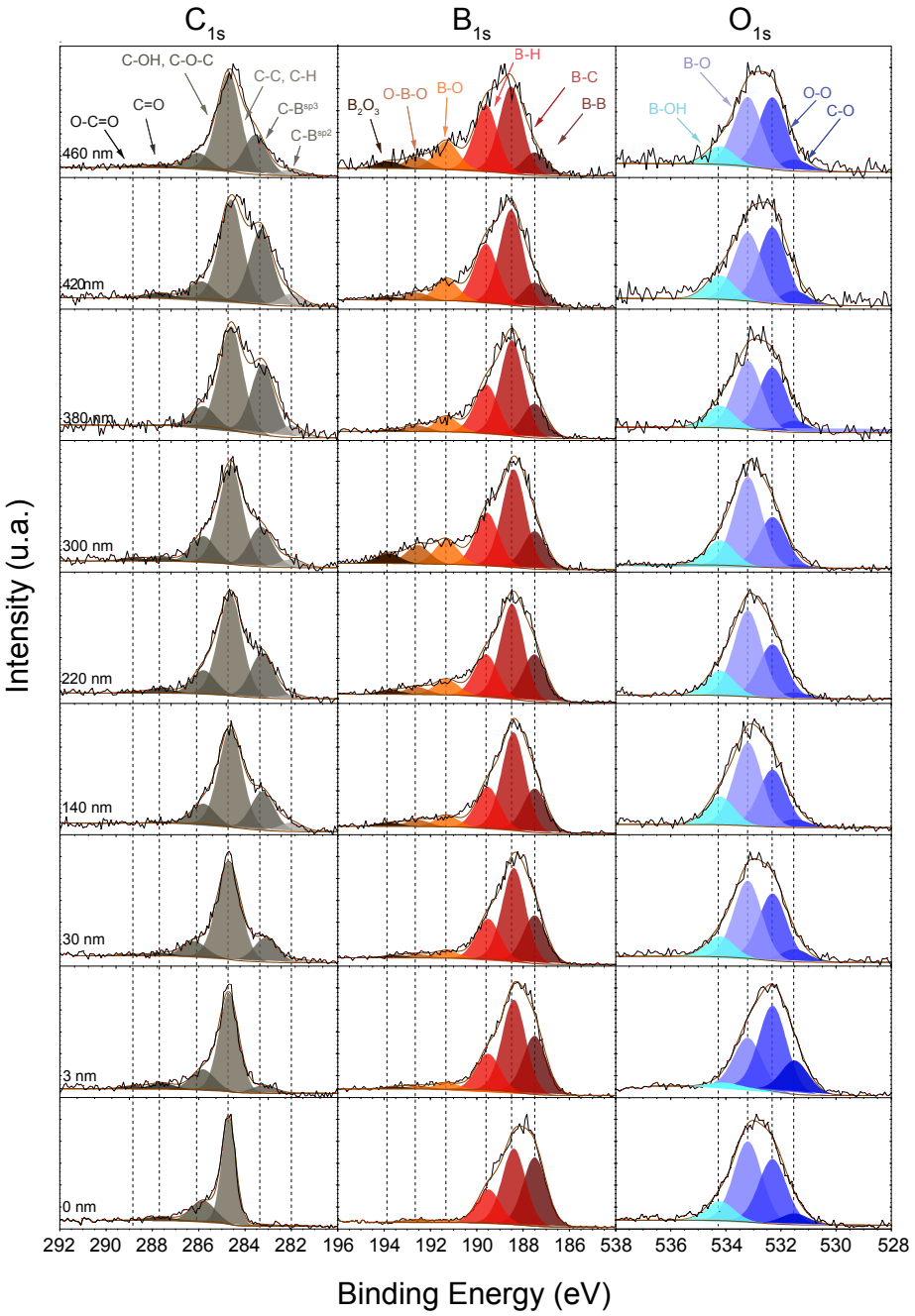

Figure 4.30: B_{1s}, C_{1s} and O_{1s} spectra of the in-depth boron content with a stepwise Ar^+ sputtering of sample #56 (535 W boronization) along with the core line deconvolution.

b. Fine analysis of boron- oxygen/hydrogen in-depth chemical states

The fractions of the previously introduced chemical states of boron, carbon and oxygen throughout the depth profile of the deposited film on samples #29 and #56 have been computed from the deconvoluted sub-peaks. In fig 4.31 the depth profiles of the chemical interactions estimated from the the B_{1s}, C_{1s} and O_{1s} spectra are shown.

B_{1s} core line fine analysis The results for the sample #29 exposed at low 100 W borononization glow plasma power show a widely oxygen and hydrogen contaminated profile. The latter can be particularly seen in the B_{1s} where boron contamination with hydrogen and oxygen exceeds 80% in the bulk. A prominent excess in contamination is observed at the boron/graphite interface with a remarkable increase of the B–H and O–B–O bonds. As already commented earlier, this is most likely due to the highly reactive primary boron deposited atoms on a highly oxygen- and hydrogen-contaminated graphite surface. The analysis of the same core line in sample sample #56 exposed at high 535 W borononization glow plasma power shows a relatively low oxygen contamination: nearly at noise level at the surface, an average of about 7% in the first 70 nm below the surface and about 15% in the subsequent 350 nm. Oxygen contamination at the graphite interface reaches 21% globally among which 12% account for B–O bonds only. With regard to the hydrogen contamination in terms of B–H bonds, the values range between 20% in the first 300 nm below the surface and linearly increases in the following 160 nm until it reaches 30% at the graphite substrate interface. The latter linear increase of the B–H fraction can be reasonably attributed to hydrogen uptake from the hydrogen release/adsorption from the graphite substrate while the constant trend in the first sputtered 300 nm can be due to hydrogen co-deposition from the working diborane gas. The maximum hydrogen uptake that can be estimated from the B–H fraction throughout the film depth profile is ~30% in both samples. This maximum value is measured at the surface of sample #29 while in the case of sample #56 it is estimated to 18%. Therefore, the boronization performed at high 535 W glow discharge plasma power presents not only the benefit of a boron film poorly oxygen-contaminated throughout the boron film thickness and nearly oxygen-free at the surface but also a boron surface that has the capability of further up-taking hydrogen.

C_{1s} core line fine analysis The analysis of the fine chemical states in the C_{1s} core line confirms and further validate the previously discussed surface and bulk contamination of the deposited film. In fact, the analysis of the two samples show a similar C–C fraction throughout the sputtered depths of about 60%, however the most prominent contamination with oxygen and hydrogen measured in terms of C–OH, C=O and O–C=O bonds is observed

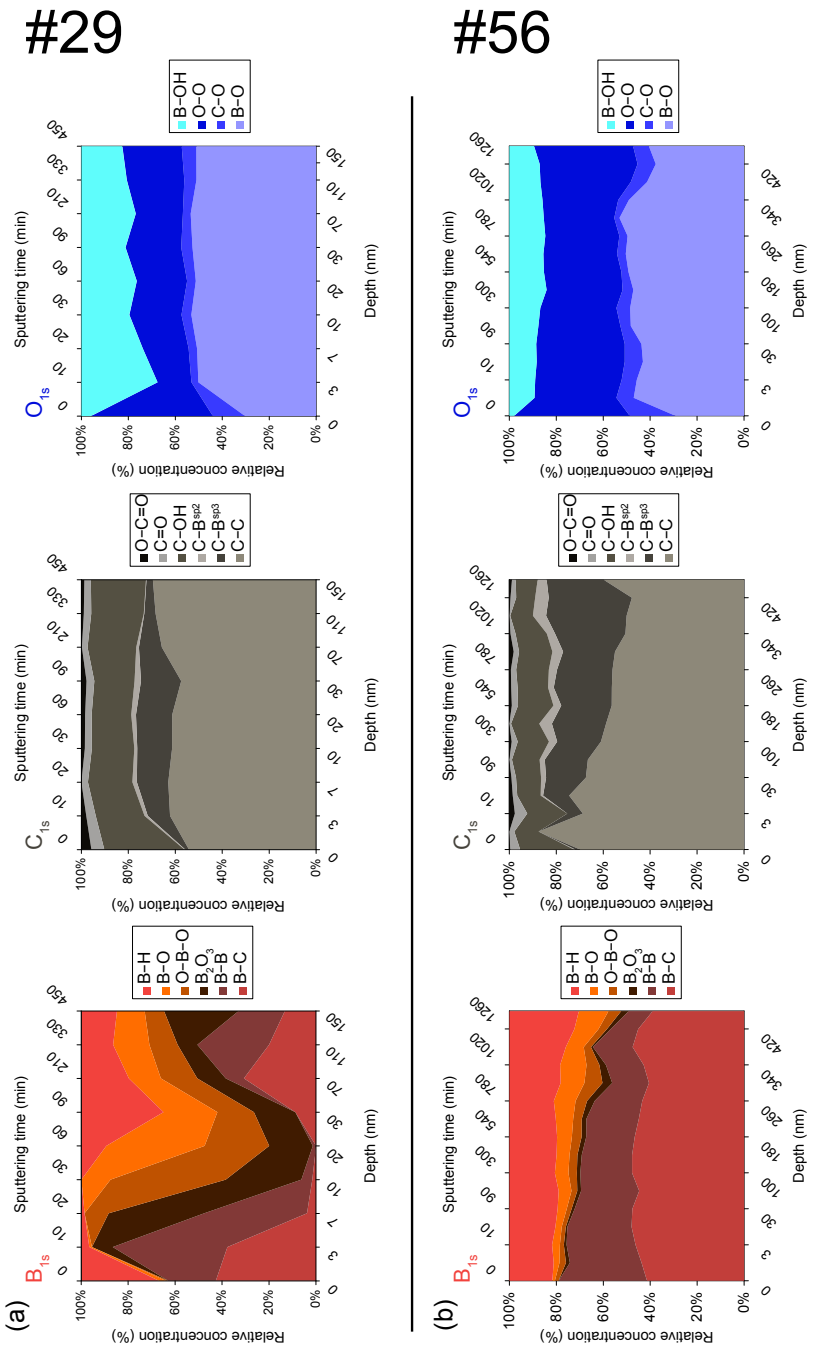

Figure 4.31: Depth profiles of the chemical states of boron and contaminant impurities obtained from the deconvolution of the B_{1s}, C_{1s} and O_{1s} core lines for sample #29 (top panel) and sample #56 (bottom panel). The order order of the bonds trends is arbitrary.

in sample #29 reaching ~44% at the surface and ranging between 21% and 27% in the bulk. While in sample #56 the overall contamination in the bulk is ~15% while at the surface it only ~27%. The relative variations in the fractions of the surface chemical states observed in C_{1s} core line is comparable to the high roughness of the graphite surface. With regard to the boron bonds with carbon that can be further refined in the analysis of this core line, in average the combination of the fractions of the C–B^{sp3} and C–B^{sp2} exceeds by a factor of 2 in the case of sample #56 in contract with sample #29. Remarkably, on the surface of both samples, these bonds that are relative to the boron content extinguish. Moreover and as a final note regarding the C_{1s} core line fine analysis, the further examination of the boron film in the case of sample #56 shows a correlation among the C–B bonds fraction trend, either as C–B^{sp3} or as C–B^{sp2} form, and the B-B bonds in the B_{1s} core line as it is shown in fig. 4.32. This result can be reasonably interpreted as the result of the trend of boron atoms to preferably bound with other boron atoms as the boronization progresses with an epitaxial growth of the boron film. This feature is only observed in the case of sample #56 and can be therefore attribute to the difference in terms of glow discharge plasma power

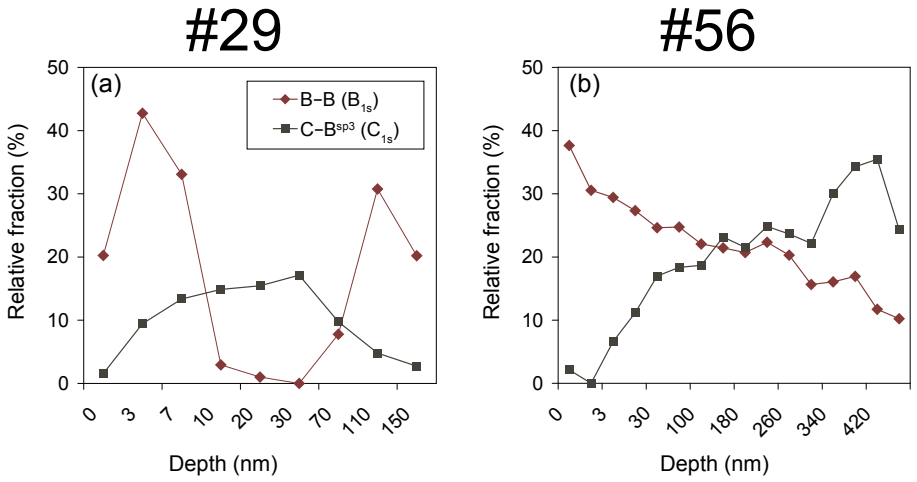

Figure 4.32: Depth profiles the C–B^{sp3} and B–B bonds relative fraction in the C_{1s} and B_{1s} core line respectively for sample #29 (a) and sample #56 (b).

O_{1s} core line fine analysis The most prominent feature that can be gained from the fine analysis of the O_{1s} core line concerns the fraction of free oxygen, carbon-bounded and boron-bounded oxygen in the bulk and the surface of the two samples in terms of O–O, C–O and B–O bonds. In sample #56 the fraction of O–O bonds is about 1.5× more than what was measured in sample #29, while comparable and constant C–O bonds fraction of about 7% has been measured. The fraction of O–O bonds can be accounted for the degree

of oxidation of the boron film with a lower value assigned to a high degree of oxidation. In these terms, the boron film analyzed in the case of sample #29 is highly oxidized in the bulk and a 2× lower oxidation can be seen on the surface. The degree of oxidation of the boron atoms on the surface is similar in both samples. In fig. 4.33 the fraction of the B–O bonds is plotted as a function of the fraction of the O–O bonds. As it can be seen, in the case of sample #29 (fig. 4.33 (a)) the increase of the O–O bonds fraction throughout the film thickness is correlated to no changes in the fraction of B–O bonds, except at the surface of the sample. Therefore, all the boron content in the film can be considered oxygen-saturated. In contrast in sample #56 (fig. 4.33 (b)), the fraction of B–O bonds decreases with increasing the O–O bonds fraction which implies that, although a large number of boron atoms (localized in the bulk of the film) are highly oxidized, the 10-200 nm subsurface is rich in oxygen-free boron content. The latter is consistent with the previous discussion regarding the increase of oxygen content at the graphite interface due to the higher contamination of the graphite surface at the beginning of the boronization, progressively decreasing in the course of the boronization glow discharge.

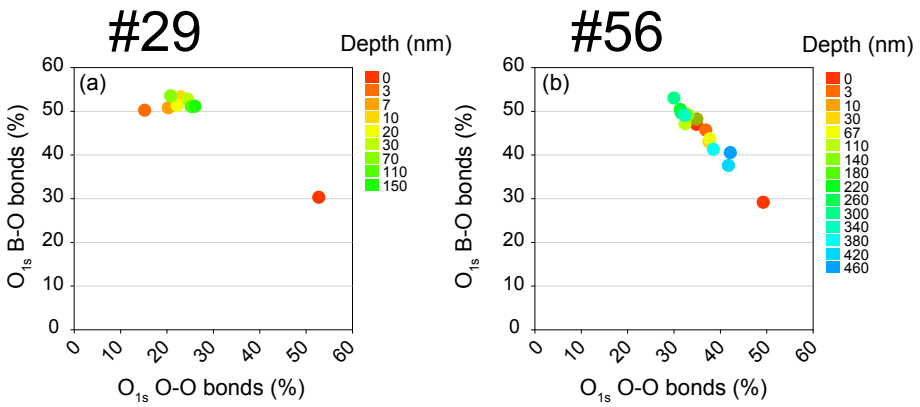

Figure 4.33: The B–O bonds fraction in the O_{1s} core line (measure of the boron content in the deposited film) as a function of the O–O bonds fraction (inverse measure of the degree of oxidation of boron) in sample #29 (a) and sample #56 (b).

4.5 Conclusions

In this chapter, a physical and chemical analysis of boron wall conditioning has been performed. In RFX-mod, several unfavorable aspects of boron deposition have been observed and needed to be addressed in order to gain further benefits of boron wall conditioning. The features that have been tackled in this chapter are: (i) the spatial uniformity of boron deposition; (ii) the correlation among the boron wall conditioning duration

and the final boron content deposited on the first wall; (iii) the oxygen and hydrogen gettering efficiency of boron. The latter has been investigated by looking at the surface and bulk chemical states of boron related to hydrogen, carbon and oxygen.

To address these issues, graphite samples have been exposed to a number of boronizations and *ex-situ* post-mortem analyses by means of high resolution surface analysis techniques were carried out. The boronizations were performed at different experimental conditions in terms of glow discharge parameters (current, voltage and pressure), duration and wall temperature in order to explore a wide range of parameters that directly affect boron deposition and boron interaction with the machine main impurities that are oxygen and carbon. On the one hand, the physical analysis has been carried out by means of SIMS to obtain the broad elemental in-depth composition of the deposited content, XPS to obtain high sensitivity measurements of the surface and near subsurface elemental composition, SEM to characterize the surface morphology and EDS/X and RBS to probe the bulk physical properties. On the other hand, in order to interrogate the fine chemical structure of the boron deposition and the interactions of boron atoms with oxygen, carbon and hydrogen, a chemical analysis has been performed by means of High Resolution X-ray Photoelectron Spectroscopy (HR-XPS).

A strong toroidal asymmetry of boron deposition has been found, in agreement with the characterization of the glow discharge operational regimes performed in Chapter 3. The study of the effect of the wall temperature has shown that the total boron content is doubled for a heated wall compared to a room temperature boronization, depicting an enhanced boron affinity with hot wall surfaces. Although, boronizations in RFX-mod performed at ambient machine vessel wall temperature are relatively simple and cheaper, the latter result shows that boronizations performed while baking the vessel are more profitable in terms of the final boron content on the first wall. The study of the effect of plasma discharges post boron deposition has shown that 25s of effective plasma operation induced a dramatic variation of the boron content. Erosion and redeposition in a location close to the glow discharge anode resulted lower than in a distant location, illustrating the toroidal variation in plasma-wall interaction. In addition to the spatial assymetry in boron deposition, a global inconsistency was found among the boronization duration and the boron thickness measured by SIMS. In order to study the effect of the glow discharge parameters on the final boron content deposited on the wall, the boron deposition rate computed from the SIMS measurements has been correlated to the glow discharge voltage, current and pressure. A clear correlation among the deposition rate and the glow discharge I×V (plasma power) was found and further confirmed by gas exhaust analysis. Boronizations performed at a low glow plasma power $\leqslant$ 200 W have shown ~7× lower

boron deposition rate compared to boronizations performed at a higher plasma power. The latter result has been found consistent with earlier studies on the behavior of boron deposition with increasing plasma power. It was found that the boron growth reaction order (n) makes a transition from 1/2 to 1 at 900 W with an increase of the plasma power, accompanied by a corresponding morphological transition [37–40].

The latter result that explains therefore the inconsistency of boron deposition observed in RFX-mod has been further examined qualitatively and quantitatively by SEM, EDS/X, RBS and XPS. The analyses were focused on two boronizations of the same duration but performed at different glow plasma power, about 100 W (named type-I) in the first case and 535 W in the second case (named type-II). Compared to type-I, a SEM image of a boronized sample obtained in the case of the type-II boronization has shown a more compact surface with an apparent boron coverage characterized by the presence of well-faceted crystallites of several μm above the graphite surface. SEM characterization confirmed therefore the presence of a surface morphology transition in boron deposition with increasing plasma power, similarly to what has been documented by Komatsu et al. in [37–40]. RBS and EDS/X measurements have shown respectively a 5× and 2× higher boron content, and a lower oxygen/boron ratio in the type-II case (both results are consistent taking into account the probed depth and volume of the two techniques). Similar results were found with quantitative HR-XPS measurements. Therefore, RBS and EDS/X have shown that boronizations peformed under high plasma power, a thick, oxygen-free (< 3%) and boron-rich film is deposited on the graphite substrate, while HR-XPS has shown that in addition, the very first thin 10 nm of the boron film that will be in contact with the power plasmas has a 2× richer boron content for the same oxygen content compared to boronizations performed at low plasma power.

With regard to the chemical analysis of the boron-graphite complex, the HR-XPS measurement were made on the two types of coatings previously analyzed. It was found that in both cases the deposited boron layer could be identified as amorphous hydrogenated boron carbide, similarly to other investigations found in literature [110, 113]. The HR-XPS analysis of the surface boron layer in the two types of boron coatings has shown non-Gaussian B_{1s}, C_{1s} and O_{1s} peak shapes which indicated that he boron film in both samples do not consist of a homogeneous single phase. Overall, the analysis of the peaks shape and shifts shows a clear chemical difference among the two analyzed samples. The difference was more evidenced in the subsurface rather than in the surface where contamination by adventitious carbon could be hindering the underlining chemical states of boron. The fine HR-XPS analysis of both coatings types has shown the presence of B–B, B–C, B–H, B–O, O–B–O and B_2O_3 types of boron related bonds, while other bonds related to oxygen an carbon core spectra were found. The surface analysis of the boron

chemical states among the two different boronizations has shown a slightly higher surface oxygen and hydrogen contamination in the case of the 100 W boronization mainly in the form of O–O and B–H bonds. The contamination of the boron layer is more clearly seen after 3 nm Ar^+ sputtering below the surface. The hydrogen content bounded with boron resulted more noticeable in the case of the 100 W boronization. The latter result has been attributed to the lower cracking of the diborane in the case of the low plasma power which could induce hydorgenated boron to be directly deposited rather than atomic boron. The fine chemical analysis of the sample bulk has also shown that in the case of the type-I boronization a high oxygen and hydrogen contamination of the boron film. While the type-II boronization presented not only the benefit of a boron film poorly oxygen-contaminated throughout the boron film thickness and nearly oxygen-free at the surface but also a boron surface that has the capability of further up-taking of hydrogen. Moreover, in the case of the type-II boronization ,an epitaxial-like growth of boron has been observed, in consistency with the surface morphology characterization. The latter was deduced from the comparison of the C–B bonds fraction trend, either as C–B^{sp3} or as C–B^{sp2} form, and the B-B bonds in the B_{1s} core line. At last, the comparison of the O–O bonds and B–O bonds in the O_{1s} spectra has shown that in the case of the type-I boronization, the boron film is entirely oxygen-saturated. A feature that is detrimental to the boronization purposes.

Chapter 5

Lithium wall conditioning: a physical and chemical analysis

5.1 Introduction

Lithium is the least dense and least heavy of all solid elements (~0.53 g/cm^3). It is also the lightest metal (mass number of ~7), and like all alkali metals, lithium is highly chemically reactive and flammable. Lithium has a relatively low melting temperature of 180.54 °C. Interestingly, this readily melting light alkali metal has shown incredible beneficial effects when applied as a thin coating film on the first wall of many fusion devices worldwide. In fact, wall conditioning by the application of a lithium layer has shown great results in terms of plasma performance improvements experimented in several devices, both equipped with metallic (FTU [128], TJ-II [129]) and carbon (NSTX [130], EAST [131]) first walls. In these devices, in addition to a significant decrease in impurities and gas recycling, an enhanced energy and particle confinement time has been reported as an effect of lithiumization, in some cases associated with a reduction in the L-H mode power threshold or with a better Edge Localized Mode (ELM) control [132, 133]. An extensive review of lithium wall conditioning can be found in ref. [134].

While lithium has been studied in tokamaks for over 2 decades, an understanding of its behavior, especially in a high temperature plasma environment is still at its infancy. RFX-mod is the first RFP device where lithiumization has been used for wall conditioning. Two different techniques have been tested: evaporation by a Liquid Lithium Limiter (LLL) [69] and Li non-cryogenic pellet injection (single or multiple). These techniques are presented and extensively documented in Section 2.3.4. Regardless of the used technique in RFX-mod, lithium conditioning is demonstrated to reduce wall recycling, improve density control and decrease impurity content. In spite of these positive results, there is not yet a significant impact on confinement, observed instead in other devices as an effect of the

pronounced change in the pedestal parameters [128, 129, 131, 132]. It is a known fact [135–138] that unlike depositing lithium films on a flat impermeable substrate, lithium promptly intercalates into graphite. Likewise, multi-scale micron and nanometer sample roughness increases the sample surface area resulting in further deviation from the nominal lithium dose that would be deposited on a perfectly flat surface [139]. Furthermore, on the microscopy level, the observed improvements in terms of fuel recycling have been intimately linked to a preferential interaction of lithium with given tokamak impurities, in particular oxygen, dramatically enhancing the uptake of hydrogenic species [140].

In this chapter, a physical and chemical analysis of the obtained lithiated graphite first wall with the different lithiumization techniques in RFX-mod is performed by *ex-situ* analysis of graphite samples exposed to lithium injection. At different toroidal location around RFX-mod torus, the deposition uniformity for each technique is assessed by means of Secondary Ion Mass Spectrometry (SIMS) and the results are compared to Li spectroscopic emission during subsequent plasma discharges. The high resolution surface analysis has been conducted by Auger Electron Spectroscopy (AES) and the chemical analysis by High Resolution X-ray Photoelectron Spectroscopy (HR-XPS) measurements. Both analyses are performed on sample exposed and unexposed to H and He plasma to asses the redistribution of the lithium content after plasma exposure and the effect of the plasma on the lithium-graphite chemistry. The chapter is organized as follows: in Section 5.2 a brief summary of the effect of lithium wall conditioning on plasma performances in RFX-mod is presented. The deposition uniformity, erosion and redeposition of lithium is addressed in Section 5.3. At last, in Section 5.4 the chemical analysis is presented and a correlation of the results to the improvements observed in RFX-mod is discussed.

5.2 Brief summary of Li wall conditioning benefits in RFX-mod

In RFX-mod, lithiumization has been for the first time experimented on a RFP fusion device. Two different techniques have been tested: Li non-cryogenic pellet injection, single [68] or multiple [141], and evaporation by a Lithium Capillary Porous System (LCPS) [65, 70]. Overall, lithium wall conditioning in RFX-mod resulted as good as boron wall conditioning and outperform it in some cases. In this section a summary of the main plasma performance improvements observed following lithium wall conditioning is given and compared to the performances obtained with boron wall conditioning. A detailed description of lithium injection techniques in RFX-mod can be found in Chapter 2, Section 2.3.4.

5.2.1 Li non-cryogenic pellet injection

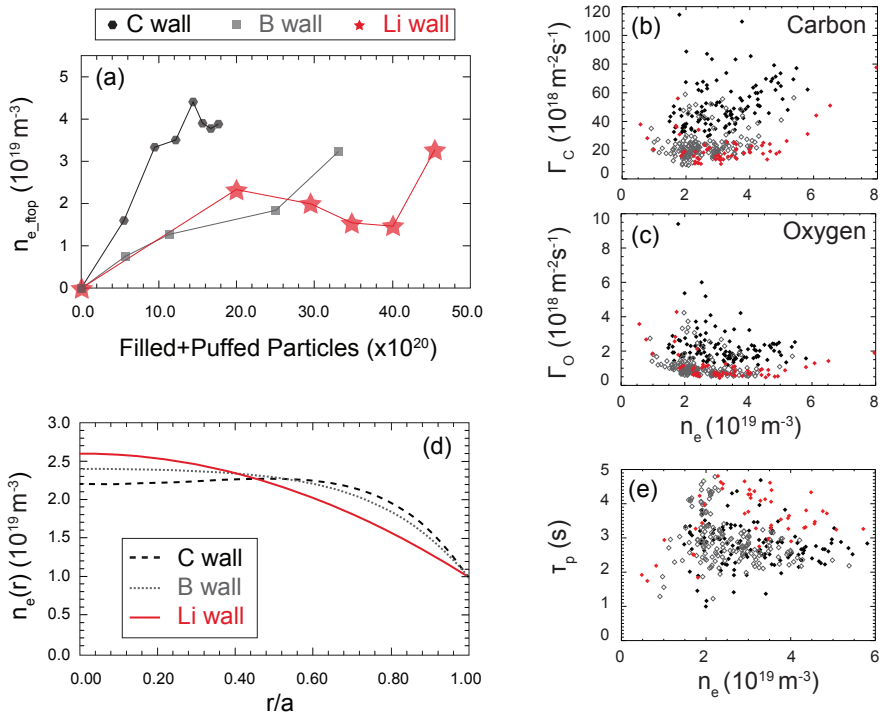

Figure 5.1: Comparison of plasma performances between a LPI lithium conditioned wall (red), a boron wall (grey) and a clean graphite wall (black) in terms of (a) gas adsorption capacity, (b and c) impurity reduction, (d) density peaking factor and (e) particle confinement time [68, 142].

Single pellet lithiumization in RFX-mod performed by the Lithium Pellet Injector (LPI) system [68] improves the gas adsorption capacity with respect

to a clean graphite wall (see fig. 5.1 (a)). The improved gas retention of a lithiated wall has allowed to achieve, for the first time in RFX-mod, a plasma current Ip $\geqslant$ 1.9 MA with an average electron density greater than $4{\times}10^{19}$ m^{-3}. Moreover, for comparable average densities, lithiumization was found slightly more effective in reducing the carbon content in the plasma than boronization, while similar performances in terms of oxygen screening were found. Furthermore, similarly to results found in tokamak devices where wall lithiumization has been tested, lithium wall conditioning in RFX-mod by single pellet injection has allowed to increase the density peaking factor and the particle confinement time (see fig. 5.1 (d) and (e)).

Multiple pellet lithiumization in RFX-mod performed by the Multi-Pellet Injector (MPI) system [141] confirmed most of the observations on plasma parameters already found with the LPI technique. In particular, lithium wall coating with MPI allowed a better density control than the carbon wall case, an impurity reduction similar to that previously observed in the case of the Lithium Pellet Injector (LPI) lithiumization and boronizations and a comparable effect has been seen in terms of particle and energy confinement.

5.2.2 Li evaporation by a Lithium Capillary Porous System (LCPS)

Li evaporation in RFX-mod has been implemented to reduce fuel recycling with the operative advantage of a better density control. In terms of lithium injection, the evaporation technique allows to deposit a much larger lithium quantity than the pellet injection method: the total amount of evaporated lithium by the LCPS during the experimental campaign was about 14 g which is significantly higher than the quantity injected by the single/multiple pellet injection technique (1 to 2 g globally). However, the deposition is made in a single toroidal section, and is therefore not uniform which resulted detrimental for this technique (this matter will be further investigated in the following section).

In terms of performance, a better control of the plasma density with a lower recycling has been observed as a macroscopic effect [60]. In addition, it is observed that when the wall is Li-conditioned, a higher feeding rate is necessary to sustain the plasma density. A reduction of fuel recycling has been therefore obtained at higher density values. Though reduced, the recycling with a lithiated wall remains close to 1 (see fig. 5.2 (a) and (d)). Concerning impurities, similarly to the pellet injection technique, lithium evaporation is equivalent to boronization for its effect on oxygen, while the reduction of carbon influxes is on the contrary more pronounced when the wall is Li-conditioned (fig. 5.2 (b)). As previously found with Li pellet conditioning [68], the edge density is lower and in some cases an effect on the edge temperature, that has a tendency to stay somewhat higher was observed (fig. 5.2 (c)). Reducing the recycling with a better density control has allowed to decrease the plasma density at high plasma current up to $n_e/n_G \simeq 0.5$, allowing to fill the Greenwald plot for RFX-mod data in the region of higher n_e, in particular

at high plasma current.

The detrimental effect of the toroidal asymmetry of lithium deposition has been particularly noticed with the evaporation technique. The latter was particularly seen with different behavior of hydrogen influxes at different locations with high variation in lithium deposition. The toroidal asymmetry obtained with the different lithumization techniques in RFX-mod is analyzed in the following section, while the chemistry of lithium with carbon and other in-vessel impurities is investigated and correlated to the amount of lithium effectively deposited.

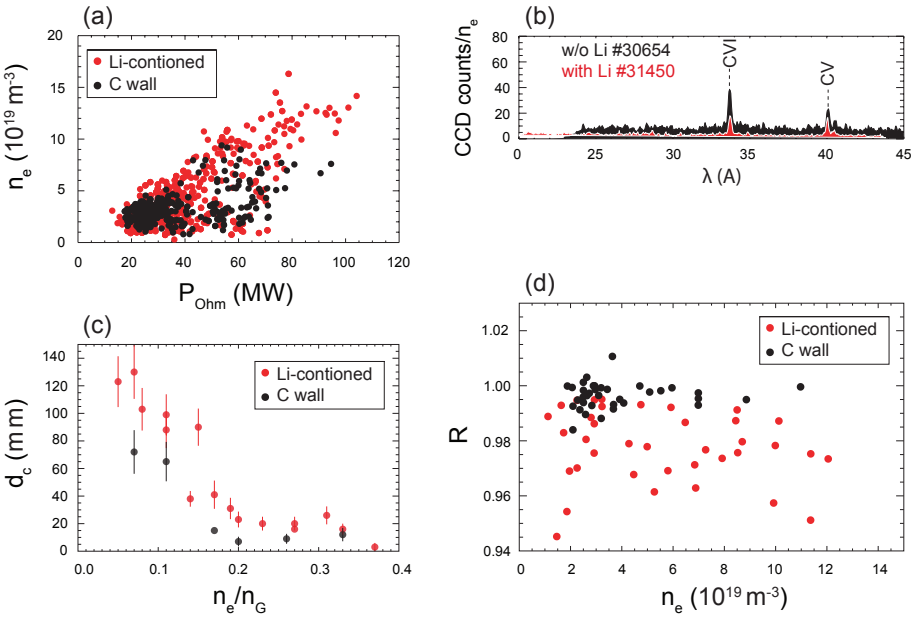

Figure 5.2: Comparison of plasma performances between lithium conditioned wall by Li-evaporation (red) and a clean graphite wall (black) in terms of (a) average density as a function of applied ohmic power, (b) carbon impurity screening, (c) edge density and (d) changes in recycling factor [60].

5.3 Lithium spatial deposition, erosion and redeposition

In RFX-mod it is experimentally observed that, if the wall is only partially covered during lithium wall conditioning, a large H saturated wall region contributes to the fueling and carbon redeposition promptly occurs. The effect is two-fold: first, the average recycling is not reduced as it would be with a fully lithium-coated wall and second, time-consuming cleaning procedures must be performed before the next Li deposition. In this section, first the spatial coverage and depth distribution of lithium upon lithium wall conditioning in RFX-mod is studied for each lithiumization technique. The latter is carried out by post-mortem SIMS spectrometry on exposed graphite samples at three different toroidal locations and by spectroscopic measurements in discharges immediately after the lithiumization sessions. Second, the erosion and redeposition of lithium is estimated by a set of graphite samples exposed at different stages of a lithiumization performed by pellet injection and to subsequent hydrogen and helium plasma discharges. The aim of this section is to provide answers to the following questions:

(i) Which lithium wall conditioning techniques in RFX-mod allows the least toroidal asymmetry of lithium deposition: pellet injection during plasma discharges or lithium evaporation prior to power plasma operation?
(ii) Taking into account the known intercalation phenomena of lithium into the graphite matrix [135–138], which technique allows a more surface confined lithium content?
(iii) At which extent, erosion and redeposition of plasma facing materials hinder the effect of lithium wall coating?

5.3.1 Experimental setup

Lithiumizations in RFX-mod have been performed by two different techniques and four different methods. The difference in techniques consists in the principle used for providing lithium to the first wall while the methods differ in the used system. The first technique consists in injecting lithium during plasma discharges by pellet injection or by a Lithium Capillary Porous System (LCPS) operated as a Liquid Lithium Limiter (LLL). Pellet injection is performed either by injecting relatively large (⌀=1.5 mm, l=4.5 mm) lithium pellets using a Lithium Pellet Injector (LPI) or through smaller (⌀=1.0 mm) diameter lithium granules using a Multi-Pellet Injector (MPI). The second technique consists in evaporating lithium in vacuum conditions before plasma operation and it is achieved using the same Lithium Capillary Porous System (LCPS) in a different experimental configuration. In earlier lithiumization stages in RFX-mod the LCPS has been used as a Liquid Lithium Limiter (LLL)

before a failure in the system rendered its use possible only as an evaporator. More details about the experimental setups can be found in Chapter 2 and in ref. [68, 70, 141]. In fig. 5.3 a schematic of RFX-mod vessel and the lithiumization wall conditioning system is shown as well as the position where graphite samples were exposed to undergo subsequent post-mortem analysis.

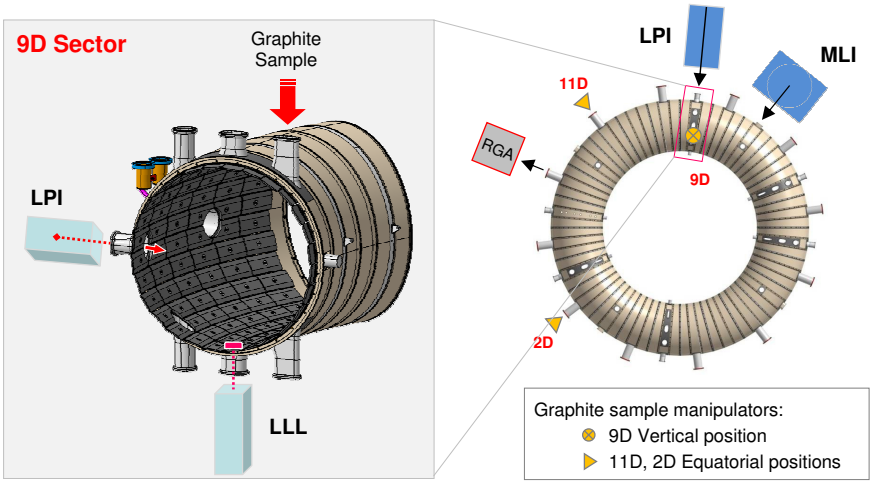

Figure 5.3: Schematic view of RFX-mod torus, LPI, LLL and MPI lithiumization systems (not to scale) and the graphite samples positions selected for post mortem surface analysis.

In RFX-mod and more generally in RFPs, the edge magnetic field is nearly poloidal (see fig. 1.2, ref. [143] and references therein), so the plasma interacts with a toroidal injection system, such as the LCPS, with a small toroidal angle. Lithiumizations with the LCPS device operated as a limiter in RFX-mod have been performed with the premise that a toroidally uniform lithium distribution will not be guaranteed. Whereas, lithiumizations by means of pellet injection are expected to provide a more uniform toroidal deposition as a deep penetration into the plasma is favorable to the transport of lithium and its deposition far along the field lines due to a stronger toroidal magnetic field component compared to the plasma edge. This matter will be further investigated and verified in the following analysis.

In tab. 5.1 the set of graphite samples exposed for post-mortem analysis is shown as well as the total amount of lithium injected by each lithiumization method and the characteristics of the subsequent plasma discharges. To distinguish between lithiumizations performed by the LCPS, when the apparatus has been used as limiter, it will be referred to as 'LLL' while lithiumizations performed with the LCPS as an evaporator will be referred to as 'EVAp'. The surface analyses were performed by XPS to

evaluate the surface lithium abundance and by SIMS to probe the samples depth composition. Visible spectroscopy of the LiI emission line was recorded for the study of the lithium deposition uniformity.

Table 5.1: Selected graphite samples, applied lithiumization technique, total amount of injected lithium and nature of the used gas for plasma.

Analysis technique	Li injection technique	Sample ID			Total injected lithium		Plasma discharge
		9D	2D	11D	Pellets	Weight (g)	
SIMS	LPI	15	7		57	0.23	He
	MPI	55	18		-	2.3	He/H_2
	MPI	51/52			-	2.3	H_2
	LLL	23			-	1.0	He
	EVAp	45			-	1.0	He/H_2
	EVAp	43		15	-	14.0	He/H_2
XPS	LPI	14			49	0.19	He
HR-XPS	LPI	15			57	0.23	He/H_2
	LPI	16			8	0.03	H_2
	MPI	54			-	0.09	He
	LLL	23			-	1.0	He
	EVAp	43			-	14.0	He/H_2
	EVAp	45			-	1.0	no plasma
	EVAp	47			-	1.0	He/H_2

5.3.2 Surface lithium abundance

The elemental composition of lithiated graphite sample obtained from the different lithiumizations in RFX-mod, shown in tab. 5.1, has been obtained by means of XPS measurements. For quantification, standard sensitivity factors of 0.05, 0.296 and 0.711 for Li_{1s}, C_{1s} and O_{1s} [109], respectively, were used. The approximate composition of the surface of the analyzed samples has been determined by dividing the individual peak areas, after appropriate background subtraction, by their respective atomic sensitivity and the result is shown in tab. 5.2. The measurements were made at the 9D sample insertion position that is either in font or just 30 ° away toroidally in the case of the multi-pellet injector.

Table 5.2: Film composition as determined by XPS

Injection technique	Device	Sample ID	Injected Li (g)	Li : C : O
Pellet injection:	LPI	9D_15	0.23	2.9 : 66.6 : 30.5
	MPI	9D_54	0.09	6.1 : 66.2 : 27.8
LCPS:	LLL	9D_23	1.0	15.4 : 54.2 : 30.3
	EVAp	9D_45	1.0	18.6 : 67.6 : 13.8

Clearly, as expected the greatest lithium surface abundance is obtained using the evaporation lithiumization technique with a lithium fraction of up to 18%, while only 2.8% was measured on the sample 9D_15 exposed to the

lithiumization performed by LPI. For approximately half the amount of injected lithium as in the LPI case, the MPI device on the other hand allows a higher lithium content deposited on the first wall. A surprising prominent feature is observed in the oxygen fraction measured in the case of the lithium evaporation lithiumization. While in average, all other lithium injection methods have shown an oxygen fraction ranging between 31% and 35%, in the case of the evaporator oxygen abundance is only 13%. The latter feature will be further investigated in the chemical analysis, in Section 5.4.

5.3.3 Lithium pellet injection toroidal uniformity

a. Single pellet injection by LPI

The deposition uniformity has been investigated by analyzing the surface of two graphite samples exposed at the 9D position (in front of the injection location) and at the 2D (~150° toroidally away). The SIMS depth profile of the $^{7}Li^{+}$ ions intensity normalized to the $^{12}C^{+}$ ions intensity for the LPI lithiumization is shown in fig. 5.4 along with an estimation of the global lithium content (estimation computed from the integral of the normalized intensity).

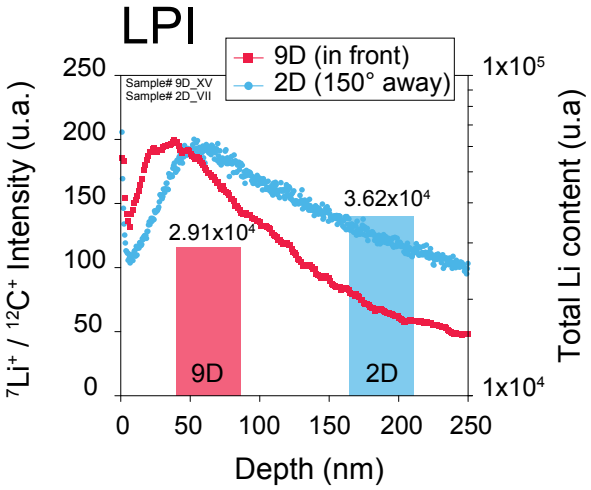

Figure 5.4: Normalized SIMS lithium depth profiles for the samples 9D (injector location) and 2D (150° toroidally away) exposed to a lithiumization performed with the LPI injection technique. The profiles were normalized against the $^{12}C^{+}$ ions intensity to remove possible instrument effects. The bars chart refers to the total lithium content measured along the first 250 nm.

The normalization to the $^{12}C^{+}$ ions intensity has been used as a standard to account for small variations in secondary-ion signals that can occur during

SIMS analysis as a result of O_2^+ primary beam current fluctuation, sample topography, and secondary-ion collection efficiency. It can be seen that the estimation of the total counts of lithium is nearly equal at the two toroidal locations; however a difference is observed on the depth profiles exhibiting a higher in-depth intercalation of lithium into the graphitic matrix for the 2D sample. Globally a uniform deposition using the LPI injection system can be deduced.

An indicator of active lithium on the wall after lithiumization and of the toroidal symmetry of lithium deposition is the lithium edge influxes in subsequent plasma discharges measured at different toroidal positions. To further evaluate the toroidal lithium deposition uniformity, the previously measured SIMS lithium profiles are compared with influxes measurements. To this aim, lithium influx measurements at two different toroidal locations were analyzed: the first one 90° toroidally from the lithium injection position and the second one 180° toroidally away. The two measurements are shown in fig. 5.5 for a discharge performed immediately after the lithiumization achieved with pellet injection using the LPI system.

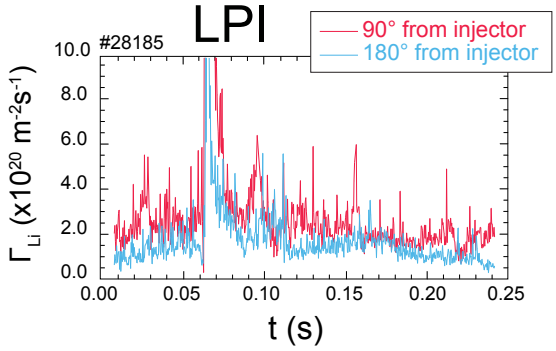

Figure 5.5: Lithium influx measured at two toroidal positions: pink curve at 90° from the injection section and cyan curve at 180°.

The two measurements are very similar at both positions. The slight difference is very likely due to the different in impact factors (distance from the geometrical axis) of the two lines of sight (p/a = 0.8 at 90° and p/a = 0.2 at 180°). Moreover, it is also because the 90° line of sight is strongly affected by Plasma-Wall Interaction (PWI) as it looks directly to the wall and because in RFX-mod higher values are usually measured for all influxes on external lines of sight on the low-field side (like the one at 90°). As a result, toroidal deposition symmetry can be achieved by the pellet injection technique in RFX-mod and it is due to multiple reasons inherent to the peculiarity of PWI in a RFP device. Indeed, different from a tokamak, strong and localized PWI are induced by large kink perturbations that develop in a RFP due to the locking of the MHD modes [144]. Pellet injection using the LPI system in

RFX-mod was characterized an ablation time of about 5 ms (time needed to completely ablate the pellet by the plasma), and a deposition time of about 20 ms (time in which the electrons coming from the pellet are confined in the plasma). Since the position where the plasma interacts strongly with the wall changes continuously during the 20 ms of the deposition time, an enhanced toroidal distribution of lithium can be achieved.

b. Multiple pellet injection by MPI

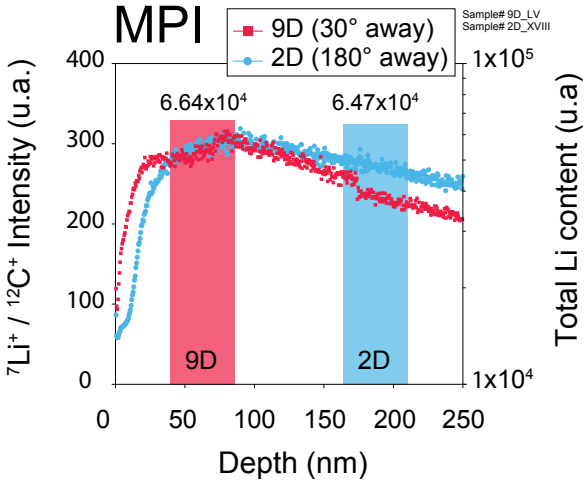

Figure 5.6: Normalized SIMS lithium depth profiles for the samples 9D and 2D exposed at 30° and 180° toroidally away respectively, to a lithiumization performed with the MPI injection technique. The profiles were normalized against the $^{12}C^{+}$ ions intensity to remove possible instrument effects. The bars chart refers to the total number of counts recorded along the first 250 nm.

As presented earlier in Section d., in contrast with the single pellet injector, the multiple pellet injector allows the injection of multiple lithium granules in a single plasma discharge. Despite the smaller pellet size and, accordingly, the shorter pellet penetration, a seven times increase has been obtained in terms of injection rate compared to the single pellet injector [141]. Two graphite samples were exposed during the lithiumization performed with the MPI apparatus. They have been exposed at the 9D and at the 2D positions, ~30° and ~180° toroidally away respectively. The SIMS depth profiles of the $^{7}Li^{+}$ ions intensity normalized to the $^{12}C^{+}$ ions intensity for two samples are shown in fig. 5.6 along with the total lithium measured content along the first 250 nm. The overall total quantity of injected lithium during the experimental campaign was 2.4 g, about 10× more that the injected quantity during the LPI lithiumization campaign. The amount of lithium effectively deposited on the wall is nonetheless

unknown as many lithium granules were lost in the vacuum duct connecting the MPI to the vessel.

The lithium distribution along the analyzed 250 nm shows a highly intercalated lithium into the graphite matrix. The total number of counts is similar in both samples which confirms the capability of lithium pellet injection to provide a toroidally uniform deposition. The depth profiles obtained are less peaked than the ones obtained with the single pellet injector and the near-surface lithium/carbon ratio appears about 1.5× larger. Moreover, the total lithium content computed from the integral of the normalized intensities resulted 2× larger, a result consistent with the difference in the injected lithium quantity. Furthermore, the very wide tails of the normalized lithium ions intensity that can be seen here are corroborated to the higher lithium coverage driving a more significant lithium intercalation into the graphite matrix.

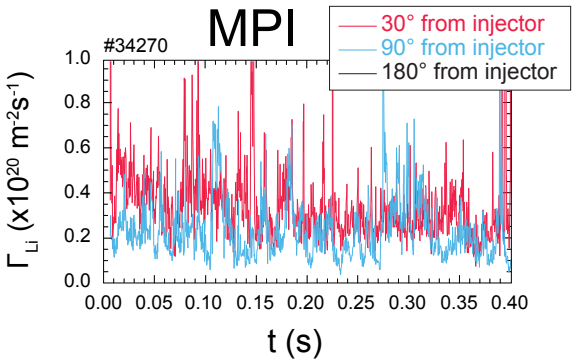

Figure 5.7: Lithium influx measured in plasma discharges after lithiumization performed with the MPI device. The measurements were made at three toroidal positions: pink curve at 30° from the injection section, cyan curve at 60° and black curve at 150°.

The SIMS post-mortem measurements have been compared to the lithium influx measurements which have been made at three different positions: 30°, 60° and 150° away from the injection location. Fig. 5.7 shows the respective emission data. The measurements show a toroidal asymmetry more pronounced than what has been observed in the post-mortem analysis measurements of the deposited lithium content. In addition to the already discussed difference in impact factors of the line of sights, the difference in the emission and post-mortem measurements is likely due to a lithium emission contribution of previously injected lithium during former lithiumizations that could not be revealed on the graphite samples as they were exposed only during the current lithiumization performed with the MPI device.

5.3.4 LCPS lithium deposition toroidal uniformity

Similarly to the previous analysis, the lithium content obtained with lithimizations in RFX-mod using the Lithium Capillary Porous System (LCPS) is investigated by *ex-situ* post-mortem SIMS and compared to lithium influx measurements. As commented earlier, the device has been used in two configurations allowing two different techniques and injection principles of lithium . On one hand, the first attempt was performed using the apparatus as a Liquid Lithium Limiter (LLL) during plasma discharges and, on the other hand, the setup was modified to allow the evaporation of lithium before plasma operation by operating the device under vacuum allowing melted lithium to evaporate and deposit evenly around the torus (herein, the technique is named 'EVAp'). The lithium influx measurements in the case of the LLL were about 500 power plasma discharges after the lithiumization was performed due to an unavailability of the lines of sight, while the measurements for the EVAp were made in a discharge immediately after the lithiumization was performed.

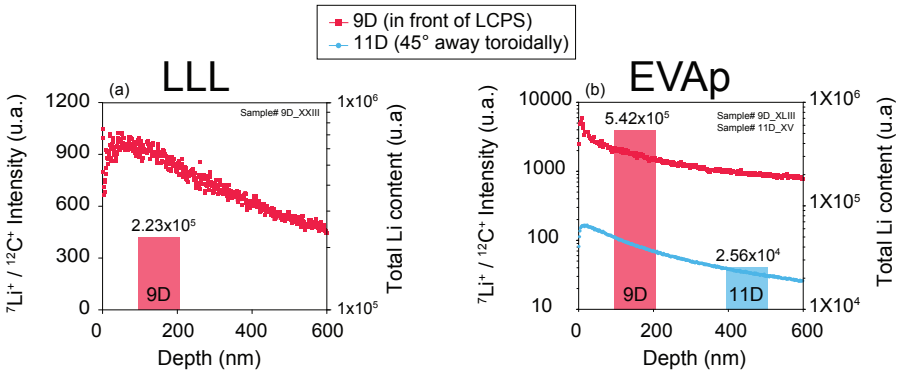

Figure 5.8: Normalized SIMS lithium depth profiles for the samples 9D (at injection location) and 11D (45° toroidall away from injection location) exposed to a lithiumization performed with the LCPS injection method, operated as (a) Liquid Lithium Limiter (LLL) and (b) as an evaporator. The bars chart refers to the total number of counts recorded along the first 250 nm.

In fig. 5.8 the depth profile of lithium obtained with the two lithiumizations using the LCPS is shown. During the LLL operation, 1 g of lithium was ejected in total from the apparatus while the evaporation was made with 14 g of lithium during the entire experimental campaign. According to the lithium depth profile of the sample exposed during the lithiumization with the LLL, the normalized $^7Li^+$ ions intensity measured at the injection location resulted 6× greater than the intensity measured for the lithiumization performed with the single pellet injector, a result consistent with the 5× difference in the injected lithium quantity. The total

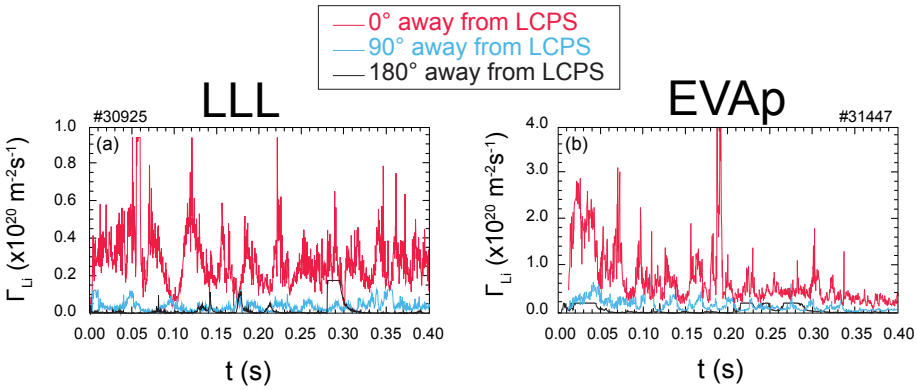

Figure 5.9: Lithium influx measured in plasma discharges after lithiumization performed with the LCPS injection method, operated as (a) Liquid Lithium Limiter (LLL) and (b) as an evaporator. The measurements were made at three toroidal positions: pink curve right at the injection section, cyan curve at 90° and black curve at 180°.

lithium content computed from the integral of the normalized intensities resulted, accordingly and consistently, one order of magnitude larger. The toroidal uniformity of deposition for the LLL operation could not be assessed from the *ex-situ* analysis, nonetheless it can be seen from the lithium influx measurements shown in fig. 5.9 that the deposition is strongly non-uniform with a prominent lithium deposition at the injection location and nearly at noise level, 90° and 180° toroidally away.

With regard to the lithiumization performed with the LCPS operated as a lithium evaporator, the results are very similar with a stronger coverage non-uniformity. Compared with the LLL case, the 14× difference in the total amount of evaporated/injected lithium is clearly apparent with 6× increase in the SIMS intensity of the $^{7}Li^{+}$ ions at the surface of the analyzed sample, one order of magnitude greater in the number of counts and up to 4× increase in lithium influxes observed in the 3 different available lines of sight. In both lithiumization cases, lithium is detectable in the SIMS signal up to a depth of 2 μm, which highlights a significant intercalation depth of lithium into the graphite matrix.

5.3.5 Plasma discharges and lithium toroidal asymmetry mutual effect

In principle, the sputtering, evaporation, transport, erosion and redeposition of lithium may contribute to its toroidal redistribution and reduce for example the strong deposition asymmetry that has been revealed in the case of the LCPS lithium deposition technique. One can expect that the highly localized deposition in front of the evaporator can be gradually eroded and lithium may be transported and redeposited around the torus.

Such a scenario would solve the issue of the strong localized deposition and offer the possibility to deposit a larger toroidally distributed coverage of lithium. However, given the peculiar RFP magnetic field configuration that is mainly poloidal at the edge, the latter may not be the case and the toroidal redistribution of lithium may be not occur.

In this section, first, the long term effect of plasma operation in terms of lithium erosion, redeposition, intercalation and spatial redistribution in RFX-mod is assessed. Second, the effect of the toroidal asymmetry is evaluated in terms of hydrogen influxes.

a. Effect of plasma discharges on lithium erosion and redeposition

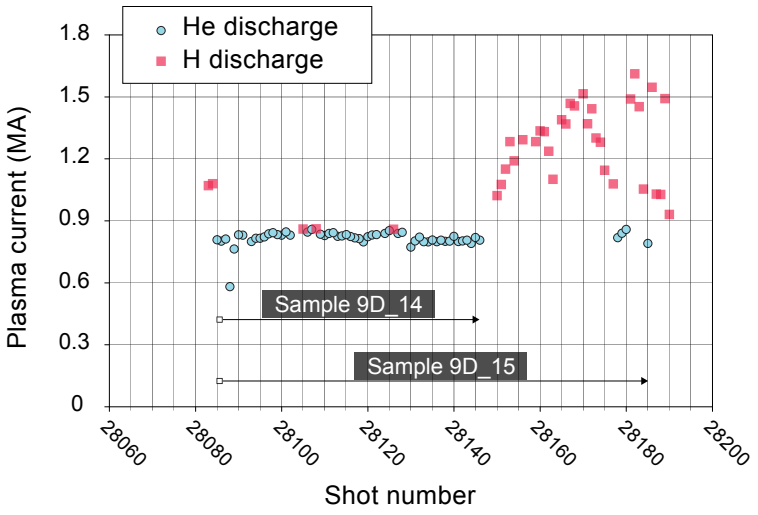

Figure 5.10: Shot-by-shout history of He/H plasma discharge current performed during the LPI experimental campaign during which sample 9D_14 and 9D_15 were exposed.

The effect of power plasma discharges on the erosion and redeposition of lithium is investigated by means of *ex-situ* post-mortem analysis. In particular, three lithiumizations were considered for the analysis: a first one performed with the LPI technique during which graphite samples were exposed at different stages of lithium injection and plasma exposure and subsequently analyzed by XPS spectroscopy and SIMS spectrometry; a second one performed with the MPI technique during which graphite samples were also exposed at different stages of lithium injection and analyzed by SIMS spectrometry; and a third lithiumization performed with theLCPS operated as an evaporator for which only lithium influx data were available. The latter lithiumization has the scope to evaluate if plasma

operation allows the toroidal redistribution of lithium and reduces the deposition asymmetry. To this purpose, lithium influxes in discharges performed immediately after lithium injection and about 400 discharges latter are compared.

Table 5.3: Experimental conditions of sample exposure and composition as determined by XPS

Sample ID	Total injected lithium		Plasma	Elemental composition (%)
	Pellets	Weight (g)	discharge	Li : C : O
9D_14	49	0.19	He	0.66 : 68.9 : 30.4
9D_15	49+8	0.19+0.04	He/H_2	2.89 : 66.6 : 30.5

The shot-by-shot history of plasma discharges performed during the LPI experimental campaign is displayed in fig. 5.10 while the exposed samples and their surface elemental composition obtained by XPS (peak area weighted to the standard sensitivity factors [109]) are shown in tab. 5.3. In fig. 5.11 the SIMS measurements on the same samples are shown, while fig. 5.12 shows the depth profiles of the $^{7}Li^{+}$ ions intensity normalized to the $^{12}C^{+}$ ions intensity for the two samples exposed to the MPI lithiumization and subsequent plasma operation.

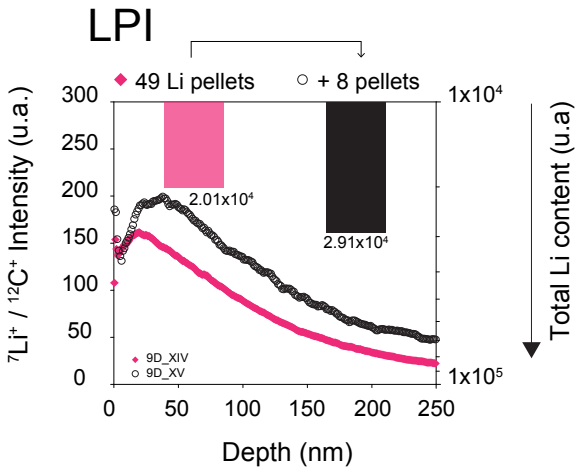

Figure 5.11: Normalized SIMS lithium depth profiles for two graphite samples exposed at the 9D position (injection location): sample 9D_14 was exposed to the injection of 49 Li pellets during aLPI lithiumization (⋄) and sample 9D_15 was exposed to an extra 8 pellets (∘). Accordingly, the bars chart refers to the total number of counts recorded along the first 250 nm.

Samples 9D_14 and 9D_15 were both inserted at the beginning of the lithiumization. After the injection of 49 Li pellets in He plasma discharges, the 9D_14 sample was removed while the other one was left to be exposed to the injection of 8 more pellets in H plasma discharges. This combination

allows to evaluate the changes in lithium content induced by different plasma types. For the same number of injected pellet, the XPS measurements show an enhanced lithium deposition by H plasma compared to He plasma. Indeed, the injection of only 8 pellet in H discharges resulted in a ~5× higher surface lithium concentration. The SIMS measurements confirm the higher lithium content in the sample exposed to the total of 57 Li pellets, however with only a 1.5× factor, in disagreement with the fraction of the extra injected pellets. Overall, the exposure to H_2 plasma of lithium coatings while injecting additional lithium does increase the surface coverage. Redeposition of lithium from other locations may explain the disproportional surface coverage increase. In fact, in RFX-mod it is experimentally observed that in some locations redeposition is prominent while in other locations erosion is more dominant. The higher performance (higher plasma current) H plasma discharges may favor Li deposition compared to He plasma and explain the dramatically enhanced lithium deposition observed in the analysis of sample 9D_15.

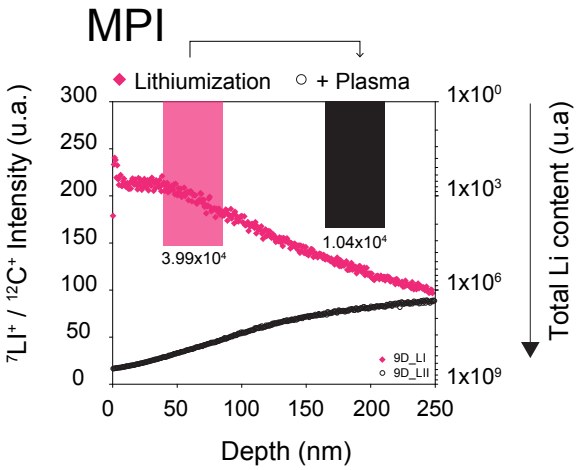

Figure 5.12: Normalized SIMS lithium depth profiles for two graphite samples exposed at the 9D position (injection location): the first one was exposed to a MPI lithiumization (⋄) and second one exposed in addition to 65 plasma discharges (∘). Accordingly, the bars chart refers to the total number of counts recorded along the first 250 nm.

With regard to the lithiumization performed with the MPI technique, similarly to the previous analysis, the aim was to assess the effect of plasma discharges performed immediately after a fresh lithium content was deposited. Two graphite samples were exposed to this lithiumization. While the first one has seen only the lithiumization, the second one has been further exposed to 65 subsequent He/H plasma discharges during which no more Li pellets were launched. The SIMS depth profiles in fig. 5.12 show that the lithium/carbon ratio on the surface and along the first 250 nm below the surface is significantly

reduced in the sample exposed to the plasma, reaching the same value after the 250 nm threshold. The total lithium content is about 1.5× higher in the case of the sample unexposed to plasma after lithiumization. Erosion of the surface lithium can explain the lower lithium content in the case of the sample exposed to plasma, while the difference in depth profiles is very likely due to an inward diffusion of lithium into the graphite substrate. The result of exposure of the lithiated graphite sample to plasma operation is, therefore, two-fold: a lower lithium fraction at the surface and in the first 250 nm below the surface, and a decrease in the total lithium content due to lithium intercalation in the graphite substrate.

Finally, to evaluate if plasma operation subsequent to lithium wall conditioning allows to reduce or suppress the strong toroidal asymmetry in lithium deposition, lithium influxes were obtained at different toroidal positions in immediately and a long time after lithium injection. The latter was done in the case of a lithiumization performed with evaporator technique that has shown the strongest toroidal asymmetry: 14 g were almost all evaporated in the quarter of the machine, in front of the evaporator toroidal position. Fig. 5.13 show the lithium influx measurements in two discharges: the discharge #31447 was conducted immediately after the lithiumization experimental campaign, while the discharge #31868 was conducted about 400 power discharges after.

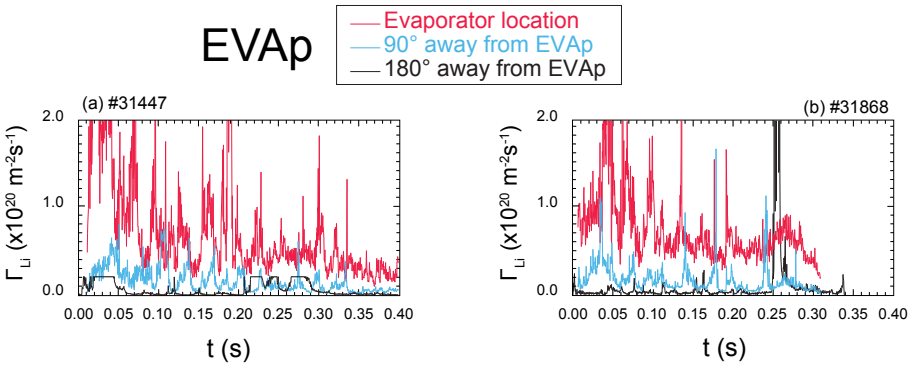

Figure 5.13: Lithium influx measured in a plasma discharge (a) immediately after a lithiumization performed with the LCPS injection method operated as an evaporator and (b) about 400 subsequent plasma discharges. The measurements were made at three toroidal positions: pink curve right at the injection section, cyan curve at 90° and black curve at 180°.

The erosion and redeposition of lithium after multiple plasma pulses is not effective in establishing a uniformity of lithium wall conditioning. In fact, the Li influx levels measured at the three toroidal positions, close to the evaporation, displaced by 90° and by 180°, respectively, though decreasing, maintain roughly the same ratio after several hundreds of plasma pulses without any evaporation (see fig. 5.13(b)). A possible explanation, in

addition to the prompt hydrogen saturation of lithium as reported in other graphite machines such as NSTX [145], is that in RFX-mod as in any RFP device, the magnetic field at the edge is nearly poloidal. Consequently, a relevant fraction of lithium is promptly redeposited close to the toroidal position where it is extracted. The reduction of the absolute value of Li influx may instead be due to the progressive redeposition of carbon atoms.

b. Effect of toroidal asymmetry on hydrogen recycling

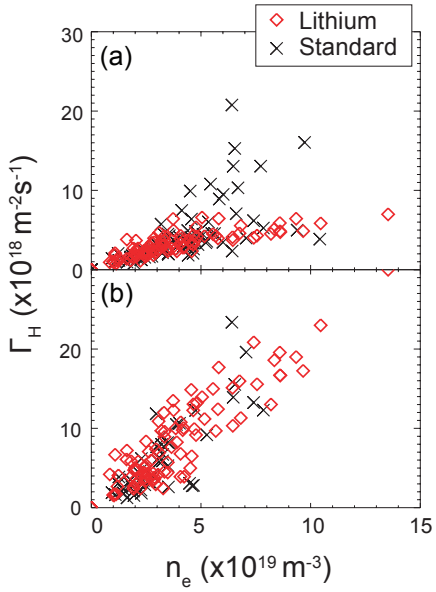

Figure 5.14: Hydrogen influxes at the same toroidal location where evaporation occurs (top) and toroidally displaced by 90° (bottom) (taken from ref. [60].

Lithium wall conditioning in RFX-mod resulted very effective in reducing recycling [60]. As it can be seen in fig. 5.14(a), after the lithiumization performed with the evaporator, the H influx resulted significantly reduced, especially at a high density (three-fold decrease). To study the effect of the asymmetry in lithium deposition, H influx obtained at a location toroidally displaced by 90° from the evaporator has been compared to H influx at the evaporator section. The results are shown in fig. 5.14(b).

The discharges denoted as 'standard' in the figure were performed during the same lithiumization campaign. The only difference is that the discharges denoted 'lithium' are related to discharges where fresh lithium injection was carried out before the H influx measurements were made. As it can be seen lithiumization has little or no influence on H influx at a location toroidally displaced by 90° from the lithium evaporation position.

5.3.6 Discussion

With regard to the toroidal lithium deposition uniformity, the injection of lithium pellets/granules during plasma discharges, allows a relatively uniform toroidal coverage compared to lithium injection/evaporation using the LCPS injection method. In-depth ablation of lithium pellets/granules and deposition of lithium along the field lines is favorable in the former case because of the shorter ablation time (5 ms) compared to the deposition time (20 ms) in RFX-mod. While in the case of the LCPS, the highly localized lithium deposition is undoubtedly due to the peculiarity of the magnetic field configuration characteristic of an RFP that is nearly poloidal at the edge resulting in a prompt redeposition of lithium near the deposition location.

Taking into account the high porosity and surface roughness of the graphite, the surface and in-depth lithium content probed by SIMS is relatively consistent with the amount of injected lithium in all lithiumization cases. Furthermore, different depth profile of lithium/carbon ratio were found. First, peaked profiles were observed in the case of the single pellet injection while flat profiles were found in the case of the multiple pellet injection. Thus, the increase in frequency injection allows to obtain a relatively less contaminated lithium content on the plasma facing surface which is a positive aspect of this lithiumization that has been recently implemented in RFX-mod. Second, a peculiarity in the lithium depth profile was observed in the case of lithium evaporation (see fig. 5.8 (b)), with a large surface lithium concentration and a long in-depth shoulder. As opposite to injecting lithium during plasma discharges such as in the pellet injection (LPI and MPI) or the lithium limiter (LLL) cases, lithium evaporation is achieved before plasma operation. As a consequence, lithium deposition in the first cases is mainly achieved by lithium particles ionized in the plasma and redeposited along the field line while in the evaporation case, lithium atoms are directly deposited without plasma ionization. This difference in deposition principles may therefore explain the difference in the lithium depth profiles. Direct deposition of lithium atoms may be more favorable for lithium migration into the graphite bulk, in contrast with ionization of lithium and its redeposition that may lead to sustain a surface Li content that is less prompt to intercalation. In fact, lithium remained detectable to a depth up to 1 μm in the case of pellet injection and up to 2 μm in the case of lithium evaporation. The latter results were found consistent in SIMS and XPS *ex-situ* post-mortem measurements and confirmed by lithium influx data during plasma discharges.

With regard to the effect of plasma operation during and following lithium deposition, SIMS and XPS *ex-situ* measurements have shown that the injection of lithium pellets in hydrogen plasmas resulted more efficient in depositing lithium on the first wall compared to the injection in helium plasmas. The latter is very likely due to the higher provided ohmic power and accordingly higher particle fluxes during hydrogen discharges.

Moreover, the exposure of a lithiated graphite sample to 65 power plasma discharges resulted in a lower lithium fraction at the surface of the sample and in the first 250 nm below the surface. The total integrated lithium content along the same depth was also reduced by a factor of 4. In addition, spectroscopic emission data has shown that the erosion and redeposition of lithium after multiple plasma pulses is not effective in establishing uniformity of wall conditioning.

The toroidal asymmetry of lithium coverage was found to be detrimental as little or no influence on H influx was found at locations where lithium coverage is reduced. The latter result was found in the case of a lithiumization performed by lithium evaporation in which a highly localized lithium deposition was seen.

5.4 High resolution surface chemical analysis

In RFX-mod, the reduction in hydrogen recycling subsequent to lithium wall conditioning is correlated to a reduction in hydrogen influx [60]. The mechanism by which lithiated graphite retains hydrogenic species remains largely unknown. In this section, we examine the surface chemistry resultant when lithium is deposited on RFX-mod graphite at variable Li doses. The analysis is performed for lithiated graphite obtained with lithium wall conditioning using the different available methods in RFX-mod. As the principle of lithium deposition on the graphite first wall differs from injecting Li pellets during plasma operation to evaporating lithium directly on top of the first wall before plasma operation, it appeared of interest to study the chemical states of lithium in each lithiumization case and correlate the results to the total injected lithium.

The interaction of the hot fusion plasma with conditioning low-Z thin films when applied in fusion devices mostly occur at the surface and within the first 10 nm below the plasma facing components surface. In order to interrogate the fine chemical states of lithium and bounding impurities, it is necessary to probe the near surface of the lithiated graphite with a high resolution surface analysis technique. High Resolution X-ray Photoelectron Spectroscopy (HR-XPS) measurements have been made on graphite samples that have been exposed to a number of lihtiumizations in RFX-mod (see tab. 5.1). The samples are characterized and analyzed in their pristine state and after lithium injection. Via the photoelectric effect, incident x-rays eject inner core photoelectrons within their escape depth ($\leqslant$10 nm) from the sample surface which are then collected by an energy selective hemispherical analyzer. Because elements and chemical bonds have characteristic photoelectron binding energies, XPS provides a valuable tool in qualitative analysis for determining binding functionalities. The probing depth of XPS is ~10 nm and thus is within range of the implanted hydrogenic ions. A 7.5 kW rotating anode monochromatic Al Kα X-ray source (1486.6 eV) is used for the X-ray production. Analyzer resolution (0.5 eV) and statistical standard error (SE) contribute to XPS spectral error. The XPS spectra in this study have a SE of less-than 0.02 eV and therefore error propagation is dominated by analyzer resolution. In order to reveal buried chemical states, lithiated samples are sputtered by Ar^+ ion etching, so the 'as received' state refers to samples that did not undergo any type of surface treatment.

5.4.1 Chemical response of pristine graphite to lithium

a. Pristine graphite vs 'as received' lithiated graphite

Pristine graphite shows two primary peaks in the photoelectron spectrum at 532.8±0.5 eV and 284.8±0.5 eV, corresponding to O_{1s} and C_{1s} respectively, in addition to a Na_{KLL} Auger peak that is inherent to the graphitic matrix. A typical XPS spectrum for RFX-mod pristine graphite and an 'as received' RFX-mod post-mortem lithiated sample are shown in fig. 5.15(a) and (b)

respectively. While the pristine graphite sample shows a very narrow graphitic C_{1s} peak, the 'as received' sample has a wider non-Gaussian in appearance peak, an indication that the spectrum consists of more than one primary bond. The O_{1s} peak on the other hand, appears with a Gaussian shape in the case of the pristine sample which indicates essentially a primary C-O bond. The spectrum also shows the presence of satellite peaks at slightly higher binding energies with respect to core peaks arising due to non-monochromaticity of the X-ray source. The post-mortem lithiated sample shows oxygen bonds that dominate the carbon bonds in the XPS spectrum, characteristic of surface oxidation. In addition, lithium is observed at 56 eV [146].

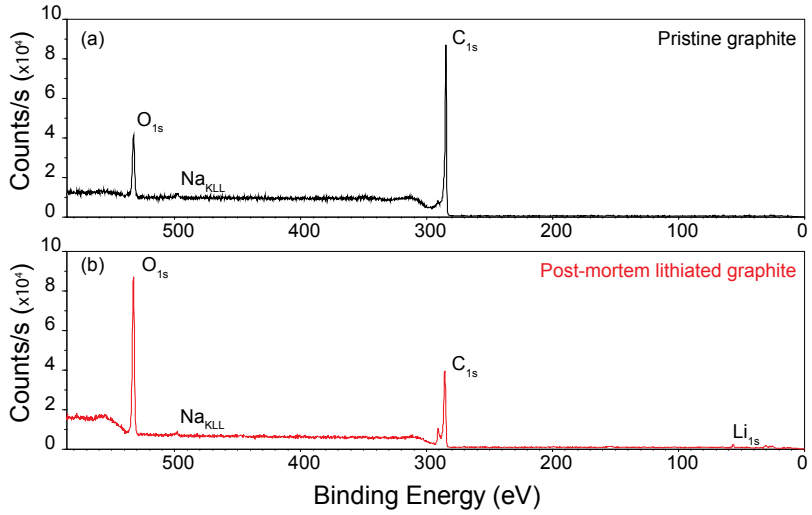

Figure 5.15: XPS wide energy range scan showing the prominent photoelectron peaks for (a) pristine RFX-mod first wall graphite sample, and (b) post-mortem lithiated sample. Primary peaks correspond to the O_{1s} and C_{1s} energies.

5.4.2 Lithium chemical states with varying lithium injection doses in RFX-mod

a. Overview of lithiated graphite chemical interactions

The interaction of lithium with graphite substrate has been extensively studied both in offline experiments under controlled conditions and after lithiumizations in fusion devices in order to correlate the lithium-graphite chemical states found in control laboratory experiments to the fusion machine environment. Taylor et al. [135] found by means of XPS analyses that upon progressive exposure of graphite to lithium doses, lithiated graphite has two prominent chemical interactions in the O_{1s} photoelectron energy range at 532.0±0.6 eV and 529.5±06 eV corresponding to the chemical functional groups (as opposed to a stoichiometric notation of a

known chemical bond) O–C and Li–O. Moreover, it was found that deuterium irradiation resulted in the formation of an additional O_{1s} peak located at 532.9±0.6 eV and a C_{1s} peak located at 291.26±0.6 eV attributed respectively to Li-O-D and Li-C-D interactions. The post-mortem analysis of NSTX tiles exposed to multiple lithiumizations has shown a direct correlation with the control laboratory experiments only after 3h of Ar^+ sputtering and further annealing at ~550°C of the tiles allowing to uncover the lithium-graphite chemical history. In an earlier work performed on the same subject by Harilal et al. [147], the *in situ* XPS analysis carried out on NSTX ATJ graphite surfaces during stepwise lithium deposition has shown that a new binding energy peak at 530.2 eV attributed to lithium peroxide is observed in the O_{1s} binding energy range. Moreover, when the sample was exposed to air for a short time (one hour), lithium carbonate radicals (Li_2CO_3 at 290.2 eV) appeared at the expense of the latter peroxide functionality.

In light of these consideration, lithiated graphite samples obtained with the injection of the different quantities of lithium listed in tab. 5.1 and using the different lithiumizations techniques in RFX-mod, are analyzed and compared to the results found in other fusion devices with a graphite first wall and lithium wall conditioning. In particular, the results are compared to the analysis of post-mortem NSTX lithiated tiles [135, 147, 148].

b. Chemical response to a low lithium dose

In order to evaluate the response of pristine graphite to a small injection of lithium dose in RFX-mod, graphite samples have been exposed to lithiumizations where only a small amount of few milligrams of lithium was injected. To this purpose, graphite samples were exposed and immediately retrieved after two different lithiumizations: a first one performed with the LPI system injecting 8 Li pellets equivalent to 0.03 g and exposing sample #16 (see tab. 5.1 for more details); and a second lihiumization performed with the MPI method, injecting the equivalent of 0.09 g of Li granules and exposing sample #54. Previous SIMS measurements have shown that approximately 20±10 nm of lithium was deposited in both cases (very rough approximation). In order to avoid the prompt oxidation of the lithium coating, both samples were sealed in a plastic vacuum container after being retrieved from RFX-mod vessel. The HR-XPS spectra of the two samples obtained for C_{1s} and O_{1s} are given in fig. 5.16 along with representative fitted peaks. Because of the few photoelectrons that are emitted from the Li_{1s} core line to enable the accurate deconvolution of its spectra, the analysis has been focused on the C_{1s} and O_{1s} core spectra where the most interesting features are observed. For reference, the HR-XPS signal obtained from the pristine graphite is also given in the bottom panels of fig. 5.16. For curve fitting of the data, Gaussian profiles have been used.

With regard to the C_{1s} core line, the spectra were fitted with three main contributions. According to the chemical interactions found in

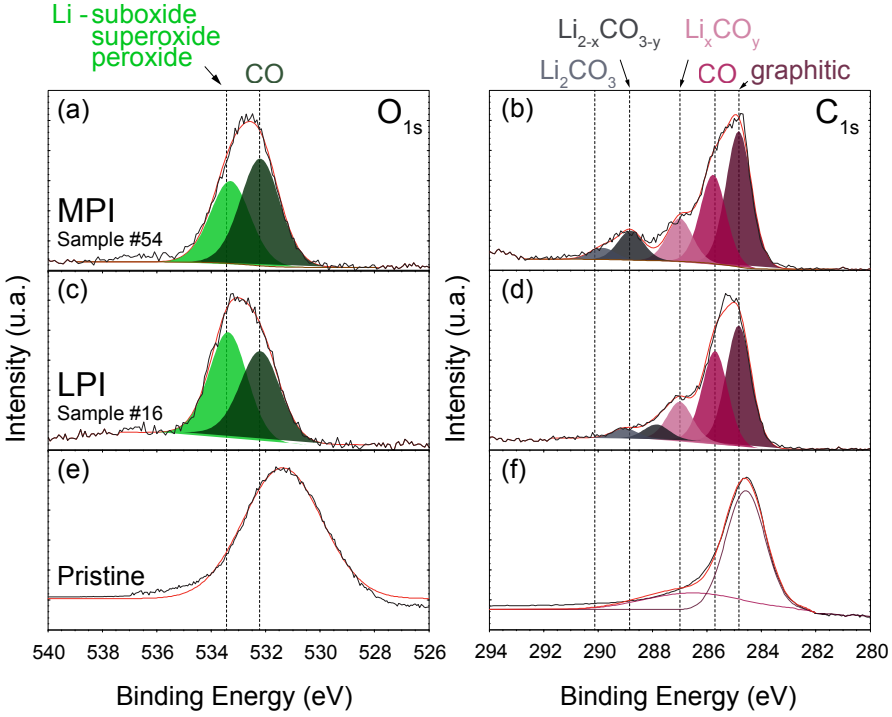

Figure 5.16: HR-XPS spectra showing chemical interactions for graphite samples #16 and #54 exposed to a lithiumization injecting the equivalent of 0.03 g and 0.09 g of Li using respectively the LPI and the MPI injection methods. Only the O_{1s} (left panels) and C_{1s} (right panels) core lines are shown. For reference, the HR-XPS spectra of a pristine graphite sample are shown as well.

[135, 147, 148], the binding energies equal to 284.8 eV and 285.7 eV were associated to the graphitic and C–O bonds respectively, while the peak at 290.1 eV was attributed to the formation of lithium carbonate. In the binding energy range between the C–O bonds and the lithium carbonate bonds, two other prominent deconvoluted peaks were obtained which were reasonably attributed to non-stoichiometric interactions between Li, C and O and refereed to with the notation Li_xCO_y. On the other hand, the O_{1s} core line is fitted with two main constituents: a primary C–O bond found at 532.2 eV and a second chemical interaction involving lithium in the form of sub-, super- and peroxide at 533.3 eV [149, 150].

The O_{1s} core line in the left (a) and (c) panels of fig. 5.16, has an apparent Gaussian shape, while on the other hand the C_{1s} core line has an apparent asymmetric shape. Similarly, the analysis of NSTX tiles at different vessel locations [148], has shown that in the vicinity of the private flux region at the divertor where higher lithium deposition was expected, broad non-Gaussian XPS peaks were obtained for O_{1s} while, symmetric nearly Gaussian peaks

were obtained outside of the high flux region where low lithium deposition was expected. In RFX-mod, the O_{1s} core line for the low dose of injected lithium is observed to be symmetric and few lithium chemical interactions were found. In addition, similar binding energies were found for the C_{1s} and O_{1s} spectra showing that comparable lithium chemistry has been obtained with the lithiumizations in the two machines.

At last, a final observation regarding the low dose deposition analysis, by comparing the Li bonds in the C_{1s} core line relative to the two samples #16 and #54 in fig. 5.16 (b) and (d), a greater lithium carbonate can be seen in the case of the lithiumization performed with the multi-pellet injector. The small difference is also reflected in the O_{1s} core line. A higher contribution of lithium sub-, super and peroxides at binding energy equal to 533.3 eV can be seen compared to the C–O bonds peak area.

c. Chemical response to a medium lithium dose

In RFX-mod, lithium wall conditioning with medium lithium injection of about 0.23 g was performed using the lithium pellet injector. SIMS measurements on a twin graphite sample have shown that about 50 nm of lithium are present on the surface. Similarly to sample #16 analyzed above, graphite sample #14 was exposed during the wall conditioning session and retrieved after being sealed in a plastic vacuum container to avoid the prompt oxidation of the lithium coating. HR-XPS measurements were made on the sample on its 'as received' state and after 10 min of Ar^+ ion etching to uncover buried chemical interactions, following recommendations in ref. [148]. The HR-XPS spectra of the two samples obtained for C_{1s} and O_{1s} are given in fig. 5.17 along with representative fitted peaks and the spectra obtained from the pristine graphite for reference. Similarly to above, the analysis has been focused on the C_{1s} and O_{1s} core spectra.

The previous correlation among the lithium oxide peak deconvoluted in the O_{1s} spectrum and the lithium carbonate peaks in the C_{1s} spectrum can be clearly seen here with an overall increase of both chemical interactions compared to the low lithium injection dose. About 75% of the peak area in the O_{1s} spectrum is related to lithium sub-, super and peroxides and more than half of the chemical states in the C_{1s} spectrum are related to lithium carbonate. Moreover, while for the low dose injection the C–O bonds in the C_{1s} spectrum have a relatively medium contribution compared to the graphitic bonds, here the increase in carbonate bonds also relates to a prominent C–O peak with nearly 3× the graphitic bonds peak area. Overall the increase of lithium dose relates to an increase in lithium carbonate chemical states. An interesting feature that was also observed in the post-mortem analysis of NSTX lithiated graphite is the broader O_{1s} peak in the case of higher lithium deposition, very likely due to an increase in the oxidation states of lithium. Also similarly to NSTX analysis results, Ar^+ ion etching has allowed here to uncover buried chemical states that appeared with more apparent peaks after the etching.

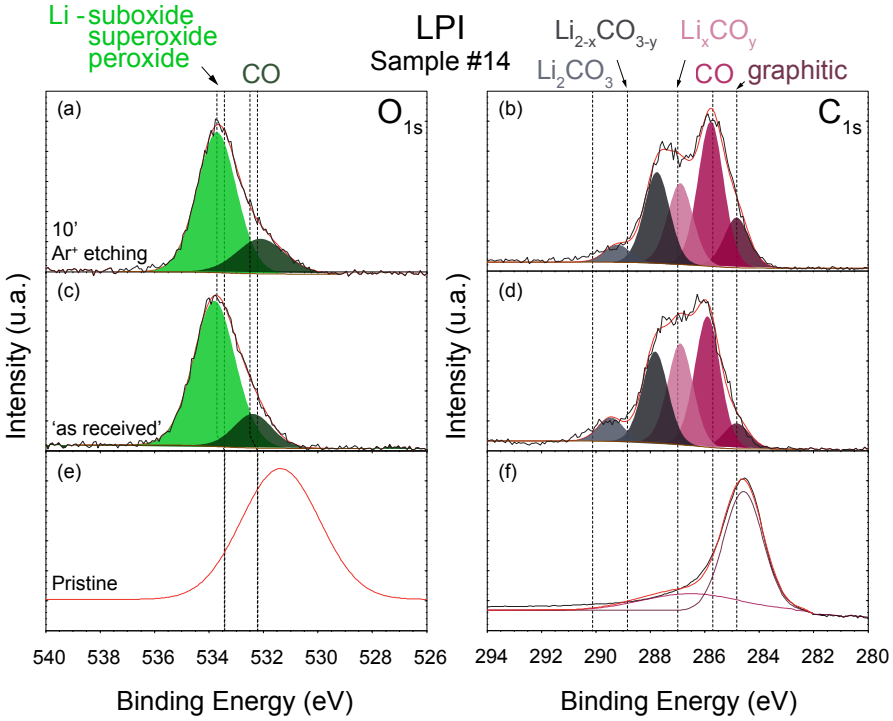

Figure 5.17: HR-XPS spectra showing chemical interactions of sample #14 exposed to a lithiumization injecting the equivalent of 0.23 g of Li using the LPI injection method. Bottom panels show the spectra of a pristine graphite surface for reference, middle panels show the 'as received' spectra and top panel show the spectra after 10 min of Ar^+ ion etching.

d. Chemical response to a high lithium dose

High lithium dose deposition in RFX-mod lithiumization is achieved with the use of the Lithium Capillary Porous System (LCPS) injection method. Two lithium conditioning sessions are considered here where 1 g of lithium was injected in total in each case.

Ex-situ SIMS measurements on graphite samples (see fig. 5.8) have shown that about 200 nm of lithium was deposited in both cases. Sample #23 and #45 were exposed during the lithiumizations where the LCPS was operated respectively as Liquid Lithium Limiter (LLL) then as an evaporator. Similarly to the previous analyses, after being retrieved from the vessel, the samples were sealed in plastic vacuum containers to avoid the prompt oxidation of the lithium coating. The HR-XPS spectra of the two samples obtained for C_{1s} and O_{1s} are given in fig. 5.18.

The most interesting feature in this case is observed with the analysis of the lithium chemical states of sample #45 (top panels in fig. 5.18) that has been exposed to 1g of lithium injection by evaporation before plasma

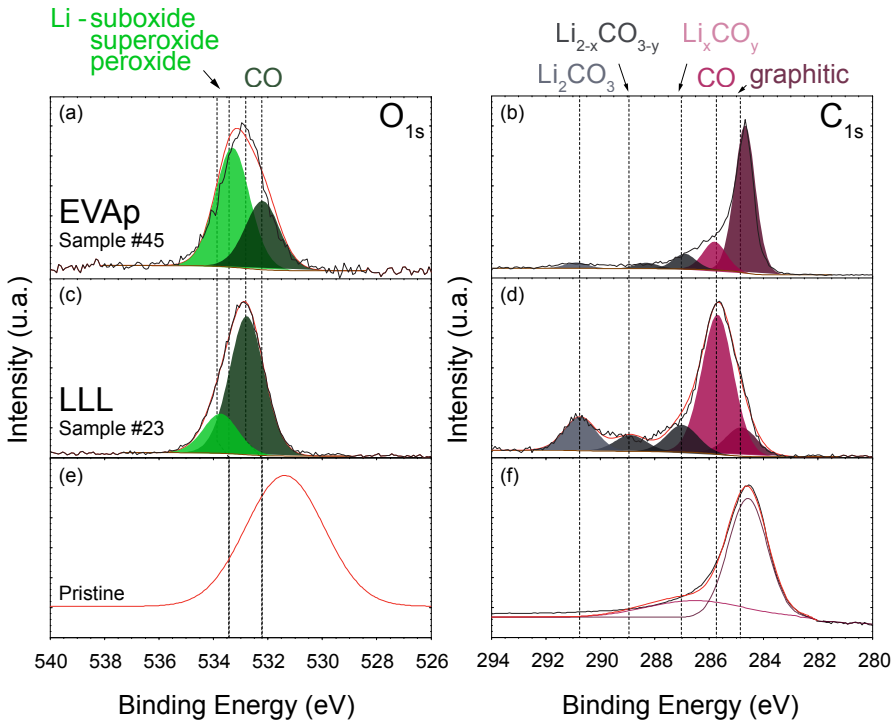

Figure 5.18: HR-XPS spectra showing chemical interactions of samples #23 and #45 exposed to lithiumizations injecting the equivalent of 1 g of Li using the the Lithium Capillary Porous System (LCPS) injection method operated respectively as LLL then as an evaporator. Bottom panels show the spectra of a pristine graphite surface for reference, middle panels show the spectra for sample #23 and top panel show the spectra for sample #45.

operation (as opposite to the LLL method where lithium is injected during plasma discharges). A salient graphitic peak can be seen in the C_{1s} spectrum with a significantly smaller contribution from lithium carbonate peaks in binding energies > 287 eV. As commented in previous sections, the amount of lithium carbonate relates to the total amount of measured lithium, therefore the presence of a prominent graphitic peak is related to a small amount of lithium on the surface. Lithium evaporation directly on the surface is more favorable with regard to lithium intercalation into the graphite substrate. With regard to sample #23, a significant Li_2CO_3 peak at BE equal to 290.1 eV in the C_{1s} spectrum can be seen consistent with the higher lithium injected dose. The latter is correlated to prominent C–O bonds observed in both O_{1s} and C_{1s} core lines.

5.4.3 Effect of high current 1.5-2.0 MA H plasma discharges on Li-graphite chemistry

With the purpose to investigate the Li-graphite chemical changes induced by H power discharges subsequent to lithium wall conditioning, a dedicated experimental procedure has been undertaken. In parallel to sample #45 that was exposed to 1 g of lithium evaporation and which HR-XPS spectra were discussed in the previous section, sample #47 has been similarly exposed to 1 g of lithium evaporation and kept in the vessel to be further exposed to a set of two hydrogen discharges. The plasma parameters of the performed discharges are shown in fig. 5.19.

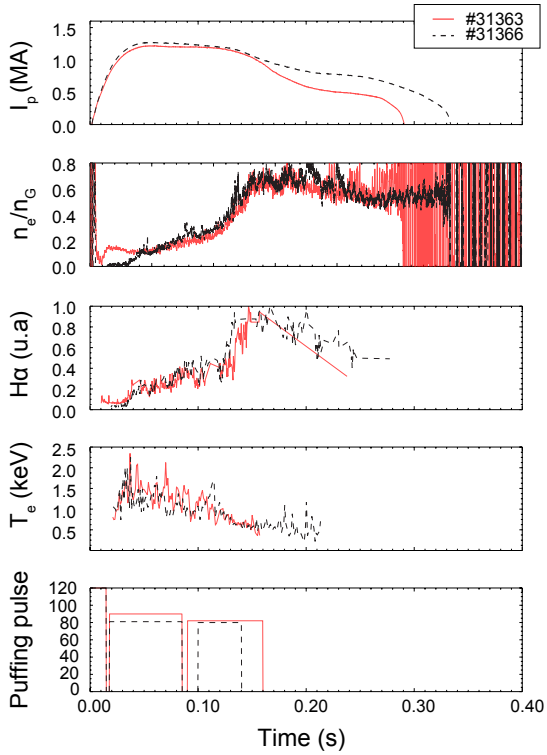

Figure 5.19: H plasma discharges #31363 (—) and #31366 (- - -) performed after evaporation of 1 g of lithium using the LCPS device operated as an evaporator.

After exposure, sample #47 was retrieved and *ex-situ* HR-XPS measurements were carried out then compared to the spectra of sample #45. The HR-XPS spectra of the two samples obtained for C_{1s} and O_{1s} are given in fig. 5.20 along with representative fitted peaks and the spectra obtained from the pristine graphite for reference. Similarly to above, the analysis has been focused on the C_{1s} and O_{1s} core spectra.

The analysis of the spectra shows very comparable chemical interactions.

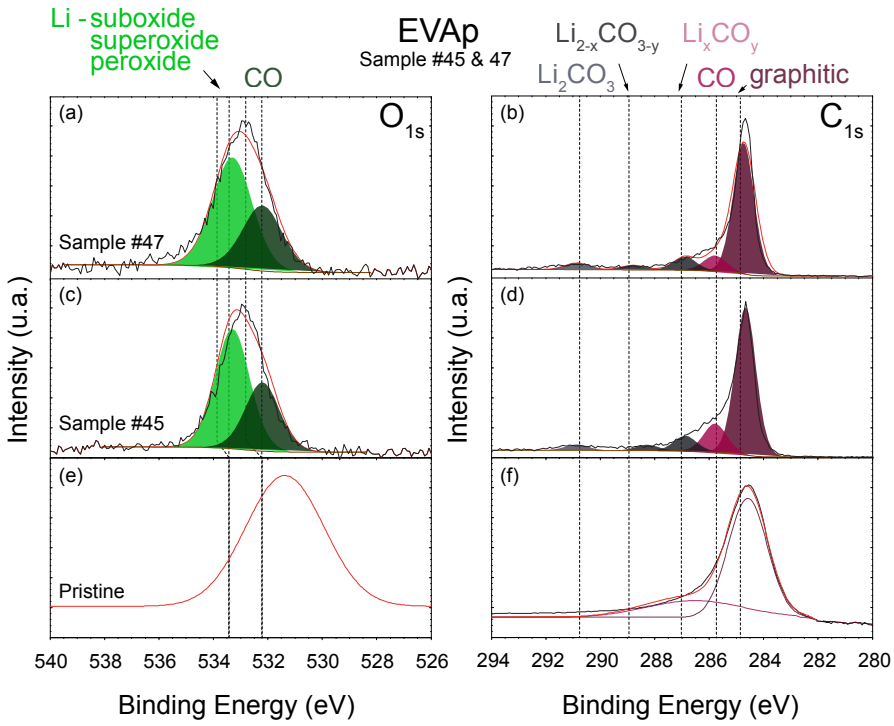

Figure 5.20: Comparison of HR-XPS spectra of sample #45 exposed to the evaporation of 1 g of lithium and #47 subsequently exposed in addition to a set of two H plasma discharges.

The exposure to H plasma discharges leads to no or few apparent changes in surface chemistry of the lithium coating. The most prominent changes can be seen in the O_{1s} core spectra with a wider full width at half maximum (FWHM) of the lithium sub-, super- and peroxide peak. Hydrogen plasma may lead to slight oxidation of the fresh lithium deposited by evaporation. In addition, the overall FWHM widening of the O_{1s} peak may suggest a less ordered structure of the surface. In fact, FWHM is largest in the least ordered compounds [150]. As a consequence, the set of two H plasma discharges performed subsequently to lithium deposition do not lead to the formation of new lithium-graphite chemical interactions but do induce variation in lithium oxidation.

XPS post-mortem analysis of lithium-conditioned NSTX graphite plasma facing components has shown that the apparent presence of hydrogenic related lithium chemical interactions, such as Li–O–D and Li–C–D, is only observed after a minimum lithium dose of 100-500 nm was deposited [148]. Furthermore, the most effective lithium enhanced retention of deuterium in pre-lithium discharges was found to occur at nominal lithium doses $\geqslant$100-500 nm in high recycling regions. The absence of apparent chemical changes after exposure to plasma discharges of RFX-mod lithium-conditioned graphite may be due to a low lithium coverage in spite

of the 1 g of Li evaporation.

5.5 Conclusions

In this chapter, a physical and chemical analysis of the obtained lithiated graphite first wall with the different lithiumization techniques in RFX-mod has been performed by *ex-situ* analysis of material samples. At different toroidal locations around RFX-mod torus, the deposition uniformity for each technique has been assessed by SIMS spectrometry and the results were compared to Li spectroscopic emission during subsequent plasma discharges. The high resolution Li-graphite chemical analysis at varying lithium dose injection with and without plasma exposure has been conducted by HR-XPS measurements.

The toroidal asymmetry analysis has shown that compared to lithium injection/evaporation using the LCPS injection method, the injection of lithium pellets/granules during plasma discharges allows a relatively more uniform toroidal coverage. Pellet injection finds its advantage in the in-depth ablation of lithium and deposition along the field lines that is favorable due to the shorter ablation time (5 ms) compared to the deposition time (20 ms) in RFX-mod, whereas in the case of the LCPS, the highly localized lithium deposition is a result of the magnetic field configuration characteristic of RFPs that is nearly poloidal at the edge, resulting in a prompt redeposition of lithium near the deposition location. The latter results were consistently confirmed in both *ex-situ* post-mortem analysis and Li influx measurements.

Taking into account the high porosity and surface roughness of graphite, the surface and in-depth lithium content probed by SIMS is relatively consistent with the amount of injected lithium in all lithiumization cases. However, the lithium content after deposition and plasma operation was found contrasting from one lithiumization technique to the other and different depth profiles of lithium/carbon ratios were found. First, peaked profiles were observed in the case of the single pellet injection while flat profiles were found in the case of the multiple pellet injection. Thus, the increase in frequency injection allows to obtain a relatively less contaminated lithium content on the plasma facing surface, which is a positive aspect of this new lithiumization technique that has been recently implemented in RFX-mod. It is proposed that a higher lithium injection frequency would logically cause a more pronounced lithium concentration on PFCs compared to a single pellet injection system. Second, a peculiarity in the lithium depth profile was observed in the case of lithium evaporation by LCPS, with a large surface lithium concentration and a broad in-depth content up to to 2 μm. The latter result has been ascribed to the difference in lithium injection principles: direct deposition of lithium atoms (evaporation case) is proposed to be favorable for lithium migration into the

graphite bulk, whereas ionization of lithium and its redeposition (pellet injection and LLL cases) is favorable to sustain a surface Li content that is less prompt to intercalation. Since in a fusion device, the plasma wall interaction takes place within the first 10 nm of the plasma facing components, the latter result is crucial for the optimization of lithium injection. Due in part to its small size, Li intercalates rapidly and in large amounts into graphite. Therefore it is more profitable to inject small amounts of Li such as with the MPI technique that allows to sustain a surface Li coverage rather than depositing greater amounts that are more prompt to intercalation.

With regard to the effect of plasma operation during and following lithium deposition, SIMS and XPS *ex-situ* measurements have shown that the injection of lithium pellets in hydrogen plasmas resulted more efficient in depositing lithium on the first wall compared to the injection in helium plasmas. Moreover, the exposure of a lithiated graphite sample to 65 power plasma discharges resulted in a lower lithium fraction at the surface of the sample and in the first 250 nm below the surface. The total integrated lithium content along the same depth was also reduced by a factor of 4. In addition, spectroscopic emission data have shown that the erosion and redeposition of lithium after multiple plasma pulses is not effective in establishing uniformity of wall conditioning. Moreover, the toroidal asymmetry of lithium coverage was found to be detrimental as little or no influence on H influx was found at locations where lithium coverage is reduced. The latter result was found in the case of a lithiumization performed by lithium evaporation in which a highly localized lithium deposition was seen.

The HR-XPS chemical analysis has shown several results in agreement with previous studies on Li-graphite chemistry performed in NSTX tokamak. In particular, Gaussian O_{1s} XPS peak shapes were found when a low lithium dose was injected while a non-Gaussian shapes where found for higher lithium doses. Lithium carbonate radicals (Li_2CO_3 at 290.2 eV) were systematically found in all the analyzed samples in both C_{1s} and O_{1s} core spectra. Often the fraction of lithium carbonate correlates to the total injected lithium dose. Also similarly to NSTX analysis results, Ar^+ ion etching has allowed here to uncover buried chemical states that appeared with more apparent peaks after the etching. Pronounced lithium intercalation when lithium deposition is performed by evaporation has been further demonstrated by HR-XPS. In consistency also with results found in NSTX, at low doses of lithium injection $\leqslant$100-500 nm, the exposure of Li-coated graphite to H plasma discharges has shown no or few apparent changes in surface chemistry of the lithium coating. Accordingly, the analysis of the plasma parameters obtained in those plasma discharges, during which the lithium content was exposed, has also shown a low hydrogen pumping effect by the freshly deposited lithium.

Chapter 6

Qualification of plasma-facing materials towards RFX-mod^2 upgrade

6.1 Introduction

RFX-mod graphite first wall has provided great benefits to the machine in terms of good response to high thermal loads that can reach tens of MW/m^{-2}. As a counterpart, the high hydrogen retention capability of carbon is associated to a high recycling factor often exceeding 1, and ultimately making it very difficult to control the plasma density, especially at high Greenwald fraction $n_e/n_G > 0.4$ (with n_e electron density and $n_G(10^{20}m^{-3}) = I_p/\pi a^2(m^2)$ the Greenwald density, which in RFPs as in tokamaks seems to be a limit in density [151]). Wall conditioning in RFX-mod has allowed to partially overcome the density control issue [60] and has permitted to explore high plasma performance parameters and improved confinement regimes. However the beneficial effects of all wall conditioning techniques in RFX-mod, such as the reduction in fuel recycling and impurity influxes, are circumscribed to a limited number of discharges with often detrimental side effects such as the non uniformity of the conditioning of the wall.

The carbon first wall issues encountered in RFX-mod have been experienced in other fusion devices in the past. In ASDEX [152] and JET [153], the use of carbon first walls has improved the performance significantly and enabled a steadily increase of the fusion performance. However, for further development of fusion plasmas in particular in view of reactor scale devices, a transition from carbon resulted unavoidable to fulfill a number of additional requirements that the carbon first wall could not meet, such as (i) a sufficient lifetime, (ii) a negligible or small long term retention of tritium (T) fuel in the wall components (<1 kg, for safety reasons and limitations in fuel supply), (iii) an acceptable neutron resistance connected with low long term activation.

The alternative plasma-facing materials that satisfy the previous requirements are high-Z materials, with tungsten (W) and molybdenum (Mo) the most promising candidates. W and Mo present the advantage of low or negligible sputtering at low plasma temperatures, a small uptake of T and the high melting point (2896 K and 3680 K respectively). The use of a full high-Z Mo wall has been tested already successfully in Alcator C-mod [154] and FTU [155], while large scale experience with W have only been obtained recently with the operation of ASDEX-Upgrade (AUG) with full W wall [156] and the JET ITER-like wall project [157].

With less challenging aims, a transition towards a metallic wall aiming at providing RFX-mod with a non-recycling first wall surface has been undertaken. The preliminary studies, tests and qualification of high-Z plasma facing materials are presented in this chapter of the thesis. In particular, following the well documented experience in FTU, AUG and JET, among W and Mo as leading candidates, the choice of W has been shortlisted for several reasons. First, the W melting temperature is higher (3680 K for W, to be compared 2896 K for Mo) and comparable to the carbon one (3800 K), allowing the sustainment of the highest power loads that in particular circumstances (e.g. stationary mode wall locking) can increase up to tens of MW/m^2. Moreover, due to the higher W mass, the reflection energy of the incident neutral atoms is higher (70% for W, 60% for Mo and 40% for C). To avoid excessive weight (not sustainable by the RFX mechanical structure) and cost, as for JET and AUG, the choice was made to coat the existing graphite tiles will W using optimized coating techniques.

In this chapter, the initial studies of compatibility of RFX-mod with a new high-Z first wall material, the elaboration of graphite W-coated samples, their exposure to RFX-mod plasmas and the evaluation of the coating properties pre and post plasma exposure are presented. In particular, in Section 6.2 the choice of W as the primary candidate for RFX-mod is discussed; in Section 6.3 the elaboration of the first W-coating mock-ups and the adhesion characterization is presented; in Section 6.4 the experimental campaigns performed for the exposure of the supplied W-coating prototypes are presented, in particular the exposure sample manipulator and the dedicated diagnostics are described; in Section 6.5 the post-exposure inspection and post-mortem analysis of the exposed W-coating prototypes are presented and the results are discussed.

6.2 The choice of W as an alternative among other prominent candidates

6.2.1 Material properties perspectives

From the material properties aspect, the most detrimental feature of the graphite first wall on RFX-mod operation is its characteristic property for H retention up to saturation. In RFX-mod the layer of hydrogen-saturated graphite can reach up to 0.1 μm and more severely, fuel retention is more

critical in amorphous carbon layers that are redeposited above the graphite tiles whose thickness can reach the mm range. The redeposition of carbon is the result of physical and chemical sputtering. With a graphite first wall, hydrogen saturation is reached at $3{\times}10^{20}$ atom/m^2. In RFX-mod, the total first wall surface is about 36 m^2 meaning that the wall can therefore retain up to 10^{22} atoms. These numbers can be even more important taking into account the formation of redeposition hydrocarbon layers.

Aside from the high fuel retention capability of graphite, as a counterpart its high sublimation temperature of about 4000 K has allowed to withstand the variable heat loads in RFX-mod that can exceed at given circumstances the tens of MW/m^2. The change of the carbon first wall in RFX-mod must be carried out with a material that allows on the one hand to scale down the retention and random release of hydrogen during plasma operation, and on the other hand the same material need to have a high melting point that can withstand the heat loads in question. In a laboratory experiment [158], deuterium (D) ion bombardment of different materials with different atomic number (Z) has shown that the Balmer series emission of deuterium increases with increasing Z. Considering that the emission relates to the reflection of recombined D atoms, the increase in emission with Z is due to higher reflection of D. In [159] similar measurements have been made on D_γ with W and C limiters. High-Z material compared to carbon are proved to highly reduce hydrogen retention.

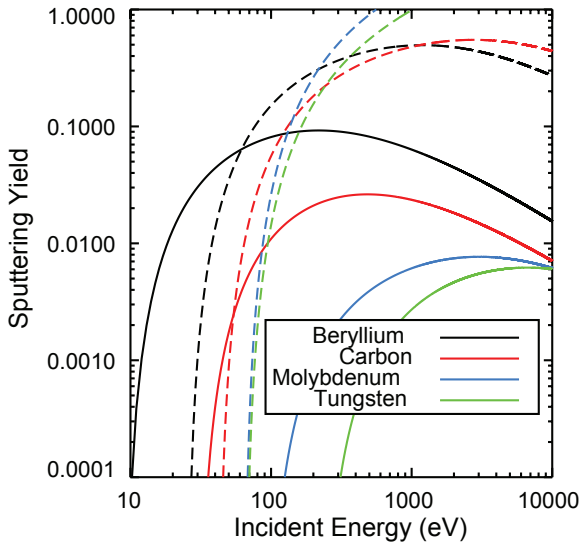

Figure 6.1: Physical sputtering yield: Bohdanski curves for beryllium, carbon, tungsten and molybdenum due to deuterium incidence (solid curves) and self sputtering (dashed curves) as a function of the incident ion energy (from Ref. [160]).

In light of these considerations, W and Mo appeared to be the most

prominent candidates to achieve such a task in RFX-mod: reducing hydrogen retention/recycling and withstanding high heat loads. Both materials have a high melting point (2896 K and 3680 K respectively) and a considerably lower physical sputtering yield. Typical physical sputtering yields from beryllium, carbon, molybdenum, and tungsten targets are plotted in fig. 6.1, resulting from incident deuterium (solid lines) and self sputtering (dashed lines) at normal incidence from Ref. [160].

The experience in FTU with Mo plasma facing components [155] has shown good benefits in terms of energy confinement, nonetheless boron wall conditioning of the wall remained mandatory to reduce plasma core contamination from Mo. Compared to W, Mo has a significantly lower melting temperature which can be an issue in RFX-mod. Moreover, studies on particle reflection of incident neutral hydrogenic atoms [161], have attributed the highest reflection coefficients to W, particularly at higher energies as it can be seen in fig. 6.2.

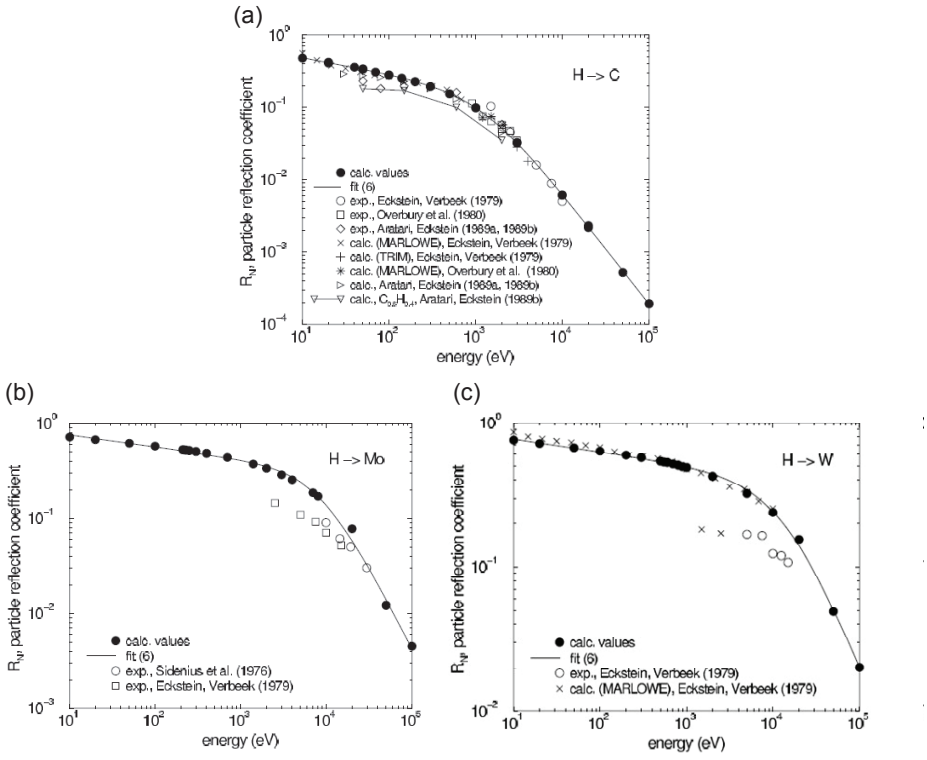

Figure 6.2: Particle reflection coefficients for hydrogen atoms on carbon (a), molybdenum (b) and tungsten (c) from ref. [161].

Subsequently to the previous considerations, W has been preferred to Mo to be the material on which compatibility tests and stepwise experimentation in RFX-mod have been carried out to gain confidence on the feasibility of the transition.

6.2.2 Effect of high-Z PFMs on RFX-mod plasmas

Theoretically, the higher particle reflection coefficients for W would lead to a stronger peaking of the plasma density profiles. In order to evaluate the actual effect on RFX-mod plasma density, a simulation has been obtained of a discharge where transport coefficients suitable to reconstruct the density behavior have been found (see ref. [36] and references therein). The latter was conducted assuming the same transport but changing the reflection coefficients of C (cf. fig. 6.2) with those typical for W. Fig. 6.3 shows the results of the simulation, where it can be indeed seen that the obtained density profiles with W are further peaked.

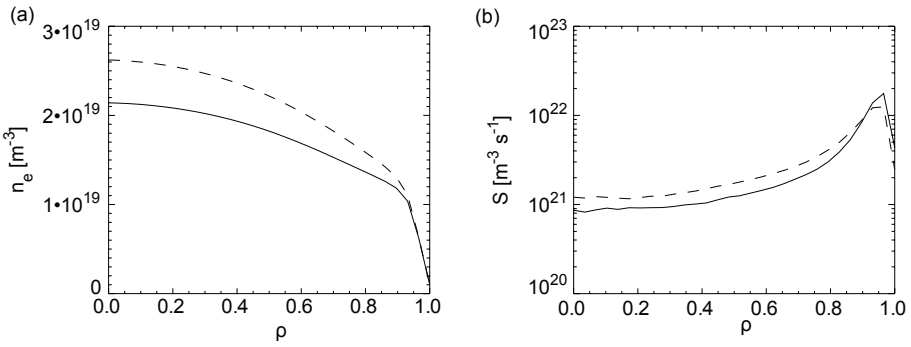

Figure 6.3: Left: simulated density profiles with carbon (solid line) and tungsten (dashed line) wall; right: corresponding profiles of the neutral source (taken from ref. [36]).

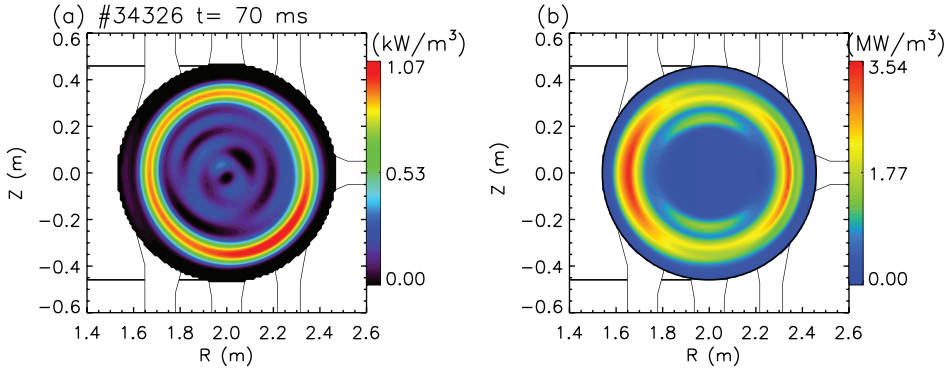

Figure 6.4: Tomographic inversion of soft x-ray emissivity (left) and total radiation (right) during a W laser blow off injection (taken from ref. [36]).

The main concern of high-Z PFMs is the strong poisoning effect of the plasma due to radiation cooling and the transport behavior in the plasma core. While a transition to a tungsten wall in RFX-mod would offer a lower

desorption surface than carbon, it also raises the issue of plasma contamination. To address the point, laser blow off experiments (LBO) injecting W to study the penetration of metals in the plasma core have been performed [36]. The resulting tomographic inversion of soft x-ray emission (frame (a)) and total radiation (frame (b)) after a W LBO pulse is shown in fig. 6.4. It can be seen that W does not penetrate into the plasma core. The previous experimental results confirm an already predicted result from RFP theory and simulations that anticipate the existence of a strong outward velocity developing outside the region of high temperature gradients.

6.2.3 Mechanical structure and existing PFCs perspective

The W Plasma First Component (PFC) transition experience in JET and AUG has shown the considerable cost of using bulk W PFCs. Moreover, the mechanical structure of RFX-mod vessel is not adapted to support the excessive weight of 2016 W-bulk tiles. Indeed, W has an electrical conductivity 200× larger than that of carbon based materials, which leads to considerably higher load of the support structures due to eddy currents and halo currents if bulk tungsten tiles are used. Furthermore, reinforcement of the support structures is very costly and time consuming. Therefore, similarly to the solution adopted in JET and AUG, the coating of the already present graphite tiles with thin W film is the solution that has been chosen to make the transition in RFX-mod.

Thin coatings (d<10 μm) are reliably produced by many suppliers on graphite using for example physical Physical Vapor Deposition (PVD) techniques. These thin coatings withstood power loads of more than 15 MW/m^2 up to melting conditions and the initial tests in ASDEX have shown a very good adhesion when produced by plasma arc deposition [162]. They even survived thermal shocks using an ion beam with power loads above 30 MW/m^2 for 0.3 s. In the case of JET, W coatings on Carbon Fiber Composites (CFC) PFCs resulted less reliable than on graphite: this was very likely due to the very inhomogeneous surface characteristics and the strong mismatch of thermal expansion coefficients that depend on the fiber orientation of the CFC. In the case of RFX-mod graphite however, both Mo and W have shown good match in terms of thermal expansion as shown in fig. 6.5. For reference, thermal expansion coefficients of low-isotropic graphite and JET CFC are plotted as well and the properties of RFX-mod graphite are summarized in tab. 6.1. One can notice that at higher temperatures >1000 K, W has a higher compatibility with RFX-mod graphite than Mo.

In order to comply with the mechanical structure limit, two approaches for testing W coating in RFX-mod have been undertaken: on the one side experiments have been conducted to define the minimum coverage of the vessel that would protect it in a limiter configuration, so to reduce the volume of the PFCs; on the other side, following the experimentation of the past years in JET and AUG, testing of W coatings on graphite samples and

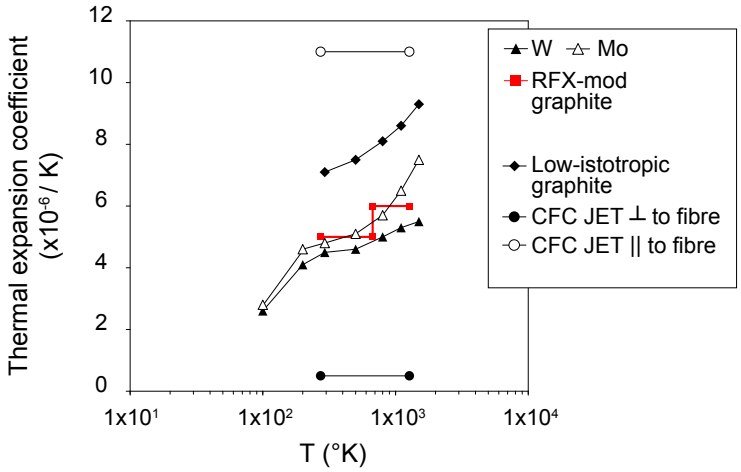

Figure 6.5: Thermal expansion coefficient for W (▲), RFX-mod graphite (■), Mo (△), low-istotropic graphite (◆), JET CFC perpendicular to fiber (●) and JET CFC parallel to fiber (○).

Table 6.1: Properties of RFX-mod polycrystalline graphite (manufacturer Carbone Lorraine (now MERSEN), type 5680PT)

Grain size	$\leqslant 50\ \mu$m
Density at 20°C	$\geqslant 1.75$ g/cm^3
Open Porosity	$\leqslant 15$ %
Electrical Resistivity	$\geqslant 10\ \mu\Omega$·cm
Coefficient of Thermal Expansion:	
20 to 400°C	$\leqslant 5\times10^{-6}$K^{-1}
20 to 1000°C	$\leqslant 6\times10^{-6}$K^{-1}
Thermal Conductivity	$\geqslant 70$ W/m·K
Tensile Strength	$\geqslant 20$ MPa

RFX-mod tiles with multiple coating techniques have been performed and are presented in this thesis. The experimentation is carried out with the goal to ultimately achieve a full coverage of the vessel with tolerable weight increase. The coatings are provided from different suppliers. Upon delivery, SEM cross-section images where analyzed to characterize the coatings structure and their adhesion properties have been evaluated by means of surface mechanical resistance using scratch tests [163, 164].

6.3 W-coating mock-ups elaboration and adhesion characterization

The experimental strategy adopted in RFX-mod is to progressively test W coatings of the order of 1 μm on sample size and real scale tiles from the existing graphite PFCs. The coating techniques that have been selected were chosen taking into account that in case of success, they could be easy applied at an industrial-scale to be able to entirely coat the 2016 set of RFX-mod graphite tiles. Although the coatings that have been targeted are mostly known techniques that were already implemented in AUG and JET which proved to deliver industrial scale number of tiles, other promising coatings technique that are still in their technical infancy were not discarded. The techniques that have been considered for coating RFX-mod graphite are Physical Vapor Deposition (PVD) and Plasma Spray (PS). Two type of PVD resulted possible to try in RFX-mod: the first one consists in a High Power Impulse Magnetron Sputtering (HiPIMS) deposition system from the IENI institute which is located at the same site of our laboratory; and the second PVD is the already tested coating technique in JET [165] named Combined Magnetron Sputtering and Ion Implantation (CMSII) (see ref. [166] and references therein), developed at MEdC-Romanian Euratom Association. With regard to the PS technique, this method allows to obtained thicker coatings in the range of 100 μm and is provided by the CSM laboratory in Rome. This technique has been successfully tested [167, 168] in AUG tokamak where about 200 graphite tiles coated with 0.5 mm W and provided from different suppliers have been installed in the divertor zone.

While the CMSII PVD technique has been already tested on CFC PFCs in JET and in AUG providing more than 1000 fine grain graphite coated tiles, the HiPIMS is an innovative PVD technique capable to provide high density W coatings with a controlled structure and morphology by applying a high bias voltage on the sample holder. Although, the latter is not yet designed for large scale industrial manufacturing, the technique has shown great interest for RFX-mod and graphite samples coated at varying bias voltage have been produced and tested for the first time in a fusion device.

6.3.1 CMSII coating prototypes for RFX-mod

a. Mock-up

The initial studies of the applicability of the Combined Magnetron Sputtering and Ion Implantation (CMSII) technology for RFX-mod have been made on a 30×30×6 mm graphite mock-up provided by the MEdC-Romanian Euratom Association. Fig. 6.6 shows the coating aspect of the sample.

Prior to coating, the sample underwent a serie of surface treatments undisclosed by the coating supplier. The sample was then dried in an oven

at 150°C for 4 hours. The sample was coated with 10-25 μm W coatings in similar conditions that were applied on JET divertor CFC tiles. A detailed description of the CMSII deposition method and equipment can be found in ref. [169]. In particular, the technique involves simultaneous magnetron sputtering and high energy ion bombardment. In the case of JET, W coatings on CFC with a thickness of up to ~25 μm have been produced. Direct deposition of W on CFC substrate resulted not successful because of the poor adhesion, but an intermediate Mo layer of 2-3 μm has solved the problem. The beneficial role of Mo was due to the adjustment of the thermal expansion mismatch between CFC and W (see fig. 6.5). The produced JET CFC tiles were successfully tested at 100 pulses of up to 16.5MW/m^2 for 1.5 s.

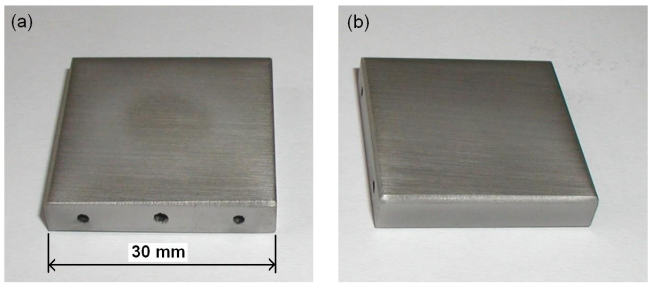

Figure 6.6: Graphite mock-ups W-coated with CMSII technology. Left image (a) shows the trace if the electron beam spot used for HHF tests carried out with at a temperature of 1250±6 °C.

For RFX-mod, although a less significant thermal expansion mismatch is expected between RFX-mod graphite and W, an intermediate Mo layer of 2-3 μm has been also adopted for initial tests.

b. Quality control

Glow discharge optical emission spectrometry (GDOES) has been performed by the prototype supplier to measure the coating thickness and assess the co-deposition of impurities within the W coating. For this purpose, a DA - 750 HP machine supplied by SPECTRUMA GmbH, Germany has been used on a titanium sample introduced during the coating course. The provided depth profiles of the W coating, Mo interlayer and detected impurities are shown in fig. 6.7.

The most significant contaminants found were C and O co-deposited from the ambient atmosphere of the facility. The impurities are only present on the surface and 1μm below of the coating with a maximum of ~15% and ~35% for C and O respectively, while the concentrations within the bulk W coating are negligible. Oxygen and carbon peaks are due to the surface contamination after exposure of the coating to the atmosphere.

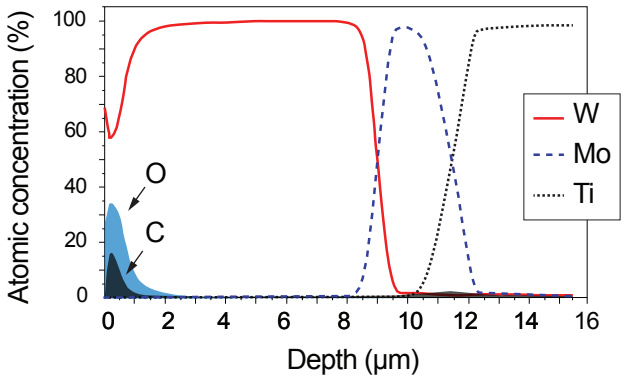

Figure 6.7: GDOES depth profiles of W, Mo, C and O for a W coating deposited on Ti substrate.

c. Thermo-mechanical properties

To test the resistance of the prototype to head loads, the produced coated sample has been tested by High Heat Flux (HHF) tests at the National Institute for Laser, Plasma and Radiation Physics - Romanian Euratom Association. To this aim, an electron beam High Temperature Test Facility (HTTF) has been used [170]. The main operating parameters of the electron beam were given by the supplier were: (i) I_{beam}: 44-46 mA; (ii) UHV: 16 kV; (iii) Pulse duration: 15±1 s; (iv) Inter-pulse duration: 37 s; (v) Thermal loaded area: ~140 mm^2; (vi) Peak temperature: 1250±6 °C; (vii) Minimum temperature: 270±10 °C; Total number of pulses: 500 (total cycling time for T>1000 °C: about 1 hour, equivalent with ~7000 pulses in RFX).

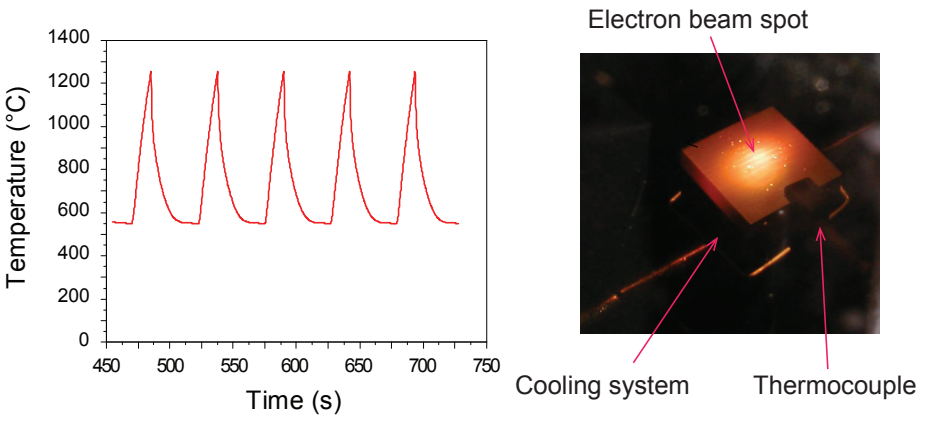

Figure 6.8: Time trace of a heat cycle performed at the High Temperature Test Facility (HTTF).

Fig. 6.8 shows the time trace for 5 pulses of the performed heat cycle. The electron beam spot area on the W coating surface is an ellipse with axes of ~5 mm and ~12 mm. This means a total surface area of about 141 mm^2. In order to get relevant information about the HHF resistance of the coatings, a large number of heating-cooling cycles (about 500) were applied to the coatings. The surface temperature was measured with an IR pyrometer in the wavelength range 1.45-1.8 μm. The emissivity was set to 0.50. The sample temperature was monitored with a thermocouple of C type (W5%Re/W26%Re) with a length of 150 mm and a diameter of 1.5 mm was inserted till the middle of the sample, parallel with the surface at 3 mm below the W coating.

After a number of testing cycles the samples surface was inspected by means of an optical 40× stereo-microscope in order to estimate any delaminated area. The inspection carried out at the end of test revealed two small spots with approximate dimensions 200×125 μm and 125×125 μm where the coating seems to be melted. No delaminations have been detected. This is a good behavior and it is similar to that of W coatings deposited on CFC material.

6.3.2 HiPIMS W-coating technique

a. Mock-up

Similarly to the CMSII prototype obtained from MEdC, a PVD W-coated graphite sample has been provided on site at Padova by IENI laboratory using the High Power Impulse Magnetron Sputtering (HiPIMS) technique. In addition, Mo-coated samples were also provided by the supplier for comparison purposes. The HiPIMS utilises extremely high power densities of the order of $kW \cdot cm^{-2}$ in short pulses (impulses) of tens of microseconds at low duty cycle (on/off time ratio) of < 10%. Distinguishing features of HiPIMS are a high degree of ionisation of the sputtered metal and a high rate of molecular gas dissociation which result in high density of deposited films and higher adhesion on of the deposited material. No particular surface pre-treatments of the surface were disclosed by the coating supplier. The provided coatings surface and cross section were characterized by Scanning Electron Microscopy (SEM) and subsequently scratch tests were carried out to test their mechanical adherence on the substrate.

b. Morphological characterization

Fig. 6.9 shows SEM cross-section and top-view micrographs of the W coating grown without a Mo interlayer. While the top-view of the W-coating is grown on a graphite substrate, the cross-sectional view is made on a W-coating grown on a Si substrate to allow an accurate determination of the coating thickness. The coatings were deposited on room-temperature substrates. The deposited coating with the applied low bias on the sample holder (the precise values of the voltage were non disclosed by the coating

institute) displays a dense structure with a relatively smooth surface in which the root mean square roughness (Rrms) value, measured with a fixed area of 2μm $\times$ 2μm, was 15.5 nm. On the other hand, the coating shows a continuous columnar structure that can be seen from the cross-section view, a feature that is very similar to the W-coating aspect obtained with a sputter-deposition technique tested on graphite samples in AUG [171]. The sputter-deposition technique in AUG resulted unappropriated as the columnar aspect of the deposition lead to the quick delamination of the film when a thickness threshold was exceeded. Moreover, an intrinsic surface roughness has been observed with the same technique. The reason of the loss of adhesion was related to the formation of excessive compressive stress. Here in the case of the HiPIMS deposition technique, in order to assess the delamination of the coating, scratch tests were performed and will be discussed in the following paragraph.

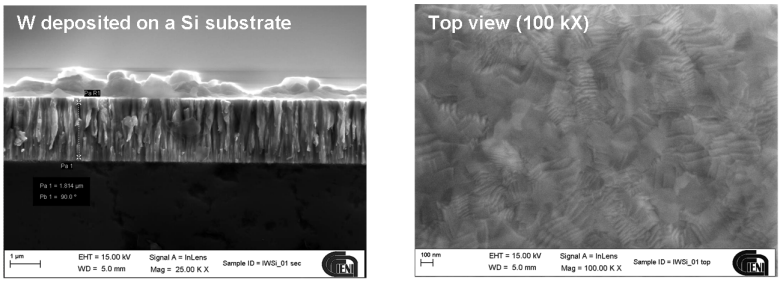

Figure 6.9: SEM micrograph of the W coating deposited by High Power Impulse Magnetron Sputtering (HiPIMS) grown with a low applied deposition bias. Left: cross-section view; right: top-view. Note the columnar structure in the cross-section image.

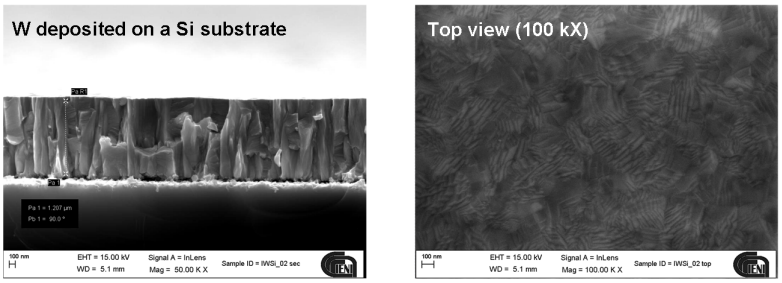

Figure 6.10: SEM micrograph of a W coating deposited by HiPIMS grown at a high applied deposition bias. Left: cross-section view; right: top-view.

After providing the first W-coating, a second try has been attempted with a coating performed at a higher bias of the sample holder (voltage value undisclosed by the institute). Fig. 6.10 shows SEM cross-section and top-view

micrographs of the W coating grown at the higher bias. As it can be seen from the comparison of the cross-section views of the two coatings, the higher bias coating displays a thicker and a more dense structure. The columnar feature is present in both cases with a finer aspect when a lower bias is applied.

c. Mechanical adherence characterization

The tests of the mechanical adherence have been performed by a parameter study on a series of W-coatings with and without Mo interlayer. Scratch test measurements were made in compliance with the European standard UNI EN 1071-3-2005 by using a CETR UMT-2 tester equipped with a Rockwell C standard spherical diamond indenter of 50 μm radius and a 400× optical microscope. The first sample that has been tested is coated with 2.4 μm of W without Mo interlayer and the results of the test are shown in fig. 6.11.

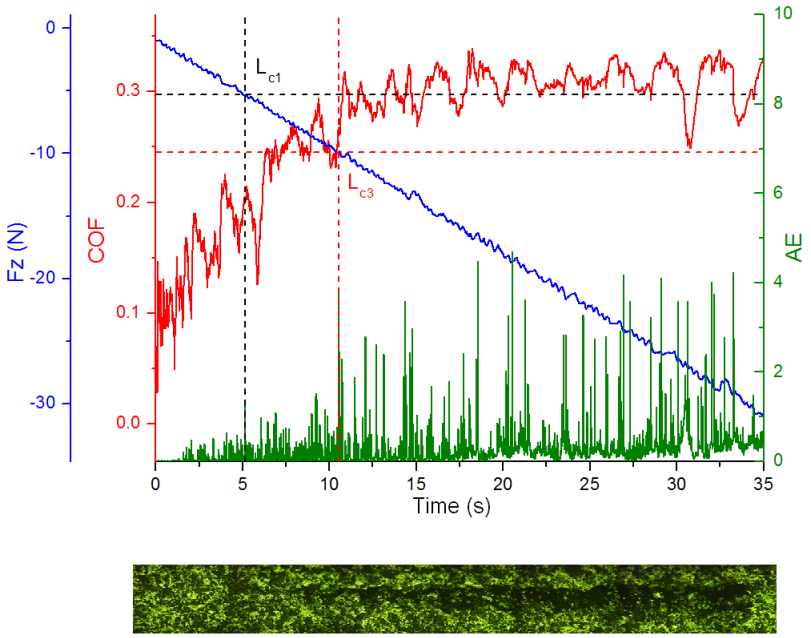

Figure 6.11: Scratch test diagram of a 2.4 μm W-coating. An optical micrograph of the track is shown at the bottom. Red line: coefficient of friction (COF) as a function of time; green line: acoustic emission (AE) as a function of time; blue line: normal load (Fz) as a function of time.

The coefficient of friction (COF), the acoustic emission (AE), the indenter penetration depth (z) and the normal load (Fz) are reported as a function of time. An optical micrograph of the scratch is also reported. The scratch is performed by Progressive Load Scratch Test (PLST) mode in which the applied normal load increases linearly with time. The slide

velocity of the indenter and the applied load were fixed to 9.0 mm.min^{-1} and 9.0 N.min^{-1}, respectively, starting from a contact load of 0.4 N. After a short initial transient period, COF was observed to increase with the load until a sharp change of was observed. In the region before the L_{c1} point, as can be observed in the scratch micrograph, the coating undergoes a plastic deformation without any cracks and the tip interacts mainly with punctual defects of the coating. Looking over the optical micrograph in fig. 6.11, a groove within the scratch track is found from point L_{c1} onward, which becomes much more pronounced as the applied load increases. The L_{c1} point refers to the first degree 'critical load' which relates to the smallest load at which a first recognizable failure of the coatings occurs. A second degree critical load L_{c2} is defined when regular occurrence of greater failure of the coating is observed. The previous test has been performed under the same conditions varying the biasing on two other samples where a Mo layer has been introduced with different thicknesses. In tab. 6.2 the different thicknesses of Mo and W layers and the critical loads valued obtained from the scratch tests are shown, and in fig. 6.12 the respective optical micrographs are shown.

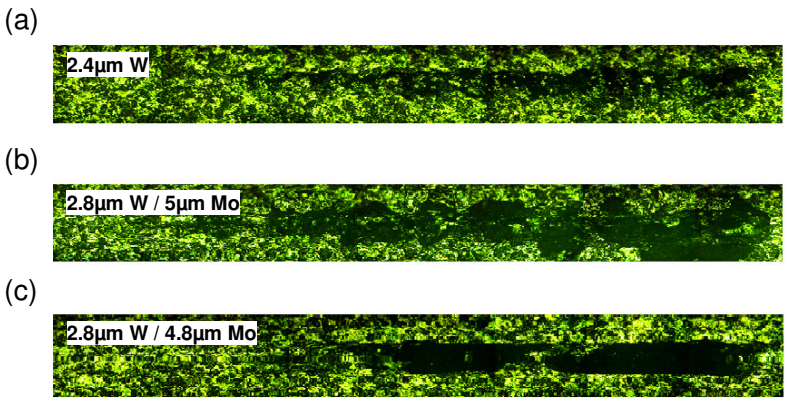

Figure 6.12: Scratch test optical micrographs for (a) 2.4 μm W-coating obtained without Mo interlayer with no bias, (b) a 2.8 μm W-coating with a 5.0 μm Mo interlayer and low bias, (c) a 2.8 μm W-coating with a 4.7 μm Mo interlayer and high bias.

Table 6.2: Parameter study: W/Mo thickness, first and second degree critical loads and sample bias.

Coating ID	Mo layer (mm)	W layer (mm)	L_{c1} (N)	L_{c2} (N)	Bias
IW-07	-	2.4	5.32	9.87	-
IW-09_IMo-02	5.0	2.8	3.05	6.51	low
IW-09_IMo-03	4.7	2.8	3.33	11.66	high

W coatings without Mo interlayer (sample IW-07) are mechanically more resistive to first stage fractures whereas coatings with Mo interlayer (samples IW-09_IMo-02 and 03) showed greater resistance to higher mechanical loads provided that a higher bias voltage was applied (sample IW-09_IMo-03).

6.3.3 Plasma Spray (PS) W-coating technique

A known characteristic of plasma spray coatings is their porosity, which can vary within a wide margin, depending on the spray parameters, as opposed to PVD coatings that are typically very dense (average porosity below 1%). The experience with PS W-coatings in fusion during the past two decades has shown that the porosity in plasma spray layers reduces the mechanical strength and thermal conductivity in comparison to bulk tungsten and leads to a higher hydrogen retention [172].

For RFX-mod the applicability of this technique resides in its capability to produce a large number of coated tiles in a short process time. A national provider, the CSM (Centro Sviluppo Materiali) in Rome has provided similarly to the previously presented PVD technique, a 5×4 cm RFX-mod coated graphite sample (fig. 6.13). The equipment shown in fig. 6.14 has been used to manufacture the coating. It is an industrial scale Controlled Atmosphere Plasma Spray (CAPS) manufactured by Sulzer Metco whose main working characteristics are: 80 KW plasma torch, 7 m^3 vessel, spraying pressure 10-2000 hPa, argon and hydrogen working gases. The technique used here is named Inert gas Plasma Spray (IPS) in which the spraying process is carried out in an inert gas atmosphere (mostly argon) at higher pressures (here 120 hPa), without a subsequent thermal treatment, as opposite to the Vacuum Plasma Spray (VPS) in which the spraying process is carried out in a controlled low-pressure atmosphere with a subsequent thermal treatment.

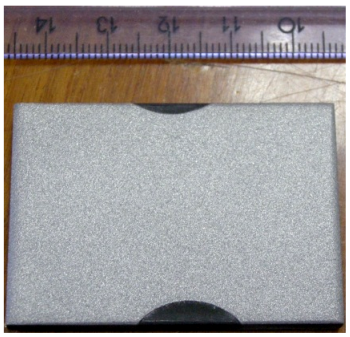

Figure 6.13: Top view of a 5×4 cm W-PS coated RFX-mod graphite mock-up.

The first W coating was achieved with a surface of about 20 cm^2. Argon gas was used to fill the chamber at a pressure of about 120 hPa. The Substrate distance from the torch was about 120 mm. The final achieved thickness of

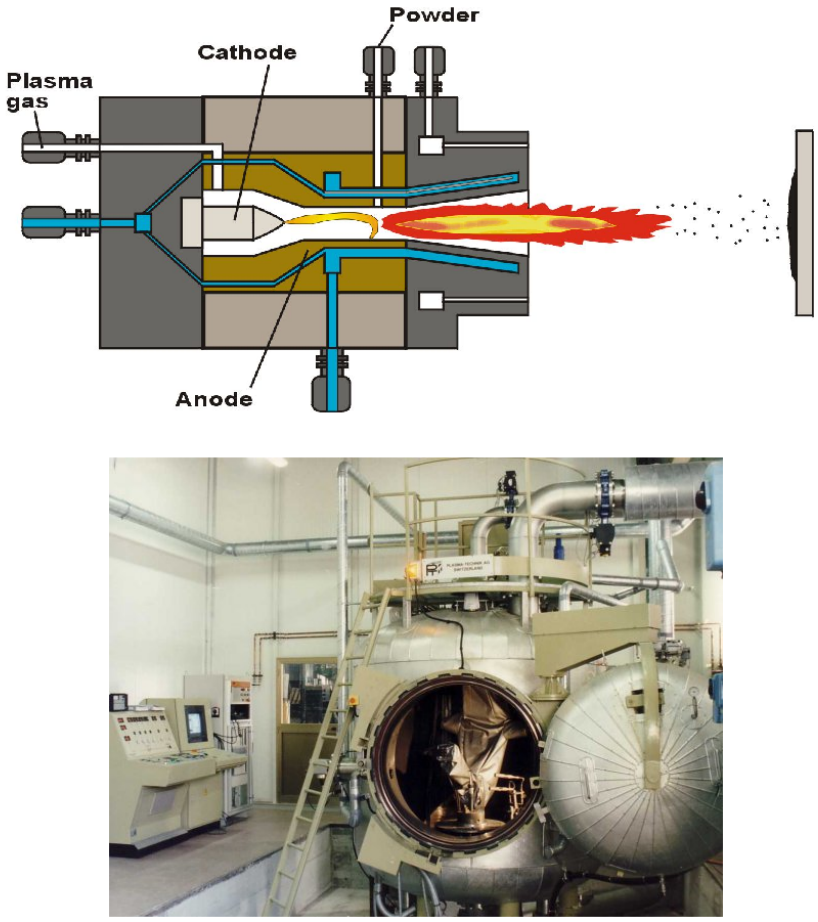

Figure 6.14: Controlled Atmosphere Plasma Spray facility at CSM (Centro Sviluppo Materiali), Rome.

the coating was 130 μm. To increase the roughness of the surface and enhance coating adhesion, the sample was sand blasted at low pressure (3-4 bar). Both W coatings with and without Mo have been successfully achieved.

6.4 Exposure to RFX-mod power plasmas

Two approaches have been adopted to test the exposure of W-coatings to RFX-mod plasmas. On the one hand, after the evaluation of the most adequate coating technique to be tested in a first step, 5×6 cm samples cut from spare blocks of RFX-mod graphite have been designed and provided to the coating suppliers in order to be coated. On the other hand, in RFX-mod it has been chosen to also test the W-coatings on a full scale graphite tiles, so in addition to the small samples, the suppliers have provided tiles that are similarly W-coated.

6.4.1 Exposure manipulator and sample/tiles prototypes

a. LISA and samples design

To expose W-coated graphite sample, a Large Instrumented SAmple (LISA) manipulator has been arranged in RFX-mod along with a set of dedicated diagnostics. LISA manipulator allows to easily mount and unmount multiple samples and perform exposure to RFX-mod plasmas at variable distance from the first wall envelope. Two 5×6 cm samples at the same time or one 10×6 cm sample can be exposed. In particular, the design of the manipulator includes an integrated Thermal Desorption Spectroscopy (TDS) diagnostic that will allow the *in-situ* measure of the gas retained by the samples. Fig. 6.15 displays the arrangement of the LISA samples in RFX-mod vessel.

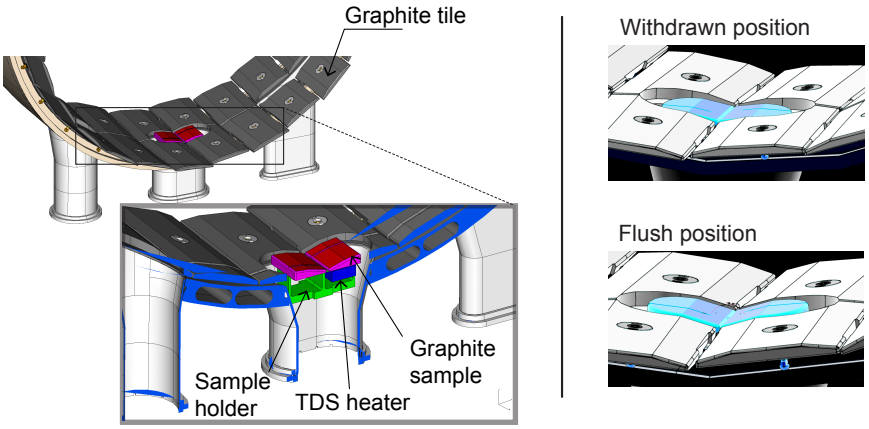

Figure 6.15: Large Instrumented SAmple (LISA) manipulator for W-coating exposure to RFX-mod plasmas.

As it can be seen, the samples can be inserted flush with the graphite floor or slightly withdraw, so for this purpose they were accordingly designed to fit into the manipulator and shaped similarly to RFX-mod tiles shaping that

allows to improve plasma-wall interaction by reducing the heat flux peaking on leading edges [173]. In addition, in order to have a reference for thermo-camera measurements, a portion of the sample surface defined by a groove has been designed to separate the part to be masked during the coating process. Fig. 6.16 displays the design of the samples and the two-fold arrangement in RFX-mod.

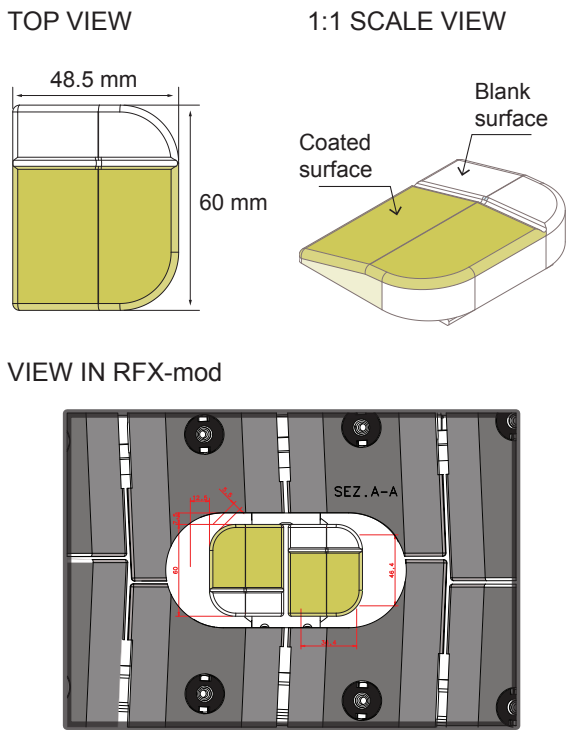

Figure 6.16: Graphite sample design for W-coating exposure.

b. Full-scale prototypes

As a first step for testing W-coatings in RFX-mod, only the two PVD W-coatings techniques presented earlier have been chosen for manufacturing the first prototypes. The Plasma Spray (PS) coating alternative will be tested in a next step. Both 5×6 cm samples and tiles along with their fixing keys W-coated were provided from the CMSII coating supplier. Fig. 6.17 displays images of the LISA samples and four W-coated RFX-mod tiles. For easy access and maintenance, the tiles selected to be coated were chosen among the closest to a vessel duct. They were therefore adequately cut in to fit the duct geometry. HiPIMS coating supplier has provided similar prototypes.

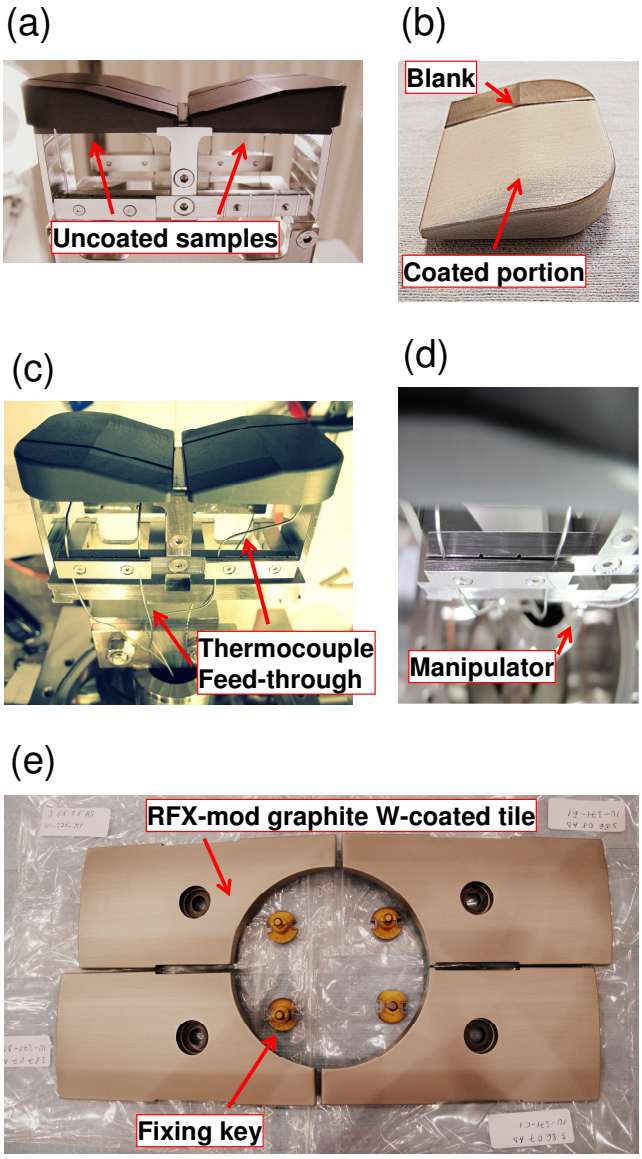

Figure 6.17: LISA graphite samples and W-coating prototypes provided from the CMSII coating supplier. (a) twin pristine LISA samples, (b) W-coated sample with a blank portion, (c) LISA sample arrangement on manipulator and thermocouples, (d) manipulator top view, (e) 4 W-coated RFX-mod graphite tiles fitting to a port geometry.

6.4.2 Exposure experimental campaigns and dedicated diagnostics

a. Diagnostics for coating exposure

A set of dedicated diagnostics has been arranged along with the Large Instrumented SAmple (LISA) manipulator. In particular, the diagnostics set include:

(i) Visible/near IR imaging of the samples during exposure by fast visible tele-camera, with frame frequency up to 20 KHz.
(ii) Fast NIR pyrobolometer (OPTRIS CT 3 MH SF, frequency 5 KHz, wavelength 2.3 mm) and a slow IR thermo-camera (FLIR SC655, max frequency 200 Hz at resolution 640×220, spectral range 7.5-13 mm) for surface temperature measurements.
(iii) Set of thermocouples embedded in samples (type K, ⊘=0.75 mm, max frequency: ~1 Hz) for bulk temperature measurements.
(iv) Two spectroscopic lines for H and impurity (C, O, W) influx measurements.

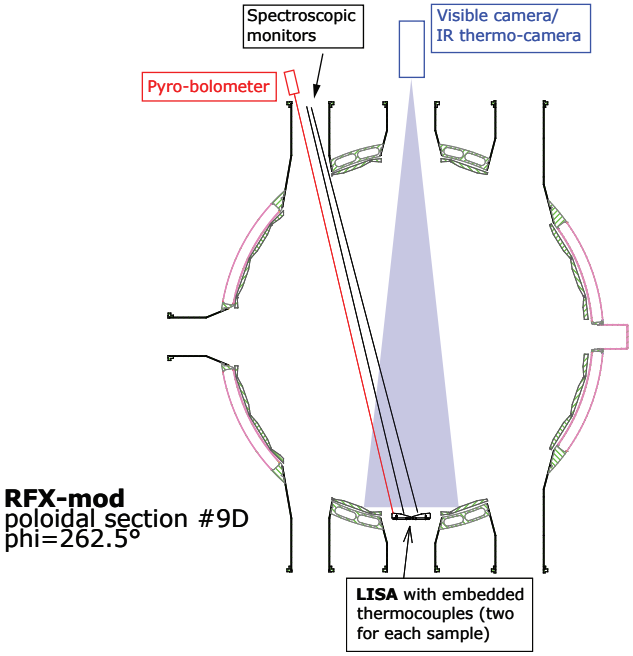

Figure 6.18: Diagnostic setup arranged for plasma exposure of W-coatings in RFX-mod.

All the mentioned diagnostics are arranged at the same section of the LISA manipulator. Fig. 6.18 shows the setup at the 9D section of RFX-mod vessel. A Thermal Desorption Spectroscopy (TDS) diagnostic has been also

designed and incorporated in the sample manipulator initial design, but will be only available for future tests. Fig. 6.19 shows the interaction of the plasma with the LISA samples at two different instants before and during the strong interaction while fig. 6.20 displays measurements of sample temperature by the infrared camera.

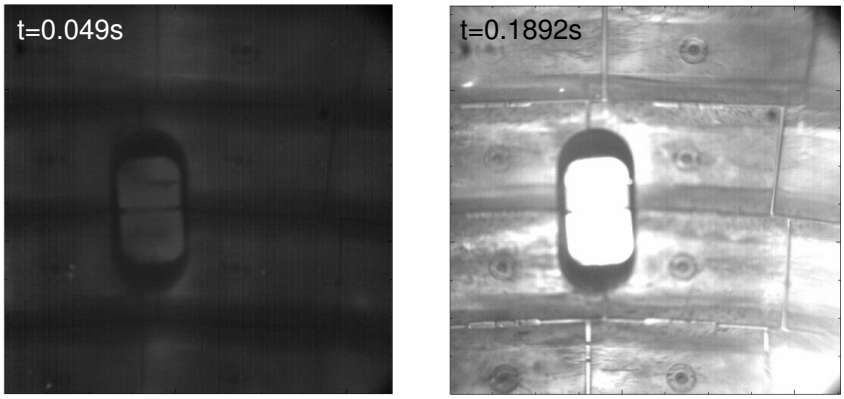

Figure 6.19: Visible fast-camera images of the two LISA samples at non-interacting (left) and interacting (right) times.

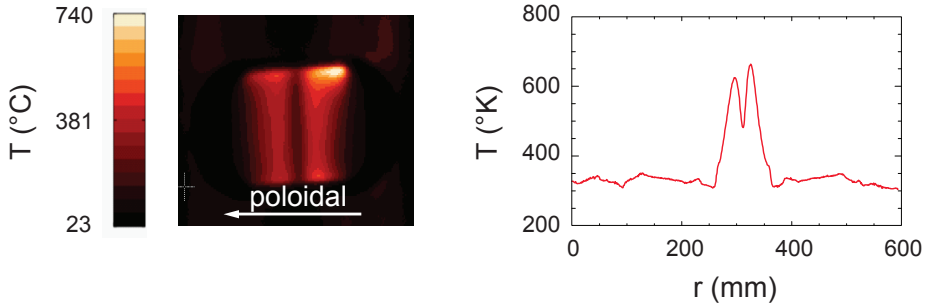

Figure 6.20: Temperature profile measurements by the IR camera on a sample exposed to a plasma discharge.

b. Plasma exposure experimental campaigns

The exposure of the PVD W-coatings using the CMSII and HiPIMS technologies has been the subject of two different experimental campaigns in RFX-mod. In a first step, the LISA 5×6 cm samples were exposed in June 2013 to H_2 discharges in order to take advantage of the manipulator

capabilities in terms of diagnostics and distance from the graphite floor of the exposed sample surface. This first campaign involved the exposure of samples coated both with the CMSII and HiPIMS coating techniques and also the exposure of pristine graphite samples (a summary of the coatings properties and exposed samples is shown in tab. 6.3). Following the first experience with the exposure of LISA samples, in October 2013 a second experimental campaign has been dedicated to the exposure of full scale W-coated graphite tiles. During the latter, only the CMSII technique has been tested and the coated tiles were exposed to several types of plasmas for a total period of about 3 months of plasma operation.

Table 6.3: LISA blank/W-coated samples exposed during June 2013 experimental campaign.

Technique	Coating thickness Mo(μm)/W(μm)		Plasma	# of shots	Dist. above
	LISA pos.1	LISA pos.2			floor (mm)
Blank:					
	Bulk-C	Bulk-C	H_2	40	0
CMSII:					
	3 / 15	3 / 20	H_2	12	0
	3 / 15	3 / 20	H_2	2	1
	pristine	3 / 15	H_2	15	0
Hi-PIMS:					
	0 / 10	6 / 10	H_2	15	0
	0 / 10	6 / 10	H_2	1	1

During the first experimental campaign the samples were exposed at two different distances from the first wall floor: flush and 1 mm above the graphite floor. The latter approach was undertaken in order to enhance the interaction of the plasma with the samples. For the same purposes, in RFX-mod it is possible to create an enhanced plasma wall interaction at a given position making use of the feedback control MHD system of the machine. The active saddle coils system allows to induce a localized small cyclic perturbation of the magnetic field which can increase the particle fluxes to as high as $2{\times}10^{22}$ $m^{-2}s^{-1}$ and generate periodic heating of the surface with a temperature range of several hundreds of degrees. Fig. 6.21 displays the time behavior of the main plasma parameters during a typical experiment with induced magnetic perturbations. The coated samples have been exposed during the experimental campaign to series of about 15 discharges each.

During the second experimental campaign starting in October 2013, W-coated RFX-mod graphite tiles where exposed to normal plasma operation in the two possible magnetic configurations of RFX-mod. In RFP configuration, exposure was performed in H_2, D_2 and He plasmas in a wide range of plasma currents (from 100 to 1500 kA) and for a total of about 200s of plasma. In tokamak configuration, experimentation was made in D_2 plasmas at low current (about 100 kA) for about 250 s of plasma. The tiles were exposed to a total 3 months of plasma operation, after which they were removed for

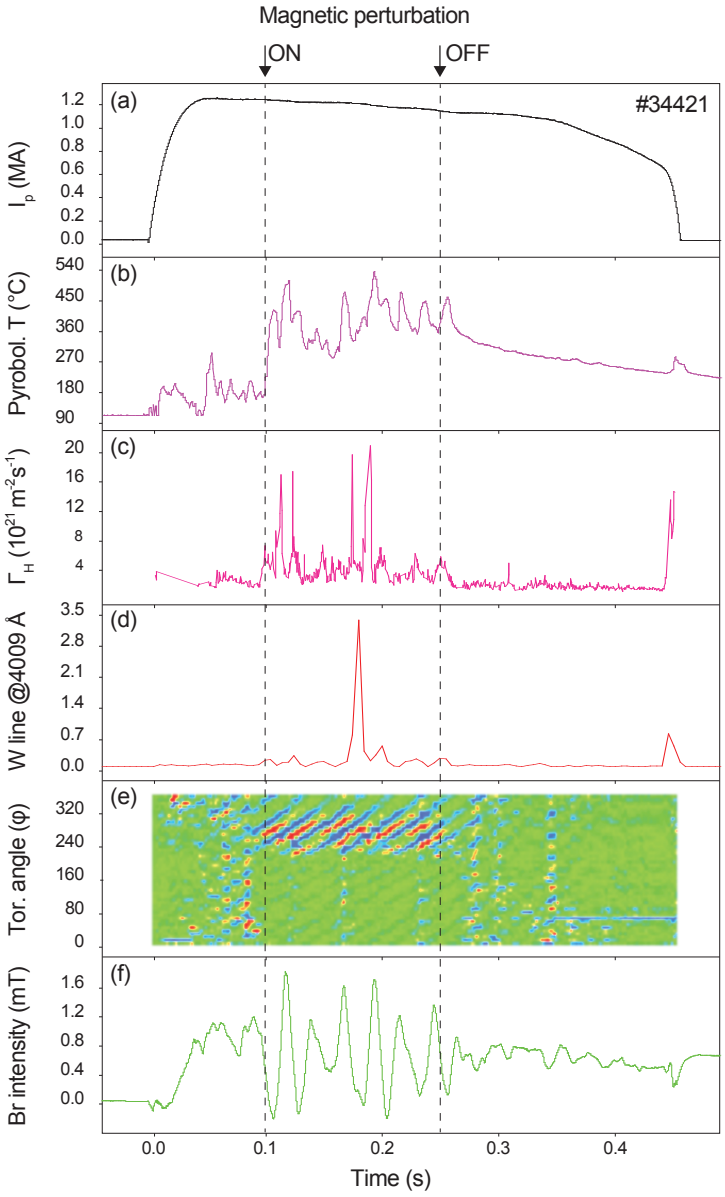

Figure 6.21: Typical experimental campaign with induced magnetic perturbation for LISA W-coating testing in RFX-mod. (a) plasma current, (b) surface temperature by pyrobolometer, (c) hydrogen influx, (d) W spectroscopic line, (e) and (f) m=1 modes intensity.

post-mortem analysis. An image of the 4 W-coated tiles arranged close to a port hole in RFX-mod is shown in fig. Fig. 6.22.

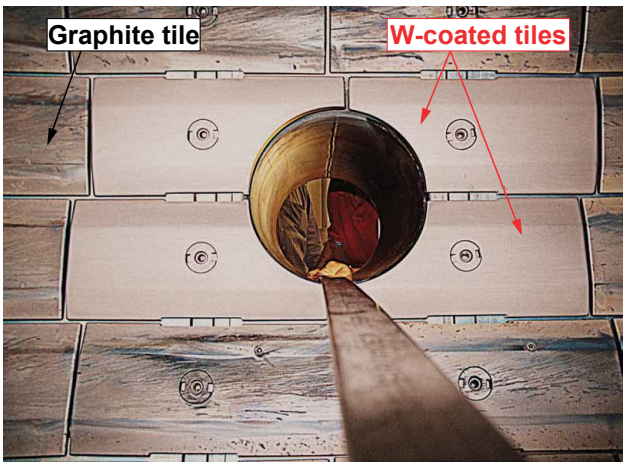

Figure 6.22: 4 RFX-mod tiles W-coated by CMSII technology set up nearby a port hole for easy mounting and removal access.

6.5 W-coatings post-exposure inspection

6.5.1 Bulk uncoated LISA samples

Prior to the exposure of the W-coated LISA samples, bulk uncoated samples where tested using the LISA manipulator in order to evaluate plasma interaction that occur at the manipulator toroidal location and assess the effect of the magnetic perturbation on a blank sample.

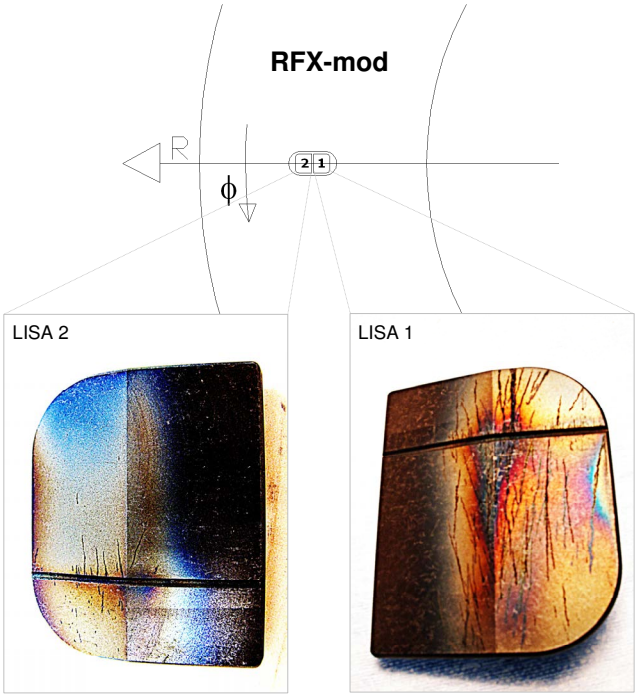

Figure 6.23: Images of graphite uncoated samples exposed during about 40 H_2/He plasma discharges. Left panel: outer position; right panel: inner position.

The two bulk-C samples were also exposed for optimizing plasma discharges and test the dedicated diagnostics. About 40 H_2/He plasma discharges with plasma current ranging between 1.2 and 1.5 MA were carried out in total. After this first test, the samples were removed and photographed and the images of the surface are shown in fig. 6.23. Evidence of strong interaction with plasma can be seen on both samples with a stronger footprint on the sample that is at the most inner position of the vessel. Deep arc traces can be seen, particularly localized at the dig that is carved on the surface of the samples to separate coated and uncoated areas when W-coatings are exposed.

6.5.2 CMSII W-coated LISA samples

As described in tab. 6.3, two types of CMSII W-coatings were exposed to 12 H_2 plasma discharges: a first sample consisted in a 15 μm W-coating with 5 μm of Mo interlayer and a second prototype had a thicker 20 μm W layer. The same samples were also exposed to two discharges with the manipulator position at 1 mm above the graphite floor for greater interaction with the plasma. Fig. 6.24 displays the post exposure surface of the two prototypes. The details of the sequence of the performed H_2 plasma discharges to which the samples were exposed are:

(i) 3 shots: I_p = 1 MA, duration = 300 ms, first wall = 0 mm
(ii) 2 shots: I_p = 1 MA, duration = 300 ms, first wall = 1 mm
(iii) 1 shots: I_p = 1.5 MA, duration = 250 ms, first wall = 0 mm
(iv) 6 shots: I_p = 1.5 MA, duration $\leqslant$ 50 ms, first wall = 0 mm

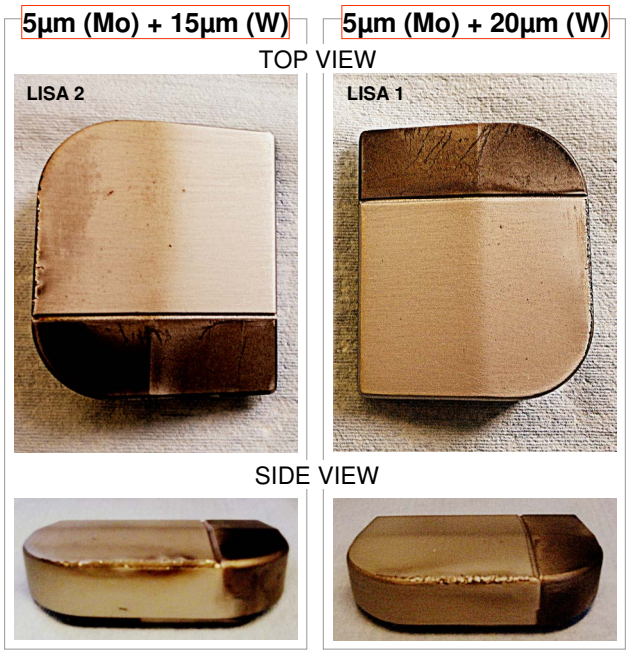

Figure 6.24: Images of CMSII W-coatings exposed to a series of 12 H_2 plasma discharges. Left panel: (15 μm W + 5 μm Mo) sample exposed at LISA post. 2; right panel: (20 μm W + 5 μm Mo) sample exposed at LISA post. 1.

The visual inspection of the two samples shows that both coatings were eroded at the edge while the surface has no apparent damage. As opposite to the uncoated samples whose results were presented in the previous section, the W-coated sample do not show the presence of arcs anywhere on the surface or the dig location. Moreover, the most prominent feature is that the less thick coating (left panel fig. 6.24) has been a slightly more damaged at the

edges with a darker surface near the damages spots. Nonetheless, overall both samples have shown good resistance. For reference, the graphite samples were pre-treated in this case before the CMSII W-coatings were applied.

6.5.3 HiPIMS W-coated LISA samples

During a second experimental day of the campaign, the HiPIMS W-coatings were exposed similarly to above. Two types of coatings were tested: a first prototype consisted in a 100% W-coating with a 10 μm thickness and a second prototype had in a addition a 5 μm Mo layer between C and W. In this case as opposed to the CMSII W-coatings, for greater interaction with the plasma the samples were exposed to only one discharge with the manipulator position at 1 mm above the graphite floor. Fig. 6.25 displays the post exposure surface of the two prototypes.

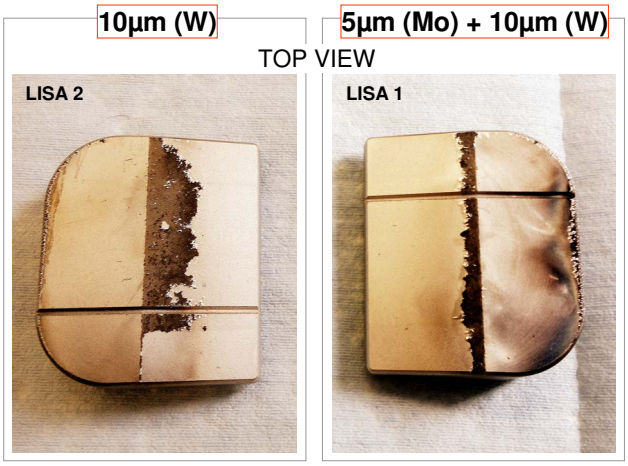

Figure 6.25: Images of HiPIMS W-coatings exposed to a series of 14 H_2 plasma discharges. Left panel: (10 μm W) sample exposed at LISA post. 2; right panel: (10 μm W + 5 μm Mo) sample exposed at LISA post. 1.

In total, the samples were exposed to 15 H_2 plasma discharges with varying parameters:

(i) 7 shots: I_p = 1 MA, duration = 400 ms, first wall = 0 mm
(ii) 1 shots: I_p = 1 MA, duration = 400 ms, first wall = 1 mm
(iii) 1 shots: I_p = 1.5 MA, duration = 300 ms, first wall = 0 mm
(iv) 6 shots: I_p = 1.5 MA, duration $\leqslant$ 50 ms, first wall = 0 mm

Both HiPIMS W-coatings have been severely damaged both on the surface and at the edges with several spots where the films were delaminated and melted. In particular, the one that has no Mo interlayer has shown a greater delamination stage. Overall, surface delamination is seen to occur at the change of the surface gradient and was observed to happen from the first

plasma discharge to which the samples were exposed. For this technique it turned out therefore, that surface smooth angles are crucial for the thermo-mechanical resistance of the coating. Moreover, the samples were not pre-treated to enhance the adhesion of the coatings.

6.5.4 CMSII full scale W-coated tiles

The exposure of full scale RFX-mod W-coated graphite tiles has been performed with coatings provided from the CMSII coating supplier. Similarly to the LISA samples, the tiles were pre-treated and coated with a 20 μm of W coating and a 5 μm interlayer of Mo. As shown earlier in fig. 6.22, 4 tiles were mounted near a port hole allowing an easy removal after exposure. From October 2013 onward, the tiles were exposed to three months of RFX-mod plasma operation (a total of 733 discharges, 450 seconds). During this period, they have been exposed to several types of plasmas in the two possible magnetic configurations of the machine.

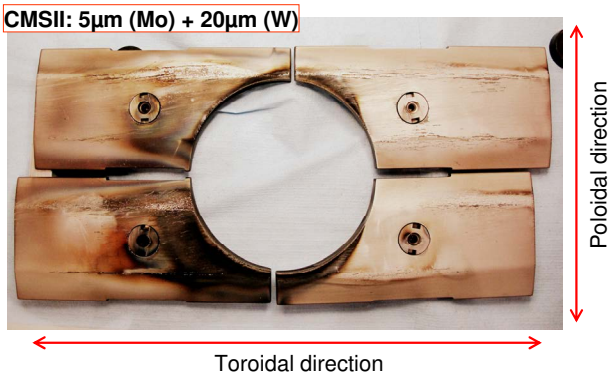

Figure 6.26: Picture of the 4 W-coated RFX-mod tiles upon retrieval after plasma exposure.

Thermal loads at the first wall in the RFP configuration can locally reach values as high as tens of MW/m^2, whereas in the tokamak configuration they are much lower. From the magnetic point of view, the main difference in the RFP and tokamak configurations is the direction of the magnetic field at the wall, toroidal in the tokamak case and poloidal in the RFP case. Fig. 6.26 displays the 4 tiles imaged after the 3 months of plasma operation. Fig. 6.27 shows more details about the occurred damages on the upper-left tile.

The visual inspection shows different failures: (i) net erosion at the edges of the tiles (with removal of the coating), especially nearby the central port-hole; (ii) arc traces that are probably deeper than the coating layer; (iii) areas of elongated shape in which the coating was removed; (iv) melting spots nearby large damaged areas; (v) carbon redeposition over wide areas.

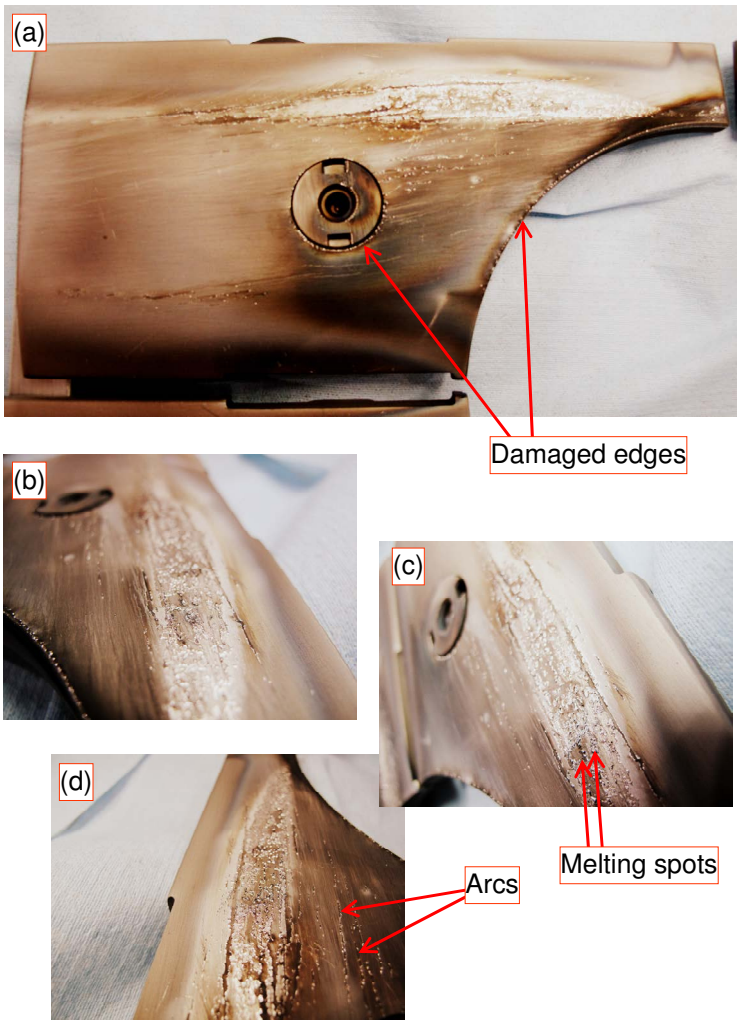

Figure 6.27: Higher resolution images of the upper-left W-coated RFX-mod graphite tile.

6.5.5 *Ex-situ* post-mortem analyses

The *ex-situ* post-mortem analyses have been made on the full-scale tiles prototypes coated by the CMSII coating technique. The analyses were performed after the second plasma exposure experimental campaign which consisted in about 3 months of plasma operation. The surface analysis techniques used here were mainly SEM and optical microscopy in addition to scratch tests for adhesion characterization.

a. Optical microscopy

Fig. 6.28 displays an optical microscopy survey of different spots on the surface of the upper-left tile. The latter was chosen as it presented most of the observed macroscopic damages.

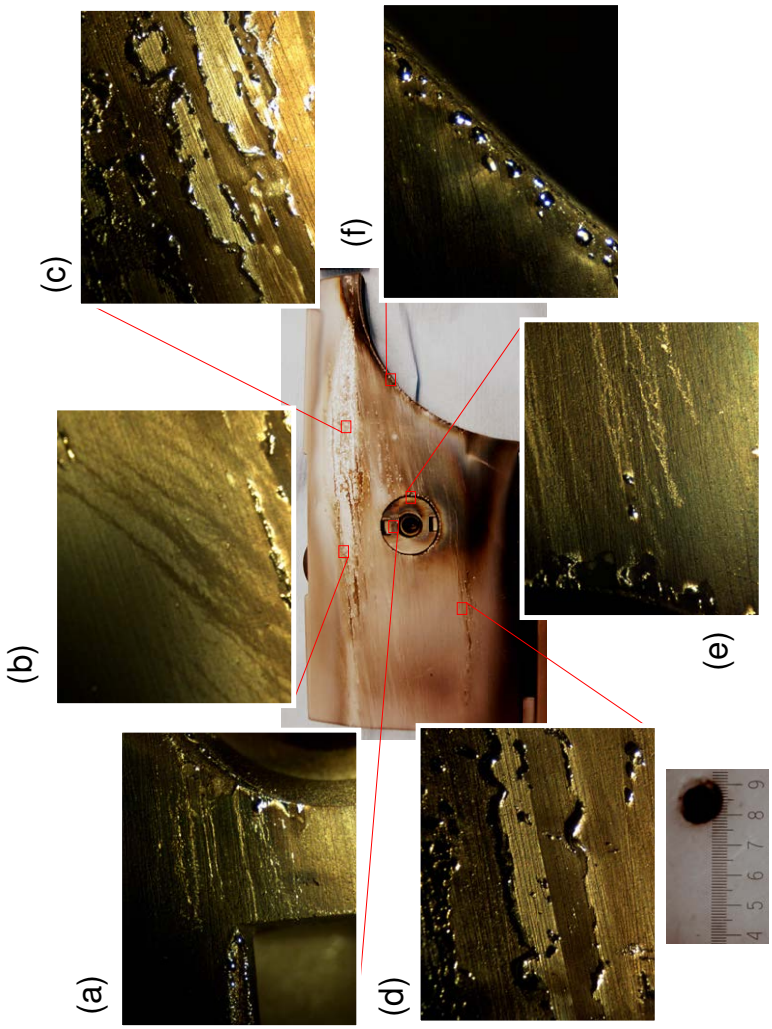

Figure 6.28: Optical microscope images of six spots on the surface of the upper-left tile (see fig. 6.26) coated with a 20 μm of W coating and a 5 μm interlayer of Mo then exposed to 3 months of plasma operation in RFX-mod.

The careful examination of the images shows melting of the W-coating at every imaged spot. W melting is often localized at the edges but also in areas of elongated shape in which the coating was removed (fig. 6.28 (c)

and (d)). Also, where melting spots are localized, often arcing traces are associated to those locations which may infer that melting is a consequence of arcing. In addition, to the melting spots, in some cases the coating has appeared completely removed. In other cases delaminations occurred with W chips loosing the contact with the substrate (fig. 6.28 (b)). Furthermore, in some cases, a number of spots can be seen where the coating is displaced, very likely subsequent to melting or delamination. The images show also a very weak adhesion of the coating as large surfaces where the film has been removed appear similar to a pristine graphite surface without any trace of the coating. The long delaminated shapes are initiated at the boundary of line traces that are the made by the pre-treatment of the surface before coating the tile.

b. Scanning Electron Microscopy (SEM) microscopy

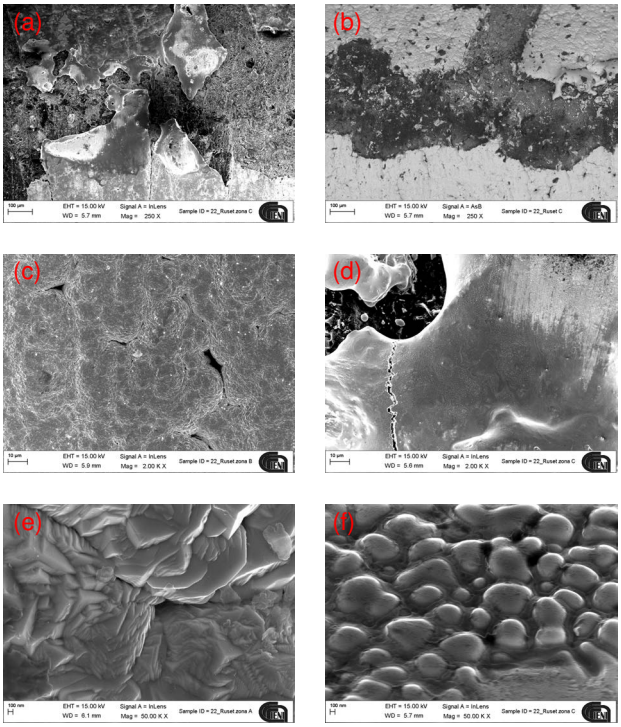

Figure 6.29: SEM images post plasma exposure of the upper-left tile coated with a 20 μm of W coating and a 5 μm Mo interlayer: magnification (a) and (b) 250×; (c) and (d) 2000×; (e) and (f) 50000×.

Fig. 6.29 shows SEM images of the upper-left tile at different spots and different magnifications, taken at chosen spots where characteristic damages were localized. A millimeter scale melted and recrystallized W spot can be seen in fig. 6.29 (a). The graphite substrate can be identified in the same

image under the W coating with some material mixing. Also the image shows the initiation of a number of blisters as well. Fig. 6.29 (b) has been taken at the same 250× magnification and show well delimited areas were the coating has been removed. A larger mixing degree between the carbon substrate (darker spots) with the W coating can be clearly seen.

While the two middle images displayed in fig. 6.29 (c) and (d) were taken at a 2000× magnification and show the comparison of a well conserved and a damaged area, the bottom images (fig. 6.29 (e) and (f)) compare the same conditions of the coating at a higher magnification of 50000×. Swellings, blisters and buckling can be seen in the images of the damages areas with blobs very likely induced by an increase of the surface temperature and a mismatch between the coating and the carbon substrate.

c. Scratch test survey

Scratch tests were performed on the same tile at different spots to characterize the mechanical adherence of the coating after plasma exposure. Fig. 6.30 shows an image of the tile along with alphabetically assigned areas where the tests were performed (the numbers refer to the optical microscopy images presented previously).

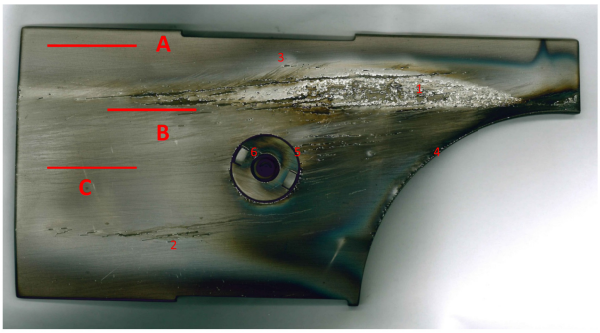

Figure 6.30: Image of the upper-left tile along with marked red lines where scratch tests were carried out. The numbers refer to the previously shown optical microscope images.

The results of the tests in terms of the critical loads L_{c1}, which relate to the smallest loads at which a first recognizable failure of the coatings occurs, are shown in tab. 6.4. The corresponding micrographs of the tests that show the aspect of the failure groves are show in fig. 6.31

The results show that zone C which is located in an flat area of the tile displays the strongest adhesion of the coating, although this is an area of the tile were the highest degree of interaction with the plasma is expected, given the rounded shape of the tile. The latter is seen in the resistance of the coating to higher vertical pressure loads of the scratch test tip (8.82 N) compared to zone A and B, and also in the micrographs as the first signs

Table 6.4: Scratch test results in terms of critical loads of zone A, B and C (see fig. 6.30).

Tested zone	L_{c2} (N)
A	8.29
B	8.40
C	8.82

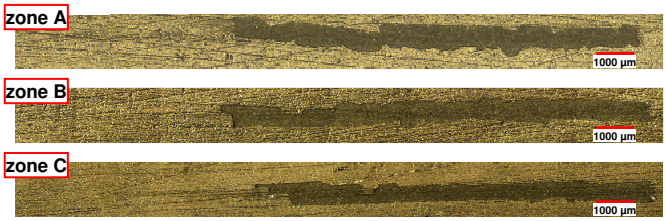

Figure 6.31: Scratch test optical micrographs of zone A, B and C.

of failure appear after a longer run of the probing tip. Zone A on the other hand appeared to be an area of the tile with the least mechanical adhesion of the coating while zone B which is located in an area where deep arcing occurred on the surface has shown an intermediate adhesion degree. Since the surface gradient corresponds to a similar gradient in adhesion properties, plasma exposure and different plasma wall interaction shapes may not be the cause of such a feature but it is the deposition of the coating itself that may be the reason. Surface uniformity before the deposition is therefore important to the global adhesion of the coating.

6.5.6 Discussions

The service lifetime of the W coatings is affected by a number of macroscale and microscale phenomena which have been already identified in the past in ASDEX with the CMSII coating technique [170]. The most significant phenomena identified in laboratory experiments were:

(i) Thermal fatigue.
(ii) Carbidization of both Mo and W layers due to the diffusion of the carbon from the substrate. As a result brittle Mo_2C, W_2C and WC were formed.
(iii) Melting of W/Mo layers.

In those tests thermal fatigue and carbidization were mainly involved in experiments where the surface temperature was in the range of 1200-1500 °C. The coatings were gradually (with increasing the number of heating pulses) damaged by swellings, blisters and buckling. In some cases delaminations occurred and when a chip of W coating had lost the contact

with the substrate it became very hot and sometimes melted. Moreover, the transfer of the energy from the surface to the substrate was found to be a key factor determining the thermo-mechanical properties of the W coatings. The structure of the substrate and its roughness are also important parameters for the thermo-mechanical properties of the W coatings. Thinner coatings were found to show better thermo-mechanical properties than thicker coatings mainly because the energy is quickly transferred from the surface to the substrate. Furthermore, the internal stress into the W coatings increases with increasing the coating thickness.

As a consequence, the observed damages with the testing of the W coatings in RFX-mod are typical and to a certain extent were expected. In fact, the most comparable tests on similar W-coatings were carried out in the GLADIS experiment [174, 175], which was designed as a high heat flux test bed to qualify large plasma facing components for ASDEX tokamak, simulating ELMs pulses in particular. Both 10 μm and 20 μm survived 1000 pulses at the following parameters: pulses with 30 MW/m^2 for 25 ms and pulses with 30 MW/m^2 for 70 ms. The base temperature during this test was below 1000 °C. However, they did not survive at 30 MW/m^2, 140 ms. The damage was produced by buckling followed by local melting. Although the same coatings survived 2-3 pulses at 23.5 MW/m^2 with duration of 1.5 s during the HHF screening test with a surface temperature exceeding 2100 °C, the thermal loading conditions in RFX-mod (tens of MW/m^2, pulse duration ~0.5 s) largely exceed the experimental conditions tested in GLADIS.

The W coatings were performed with a thin Mo interlayer whose melting temperature is 2623 °C. During plasma exposure in RFX-mod this temperatures were reached, which explains the excessive melting in many areas of the coated tiles. The melting may also be a consequence of arcing phenomenon that could have been initiated on the W-coating surface and only happen subsequently to a macroscopic damage of the coating. However, the latter hypothesis could not be verified as the shot-by-shot history of the exposed tiles is not available since the position where the tiles were exposed was not suitable for diagnostics during plasma discharges. Apart from the areas where the coatings were removed at a macroscopic level, clear signs of delamination were not observed and it is likely due to the thermal expansion match among the graphite substrate and the Mo and W layers.

6.6 Conclusions

The damages that have been observed on the exposed W-coatings were expected, however the size of these damages and particularly the removal of the coating in some areas and its melting may discard this solution path towards such a metallic PFC transition in RFX-mod. Melting is the most critical feature as macroscopic melted droplets may be accelerated, impinge and irreversibly damage the first wall or the vacuum vessel, while the significant edge erosion issue can possibility be solved with an adequate reshaping of the tiles. In fact, net erosion at the edges of the bulk graphite tiles in RFX-mod occurs during normal plasma operation, in particular close to the port holes. Therefore, a new design of the tiles that could minimize the phenomenon is under consideration, or ultimately consider bulk W instead of coated PFCs at those critical areas where singular PWI takes place. Moreover, as mentioned above, the internal stress in the W coatings increases with increasing coating thickness, therefore further optimization of the thickness may be a solution that could prevent some of the observed damages such as the elongated areas where the coating has been completely removed.

The future developments and tests in RFX-mod on W coatings include:

(i) Testing of thinner 5-15 μm W coating with the same CMSII technique to explore the possibility of lower internal stresses and accordingly a higher adhesion of the coating.
(ii) Testing of 100-200 μm plasma spray W coatings on present graphite tiles (that is still compatible with wall weight tolerance). Although, the experience in AUG with similar coatings has shown that they are prompt to delamination [176], this technique may give better results in terms of resistance to plasma interaction in particular in locations where strong plasma wall interaction usually takes place in RFX-mod.
(iii) Testing of the High Power Impulse Magnetron Sputtering (HiPIMS) deposition technique on larger scale prototypes and with further optimization of the coating deposition.

Chapter 7

Summary and Future Work

7.1 Conclusions

Mitigation of impurity influxes and recycling control during plasma operation is necessary in RFX-mod for the attainment of the improved confinement regimes associated to the SHAx. In this thesis, two interconnected activities have been carried out: (i) the characterization, optimization and further implementation of the main wall conditioning techniques; and (ii) the study of a transition from the present graphite to metallic Plasma First Components (PFCs) for RFX-mod^2 machine-upgrade.

The work performed on wall conditioning by Glow Discharge Cleaning (GDC) consisted in characterizing the GDC operational regimes, thereby optimizing the global parameters and allowing to operate the weakly ionized plasmas at favorable regimes in terms of hydrogen wall-depleting in the case of HeGDCs. The characterization has been performed by means of an extensive set of diagnostics including *ex-situ* post-mortem analyses, electrostatic probes and spectroscopic measurements. A scan in the operational parameters was done and the results have shown that: (i) in contrast with results found in TEXTOR, RF-assistance and pre-ionization have no apparent benefit in RFX-mod; (ii) a clear dependence on the glow current of the effectiveness in particle-depleting from the wall was observed, whereas no clear dependence on pressure or voltage alone could be deduced; (iii) I_{0V} measurements (ion flux to the wall) suggest that a lower in-vessel pressure is a favorable regime, as foreseen by simulations on other machines, instead spectroscopic data show an opposite behavior since the difference between the emission measured by the chords at the anode and those far from it decreases with increasing pressure. Further optimization is needed to understand the discrepancy between the two diagnostics; (iv) a strong toroidal asymmetry was found by *ex-situ* post-mortem analysis and confirmed by measurements of the ion flux to the wall. Intershot HeGDC has been tried for the first time in RFX-mod and the preliminary analysis was found promising. The combination of He power

discharges with short ±10 min HeGDC resulted relatively more efficient in enhancing hydrogen depleting from the graphite first wall compared to longer HeGDC occasionally performed during an experimental day. As a macroscopic effect, a better control of the plasma density with a lower recycling was obtained in H test discharges subsequent to the intershot HeGDC experimental campaign. While immediate benefits of using routine intershot HeGDC were found in RFX-mod in terms of faster recovery from machine openings, the most detrimental effect consisted in the progressive He loading of the wall that in the long run may affect plasma impurity content.

In RFX-mod, several unfavorable aspects of boron deposition have been observed and needed to be addressed in order to gain further benefits of boron wall conditioning. The features that have been tackled in this thesis consisted in: (i) the spatial uniformity of boron deposition; (ii) the correlation among the boron wall conditioning duration and the final boron content deposited on the first wall; (iii) the oxygen and hydrogen gettering efficiency of the boron-coated first surfaces. To address these issues, graphite samples have been exposed to a number of boronizations and *ex-situ* post-mortem analyses including SIMS, XPS, SEM, EDS/X, RBS and HR-XPS were carried out. The latter feature has been investigated by looking at the surface and bulk chemical states of boron related to hydrogen, carbon and oxygen. A strong toroidal asymmetry of boron deposition and an inconsistency among the boronization duration and the final boron content were found. The study of the effect of the wall temperature has shown a higher affinity of boron with hotter first wall surfaces. The inconsistency in boron deposition was resolved looking at the boron deposition rate measured by SIMS and gas exhaust analysis and correlated to the glow discharge parameters: boronizations performed at a low glow plasma power < 200 W have shown ~7× lower boron deposition rate compared to boronizations performed at a higher plasma power > 200 W. Accordingly, a morphological transition in boron deposition with increasing glow discharge plasma power has been found by SEM. XPS, EDS/X, RBS quantitative and qualitative measurements consistently confirmed the presence of this transition in boron growth, in agreement with previous studies found in literature [37–40]. The chemical analyses performed by HR-XPS have shown that boronizations performed at higher glow discharge plasma power provided oxygen-free and purer boron content which was related to lower concentrations of boron oxides in terms as B–O, O–B–O and B_2O_3 bonds. In terms of B–H bonds, the higher glow discharge plasma power provided a lesser H-contaminated boron content, suggesting that exposure to power plasmas of these low H- and O-contaminated boron films would lead to enhanced plasma performances. Future work include tests with these optimized boronizations in RFX-mod.

Lithium wall conditioning in RFX-mod performed by multiple techniques has been investigated and optimized in terms of: (i) lithium coverage; (ii) effect of variations in spatial uniformity on hydrogen influxes; (iii) Li-graphite chemistry at varying lithium injection doses; and (iv) the correlation among the quantity of injected lithium and its intercalation when deposited on the graphite first wall surfaces. To these aims, a physical and chemical analysis have been performed by *ex-situ* analysis of material samples. At different toroidal locations around RFX-mod torus, the deposition uniformity for each technique has been assessed by SIMS and XPS measurements and the results were compared to Li spectroscopic emission during subsequent plasma discharges. The high resolution Li-graphite chemical analysis at varying lithium dose injection with and without plasma exposure has been conducted by HR-XPS measurements.
Consistent results among SIMS, XPS and Li spectroscopic measurements have shown that compared to lithium injection/evaporation using the LCPS injection method, the injection of lithium pellets/granules during plasma discharges allows a relatively more uniform toroidal coverage. The recently implemented lithiumization technique by multiple pellet injection has shown positive results in terms of lithium coverage and content. The increase in frequency injection allows to obtain a relatively less contaminated lithium content on the plasma facing surface compared to the injection of a single pellet at a time. The comparison of lithium coverage provided by the different avaialable techniques in RFX-mod has shown that it is more profitable to inject small amounts of Li such as with the pellet injection technique in order to sustain a surface Li coverage rather than depositing greater amounts that are more prompt to intercalation. Different results were found with regard to the effect of plasma operation during and following lithium deposition: (i) injection of lithium pellets in hydrogen plasmas resulted more efficient in depositing lithium on the first wall compared to the injection in helium plasmas; (ii) spectroscopic emission data have shown that the erosion and redeposition of lithium after multiple plasma pulses is not effective in establishing uniformity of wall conditioning; (iii) the toroidal asymmetry of lithium coverage was found to be detrimental as little or no influence on H influx was found at locations where lithium coverage is reduced.
The HR-XPS chemical analysis has shown several results correlating the amount of injected lithium to the chemical bonds among Li, C and O. In particular, lithium carbonate radicals (Li_2CO_3 at 290.2 eV) were systematically found in all the analyzed Li-coated samples in both C_{1s} and O_{1s} core spectra and its fraction among other chemical interactions correlates to the total injected lithium dose. In consistency also with results found in studies on Li-graphite chemistry in NSTX, at low doses of lithium injection $\leqslant$100-500 nm, the exposure of Li-coated graphite to H plasma discharges resulted ineffective in H pumping and, accordingly, few apparent changes in surface chemistry of the lithium coating have been observed.

With regard to the qualification of tungsten (W) Plasma First Components (PFCs) for RFX-mod^2, after the choice of W as the most suitable material for a transition from graphite to metallic first wall PFCs, preliminary trials of plasma exposure of W-coating on graphite samples and full-scale tiles have been conducted. The choice of W is motivated by its high melting temperature allowing to sustain RFX-mod power loads which can reach tens of MW/m^2, its compatibility with the present mechanical structure, the high reflection energy of incident neutral atoms and the prediction of its low core plasma contamination and further peaking of density profiles compared to carbon and molybdenum.
Two different Physical Vapor Deposition (PVD) technologies providing thin 10-20 μm W-coatings have been tested in two different experimental campaigns. First, small 5×6 cm W-coated graphite samples were exposed to series of about 15 H/He discharges by means of a dedicated manipulator allowing the exposure at different distances from the graphite first wall floor. CMSII coating technique (most suitable technique also tested in JET and AUG) and HiPIMS technique (made by CNR-IENI institute of the same laboratory) were tested. Second, full-scale tiles W-coated by CMSII technology were mounted for long term exposure during a second experimental campaign. Post-mortem analyses were carried out mainly by means of optical and electron microscopy. Overall, the coatings did not withstand the thermal and particle loads induced by specific magnetic perturbations on the samples. Several damages were observed including critical melting in many areas of the exposed surfaces and the CMSII technique has shown better results compared to the HiPIMS technique. The damages that have been observed were expected to a certain extent, however the size of these damages and particularly the removal of the coating in some areas and its melting may discard this solution-path towards such a metallic first wall upgrade in RFX-mod^2. Future work includes: further testing of CMSII W-coating with after optimization of the coating thickness to reduce internal stresses and experimentation with 100-200 μm thick plasma spray W-coatings.

7.2 Future work

The work presented in this thesis on wall conditioning optimization and high-Z Plasma Facing Materials (PFMs) qualification for RFX-mod^2 upgrade can benefit from further experimentation. In particular:

1. With regard to the GDC optimization, investigate the discrepancy in I_{0V} measurements with increasing in-vessel pressure between the electrostatic probes and the spectroscopic diagnostics. With regard to the intershot HeGDC wall conditioning strategy, the results have shown that the combination of a set of two He plasma discharges with

one HeGDC leads to a higher H exhaust rate compared to a the combination of only one He discharge with one HeGDC. The test of different combinations, such as three consecutive He power discharges executed with one HeGDC, is a proposed future work in RFX-mod.

2. Boronizations performed at a glow discharge plasma power >200 W resulted remarkably beneficial in terms of low contamination and oxidation of the boron film when deposited on the first wall surfaces. However, the testing of these optimized boronizations has not been specifically tried to study the degree of improvements on RFX-mod plasma performances, therefore this activity is a highly recommended future activity.
3. Following the results presented in Chapter 5, it has been found that lithiumizations performed with the use of the high frequency Multi-Pellet Injector (MPI) are more favorable to obtain: (i) a relatively uniform lithium deposition and (ii) a lithium content less prompt to intercalation into the graphite first wall surface. Future lithiumizations in RFX-mod are planned with the use of the high frequency Multi-Pellet Injector (MPI) device with larger 1.5 lithium granules in order to further increase the toroidal coverage and surface content.
4. Although critical damages were observed on the tiles coated by CMSII with 20 μm W-coatings and exposed to RFX-mod plasmas, further experimentation with thinner 5-15 μm coatings that would reduce the typical internal stress that develops in such overlapping coatings are planned. In addition, although the experience in AUG with thick 100-200 μm W-coatings obtained by Plasma Spray deposition has shown prompt delamination upon plasma exposure, testing of this technique in RFX-mod is a considered solution. Testing of the High Power Impulse Magnetron Sputtering (HiPIMS) deposition technique on larger scale prototypes and with further optimization of the coating deposition is under consideration as well.

Bibliography

[1] G.L. Jackson, J. Winter, K.H. Burrell, J.C. DeBoo, C.M. Greenfield, R.J. Groebner, T. Hodapp, K. Holtrop, A.G. Kellman, R. Lee, S.I. Lippmann, R. Moyer, J. Phillips, T.S. Taylor, J. Watkins, and W.P. West. Boronization in diii-d. *Journal of Nuclear Materials*, 196-198(0): 236 – 240, 1992. ISSN 0022-3115. doi:10.1016/S0022-3115(06)80038-3.

[2] J.D. Strachan, M. Bell, A. Janos, S. Kaye, S. Kilpatrick, D. Manos, D. Mansfield, D. Mueller, K. Owens, C.S. Pitcher, J. Snipes, and J. Timberlake. Experiments on TFTR supershot plasmas. *Journal of Nuclear Materials*, 196-198(0):28–34, 1992. ISSN 0022-3115. doi:10.1016/S0022-3115(06)80008-5.

[3] R. Lorenzini, E. Martines, P. Piovesan, D. Terranova, P. Zanca, M. Zuin, A. Alfier, D. Bonfiglio, F. Bonomo, A. Canton, S. Cappello, L. Carraro, R. Cavazzana, D. F. Escande, A. Fassina, P. Franz, M. Gobbin, P. Innocente, L. Marrelli, R. Pasqualotto, M. E. Puiatti, M. Spolaore, M. Valisa, N. Vianello, and P. Martin. Self-organized helical equilibria as a new paradigm for ohmically heated fusion plasmas. *Nature Physics*, 5(8):570–574, June 2009. doi:10.1038/nphys1308.

[4] UN. World population prospects: The 2012 revision, 2012.

[5] Michael L. Ross. *Blood Barrels, Why Oil Wealth Fuels Conflict*, May/June 2008. URL http://www.foreignaffairs.com/articles/63396/michael-l-ross/blood-barrels.

[6] J. Ongena and G. Van Oost. Energy for future centuries. Prospects for fusion power as a future energy source. In ANS, editor, *Transactions of fusion science and technology*, volume 57, 2T, page 3, February 2010. URL http://epubs.ans.org/?a=9391.

[7] D.J.C. MacKay. *Sustainable Energy: Without the Hot Air*. Without the Hot Air Series. UIT, 2009. ISBN 9780954452933. URL http://books.google.it/books?id=IsgiPQAACAAJ.

[8] A. I. Miller. In Canadian Nuclear Society Bulletin, editor, *Heavy water: a manufacturers' guide for the hydrogen century*, volume 22, page 1,

2001. URL http://media.cns-snc.ca/Bulletin/A_Miller_Heavy_Water.pdf.

[9] M. Ni, Y. Wang, B. Yuan, J. Jiang, and Y. Wu. Tritium supply assessment for ITER and DEMOnstration power plant. *Fusion Engineering and Design*, 88(9 - 10):2422 – 2426, 2013. ISSN 0920 - 3796. doi:10.1016/j.fusengdes.2013.05.043.

[10] J. Wesson and D.J. Campbell. *Tokamaks*. International Series of Monographs on Physics. OUP Oxford, 2011. ISBN 9780199592234. URL http://books.google.it/books?id=BH9vx-iDI74C.

[11] Allen H Boozer. Stellarators and the path from ITER to DEMO. *Plasma Physics and Controlled Fusion*, 50(12):124005, 2008. doi:10.1088/0741-3335/50/12/124005.

[12] H.A.B. Bodin and A.A. Newton. Reversed-field-pinch research. *Nuclear Fusion*, 20(10):1255, 1980. doi:10.1088/0029-5515/20/10/006.

[13] H.A.B. Bodin. The reversed field pinch. *Nuclear Fusion*, 30(9):1717, 1990. doi:10.1088/0029-5515/30/9/005.

[14] G. Rostagni. RFX: an expected step in RFP research. *Fusion Engineering and Design*, 25(4):301 – 313, 1995. ISSN 0920-3796. doi:10.1016/0920-3796(94)00362-B.

[15] P. Sonato, G. Chitarin, P. Zaccaria, F. Gnesotto, S. Ortolani, A. Buffa, M. Bagatin, W.R. Baker, S. Dal Bello, P. Fiorentin, L. Grando, G. Marchiori, D. Marcuzzi, A. Masiello, S. Peruzzo, N. Pomaro, and G. Serianni. Machine modification for active MHD control in RFX. *Fusion Engineering and Design*, 66 - 68(0):161 – 168, 2003. ISSN 0920-379. doi:10.1016/S0920-3796(03)00177-7.

[16] Lyman Spitzer. Technical Report NYO-993 (PM-S-1, U.S. Atomic Energy Comission, 1951.

[17] Scott Robertson. Sheaths in laboratory and space plasmas. *Plasma Physics and Controlled Fusion*, 55(9):093001, 2013. doi:10.1088/0741-3335/55/9/093001.

[18] G. Federici, C.H. Skinner, J.N. Brooks, J.P. Coad, C. Grisolia, A.A. Haasz, A. Hassanein, V. Philipps, C.S. Pitcher, J. Roth, W.R. Wampler, and D.G. Whyte. Plasma-material interactions in current tokamaks and their implications for next step fusion reactors. *Nuclear Fusion*, 41(12): 1967, 2001. doi:10.1088/0029-5515/41/12/218.

[19] A. Loarte, B. Lipschultz, A.S. Kukushkin, G.F. Matthews, P.C. Stangeby, N. Asakura, G.F. Counsell, G. Federici, A. Kallenbach, K. Krieger, A. Mahdavi, V. Philipps, D. Reiter, J. Roth, J. Strachan, D. Whyte, R. Doerner, T. Eich, W. Fundamenski, A. Herrmann,

M. Fenstermacher, P. Ghendrih, M. Groth, A. Kirschner, S. Konoshima, B. LaBombard, P. Lang, A.W. Leonard, P. Monier-Garbet, R. Neu, H. Pacher, B. Pegourie, R.A. Pitts, S. Takamura, J. Terry, E. Tsitrone, the ITPA Scrape-off Layer, and Divertor Physics Topical Group. Chapter 4: Power and particle control. *Nuclear Fusion*, 47(6):S203, 2007. doi:10.1088/0029-5515/47/6/S04.

[20] ITER. The project. URL http://www.iter.org/proj#itersite.

[21] H. Zohm, C. Angioni, E. Fable, G. Federici, G. Gantenbein, T. Hartmann, K. Lackner, E. Poli, L. Porte, O. Sauter, G. Tardini, D. Ward, and M. Wischmeier. On the physics guidelines for a tokamak demo. *Nuclear Fusion*, 53(7):073019, 2013. doi:10.1088/0029-5515/53/7/073019.

[22] B.D. Wirth, K. Nordlund, D.G. Whyte, and D. Xu. Fusion materials modeling: Challenges and opportunities. *MRS Bulletin*, 36:216–222, 3 2011. ISSN 1938-1425. doi:10.1557/mrs.2011.37.

[23] J Winter. Wall conditioning in fusion devices and its influence on plasma performance. *Plasma Physics and Controlled Fusion*, 38(9):1503, 1996. doi:10.1088/0741-3335/38/9/001.

[24] J. Winter. Wall conditioning of fusion devices by reactive plasmas. *Journal of Nuclear Materials*, 161(3):265 – 330, 1989. ISSN 0022-3115. doi:10.1016/0022-3115(89)90466-2.

[25] J. Winter. Control of plasma-surface-interactions by thin films. In J. Fagerberg, D.C. Mowery, and R.R. Nelson, editors, *Physical processes of the interaction of fusion plasmas with solids*. Academic Press, 2004. URL http://books.google.it/books?id=t8DvAAAAMAAJ.

[26] Michiya Shimada and Richard A. Pitts. Wall conditioning on ITER. *Journal of Nuclear Materials*, 415(1, Supplement):S1013 – S1016, 2011. ISSN 0022-3115. doi:10.1016/j.jnucmat.2010.11.085. Proceedings of the 19th International Conference on Plasma-Surface Interactions in Controlled Fusion.

[27] H.F. Dylla. Glow discharge techniques for conditioning high vacuum systems. *Journal of Vacuum Science Technology A: Vacuum, Surfaces, and Films*, 6(3):1276–1287, May 1988. doi:10.1116/1.575689.

[28] V. Philipps, G. Sergienko, A. Lyssoivan, H.G. Esser, M. Freisinger, A. Kreter, and U. Samm. Removal of carbon layers by oxygen glow discharges in TEXTOR. *Journal of Nuclear Materials*, 363-365(0):929–932, 2007. ISSN 0022-3115. doi:10.1016/j.jnucmat.2007.01.241.

[29] J. Winter. Carbonization in tokamaks. *Journal of Nuclear Materials*, 145-147(0):131–144, 1987. ISSN 0022-3115. doi:10.1016/0022-3115(87)90318-7.

[30] J. Winter, H.G. Esser, L. Konen, V. Philipps, H. Reimer, J.v. Seggern, J. Schluter, E. Vietzke, F. Waelbroeck, P. Wienhold, T. Banno, D. Ringer, and S. Veprek. Boronization in textor. *Journal of Nuclear Materials*, 162-164(0):713–723, 1989. ISSN 0022-3115. doi:10.1016/0022-3115(89)90352-8.

[31] The ASDEX Team, The ICRH Team, The LH Team, The NI Team, U. Schneider, W. Poschenrieder, M. Bessenrodt-Weberpals, J. Hofmann, A. Kallenbach, K. Krieger, E. Muller, H. Niedermeyer, F. Ryter, J. Roth, F. Soldner, A. Stabler, K.H. Steuer, O. Vollmer, and F. Wagner. Boronization of ASDEX. *Journal of Nuclear Materials*, 176-177(0):350–356, 1990. ISSN 0022-3115. doi:10.1016/0022-3115(90)90071-T.

[32] J. Winter, H.G. Esser, H. Reimer, L. Grobusch, J. Von Seggern, and P. Wienhold. Borontrimethyl b(ch3)3 - a less hazardous substance for boronization. *Journal of Nuclear Materials*, 176-177(0):486–489, 1990. ISSN 0022-3115. doi:10.1016/0022-3115(90)90094-4.

[33] M. Saidoh, N. Ogiwara, M. Shimada, T. Arai, H. Hiratsuka, T. Koike, M. Shimizu, H. Ninomiya, H. Nakamura, R. Jimbou, J. Yagyu, T. Sugie, A. Sakasai, N. Asakura, M. Yamage, H. Sugai, and G. L. Jackson. Initial boronization of jt-60u tokamak using decaborane. *Japanese Journal of Applied Physics*, 32(7R):3276, 1993. doi:10.1143/JJAP.32.3276.

[34] W Baker, S Dal Bello, D Marcuzzi, P Sonato, and P Zaccaria. Design of a new toroidal shell and support structure for rfx. *Fusion Engineering and Design*, 63 - 64(0):461 – 466, 2002. ISSN 0920 - 3796. doi:10.1016/S0920-3796(02)00194-1.

[35] M. Valisa, T. Bolzonella, L. Carraro, E. Casarotto, S. Costa, L. Garzotti, P. Innocente, S. Martini, R. Pasqualotto, M.E. Puiatti, R. Pugno, and P. Scarin. Locked modes induced plasma-wall interactions in RFX. *Journal of Nuclear Materials*, 241-243(0):988 – 992, 1997. ISSN 0022-3115. doi:10.1016/S0022-3115(97)80179-1.

[36] M. E. Puiatti and the RFX-mod Team. Interaction between magnetic boundary and first wall recycling in the reversed field pinch. *Plasma Physics and Controlled Fusion*, 55(12):124013, 2013. doi:10.1088/0741-3335/55/12/124013.

[37] S. Komatsu and Y. Moriyoshi. Simultaneous growth of rhombohedral and amorphous boron films in a low pressure B_2H_6+H_2+He plasma. *Journal of Crystal Growth*, 89(4):560 – 570, 1988. ISSN 0022-0248. doi:10.1016/0022-0248(88)90219-9.

[38] S. Komatsu and Y. Moriyoshi. Influence of atomic hydrogen on the growth reactions of amorphous boron films in a low-pressure B_2H_6+He+H_2 plasma. *Journal of Applied Physics*, 64(4):1878–1884, 1988. doi:10.1063/1.341738.

[39] S. Komatsu and Y. Moriyoshi. Transition from amorphous to crystal growth of boron films in plasma-enhanced chemical vapor deposition with B_2H_6+He. *Journal of Applied Physics*, 66(1):466–469, 1989. doi:10.1063/1.343853.

[40] S. Komatsu and Y. Moriyoshi. Transition from thermal- to electron-impact decomposition of diborane in plasma-enhanced chemical vapor deposition of boron films from B_2H_6+He. *Journal of Applied Physics*, 66(3):1180–1184, 1989. doi:10.1063/1.343459.

[41] http://www.igi.pd.cnr.it/.

[42] www.cnr.it/.

[43] http://www.enea.it/.

[44] http://www.unipd.it/.

[45] www.acciaierievenete.com/.

[46] http://www.infn.it/.

[47] P. Martin et al. Overview of the RFX fusion science program. *Nuclear Fusion*, 51, 2011. doi:10.1088/0029-5515/51/9/094023.

[48] P. Martin et al. Overview of RFX-mod results. *Nuclear Fusion*, 49(10): 104019, 2009. doi:10.1088/0029-5515/49/10/104019.

[49] A. Lucchetta et al. Recent Results from Real-Time Active Control of MHD Modes in RFX-mod. 2006. URL http://www-naweb.iaea.org/napc/physics/FEC/FEC2006/html/node285.htm#56897. Proc. 21st Int. Conf. on Fusion Energy.

[50] S. Martini et al. Active MHD control at high currents in RFX-mod. *Nuclear Fusion*, 47(8):783, 2007. doi:10.1088/0029-5515/47/8/008.

[51] P. Zanca, L. Marrelli, G. Manduchi, and G. Marchiori. Beyond the intelligent shell concept: the clean-mode-control. *Nuclear Fusion*, 47 (11):1425, 2007. doi:10.1088/0029-5515/47/11/004.

[52] L. Marrelli et al. Active control of resistive kink-tearing modes in RFX-mod. 2008. URL http://www-pub.iaea.org/MTCD/Meetings/PDFplus/2008/cn165/cn165_BookOfAbstracts.pdf. *Proc. of the IAEA conference.*

[53] P. Zaccaria, S. Dal Bello, and D. Marcuzzi. Tests and analyses for the mechanical and thermal qualification of the new RFX first wall tiles. *Fusion Engineering and Design*, 66-68:289 – 293, 2003. ISSN 0920-3796. doi:10.1016/S0920-3796(03)00158-3.

[54] S.Ortolani and D.D. Schnack. *Magnetohydrodynamics of Plasma Relaxation*. World Scientific, 1993. ISBN 9789810208608. URL http://books.google.it/books?id=WJoySA3lxe0C.

[55] H. Ji and S. C. Prager. The α dynamo effects in laboratory plasmas. *Magnetohydrodynamics*, 18:191–210, 2002. URL http://arxiv.org/pdf/astro-ph/0110352v1.pdf.

[56] H. Ji, A. F. Almagri, S. C. Prager, and J. S.Sarff. Time-Resolved Observation of Discrete and Continuous Magnetohydrodynamic Dynamo in the Reversed-Field Pinch Edge. *Phys. Rev. Lett.*, 73:668–671, Aug 1994. doi:10.1103/PhysRevLett.73.668.

[57] F. D'Angelo and R. Paccagnella. The stochastic diffusion process in reversed-field pinch. *Physics of Plasmas (1994-present)*, 3(6):2353–2364, 1996. doi:10.1063/1.871919.

[58] M.E. Puiatti et al. High density physics in reversed field pinches: comparison with tokamaks and stellarators. *Nuclear Fusion*, 49(4): 045012, 2009. doi:10.1088/0029-5515/49/4/045012.

[59] P. Scarin et al. Magnetic structures and pressure profiles in the plasma boundary of RFX-mod: high current and density limit in helical regimes . 2010. URL http://www-naweb.iaea.org/napc/physics/fec/fec2010/papers/exd_p3-29.pdf. *Proc. of the 23th IAEA conference, EXD/P3-29*.

[60] M.E. Puiatti et al. Wall conditioning and density control in the reversed field pinch RFX-mod. *Nuclear Fusion*, 53(7):073001, 2013. doi:10.1088/0029-5515/53/7/073001.

[61] F Gnesotto, P Sonato, W.R Baker, A Doria, F Elio, M Fauri, P Fiorentin, G Marchiori, and G Zollino. The plasma system of RFX. *Fusion Engineering and Design*, 25(4):335 – 372, 1995. ISSN 0920-3796. doi:10.1016/0920-3796(94)00280-K.

[62] D. K. Mansfield et al. Enhancement of Tokamak Fusion Test Reactor performance by lithium conditioning. *Physics of Plasmas (1994-present)*, 3(5):1892–1897, 1996. doi:10.1063/1.871984.

[63] P. R. Brunsell, H. Bergsåker, M. Cecconello, J. R. Drake, R. M. Gravestijn, A. Hedqvist, and J-A. Malmberg. Initial results from the rebuilt EXTRAP T2R RFP device. *Plasma Physics and Controlled Fusion*, 43(11):1457, 2001. doi:10.1088/0741-3335/43/11/303.

[64] S. V. Mirnov, E. A. Azizov, V. A. Evtikhin, V. B. Lazarev, I. E. Lyublinski, A V. Vertkov, and D. Yu Prokhorov. Experiments with lithium limiter on T-11M tokamak and applications of the lithium capillary-pore system in future fusion reactor devices. *Plasma*

Physics and Controlled Fusion, 48(6):821, 2006. doi:10.1088/0741-3335/48/6/009.

[65] M.L. Apicella, G. Mazzitelli, V. Pericoli Ridolfini, V. Lazarev, A. Alekseyev, A. Vertkov, and R. Zagórski. First experiments with lithium limiter on FTU. *Journal of Nuclear Materials*, 363-365(0): 1346 – 1351, 2007. doi:10.1016/j.jnucmat.2007.01.237. Plasma-Surface Interactions-17.

[66] J. Sànchez, F.L. Tabarés, D. Tafalla, J.A. Ferreira, I. García-Cortés, C. Hidalgo, F. Medina, M.A. Ochando, and M.A. Pedrosa. Impact of lithium-coated walls on plasma performance in the TJ-II stellarator. *Journal of Nuclear Materials*, 390-391(0):852 – 857, 2009. ISSN 0022-3115. doi:10.1016/j.jnucmat.2009.01.224.

[67] K.V Khlopenkov, V.Yu Sergeev, S Sudo, K Kondo, F Sano, H Zushi, H Okada, K Nagasaki, B.V Kuteev, and T Obiki. Recent experiments on Li pellet injection into Heliotron E. *Fusion Engineering and Design*, 34-35(0):337 – 341, 1997. ISSN 0920-3796. doi:10.1016/S0920-3796(96)00654-0. Fusion Plasma Diagnostics.

[68] S. Munaretto et al. RFX-mod wall conditioning by lithium pellet injection. *Nuclear Fusion*, 52(2):023012, 2012. doi:10.1088/0029-5515/52/2/023012.

[69] V.A Evtikhin, I.E Lyublinski, A.V Vertkov, S.V Mirnov, and V.B Lazarev. Technological aspects of lithium capillary-pore systems application in tokamak device. *Fusion Engineering and Design*, 56 - 57 (0):363 – 367, 2001. ISSN 0920-3796. doi:10.1016/S0920-3796(01)00323-4.

[70] A. Alfier et al. Liquid Lithium Limiter on the RFX-mod experiment. *Journal of Nuclear Materials*, 415(1, Supplement):S413 – S416, 2011. ISSN 0022 - 3115. doi:10.1016/j.jnucmat.2011.01.120. Proceedings of the 19th International Conference on Plasma-Surface Interactions in Controlled Fusion.

[71] D.K. Mansfield, A.L. Roquemore, T. Carroll, Z. Sun, J.S. Hu, L. Zhang, Y.F. Liang, X.Z. Gong, J.G. Li, H.Y.Guo, G.Z. Zuo, P. Parks, W. Wu, and R. Maingi. First observations of ELM triggering by injected lithium granules in EAST. *Nuclear Fusion*, 53(11):113023, 2013. doi:10.1088/0029-5515/53/11/113023.

[72] L. Fellin, P. Kusstatscher, and G. Rostagni. Overall plant design, layout and commissioning. *Fusion Engineering and Design*, 25(4):315 – 333, 1995. ISSN 0920-3796. doi:10.1016/0920-3796(94)00279-G.

[73] G. Serianni, W. Baker, and S. Dal Bello. High-spatial resolution edge electrostatic probe system for RFX. *Review of Scientific Instruments*, 74(3):1558–1562, 2003. doi:10.1063/1.1538358.

[74] F. Bonomo, D. Bonfiglio, P. Piovesan, L. Piron, B. Zaniol, S. Cappello, L. Carraro, R. Cavazzana, M. Gobbin, L. Marrelli, E. Martines, B. Momo, M.E. Puiatti, and M. Valisa. Flow measurements and modelling in helical RFX-mod equilibria. *Nuclear Fusion*, 51(12): 123007, 2011. doi:10.1088/0029-5515/51/12/123007.

[75] M Mattioli, K B Fournier, M E Puiatti, M Valisa, L Carraro, I Coffey, M O'Mullane, F Sattin, and P Scarin. Experimental and simulated VUV spectra from the JET tokamak and the reversed field pinch RFX. *Plasma Physics and Controlled Fusion*, 44(1):33, 2002. doi:10.1088/0741-3335/44/1/304.

[76] A. Canton, S. Dal Bello, R. Cavazzana, P. Innocente, P. Sonato, C. Taliercio, and M. Breda. Density control in RFX-mod Reversed Field Pinch device. volume 32F, pages D–1.002, June 2008. URL http://epsppd.epfl.ch/Hersonissos/pdf/D1_002.pdf. 35^{th} EPS Conference on Plasma Physics.

[77] http://www.mdsplus.org.

[78] R. Castaing and G. Slodzian. Microanalyse par émission ionique secondaire. *Journal de Microscopie*, 1:395–414, 1962.

[79] H. Hertz. Ueber einen Einfluss des ultravioletten Lichtes auf die electrische Entladung. *Annalen der Physik*, 267(8):983–1000, 1887. ISSN 1521-3889. doi:10.1002/andp.18872670827.

[80] A. Einstein. Über einen die Erzeugung und Verwandlung des Lichtes betreffenden heuristischen Gesichtspunkt. *Annalen der Physik*, 322(6): 132–148, 1905. ISSN 1521-3889. doi:10.1002/andp.19053220607.

[81] Friedrich Reinert and Stefan Hüfner. Photoemission spectroscopy-from early days to recent applications. *New Journal of Physics*, 7(1):97, 2005. doi:10.1088/1367-2630/7/1/097.

[82] J.F. Moulder and J. Chastain. *Handbook of X-ray Photoelectron Spectroscopy: A Reference Book of Standard Spectra for Identification and Interpretation of XPS Data*. Physical Electronics Division, Perkin-Elmer Corporation, 1992. ISBN 9780962702624. URL http://books.google.it/books?id=A_XGQgAACAAJ.

[83] J.R. Bird and J.S. Williams. 12 - General Methods. In *Ion Beams for Materials Analysis*, pages 104–106. Academic Press, San Diego, 1989. ISBN 978-0-12-099740-4. doi:10.1016/B978-0-08-091689-7.50017-3.

[84] Yang Leng. *Materials Characterization introduction to Microscopic and Spectroscopic Methods*. John Wiley, Singapore, 2008. URL http://eu.wiley.com/WileyCDA/WileyTitle/productCd-3527334637.html.

[85] V. Petrava Y. Wang. *Focused Ion Beams*, pages 195–214. Wiley-Blackwell, 2012. ISBN 9781118229347. doi:10.1002/9781118229347.ch11.

[86] Anjam Khursheed. *Scanning electron microscope optics and spectrometers*. World Scientific, Singapore, 2011. URL https://books.google.it/books?id=pLO1gT9owEIC.

[87] D.B. Graves and K.F. Jensen. A Continuum Model of DC and RF Discharges. *Plasma Science, IEEE Transactions on*, 14(2):78–91, April 1986. doi:10.1109/TPS.1986.4316510.

[88] Z. Donkó, K. Rózsa, R. C. Tobin, and K. A. Peard. Modeling and measurements on an obstructed glow discharge in helium. *Phys. Rev. E*, 49:3283–3289, Apr 1994. doi:10.1103/PhysRevE.49.3283.

[89] A. von Engel. *Ionized Gases*. Oxford: Clarendon press, 1965. URL http://lib.ugent.be/catalog/rug01:000738415.

[90] S. Barison, A. Canton, S. Dal Bello, S. Fiameni, P. Innocente, A. Alfier, S. Munaretto, and F. Rossetto. Analysis of the interaction between plasmas and the graphite first wall in RFX-mod. *Journal of Nuclear Materials*, 415(1, Supplement):S274 – S277, 2011. ISSN 0022-3115. doi:10.1016/j.jnucmat.2010.12.311.

[91] S. Fiameni et al. Sims analysis of the interaction between plasmas and the graphite first wall in rfx-mod. *Surface and Interface Analysis*, 45 (1):423–426, 2013. ISSN 1096-9918. doi:10.1002/sia.5063.

[92] J. Winter, F. Waelbroeck, B. Brandt, K.J. Dietz, I. Ali-Khan, and P. Wienhold. On the cleaning of first wall materials by glow discharges in hydrogen. *Journal of Nuclear Materials*, 93-94, Part 2(0):812 – 819, 1980. ISSN 0022-3115. doi:10.1016/0022-3115(80)90212-3.

[93] F. Waelbroeck, J. Winter, and P. Wienhold. Cleaning and conditioning of the walls of plasma devices by glow discharges in hydrogen. *Journal of Vacuum Science & Technology A*, 2(4):1521–1536, 1984. doi:10.1116/1.572465.

[94] Institut für Plasmaphysik (Jülich) and Kernforschungsanlage. *Cleaning and conditioning of the walls of plasma devices by glow discharges in hydrogen*. Berichte der Kernforschungsanlage Jülich. Zentralbibliothek d. Kernforschungsanlage Jülich, 1980. URL http://books.google.it/books?id=PJ_inQEACAAJ.

[95] R.J.H Pearce, P Andrew, S Bryan, R Claesen, J Harling, J How, H Jensen, H McBryan, J Orchard, G Saibene, and A Vadgama. The experience with JET's combined dc/RF glow discharge cleaning (GDC) system. *Vacuum*, 47(6-8):665 – 670, 1996. ISSN 0042-207X. doi:10.1016/0042-207X(96)00042-5.

[96] J.R. Roth. *Industrial Plasma Engineering: Volume 1: Principles*. Industrial Plasma Engineering. Taylor & Francis, 1995. ISBN 9781420050868. URL http://books.google.it/books?id=woaMsQyfUDEC.

[97] A. Canton, S. Dal Bello, M. Agostini, L. Carraro, R. Cavazzana, S. Fiameni, L. Grando, **B. Rais**, M. Spolaore, and M. Zuin. Studies of spatial uniformity of glow discharge cleaning plasmas on the RFX-mod device . *Journal of Nuclear Materials*, 438, Supplement(0):S1164 – S1167, 2013. ISSN 0022-3115. doi:10.1016/j.jnucmat.2013.01.257.

[98] W.R. Wampler and S.M. Myers. Ion-induced release of deuterium from carbon. *Journal of Nuclear Materials*, 111-112:616 – 621, 1982. ISSN 0022-3115. doi:10.1016/0022-3115(82)90275-6.

[99] R. A. Langley. Initial results for ion-induced release of hydrogen and deuterium from AXF-5Q graphite by hydrogen and deuterium. *Journal of Vacuum Science & Technology A*, 7(3):1060–1064, 1989. doi:10.1116/1.576230.

[100] J. Roth, B.M.U. Scherzer, R.S. Blewer, D.K. Brice, S.T. Picraux, and W.R. Wampler. Trapping, detrapping and replacement of keV hydrogen implanted into graphite. *Journal of Nuclear Materials*, 93694, Part 2: 601 6 607, 1980. ISSN 0022-3115. doi:10.1016/0022-3115(80)90181-6.

[101] R. A. Langley. Retention of hydrogen in graphite. *Journal of Vacuum Science & Technology A*, 5(4):2205–2209, 1987. doi:10.1116/1.574956.

[102] R.A. Langley. Helium-ion-induced release of hydrogen from graphite. *Journal of Nuclear Materials*, 162-164:1030 – 1034, 1989. ISSN 0022-3115. doi:10.1016/0022-3115(89)90404-2.

[103] G. L. Jackson, T. S. Taylor, P. I. Petersen, and P. L. Taylor. Helium glow wall conditioning of the DIII-D tokamak with large area graphite coverage. *AIP Conference Proceedings.*, 199(1):39–49, 1990. doi:10.1063/1.39065.

[104] S Menmuir, L Carraro, A Alfier, F Bonomo, A Fassina, G Spizzo, and N Vianello. Impurity transport studies in RFX-mod multiple helicity and enhanced confinement QSH regimes. *Plasma Physics and Controlled Fusion*, 52(9):095001, 2010. doi:10.1088/0741-3335/52/9/095001.

[105] A. Tolstogouzov, S. Daolio, C. Pagura, and C.L. Greenwood. Energy distributions of secondary ions sputtered from aluminium and magnesium by Ne^+, Ar^+ and O_2^+: a comprehensive study. *International Journal of Mass Spectrometry*, 214(3):327 – 337, 2002. ISSN 1387-3806. doi:10.1016/S1387-3806(02)00523-7.

[106] L. Tramontin, V. Antoni, M. Bagatin, D. Boscarino, E. Cattaruzza, V. Rigato, and S. Zandolin. Erosion, redeposition and boronization lifetime in RFX. *Journal of Nuclear Materials*, 266-269(0):709 – 713, 1999. ISSN 0022-3115. doi:10.1016/S0022-3115(98)00837-X.

[107] M. Mayer. SIMNRA User's Guide Version 6.04, 2008. URL www2.if.usp.br/~lamfi/guia-simnra.pdf.

[108] R. Zehringer, H. Künzli, P. Oelhafen, and C. Hollenstein. Oxidation behaviour of boron carbide. *Journal of Nuclear Materials*, 176-177(0): 370 – 374, 1990. ISSN 0022-3115. doi:10.1016/0022-3115(90)90074-W.

[109] C.D. Wagner and G.E. Muilenberg. *Handbook of x-ray photoelectron spectroscopy: a reference book of standard data for use in x-ray photoelectron spectroscopy*. Physical Electronics Division, Perkin-Elmer Corp., 1979. URL http://books.google.it/books?id=oY5TAAAAYAAJ.

[110] Ch. Hollenstein, B.P. Duval, T. Dudok de Wit, B. Joye, H.J. Künzli, P. Oelhafen, R. Zehringer, R. Hauert, and E.M. Moser. Cold boronisation in TCA. *Journal of Nuclear Materials*, 176-177(0):343 – 349, 1990. ISSN 0022-3115. doi:10.1016/0022-3115(90)90070-4.

[111] H.W. Kugel, V. Soukhanovskii, M. Bell, W. Blanchard, D. Gates, B. LeBlanc, R. Maingi, D. Mueller, H.K. Na, S. Paul, C.H. Skinner, D. Stutman, and W.R. Wampler. Impact of the wall conditioning program on plasma performance in NSTX. *Journal of Nuclear Materials*, 313-316(0):187 – 193, 2003. ISSN 0022-3115. doi:10.1016/S0022-3115(02)01433-2. Plasma-Surface Interactions in Controlled Fusion Devices 15.

[112] Fairley N and Carrick A. *The Casa Cookbook-Part I: Recipes for XPS data Processing*. Knutsford, UK: Acolyte Science, 2005. URL http://library.wur.nl/WebQuery/clc/1848500.

[113] H. Künzli, P. Gantenbein, R. Steiner, and P. Oelhafen. Deposition and characterization of thin boron-carbide coatings. *Fresenius' Journal of Analytical Chemistry*, 346(1-3):41–44, 1993. ISSN 0937-0633. doi:10.1007/BF00321379.

[114] Akira Yoshikawa, Yohei Kikuchi, Taichi Suda, Naoko Ashikawa, Kiyohiko Nishimura, Akio Sagara, Nobuaki Noda, Yasuhisa Oya, and Kenji Okuno. Chemical behavior of hydrogen isotopes into boronized film in LHD. *Journal of Nuclear Materials*, 386-388(0):367 – 370, 2009. ISSN 0022-3115. doi:10.1016/j.jnucmat.2008.12.126. Fusion Reactor Materials Proceedings of the Thirteenth International Conference on Fusion Reactor Materials.

[115] Zhongshi Yang, Wanjing Wang, Qiang Li, Jing Wu, Kenji Okuno, Yasuhisa Oya, and Guang-Nan Luo. Surface analysis of VPS-W coatings boronized by an ICRF discharge in HT-7. *Journal of Nuclear Materials*, 417(1-3):520 – 523, 2011. ISSN 0022-3115. doi:10.1016/j.jnucmat.2010.12.110. Proceedings of ICFRM-14.

[116] N. Ashikawa, K. Kizu, J. Yagyu, T. Nakahata, Y. Nobuta, K. Nishimura, A. Yoshikawa, Y. Ishimoto, Y. Oya, K. Okuno, N. Miya, T. Hino, S. Masuzaki, A. Sagara, and N. Ohyabu. Comparison of boronized wall in LHD and JT-60U. *Journal of Nuclear Materials*, 363-365(0):1352 – 1357, 2007. ISSN 0022-3115. doi:10.1016/j.jnucmat.2007.01.271. Plasma-Surface Interactions-17.

[117] Dadong Shao, Jiaxing Li, Xiaoli Tan, Zhongshi Yang, Kenji Okuno, and Yasuhisa Oya. XPS investigation of impurities containing boron films affected by energetic deuterium implantation and thermal desorption. *Journal of Nuclear Materials*, 457(0):118 – 123, 2015. ISSN 0022-3115. doi:10.1016/j.jnucmat.2014.10.097.

[118] L.G. Jacobsohn, R.K. Schulze, M.E.H. Maia da Costa, and M. Nastasi. X-ray photoelectron spectroscopy investigation of boron carbide films deposited by sputtering. *Surface Science*, 572(2-3):418 – 424, 2004. ISSN 0039-6028. doi:10.1016/j.susc.2004.09.020.

[119] S.C. Lyu, J.H. Han, K.W. Shin, and J.H. Sok. Synthesis of boron-doped double-walled carbon nanotubes by the catalytic decomposition of tetrahydrofuran and triisopropyl borate. *Carbon*, 49(5):1532 – 1541, 2011. ISSN 0008-6223. doi:10.1016/j.carbon.2010.12.012.

[120] J.I. Onate, A. García, V. Bellido, and J.L. Viviente. Deposition of hydrogenated B-C thin films and their mechanical and chemical characterization. *Surface and Coatings Technology*, 49(1-3):548 – 553, 1991. ISSN 0257-8972. doi:10.1016/0257-8972(91)90115-D.

[121] O Postel and J Heberlein. Deposition of boron carbide thin film by supersonic plasma jet CVD with secondary discharge. *Surface and Coatings Technology*, 108-109(0):247 –252, 1998. ISSN 0257-8972. doi:10.1016/S0257-8972(98)00661-6.

[122] H. Künzli, P. Gantenbein, R. Steiner, and P. Oelhafen. Influence of B2H6/CH4 and B(CH3)3 as process gas on boron carbide coatings: an in situ photoelectron spectroscopy study. *Journal of Nuclear Materials*, 196-198(0):622 – 626, 1992. ISSN 0022-3115. doi:10.1016/S0022-3115(06)80111-X. Plasma-Surface Interactions in Controlled Fusion Devices Proceedings of the Tenth International Conference on Plasma-Surface Interactions in Controlled Fusion Devices.

[123] C Ronning, D Schwen, S Eyhusen, U Vetter, and H Hofsäss. Ion beam synthesis of boron carbide thin films. *Surface and Coatings Technology*,

158-159(0):382 – 387, 2002. ISSN 0257-8972. doi:10.1016/S0257-8972(02)00248-7. Proceedings of the 12th International Conference on SMMIB.

[124] S. Jacques, A. Guette, X. Bourrat, F. Langlais, C. Guimon, and C. Labrugere. LPCVD and characterization of boron-containing pyrocarbon materials. *Carbon*, 34(9):1135 – 1143, 1996. ISSN 0008-6223. doi:10.1016/0008-6223(96)00075-9.

[125] William Cermignani, Thomas E. Paulson, Carina Onneby, and Carlo G. Pantano. Synthesis and characterization of boron-doped carbons. *Carbon*, 33(4):367 – 374, 1995. ISSN 0008-6223. doi:10.1016/0008-6223(94)00160-2. Oxidation Protection of Carbon Composites.

[126] I. Jiménez, D. Sutherland, T. van Buuren, J. Carlisle, L. Terminello, and F. Himpsel. Photoemission and x-ray-absorption study of boron carbide and its surface thermal stability. *Phys. Rev. B*, 57:13167–13174, May 1998. doi:10.1103/PhysRevB.57.13167.

[127] Sachiko Suzuki, Yu Yang, Akira Yoshikawa, Yohei Kikuchi, Akio Sagara, Yasuhisa Oya, and Kenji Okuno. Influence of carbon concentration on chemical behavior of energetic deuterium implanted into carbon-contained boron film. *Journal of Nuclear Materials*, 390-391(0):200 – 202, 2009. ISSN 0022-3115. doi:10.1016/j.jnucmat.2009.01.167. Proceedings of the 18th International Conference on Plasma-Surface Interactions in Controlled Fusion Device Proceedings of the 18th International Conference on Plasma-Surface Interactions in Controlled Fusion Device.

[128] G. Mazzitelli, M.L. Apicella, D. Frigione, G. Maddaluno, M. Marinucci, C. Mazzotta, V. Pericoli Ridolfini, M. Romanelli, G. Szepesi, O. Tudisco, and FTU Team. FTU results with a liquid lithium limiter. *Nuclear Fusion*, 51(7):073006, 2011. doi:10.1088/0029-5515/51/7/073006.

[129] F L Tabarés, M A Ochando, F Medina, D Tafalla, J A Ferreira, E Ascasibar, R Balbín, T Estrada, C Fuentes, I García-Cortés, J Guasp, M Liniers, I Pastor, M A Pedrosa, and the TJ-II Team. Plasma performance and confinement in the TJ-II stellarator with lithium-coated walls. *Plasma Physics and Controlled Fusion*, 50(12):124051, 2008. doi:10.1088/0741-3335/50/12/124051.

[130] Kugel et al. The effect of lithium surface coatings on plasma performance in the National Spherical Torus Experiment. *Physics of Plasmas (1994-present)*, 15(5):056118, 2008. doi:10.1063/1.2906260.

[131] G Z Zuo et al. Comparison of various wall conditionings on the reduction of H content and particle recycling in EAST. *Plasma Physics and Controlled Fusion*, 54(1):015014, 2012. doi:10.1088/0741-3335/54/1/015014.

[132] R. Maingi et al. The effect of progressively increasing lithium coatings on plasma discharge characteristics, transport, edge profiles and ELM stability in the National Spherical Torus Experiment. *Nuclear Fusion*, 52(8):083001, 2012. doi:10.1088/0029-5515/52/8/083001.

[133] J. Li. High power and long pulse operation on the superconducting tokamak EAST. July 2012. URL http://epsicpp2012.spp.ee.kth.se/. 39^{th} EPS Conference on Plasma Physics (Invited paper).

[134] Masayuki Ono. *Lithium As Plasma Facing Component for Magnetic Fusion Research*. Sep 2012. doi:10.2172/1056493.

[135] C. N. Taylor, B. Heim, and J. P. Allain. Chemical response of lithiated graphite with deuterium irradiation. *Journal of Applied Physics*, 109 (5):053306, 2011. doi:10.1063/1.3555097.

[136] H Estrade-Szwarckopf and B Rousseau. U.P.S. and X.P.S. studies of alkali-graphite intercalation compounds. *Synthetic Metals*, 23(1-4):191–198, 1988. ISSN 0379-6779. doi:10.1016/0379-6779(88)90482-1. Proceedings of the Fourth International Symposium on Graphite Intercalation Compounds.

[137] N. Itou, H. Toyoda, K. Morita, and H. Sugai. Rapid diffusion of lithium into bulk graphite in lithium conditioning. *Journal of Nuclear Materials*, 290-293(0):281–285, 2001. ISSN 0022-3115. doi:10.1016/S0022-3115(00)00630-9. 14^{th} Int. Conf. on Plasma-Surface Interactions in Controlled Fusion D evices.

[138] S. Kato, M. Watanabe, H. Toyoda, and H. Sugai. Laboratory experiment on lithium chemistry and its application to effective wall conditioning. *Journal of Nuclear Materials*, 266-269(0):406 – 411, 1999. ISSN 0022-3115. doi:10.1016/S0022-3115(98)00889-7.

[139] P. Krstic, J. Allain, C. Taylor, J. Dadras, S. Maeda, K. Morokuma, J. Jakowski, A. Allouche, and C. Skinner. Deuterium Uptake in Magnetic-Fusion Devices with Lithium-Conditioned Carbon Walls. *Physical Review Letters*, 110:105001, Mar 2013. doi:10.1103/PhysRevLett.110.105001.

[140] C. N. Taylor, J. Dadras, K. E. Luitjohan, J. P. Allain, P. S. Krstic, and C. H. Skinner. The role of oxygen in the uptake of deuterium in lithiated graphite. *Journal of Applied Physics*, 114(22):223301, 2013. doi:10.1063/1.4841115.

[141] P. Innocente, D.K. Mansfield, A.L. Roquemore, M. Agostini, S. Barison, A. Canton, L. Carraro, R. Cavazzana, G. De Masi, A. Fassina, S. Fiameni, L. Grando, **B. Rais**, F. Rossetto, and P. Scarin. Lithium wall conditioning by high frequency pellet injection in RFX-mod. *Journal of Nuclear Materials*, 2014. ISSN 0022-3115. doi:10.1016/j.jnucmat.2014.11.088.

[142] S.Menmuir, L.Carraro, M.Agostini, P.Innocente andS.Munaretto, M.E.Puiatti, and P.Scarin. Edge spectroscopic characterization of RFX-mod after Li wall conditioning. June 2010. URL http://ocs.ciemat.es/EPS2010PAP/pdf/P2.149.pdf. 37^{th} EPS Conference on Plasma Physics.

[143] N. Vianello et al. 3D effects on the RFX-mod boundary. *Nuclear Fusion*, 53(7):073025, 2013. doi:10.1088/0029-5515/53/7/073025.

[144] M. Valisa et al. High current regimes in RFX-mod. *Plasma Physics and Controlled Fusion*, 50(12):124031, 2008. doi:10.1088/0741-3335/50/12/124031.

[145] H.W. Kugel. NSTX plasma response to lithium coated divertor. *Journal of Nuclear Materials*, 415(1, Supplement):S400 – S404, 2011. ISSN 0022-3115. doi:10.1016/j.jnucmat.2010.12.016.

[146] Nist standard reference database. URL http://www.nist.gov.

[147] S.S. Harilal, J.P. Allain, A. Hassanein, M.R. Hendricks, and M. Nieto-Perez. Reactivity of lithium exposed graphite surface. *Applied Surface Science*, 255(20):8539 – 8543, 2009. ISSN 0169-4332. doi:10.1016/j.apsusc.2009.06.009.

[148] C.N. Taylor, K.E. Luitjohan, B. Heim, L. Kollar, J.P. Allain, C.H. Skinner, H.W. Kugel, R. Kaita, A.L. Roquemore, and R. Maingi. Surface chemistry analysis of lithium conditioned NSTX graphite tiles correlated to plasma performance. *Fusion Engineering and Design*, 88(12):3157 – 3164, 2013. ISSN 0920-3796. doi:10.1016/j.fusengdes.2013.09.007.

[149] B Rousseau, M Vayer-Besancon, and H Estrade-Szwarckopf. XPS and UPS study of the oxidation of a stage 1 Cs-graphite intercalation compound: Comparison with alkali films deposited on substrates. *Solid State Communications*, 99(3):143 – 147, 1996. ISSN 0038-1098. doi:10.1016/0038-1098(96)00220-7.

[150] M. Töwe, P. Reinke, and P. Oelhafen. Reactivity of lithium-containing amorphous carbon (a-C) films. *Journal of Nuclear Materials*, 290-293 (0):153 – 157, 2001. ISSN 0022-3115. doi:10.1016/S0022-3115(00)00432-3. 14^{th} Int. Conf. on Plasma-Surface Interactions in Controlled Fusion Devices.

[151] M.E. Puiatti et al. High density physics in reversed field pinches: comparison with tokamaks and stellarators. *Nuclear Fusion*, 49(4): 045012, 2009. doi:10.1088/0029-5515/49/4/045012.

[152] R. Neu et al. Overview on plasma operation with a full tungsten wall in ASDEX Upgrade. *Journal of Nuclear Materials*, 438, Supplement: S34 – S41, 2013. ISSN 0022-3115. doi:10.1016/j.jnucmat.2013.01.006.

[153] S. Brezinsek et al. Overview of experimental preparation for the ITER-Like Wall at JET. *Journal of Nuclear Materials*, 415(1, Supplement): S936 – S942, 2011. ISSN 0022-3115. doi:10.1016/j.jnucmat.2010.10.037.

[154] B. Lipschultz, D.A. Pappas, B. Labombard, J.E. Rice, D. Smith, and S.J. Wukitch. A study of molybdenum influxes and transport in alcator C-Mod. *Nuclear Fusion*, 41(5):585–596, 2001. doi:10.1088/0029-5515/41/5/311.

[155] F. Alladio. Results from the Frascati tokamak FT. *Nuclear Fusion*, 25 (9):1069–1072, 1985. doi:10.1088/0029-5515/25/9/012.

[156] Kallenbach et al. Tokamak operation with high-Z plasma facing components. *Plasma Physics and Controlled Fusion*, 47(12 B):B207–B222, 2005. doi:10.1088/0741-3335/47/12B/S16.

[157] V. Philipps, Ph. Mertens, G.F. Matthews, and H. Maier. Overview of the JET ITER-like wall project. *Fusion Engineering and Design*, 85 (7-9):1581–1586, 2010. doi:10.1016/j.fusengdes.2010.04.048.

[158] K. Shimada, T. Tanabe, R. Causey, T. Venhaus, and K. Okuno. Hydrogen recycling study by Balmer lines emissions in linear plasma machine TPE. *Journal of Nuclear Materials*, 290-293:478 – 481, 2001. doi:10.1016/S0022-3115(00)00515-8.

[159] A. Huber et al. Comparison of impurity production, recycling and power deposition on carbon and tungsten limiters in TEXTOR-94. *Journal of Nuclear Materials*, 290-293:276 – 280, 2001. ISSN 0022-3115. doi:10.1016/S0022-3115(00)00629-2.

[160] P.C. Stangeby. *The Plasma Boundary of Magnetic Fusion Devices*. Series in Plasma Physics. Taylor & Francis, 2000. ISBN 9780750305594. URL http://books.google.it/books?id=qOliQgAACAAJ.

[161] W. Eckstein. Reflection. Technical report, Max-Planck-Institut für Plasmaphysik, August 2009.

[162] H. Maier, J. Luthin, M. Balden, J. Linke, F. Koch, and H. Bolt. Properties of tungsten coatings deposited onto fine grain graphite by different methods. *Surface and Coatings Technology*, 142-144:733 – 737, 2001. ISSN 0257-8972. doi:10.1016/S0257-8972(01)01177-X.

[163] ASTM C1624-05. *Standard Test Method for Adhesion Strength and Mechanical Failure Modes of Ceramic Coatings by Quantitative Single Point Scratch Testing, Refractories, Activated Carbon; Advanced Ceramics*, volume 15.01. ASTM International: West Conshohocken, PA, USA, Marcht 2010.

[164] The relationship between hardness and scratch adhesion: P J Burnett and D S Rickerby, Thin Solid Films, 154, 1987, 403-416. *Vacuum*, 39 (5):500, 1989. ISSN 0042-207X. doi:10.1016/0042-207X(89)90364-3.

[165] C Ruset, E Grigore, H Maier, R Neu, X Li, H Dong, R Mitteau, and X Courtois. Tungsten coatings deposited on CFC tiles by the combined magnetron sputtering and ion implantation technique. *Physica Scripta*, 2007(T128):171, 2007. doi:10.1088/0031-8949/2007/T128/033.

[166] André Anders. From plasma immersion ion implantation to deposition: a historical perspective on principles and trends. *Surface and Coatings Technology*, 156(1-3):3 – 12, 2002. ISSN 0257-8972. doi:10.1016/S0257-8972(02)00066-X.

[167] H Bolt et al. Materials for the plasma-facing components of fusion reactors. *Journal of Nuclear Materials*, 329-333, Part A:66 – 73, 2004. ISSN 0022-3115. doi:10.1016/j.jnucmat.2004.04.005.

[168] C. García-Rosales et al. High-heat-flux loading of tungsten coatings on graphite deposited by plasma spray and physical vapor deposition. *Fusion Technology (1997), 32(2)*, 32-2:263–276, 1997. URL http://www.ans.org/pubs/journals/fst/a_19896.

[169] C. Ruset, E. Grigore, I. Munteanu, H. Maier, H. Greuner, C. Hopf, V. Phylipps, and G. Matthews. Industrial scale 10 μm W coating of CFC tiles for ITER-like Wall Project at JET. *Fusion Engineering and Design*, 84(7-11):1662 – 1665, 2009. ISSN 0920-3796. doi:10.1016/j.fusengdes.2008.11.053.

[170] C. Ruset et al. The impact of thermal fatigue and carbidization on the W coatings deposited on CFC tiles for the ITER-like Wall project at JET. *Fusion Engineering and Design*, 88(9-10):1690 – 1693, 2013. ISSN 0920-3796. doi:10.1016/j.fusengdes.2013.02.017.

[171] H. Maier, J. Luthin, M. Balden, S. Lindig, J. Linke, V. Rohde, and H. Bolt. Development of tungsten coated first wall and high heat flux components for application in ASDEX Upgrade. *Journal of Nuclear Materials*, 307-311, Part 1(0):116 – 120, 2002. ISSN 0022-3115. doi:10.1016/S0022-3115(02)00941-8.

[172] C. García-Rosales, P. Franzen, H. Plank, J. Roth, and E. Gauthier. Re-emission and thermal desorption of deuterium from plasma sprayed tungsten coatings for application in ASDEX-upgrade. *Journal of Nuclear Materials*, 233-237, Part 1:803 – 808, 1996. ISSN 0022-3115. doi:10.1016/S0022-3115(96)00185-7.

[173] P. Zaccaria, S. Dal Bello, and D. Marcuzzi. Tests and analyses for the mechanical and thermal qualification of the new RFX first wall tiles. *Fusion Engineering and Design*, 66-68:289 – 293, 2003. ISSN 0920-3796. doi:10.1016/S0920-3796(03)00158-3.

[174] H. Greuner et al. Design, performance and construction of a 2 MW ion beam test facility for plasma facing components.

Fusion Engineering and Design, 75-79(0):345 – 350, 2005. doi:10.1016/j.fusengdes.2005.06.021.

[175] H. Greuner, B. Boeswirth, J. Boscary, and P. McNeely. High heat flux facility GLADIS: Operational characteristics and results of W7-X pre-series target tests. *Journal of Nuclear Materials*, 367-370, Part B(0): 1444 – 1448, 2007. doi:10.1016/j.jnucmat.2007.04.004.

[176] A Herrmann, H Greuner, J C Fuchs, P de Marné, R Neu, and ASDEX Upgrade Team. Experiences with tungsten coatings in high heat flux tests and under plasma load in ASDEX Upgrade. *Physica Scripta*, 2009(T138):014059, 2009. doi:10.1088/0031-8949/2009/T138/014059.

List of Publications

[CBA+13] A. Canton, S. Dal Bello, M. Agostini, L. Carraro, R. Cavazzana, S. Fiameni, L. Grando, **B. Rais**, M. Spolaore, and M. Zuin. Studies of spatial uniformity of glow discharge cleaning plasmas on the RFX-mod device . *Journal of Nuclear Materials*, 438, Supplement(0):S1164 – S1167, 2013.

[GLC+15] F. Ghezzi, L. Laguardia, R. Caniello, A. Canton, S. Dal Bello, **B. Rais**, and M. Anderle. XPS, SIMS and Attenuated Total Reflectance (ATR) characterization of boronized graphite from RFX-mod. *Applied Surface Science*, 2015. Submitted.

[IMR+14] P. Innocente, D.K. Mansfield, A.L. Roquemore, M. Agostini, S. Barison, A. Canton, L. Carraro, R. Cavazzana, G. De Masi, A. Fassina, S. Fiameni, L. Grando, **B. Rais**, F. Rossetto, and P. Scarin. Lithium wall conditioning by high frequency pellet injection in RFX-mod. *Journal of Nuclear Materials*, 2014.

[tea14] **B. Rais** et al. Study of the effect of the glow power on the growth of the boron coating obtained with boronizations in RFX-mod. June 2014. 41^{th} EPS Conference on Plasma Physics.

وَيَسْـَٔلُونَكَ عَنِ ٱلرُّوحِ ۖ قُلِ ٱلرُّوحُ مِنْ أَمْرِ رَبِّى وَمَآ أُوتِيتُم مِّنَ ٱلْعِلْمِ إِلَّا قَلِيلًا ﴿٨٥﴾

And they ask you, about the soul. Say, 'The soul is of the affair of my Lord. And mankind have not been given of knowledge except a little'

— (17:85)